

# Practical rectennas : far-field RF power harvesting and transport

**Citation for published version (APA):**

Keyrouz, S. (2014). *Practical rectennas : far-field RF power harvesting and transport*. [Phd Thesis 1 (Research TU/e / Graduation TU/e), Electrical Engineering]. Technische Universiteit Eindhoven.  
<https://doi.org/10.6100/IR774472>

**DOI:**

[10.6100/IR774472](https://doi.org/10.6100/IR774472)

**Document status and date:**

Published: 01/01/2014

**Document Version:**

Publisher's PDF, also known as Version of Record (includes final page, issue and volume numbers)

**Please check the document version of this publication:**

- A submitted manuscript is the version of the article upon submission and before peer-review. There can be important differences between the submitted version and the official published version of record. People interested in the research are advised to contact the author for the final version of the publication, or visit the DOI to the publisher's website.
- The final author version and the galley proof are versions of the publication after peer review.
- The final published version features the final layout of the paper including the volume, issue and page numbers.

[Link to publication](#)

**General rights**

Copyright and moral rights for the publications made accessible in the public portal are retained by the authors and/or other copyright owners and it is a condition of accessing publications that users recognise and abide by the legal requirements associated with these rights.

- Users may download and print one copy of any publication from the public portal for the purpose of private study or research.
- You may not further distribute the material or use it for any profit-making activity or commercial gain
- You may freely distribute the URL identifying the publication in the public portal.

If the publication is distributed under the terms of Article 25fa of the Dutch Copyright Act, indicated by the "Taverne" license above, please follow below link for the End User Agreement:

[www.tue.nl/taverne](http://www.tue.nl/taverne)

**Take down policy**

If you believe that this document breaches copyright please contact us at:

[openaccess@tue.nl](mailto:openaccess@tue.nl)

providing details and we will investigate your claim.

**Practical Rectennas**  
**Far-Field RF Power Harvesting and**  
**Transport**

This research was financially supported by Holst Centre/imec the Netherlands.

Practical Rectennas - Far-Field RF Power Harvesting and Transport / by S.  
Keyrouz – Eindhoven : Technische Universiteit Eindhoven, 2014 – Proefschrift

A catalogue record is available from the Eindhoven University of Technology  
Library

ISBN: 978-90-386-3639-9 NUR: 959

This thesis was prepared with the  $\text{\LaTeX} 2_{\epsilon}$  documentation system

Reproduction: TU/e print-service, Eindhoven, The Netherlands

Copyright ©2014 by S. Keyrouz. All rights reserved.

# **Practical Rectennas Far-Field RF Power Harvesting and Transport**

PROEFSCHRIFT

ter verkrijging van de graad van doctor aan de  
Technische Universiteit Eindhoven, op gezag van de  
rector magnificus, prof.dr.ir. C.J. van Duijn, voor een  
commissie aangewezen door het College voor  
Promoties in het openbaar te verdedigen  
op donderdag 5 juni 2014 om 16.00 uur

door

Shady Keyrouz

geboren te Bsharri, Libanon

Dit proefschrift is goedgekeurd door de promotoren en de samenstelling van de promotiecommissie is als volgt:

voorzitter: prof.dr.ir. P.P.J. van den Bosch  
1<sup>e</sup> promotor: prof.dr.ir. H.J. Visser  
2<sup>e</sup> promotor: prof.dr. A.G. Tjihuis  
leden: prof.dr.ir. P.G.M. Baltus  
prof.dr. E.A. Lomonova  
prof.dr.ir. G.A.E. Vandenbosch (Katholieke Univesiteit Leuven)  
prof.dr. C. Vollaire (Université Ecole Centrale de Lyon)  
dr. P. Mitcheson (Imperial London College)

”It is only with the heart that one can see rightly,  
what is essential is invisible to the eye.”

Antoine de Saint-Exupry (1900-1944)



# Contents

---

<b>Summary</b>	<b>xi</b>
<b>1 Introduction</b>	<b>1</b>
1.1 Introduction . . . . .	1
1.1.1 Trends and Needs . . . . .	2
1.2 Non-Radiative and Radiative RF Power Transfer . . . . .	3
1.2.1 Non-Radiative Transfer . . . . .	3
1.2.2 Radiative Transfer . . . . .	4
1.3 Smart Building Initiative (SBI) . . . . .	5
1.4 Challenges . . . . .	6
1.5 Organization of the Thesis and Original and Novel Contributions . . . . .	7
1.6 Figure of Merit . . . . .	10
1.6.1 Power Wave Reflection Coefficient . . . . .	10
1.6.2 Application of the Power Wave Reflection Coefficient as a Figure of Merit . . . . .	11
<b>2 Rectifier Analysis for RF Energy Harvesting and Power Transport</b>	<b>13</b>
2.1 Introduction . . . . .	14
2.2 Schottky Diode Equivalent Circuit Model . . . . .	14
2.3 Measurement Setup and Measured Results . . . . .	19
2.4 Output Voltage of the Rectifier Circuit . . . . .	22
2.5 Investigation of the Diode Parameters on the Output Voltage . . . . .	23
2.6 Voltage Multiplier . . . . .	25
2.7 Rectenna Design . . . . .	26
2.7.1 Operating Frequency . . . . .	28
2.7.2 Expected Input Power Level . . . . .	29
2.8 Conclusion . . . . .	31
<b>3 RF Power Transport Employing Rectennas Using Matching Networks</b>	<b>33</b>
3.1 Introduction . . . . .	34



3.2	Center-Fed and Step-Shaped-Fed Strip Dipoles . . . . .	35
3.3	Printed Yagi-Uda Antenna and Parameter Optimization . . . . .	37
3.3.1	Optimization of the Distance Between Feed and Director (D-D) and the Director Length (D-L) . . . . .	38
3.3.2	Optimization of the Distance Between Feed and Reflector (R-D) . . . . .	40
3.4	Modified Yagi-Uda antenna . . . . .	40
3.4.1	Modified-Yagi: Three Resonant Modes . . . . .	42
3.4.2	Optimization of the Arm Width $b$ . . . . .	43
3.4.3	Optimization of the Step Length $t$ . . . . .	44
3.4.4	Fabricated Antenna . . . . .	46
3.5	Triple-Band Modified Yagi-Uda Antenna . . . . .	48
3.6	Dual-Band Modified Yagi-Uda Antenna . . . . .	51
3.7	RF Power Transport at 868 MHz . . . . .	53
3.7.1	Lumped-Element Matching Network . . . . .	53
3.7.2	RF Power Transport Measurement Results . . . . .	55
3.8	Conclusion . . . . .	59
<b>4</b>	<b>Compact and Conjugate-Matched Antenna Design</b>	<b>61</b>
4.1	Introduction . . . . .	61
4.2	Strip Dipole Antenna . . . . .	62
4.2.1	Equivalent Radius of a Strip Dipole Antenna . . . . .	63
4.2.2	Input Impedance of a Strip Dipole Antenna . . . . .	64
4.2.3	Feeding Gap S Dependence . . . . .	67
4.2.4	Fabricated Antenna . . . . .	69
4.3	Folded-Strip Dipole Antenna . . . . .	69
4.3.1	Input Impedance of a Strip Folded Dipole . . . . .	71
4.3.2	Transmission Line Analytical Equations . . . . .	71
4.3.3	Validation of the New Analytical Procedures . . . . .	72
4.4	Modified Rectangular Loop Antenna . . . . .	76
4.4.1	Impedance Tuning Capability . . . . .	78
4.4.2	Validation of the Simulation Results . . . . .	80
4.4.3	Radiation Efficiency and Radiation Pattern . . . . .	81
4.5	Conclusion . . . . .	85
<b>5</b>	<b>RF Power Transport Using Conjugate-Matched Rectenna System</b>	<b>87</b>
5.1	Introduction . . . . .	88
5.2	Design Methodology . . . . .	88
5.2.1	Antenna Matched to the Rectifier . . . . .	90
5.2.2	Maximizing the Output Voltage . . . . .	91
5.3	Power Transport Using Commercially Available Diodes . . . . .	94
5.3.1	Rectenna Design . . . . .	94

5.3.2	RF Power Transport Measurement Results . . . . .	97
5.4	Five Stage CMOS Rectifier with a Control Loop . . . . .	101
5.4.1	Design and Implementation . . . . .	101
5.4.2	Antenna Optimization and Chip Integration . . . . .	103
5.4.3	Measurement Results . . . . .	107
5.5	Conclusion . . . . .	109
<b>6</b>	<b>RF Power Transfer - Complete Rectenna System</b>	<b>111</b>
6.1	System Concept and Measurement Setup . . . . .	112
6.2	Measurement Results . . . . .	114
6.3	Conclusion . . . . .	118
<b>7</b>	<b>A Frequency Selective Surface for RF Energy Harvesting</b>	<b>119</b>
7.1	Introduction . . . . .	120
7.2	Square Loop FSS . . . . .	123
7.2.1	Model Verification . . . . .	124
7.2.2	Effect of the Supporting Dielectric Substrate . . . . .	127
7.3	Gridded Square Loop FSS . . . . .	129
7.3.1	Equivalent Circuit Model . . . . .	129
7.3.2	Model Verification and Waveguide Simulator Measurements . . . . .	130
7.4	Loaded Gridded Square-Loop FSS . . . . .	134
7.4.1	Equivalent Circuit Model . . . . .	134
7.4.2	FSS Loaded with Capacitors . . . . .	136
7.5	FSS Power Harvesting - Final Design . . . . .	138
7.5.1	FSS Current Density . . . . .	140
7.5.2	RF-Power Transport Measurement Results . . . . .	142
7.6	Conclusions . . . . .	144
<b>8</b>	<b>Conclusions and Recommendations</b>	<b>145</b>
8.1	Conclusions . . . . .	146
8.2	Recommendations . . . . .	148
<b>A</b>	<b>King-Middleton Second Order Method Investigation</b>	<b>151</b>
A.1	King-Middleton Second-Order Method . . . . .	151
A.1.1	Verification of the King-Middleton Equations by the Finite Inte- grating Technique . . . . .	152
A.2	Modified King-Middleton Equations . . . . .	154
A.2.1	Modified King-Middleton Equations - Real Part . . . . .	154
A.2.2	Modified King-Middleton Equations - Imaginary Part . . . . .	155
A.2.3	Comparison Between KM and Corrected KM . . . . .	156
A.3	Strip Folded-Dipole Antenna . . . . .	158

<b>B Frequency Selective Surfaces Equivalent Circuit Model</b>	<b>163</b>
B.1 Correction Factor G . . . . .	163
<b>Bibliography</b>	<b>167</b>
<b>List of publications</b>	<b>175</b>
<b>Acknowledgements</b>	<b>177</b>
<b>Curriculum Vitae</b>	<b>179</b>

# Summary

## Practical Rectennas: Far-Field RF Power Harvesting and Transport

---

Energy harvesting from renewable sources such as the sun and wind, as well as from other sources like heat and vibration have been the focus of research recently. However, an increasing number of applications, especially inside buildings where light/solar energy is not always sufficient, cannot profit from these sources. Wireless Power Transmission (WPT) overcomes the lack of different power sources, such as light, heat and vibration and is an attractive powering method for battery-less sensor nodes, and active Radio-Frequency Identification (RFID) tags.

In this thesis, different rectenna topologies are investigated and state-of-the-art rectenna systems are discussed. The basic far-field energy harvester (rectenna) consists of an antenna, which captures a part of a transmitted RF signal, that is connected to a rectifier which converts the AC captured signal into a DC power signal. For a maximum power transfer, a matching network between the antenna and the rectifier is needed. In order to decrease the size of the system and improve the power conversion efficiency, the matching network can be removed by directly matching the antenna to the rectifier. A power management circuit is needed after the rectifier to store the harvested DC power and regulate the output voltage. This thesis is divided into four main parts:

- The rectifier is investigated in the first part. Since the rectifier is a nonlinear device and its impedance changes as a function of frequency and power, an accurate analysis model of the rectifier's impedance as a function of both is presented. The model is verified using Harmonic Balance simulations and measurements. In addition, the optimization of the rectifier's parameters for maximizing the output voltage is presented.
- The second part of the thesis presents a far-field power transport system employ-

ing rectennas using matching networks. A novel, modified,  $50\Omega$  Yagi-Uda antenna is presented. The main advantage of the presented antenna is that it can operate as a broad-band, dual band or a multi-band antenna. Three prototypes are fabricated, and the simulation results are validated by measurements. A rectenna system operating at 868 MHz is experimentally validated. Results are reported, demonstrating, at an input power level of -10 dBm, an RF to DC power conversion efficiency (PCE) of 49.7%. The  $50\Omega$  rectenna system exhibits an increased PCE of at least 5 % at -10 dBm and at least 10 % at -20 dBm, compared to reported state-of-the-art results.

- The focus of the third part of the thesis is on reducing the antenna size and at the same time keeping a high radiation efficiency. A novel (modified) rectangular loop antenna is presented. The benefits of the suggested novel antenna topology are the compact size and the ability to tune its input impedance while keeping a constant radiation efficiency. Using the suggested antenna, at an input power level of -10 dBm, the power conversion efficiency reaches 54%. The novel compact rectenna system is smaller in size and exhibits an increased PCE of at least 10 % at -10 dBm compared to reported state-of-the-art results.
- The fourth part of the thesis introduces a method to harvest RF power using Frequency Selective Surfaces (FSS). The novel FSS design is capable to harvest power from arbitrarily polarized incident waves. The design does not involve a matching network which results in a simple, polarization-independent power harvester. A simple equivalent circuit model to predict the transmission and reflection characteristics of the gridded-square-loop FSS is employed. Two prototypes have been fabricated and an RF to DC conversion efficiency of 25 % for the first prototype and 15.9 % for the second one are measured at  $3.2\mu\text{W}/\text{cm}^2$  available power density level.

Recommendations, future work, and means to enhance the power conversion efficiency as well as the system performance are addressed in the conclusion chapter.

## CHAPTER ONE

# Introduction

---

### 1.1 Introduction

In this chapter we will give the rationale for the analysis and development of *rectifying antennas* or *rectennas*. Rectennas are used for converting RF energy, radiated by a distant (intentional or unintentional) source, into usable DC energy. Rectennas are used for transferring far-field, radiative RF energy into DC energy and in that respect differ from inductive or non-radiative, resonant, RF energy transferring systems. The differences between the two ways of RF-to-DC power conversion will be given and potential applications for far-field RF energy transfer will be discussed. These applications will be linked to wireless sensors. The outline of the thesis will be discussed, highlighting the new and original contributions. The chapter will be concluded by an overview of frequency bands used throughout the thesis and a single-number Figure of Merit used to compare complex numbers resulting from various simulations and measurements.

### 1.1.1 Trends and Needs

The use of wireless devices is rapidly expanding. The number of mobile phone subscriptions worldwide, for example, has expanded more than twelve times between 1997 and 2007, see Fig. 1.1 [1].

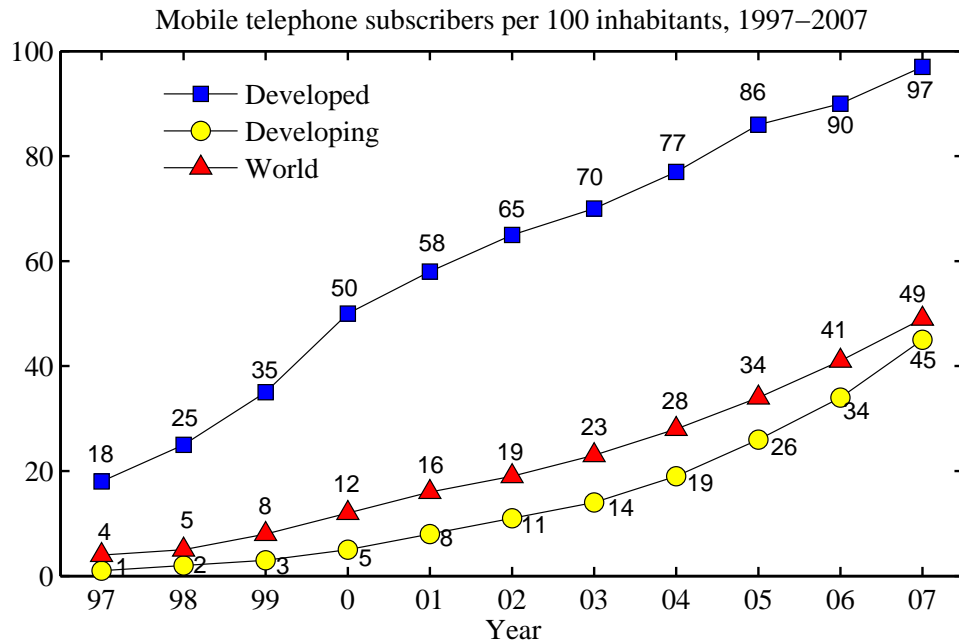


**Figure 1.1.** Mobile phone subscribers per 100 inhabitants, 1997-2007 [1]. Courtesy ITU .

Both Cisco [2] and Ericsson [3] expect 50 billion wireless devices to be connected to the internet in 2020, serving a population of 7.6 billion [2]. For wireless devices in general, the world Wireless Research Forum (WWRF) estimates 7 trillion wireless devices serving 7 billion people [4]. The total market for wireless sensor devices totaled \$532 million in 2010, \$790 million in 2011 and is expected to increase to \$4.7 billion in 2016 [5].

Next to this expected growth in the use of wireless devices, also a need is developing for an increased wireless sensor autonomy and small form factor, see Fig. 1.2 [6]. The need for long lifetime and small form factors of future wireless sensor nodes do not match up well with currently available battery technology [7]. Alternative ways of powering may be found in energy harvesting where energy is taken from ambient sources like vibration, thermal differences, light and radiofrequency (RF) signals.

One of the main potential applications we see for employing far-field RF energy harvesting and transfer is in the so-called Smart Building Initiative (SBI) concept [8]. Before discussing SBI in detail, we will first discuss the differences between inductive resonant-

coupling and radiative far-field power transfer and the differences between transfer and harvesting.

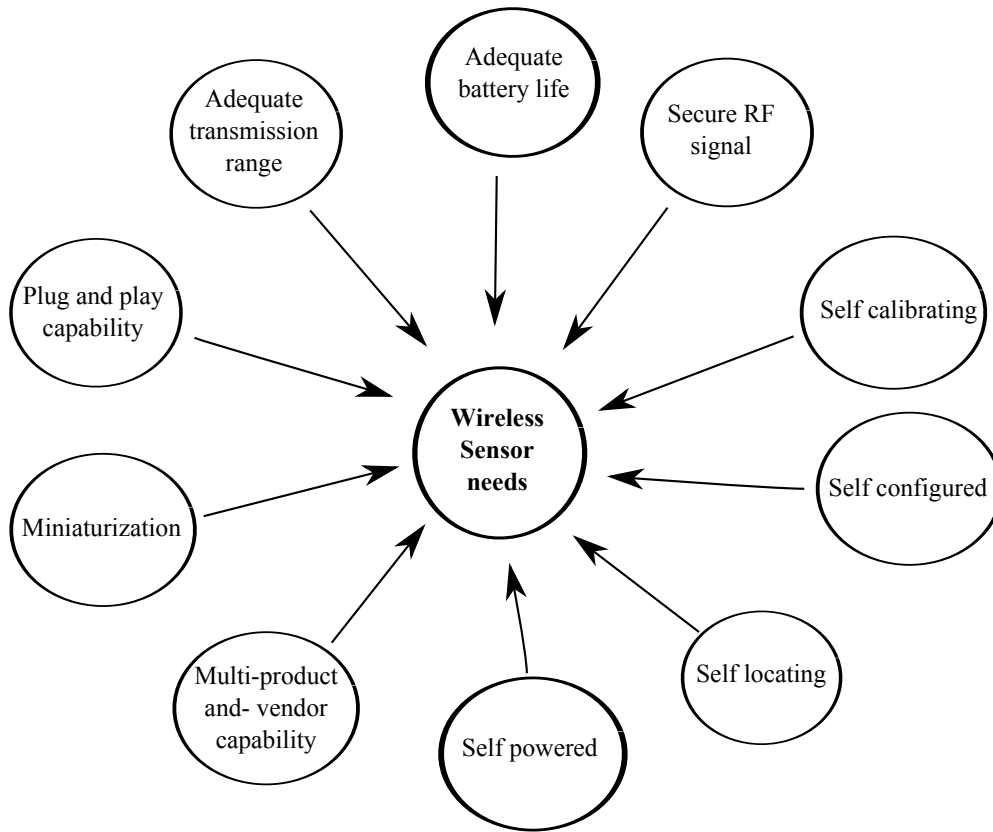


Figure 1.2. Needs for wireless sensors.

## 1.2 Non-Radiative and Radiative RF Power Transfer

When employing RF signals for the transfer of energy, we make a distinction between non-radiative and radiative RF energy transfer. The former is based on (inductive) coupling, the latter uses the transmission and reception of radio waves. When the transmitting source is unintentional, we call the transfer of energy *harvesting*. For a radiative system this might take the form of converting e.g. the energy in radio broadcasting signals into DC energy.

### 1.2.1 Non-Radiative Transfer

Non-radiative RF energy transfer is mostly employed in inductive systems, obeying the Qi standard [9]. Two coils are brought in each others vicinity for transferring RF energy, see Fig. 1.3. The two coils in close proximity form an electrical transformer. By



applying capacitors, a resonant coupling system is created [10], increasing the power transfer efficiency.

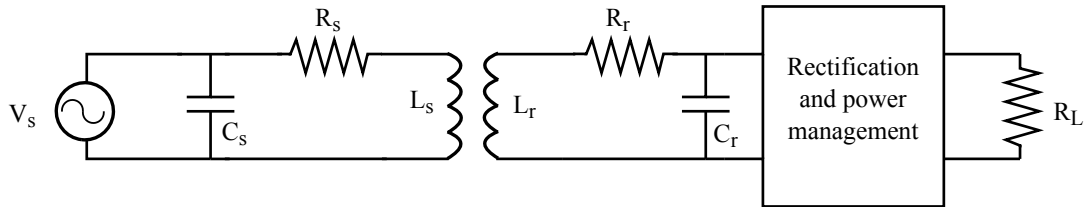


**Figure 1.3.** Resonant coupling (non-radiative) RF energy transfer system.

In the circuit shown in Fig. 1.3, a RF source is connected to a coil  $L_s$ , that is resonated with a capacitor  $C_s$ . A receiving coil  $L_r$ , resonated with a capacitor  $C_r$  is placed in close proximity and the received signal is rectified, eventually accumulated and used to power a source that is represented by load resistance  $R_L$ . The resistances  $R_s$  and  $R_r$  represent the losses in the transmitting and receiving coils, respectively. The benefit of this resonant coupling energy transfer, apart from being subject to a standard, lies in the high power transfer efficiency [11]. The drawbacks are in the limited transferring distance, the transfer efficiency falls off very steeply for distances larger than approximately one coil diameter, which also makes harvesting (taking energy from the ambient) impossible. For RF energy transfer over a distance, we need to employ radiative transfer.

## 1.2.2 Radiative Transfer

In a radiative transfer system, a RF source (unintentional or intentional) is connected to an antenna that emits radio waves. At a distance from this radio source, a receiving antenna intercepts a part of the radiated waves and the RF signal captured by the antenna is rectified, eventually accumulated and transferred to a load (wireless sensor), see Fig. 1.4. The dashed box in this figure is in fact a *rectifying antenna*, commonly known as a rectenna.

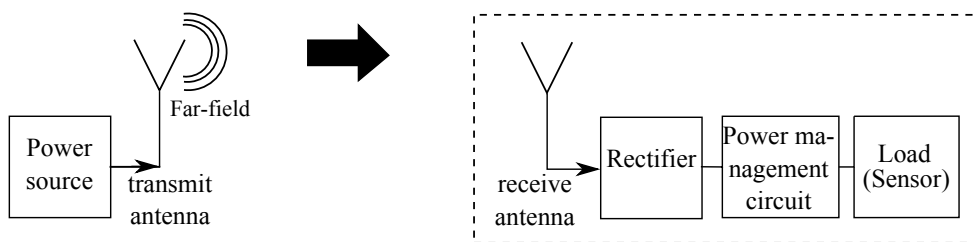


**Figure 1.4.** Radiative RF energy transfer system. The dashed box is commonly denoted rectenna.

Wireless radio-frequency (RF) energy transmission dates back to the experiments of Heinrich Hertz, in the 1880s, proving Maxwells theory of electromagnetics [12]. Initiated by an interest in short-range ( $\leq 2$  m [13]) radio-frequency identification (RFID) applications, far-field RF energy transfer has become a research topic at many European, American and Asian universities and research institutes [14–22]

### 1.3 Smart Building Initiative (SBI)

In a smart building, wireless sensors will measure, amongst others, the presence of persons, the local temperature and the lighting strength. Based on these readings that are transmitted to a central station, lighting and heating conditions will be adjusted (switched off or reduced if no persons are present). Thus energy consumption will be reduced. Artificial lighting, for instance, contributes approximately 30% of electricity consumption in a commercial building, and buildings collectively account for 40% of total world energy use [23]. SBI may also add to an increased well-being of elderly people when employed in an assisted living scenario, allowing the aged to live at home for a longer period [24], [25]. SBI relies on the use of a large number of wireless sensors, see also Fig. 1.5 [26].

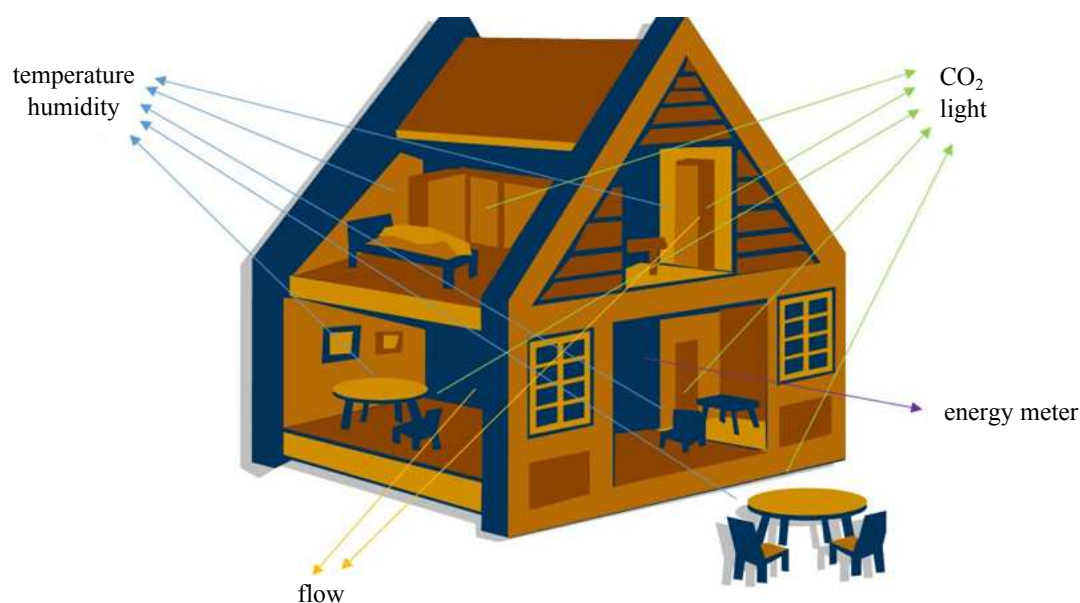


**Figure 1.5.** Wireless sensors in a smart building.

Both aspects of SBI, a reduction in energy consumption and assisted living, are expected to generate a large economic impulse. The European home automation market revenues

were US\$232.6 million in 2007 with an expected increase to US\$446.6 million in 2013 [27]. In April 2011, the European smart homes and assisted living market was estimated to grow by 16.2% from US\$1,544 million in 2010 to US\$3,267 million in 2015 [28]. Recent estimates of revenues from home automation systems in Europe and North America project a growth at a compound annual rate of 42% from US\$ 1.2 billion in 2012 to nearly US\$ 9.4 billion in 2017 [29].

This needed widespread use of wireless sensors in offices and houses has, however, been severely slowed down due to the cost of cabling. Cabling an average office unit or a four bed house is estimated at €7,000–11,000 (\$9,000–15,000) [30]. This is especially true for offices, that are, on average, reconfigured every five years [31]. Although using batteries may severely reduce these cabling costs, the maintenance issues associated with using primary batteries – i.e. locating batteries to be replaced and disposing of the old ones will not be tolerated by the market [32].

Then what remains for powering the many wireless sensors is energy harvesting. Well known sources for energy harvesting are [7]: vibration, ambient light, temperature gradients, and (ambient) radio waves. With the exception of intentional radio waves, the availability of energy harvesting sources of sufficient power cannot be guaranteed under all circumstances [12]. Therefore we will concentrate on the use of dedicated RF sources, distributed in a building for powering the wireless sensors. The investment in these sources and the costs of powering them will be more than compensated by the reduction in power consumption of the whole building by switching off lights and turning down heating.

## 1.4 Challenges

For powering the wireless sensors needed in SBI we will employ the license-free frequency bands for Industry, Science and Medicine (ISM). Although these frequency bands can be used without the need for a license, they are restricted in the maximum allowed Effective Isotropic Radiated Power (EIRP), that is the transmit power multiplied by the transmit antenna gain. For ISM frequencies between 865 MHz and 2.48 GHz the maximum allowed EIRP does not exceed 4W [12]. Due to the spherical spreading of the transmitted electromagnetic waves, the power received at the rectenna side will decrease inversely with the squared distance between transmitter and receiver so that, in general, we will have to deal with low received RF power levels. That means that all the subsystems of a rectenna, especially the antenna and the rectifier need to be designed and impedance matched very carefully. As already demonstrated in [33], the RF-to-DC power conversion efficiency of the rectenna may be maximized by directly, complex-conjugate impedance matching the antenna to the rectifier. Thus, we need to be able to determine the (complex) RF input impedance of a rectifier circuit and need

to be able to model and design antennas generating a desired complex input impedance. Furthermore, we need to be able to find the optimum input power level and frequency to operate the rectifier circuit. All these topics will be discussed in this thesis.

## 1.5 Organization of the Thesis and Original and Novel Contributions

The organization of the thesis is graphically depicted in Fig. 1.6.

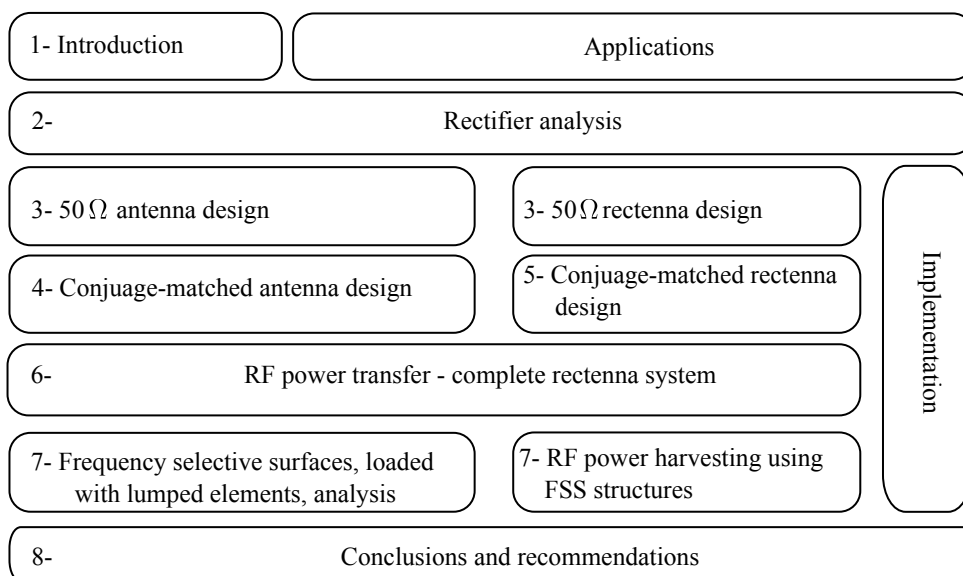


**Figure 1.6.** Outline of this thesis.

In Chapter 1 the problem of powering an increasing number of wireless devices is discussed as well as the possibilities of harvesting power from the ambient. The use of RF power transfer and harvesting is discussed in more detail and far-field, radiative RF power transfer is chosen as the preferred way to transfer power wirelessly over a substantial distance. The main application of this technology is seen in Smart Building Initiatives and assisted living. Due to restricted power densities it is concluded that the design of the subsystems of a rectifying antenna (rectenna) as well as the impedance matching between these subsystems must be carried out very carefully. Therefore it is important to develop accurate and easy to implement and use models of especially rectifying circuits and antennas. On top of that, a design strategy with respect to the choice of the operating frequency, RF input power and impedance matching needs to be developed. In Chapter 2, the analytical modeling of a high-frequency, rectifying Schottky diode is discussed. Based on the model, the influence of the bulk resistance and the

saturation current on the DC output voltage is analyzed. The main contributions and innovations of Chapter 2 are:

- The derivation of a Schottky diode selection criterion and the selection of commercially available Schottky diodes according to this criterion.

Chapters 3 to 5 deal with antenna design, where the designs are immediately applied in a co-design with a rectifier to create rectenna structures, see Fig. 1.6. Chapter 3 deals with an antenna structure that can be designed for dual, triple or broadband frequency use. Based on a reported broadband strip-dipole antenna, a Yagi-Uda like configuration is created around this active strip-dipole antenna to improve the antenna characteristics with respect to bandwidth and gain. The antenna is designed for a  $50 \Omega$  input impedance. The new configuration is used to design a rectenna, using a lumped-element network to match the antenna impedance to the complex input impedance of a voltage doubling rectifier.

The main contributions and innovations of Chapter 3 are:

- A wideband strip-dipole antenna is combined with parasitic elements in a Yagi-Uda like antenna configuration to create a dual, triple or broadband antenna having a moderate gain (3 to 6 dBi).
- The new antenna concept has been used to design a rectenna that demonstrates an increased Power Conversion Efficiency (PCE) of at least 5 % at -10 dBm and at least 10 % at -20 dBm with respect to the state of the art as published in the open literature.

Chapter 4 deals with antenna structures intended for a direct conjugate matching to the rectifier, thus omitting an impedance matching network that will lead to a higher power conversion efficiency (less loss) and a more compact design (fewer lumped elements). Started is in chapter 4 with the strip-dipole antenna analysis. The derived model is used in modeling a strip folded-dipole antenna. Evolving from this latter antenna, a modified loop antenna is introduced and full-wave analyzed. The main contributions and innovations of Chapter 4 are:

- The validity range (length and width) of the impedance equation for a strip dipole antenna has been extended by deriving new fitting equations.
- The accuracy of an existing strip-folded dipole antenna has been improved by using the improved strip-dipole antenna model.
- A new, electrically small antenna type has been invented that allows for tuning the complex input impedance and the radiation efficiency independently.

In Chapter 5 a design strategy for maximizing the sensitivity of a rectenna is outlined. As a consequence, an antenna should be designed for having a very low real part of the input impedance and a high absolute value of the imaginary part. The new antenna discussed in chapter 4 is used for this purpose and is co-designed with a lumped-element Schottky diode rectifier and with an integrated custom-made rectifier. Both realized rectennas demonstrate characteristics better than the state of the art. The main contributions and innovations of Chapter 5 are:

- The realization of a rectenna with dimensions smaller than the state of the art and demonstrating a RF-to-DC power conversion efficiency larger than state-of-the art.
- A rectenna based on a co-design of the same antenna and a custom made rectifier demonstrating the smallest dimensions paired to the highest sensitivity ever reported in the open literature.

In Chapter 6, a complete rectenna system is presented where a commercially available power management circuit, a 1000  $\mu\text{F}$  storage capacitor and a dynamic load are used. The average DC output power and the system's RF to DC conversion efficiency are measured, and compared to those measured for a commercially available rectenna system operated under the same conditions. It is shown that the commercially available rectenna system fails to operate at low power levels ( $\leq -6\text{dBm}$ ) while the presented system can operate at an RF input power level as low as  $-13\text{ dBm}$ . At an input power level of  $0\text{ dBm}$ , the power conversion efficiency of the commercially available system does not exceed  $19\%$ , while the power conversion efficiency of the presented system reaches  $40\%$ , resulting in more than  $20\%$  improved power conversion efficiency. The main contributions and innovations of Chapter 6 are:

- Full rectenna system prototyped and characterized.
- Improved performance compared to commercially available system.

In Chapter 7, the analysis of a gridded square loop Frequency Selective Surface (FSS) is extended with the inclusion of lumped elements to model the presence of Schottky diodes for harvesting RF power. The updated model that is validated through cross-simulations and waveguide simulator measurements predicts the resonance frequencies with the diodes included and thus makes it possible to design RF harvesting FSS structures. The main contributions and innovations of Chapter 7 are:

- The recognition of the harvesting structure being essentially a FSS.
- The inclusion of square loops in a grid to maximize the current density in that grid.

- The modeling of the RF power harvesting FSS and the use of this model to optimize a large area RF power harvesting structure.

Finally, Chapter 8 presents a summary of the main results, conclusions and recommendations for future research.

## 1.6 Figure of Merit

In the comparison of different simulation and measurement results for a complex impedance throughout this thesis, we want to end up with a single-number Figure of Merit. For that purpose the power wave reflection coefficient is an excellent tool, relating to a practical use [33].

### 1.6.1 Power Wave Reflection Coefficient

When a source with internal impedance  $Z_R$  is connected to a load impedance  $Z_L$ , see Fig. 1.7, the standard (voltage) reflection coefficient  $\Gamma$  is given by

$$\Gamma = \frac{Z_L - Z_R}{Z_L + Z_R}. \quad (1.1)$$

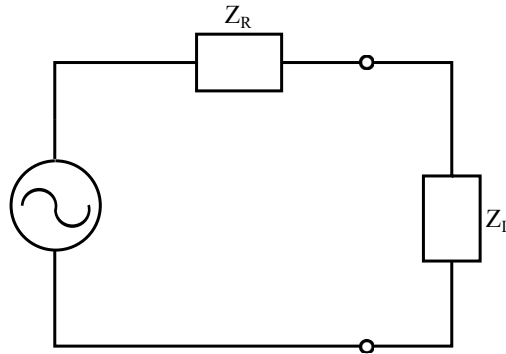


**Figure 1.7.** A source with internal impedance  $Z_R$  is connected to a load impedance  $Z_L$ .

This reflection coefficient is a direct measure for the reflected power only when  $Z_R$  is real-valued [34]. When  $Z_R$  is complex and conjugate impedance matching is applied to maximize the power transfer from generator to load, the standard reflection coefficient in Eq. 1.1 will be nonzero. Therefore, the standard definition of reflection coefficient, based on physical waves propagating along a transmission line, does not in general

represent the reflection of power. Power waves, mathematical constructs from the circuit world, have been introduced to correctly describe the reflection of power in systems with complex reference impedances. The reflection coefficient based on power waves  $\Gamma_p$  is given by

$$\Gamma_p = \frac{Z_L - Z_R^*}{Z_L + Z_R^*}, \quad (1.2)$$

where  $Z_R^*$  denotes the complex conjugate of  $Z_R$ . The reflection coefficient according to Eq. 1.2 works for both real-valued and complex impedances.

### 1.6.2 Application of the Power Wave Reflection Coefficient as a Figure of Merit

We will now apply this power wave reflection coefficient as a Figure of Merit (FoM) to describe the differences between two simulated complex impedance values or between a simulated complex impedance value and a measured value. The FoM will yield a single number describing the discrepancies between two complex impedance values. Lets assume that we have two complex impedance values,  $Z_{m1}$  and  $Z_{m2}$  and we want to compare the two. First we have to make a choice about the reference. Lets assume that we take  $Z_{m1}$  as a reference and compare the  $Z_{m2}$  value to  $Z_{m1}$ . We now assume that we have a black box with input impedance  $Z_{m1}^*$ , see Fig. 1.8.

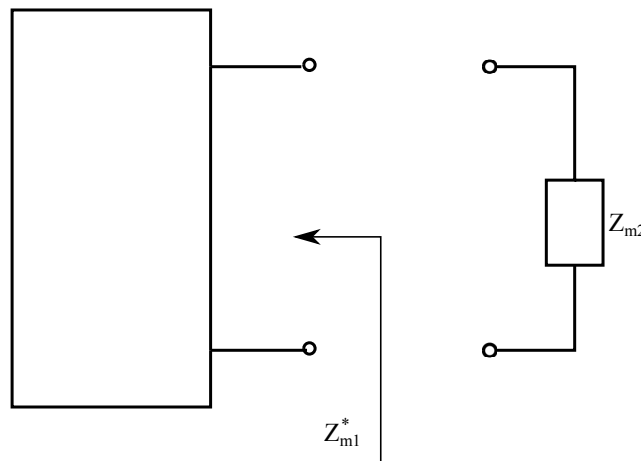


**Figure 1.8.** ‘Connecting’ the impedance to be evaluated to a black box having an input impedance that is the complex conjugate value of the reference impedance.

If we ‘connect’ an impedance  $Z_{m1}$  to this black box, we will have a perfect impedance match and the power wave reflection coefficient for this imaginary system, our Figure



of Merit, will be zero. We are not connecting  $Z_{m1}$  to the imaginary black box however but  $Z_{m2}$ . The amplitude of the power-wave reflection coefficient, our FoM, will give us a single number describing how ‘far off’ this complex impedance is from the desired value  $Z_{m1}$ . Moreover, the FoM relates to real physics, describing how the mismatch will relate to the reflection of power. A reflection of 10 % of the input power (FoM  $\leq$  -10 dB) is considered as acceptable and realizable in practice.

## CHAPTER TWO

# Rectifier Analysis for RF Energy Harvesting and Power Transport

---

In this chapter a complete design method to accurately calculate the impedance and the DC output voltage of the rectifier part in a wireless power transmission system is presented. The presented method uses circuit analysis to calculate the input impedance of a Schottky diode as a function of frequency for different RF input power levels. For the DC output voltage, the Ritz-Galerkin method is used to predict the output DC voltage across different load resistances. Moreover, the influence of the diode parameters on the output voltage is discussed. All the simulated results are validated by measurements and by Harmonic Balance (HB) simulations.

The rectenna design criteria with respect to the operating frequency and the input power level are also motivated in this chapter.

## 2.1 Introduction

Energy harvesting from renewable sources such as solar light and wind, as well as from other sources like heat and vibration, have been the focus of research recently [7]. However, an increasing number of applications, especially inside buildings where light/solar energy is not always sufficient, cannot profit from these sources. Power transport [35] might be a perfect substitute for batteries to drive wireless sensor nodes.

Recent achievements have shown that far-field energy harvesting [3] and power transport, i.e. means to send power over distances, may overcome the lack of different power sources such as light, heat and vibration.

The basic far-field energy harvester consists of an antenna, which captures part of the transmitted RF signal, connected to a rectifier (AC/DC converter) which converts the AC captured signal into a DC power signal. A power management circuit is needed to guide and store the DC power. For maximum power transfer, a matching network is needed between the rectifier and the antenna [36, 37]. The design, fabrication and measurement of an RF harvester employing a matching network will be presented in Chapter 3.

In order to decrease the size of the system, the matching network is removed in [38] and [39] and the antenna is directly matched to the rectifier ( $Z_{antenna} = Z_{rectifier}^*$ ). The design, fabrication and measurement of a rectenna directly matched to the rectifier circuit will be presented in Chapter 5. In both situations, i.e. with or without a matching network, an accurate analysis of the rectifier's RF input impedance is crucial. This chapter investigates the input impedance of the rectifier as a function of frequency for different power levels. In addition, the influence of the diode's parameters on the output voltage and consequently on the rectifier efficiency are discussed.

## 2.2 Schottky Diode Equivalent Circuit Model

The diode analysis method to be presented has been introduced in [40] and verified in [33, 41, 42]. The method uses circuit analysis to calculate the input impedance of a packaged Schottky diode as a function of frequency for different power levels.

Figure 2.1(a) shows some commercially available Schottky diodes in SOT-23 package. The equivalent electrical circuit is shown in Fig. 2.1(b).  $C_j$  is the junction capacitance,  $C_p$  and  $L_p$  are the parasitic packaging capacitance and inductance respectively.  $d$  is the ideal diode.  $V_g$  is an RF voltage generator and  $R_g$  is the internal resistance of the generator. Since the Schottky diode is a non-linear device, and its input impedance changes as a function of input power and frequency, the main objective is to present a standard analysis that is fast, accurate and reliable to calculate the impedance of the Schottky diodes.

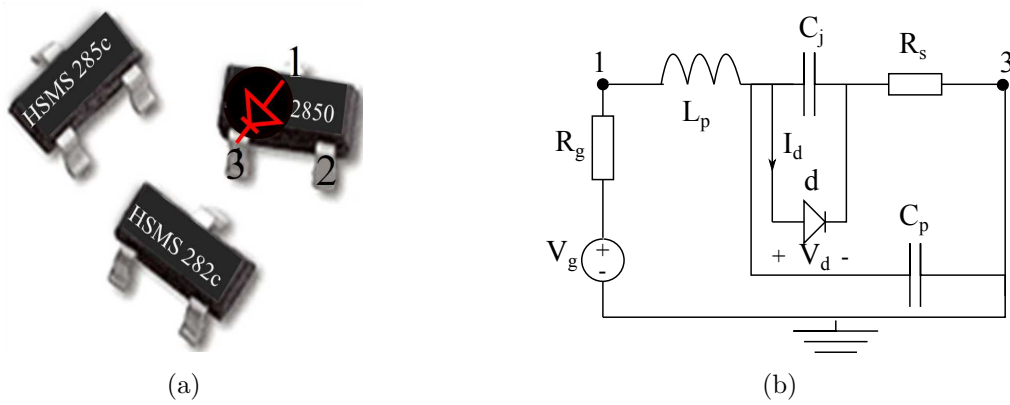


**Figure 2.1.** Commercially available, packaged Schottky diodes (SOT-23) (a) and their equivalent circuit model (b).

To be able to determine the impedance of the rectifier between pins 1 and 3 (see Fig. 2.1), the voltage across and the current through the diode  $d$  should be determined. The electrical behavior of the rectifier is investigated assuming a voltage source with a single frequency  $f_0$  as input,  $V_g = |V_g| \cos(2\pi f_0 t)$ . The electrical behavior of this circuit can be described with the following expressions, obtained by applying Kirchhoff's relations:

$$V_g = I_g R_g + L_p \frac{\partial I_g}{\partial t} + V_{C_P}, \quad (2.1)$$

$$V_{C_P} = V_d + V_{R_s}, \quad (2.2)$$

$$V_{R_s} = R_s (I_{C_j} + I_d), \quad (2.3)$$

$$I_{C_j} = C_j \frac{\partial V_d}{\partial t}, \quad (2.4)$$

$$I_d = I_s (e^{\alpha V_d} - 1), \quad (2.5)$$

so that

$$\frac{\partial V_d}{\partial t} = \frac{1}{R_s C_j} \left\{ \psi \left( \frac{\partial I_g}{\partial t} \right) - R_s I_s (e^{\alpha V_d} - 1) \right\}, \quad (2.6)$$

where  $\psi \left( \frac{\partial I_g}{\partial t} \right) = V_g - R_g I_g - V_d - L_p \frac{\partial I_g}{\partial t}$ .  $\alpha = \frac{q}{nKT}$ , where  $\frac{q}{KT}$  is the thermal voltage and  $n$  is the ideality factor. With the aid of the fourth-order Runge-Kutta method (RK4), Eq. (2.6) can be solved as in [33], and the voltage  $V_d$  across the diode  $d$  is calculated. By using Eq. (2.5), the current  $I_d$  flowing through the diode is determined. After the evaluation of  $V_d$  and  $I_d$  the input impedance of the diode  $d$  is found using Ohm's law:

$$Z_d = \frac{V_d}{I_d}. \quad (2.7)$$

After evaluating the input impedance of the diode  $Z_d$ , using the (Spice) parameters extracted from the manufacturer data sheet, the input impedance of the Schottky diode  $Z_{in}$  including its series resistance and packaging parasitics is calculated. Table 2.1 summarizes the Spice parameters for two commercially available Schottky diodes, Avago HSMS-2820 and HSMS-2850 [43].  $C_{23}$  accounts for a second diode between pins 2 and 3 and is determined empirically from measurements.

To verify the accuracy of the equivalent circuit model, the two different Schottky diodes HSMS-2820 and HSMS-2852 will be investigated. The input impedance versus frequency for different power levels is calculated with the aid of the equivalent circuit model and is compared with harmonic balance simulation results [44] and with measurement results.

**Table 2.1.** Spice parameters used to calculate the impedance of the rectifier shown in Fig. 2.1(b) using the analytical procedure.

Parameter	HSMS-2820	HSMS-2850	Units
$I_s$	2.2E-8	3.0 E-6	A
n	1.08	1.06	-
$R_s$	6.0	25	$\Omega$
$C_j$	0.7	0.18	pF
$L_p$	2.0	2.0	nH
$C_p$	0.08	0.08	pF
$C_{23}$	0.06	0.06	pF

Figures 2.2 and 2.3 show the impedance of the rectifier as calculated by using ADS harmonic balance simulations and the presented analytical expressions. Figures 2.2(a) and 2.2(b) show the real and imaginary parts of the input impedance versus frequency at an input power level of -20 dBm. It is shown in the figures that the equivalent circuit model can predict the impedance of the rectifier with a relative difference of less than 10 % for the real and imaginary parts of the input impedance. In the next paragraph, we will investigate whether this accuracy is sufficient.

In Figs. 2.3(a) and 2.3(b) the input power level is increased to -10 dBm. The input impedance is again calculated using ADS harmonic balance simulations and the equivalent circuit model. It is shown in the figure that the results of the analytical equations are matching the results obtained using harmonic balance simulations. The relative difference for the input impedance calculated by Harmonic Balance (HB) simulation and by the Analytical Expressions (AE) will be presented in detail next.

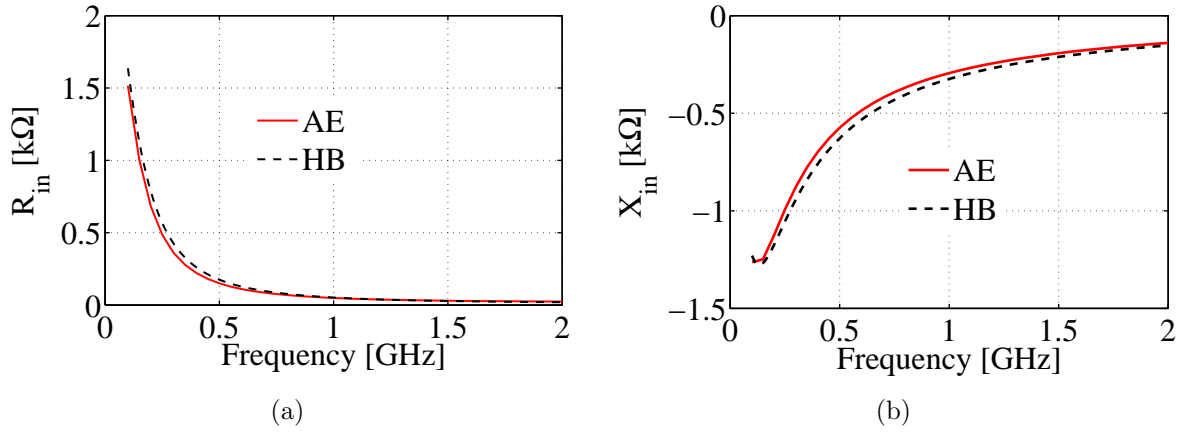


**Figure 2.2.** Real (a) and imaginary (b) parts of the input impedance of the Schottky diode HSMS-2852 versus frequency for a maximum available power level of -20 dBm calculated using the analytical equations (AE) and harmonic balance (HB) simulations.  $R_g = 50\Omega$ .

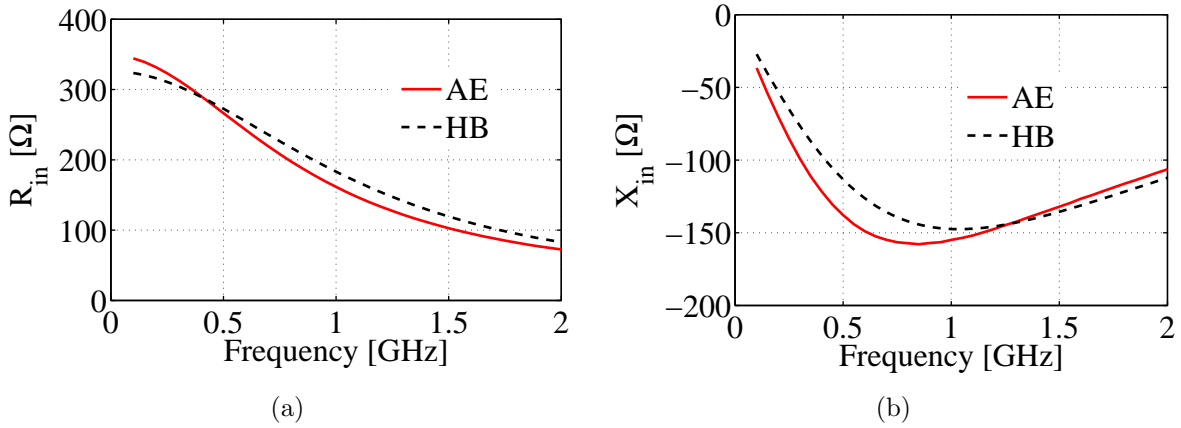


**Figure 2.3.** Real (a) and imaginary (b) parts of the input impedance of the Schottky diode HSMS-2852 as a function of frequency for a maximum available power level of -10 dBm calculated using the analytical equations (AE) and harmonic balance (HB) simulations.  $R_g = 50\Omega$ .

To quantify the accuracy of the simulated results shown in Fig. 2.2 and in Fig. 2.3, the Figure of Merit introduced in the previous chapter (see Sec. 1.6), is used. Here,  $Z_{m_1} = Z_{AE}$  and  $Z_{m_2} = Z_{HB}$ , with  $Z_{AE} = R_{AE} + jX_{AE}$  and  $Z_{HB} = R_{HB} + jX_{HB}$ .  $R_{AE}$  and  $X_{AE}$  are the real and imaginary parts calculated using the presented equivalent circuit model.  $R_{HB}$  and  $X_{HB}$  are the real and imaginary parts of the input impedance calculated using Harmonic Balance simulations. Figure 2.4 shows that the deviations between the results of the analytical circuit model (AE) and the results of Harmonic Balance (HB) simulations do not exceed -10 dB, which satisfies the FoM criterion, which leads to the conclusion that AE results are a good alternative for HB simulations.

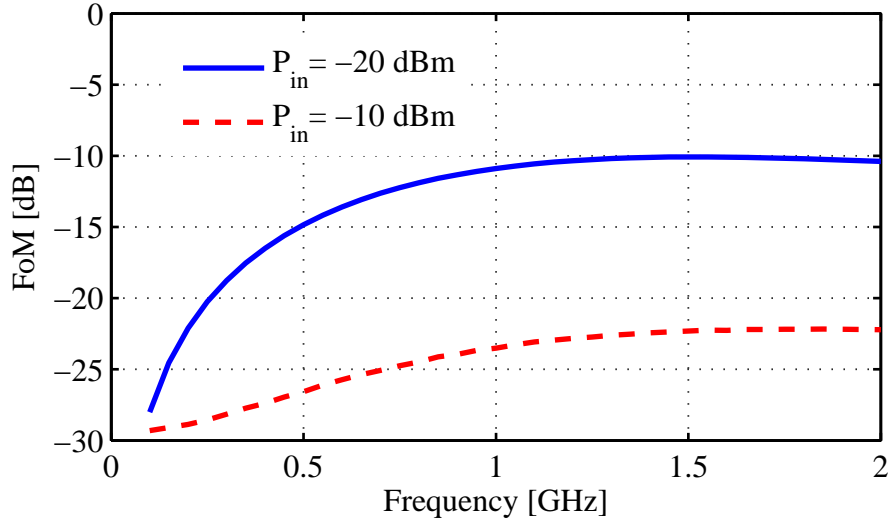


**Figure 2.4.** Figure of Merit to calculate the deviation between the results of the presented equivalent circuit model (AE) and harmonic balance simulation results (HB) as presented in Figs. 2.2 and 2.3. Note the different vertical axis scales in Figs. 2.2 and 2.3.

The real and imaginary parts of the input impedance of the commercially available Schottky diode Avago HSMS-2820 are also calculated from the analytical expressions presented in this section and are compared to the ones obtained by Harmonic Balance simulations [44]. The results at an input power level of 0 dBm and -10 dBm are plotted in Fig. 2.5 and Fig. 2.6, respectively.

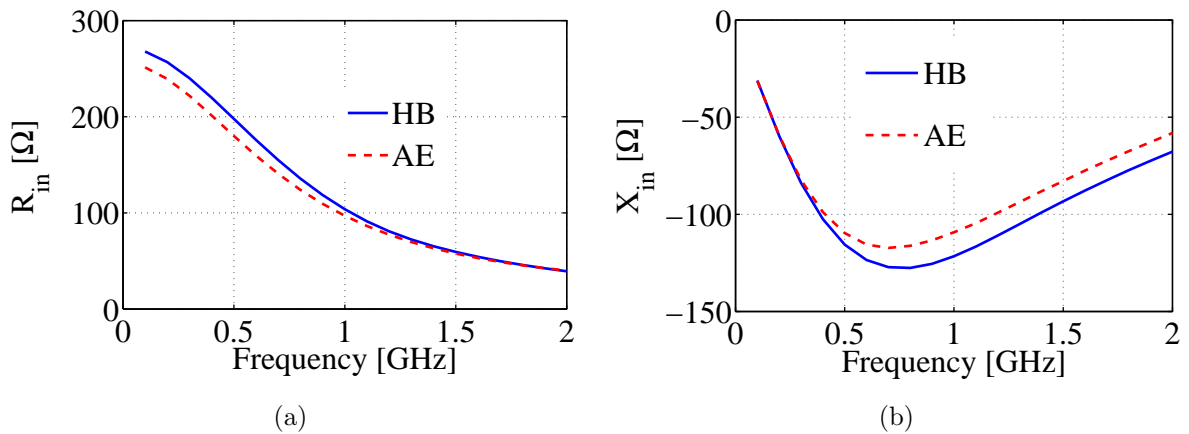


**Figure 2.5.** Real (a) and imaginary (b) parts of the input impedance of the commercially available Schottky diode Avago HSMS-2820 versus frequency for a maximum available power level of 0 dBm calculated using the analytical expressions and harmonic balance simulations. The source has a  $50\Omega$  internal resistance.

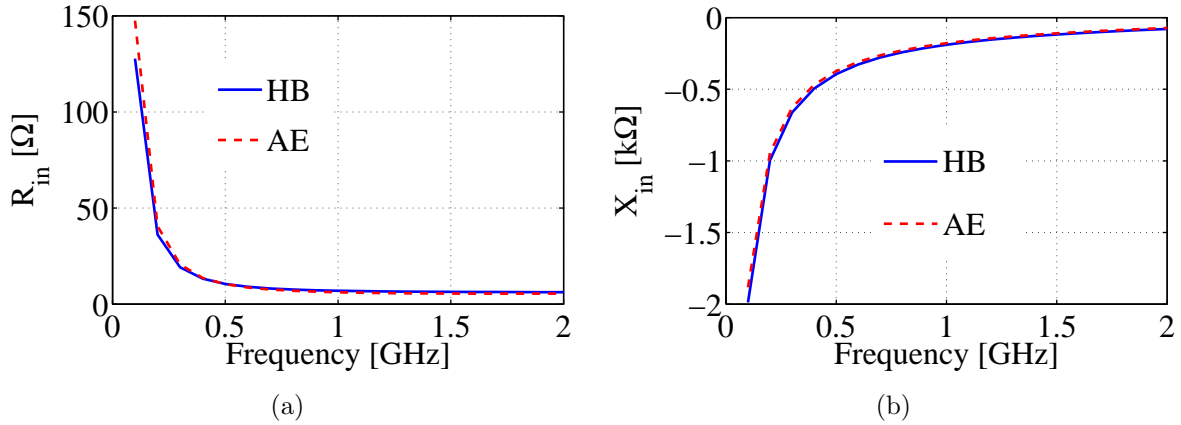


**Figure 2.6.** Real (a) and imaginary (b) parts of the input impedance of the commercially available Schottky diode Avago HSMS-2820 versus frequency for a maximum available power level of -10 dBm calculated using the analytical expressions and harmonic balance simulations. The source has a  $50\Omega$  internal resistance.

The deviations between AE and HB have been calculated as a function of frequency using the Figure of Merit introduced in Sec. 1.6. The deviations do not exceed -10 dB, which validates the accuracy of the presented equivalent circuit model, taking the Harmonic Balance results as a reference. What remains is to confirm the correctness of taking the Harmonic Balance simulation results as a reference. Therefore, we will compare both simulations (AE and HB) with measurements.

## 2.3 Measurement Setup and Measured Results

In this section, the equivalent circuit model will be verified by measurements. In order to fully verify the accuracy of the presented analytical equations, the commercial Schottky diode HSMS-2822 is used for measurements. To measure the impedance of the rectifier the setup shown in Fig. 2.7 is used. The Device Under Test (DUT) is mounted directly on a SMA connector and then connected to the Vector Network Analyzer (VNA) using a phase-stable coaxial cable. A DC blocker is used to prevent DC currents flowing through the VNA. After calibrating, the phase reference point is at the SMA connector (point 1 in Fig. 2.7), so that the phase-stable coaxial cable of length  $l$  has no influence on the measurements. The PNA-X Network Analyzer [45] is used to measure the reflection coefficient  $S_{11}$  at the DUT (Voltage reflected due to the mismatch between  $Z_0$  and  $Z_{DUT}$ ).

$$S_{11} = \frac{Z_{DUT} - Z_0}{Z_{DUT} + Z_0}. \quad (2.8)$$



The input impedance of the rectifier  $Z_{rectifier}$  is calculated from the reflection coefficient

$$Z_{rectifier} = Z_0 \frac{1 + S_{11}}{1 - S_{11}}, \quad (2.9)$$

where  $Z_0 = 50\Omega$ . It should be mentioned that this measurement setup can only be used to measure the impedance of two or more diodes in parallel. If the impedance of a single diode has to be measured, the measurement setup in Fig. 2.7 should be modified and an inductor should be connected in parallel to the rectifier so that the diode can self-bias itself allowing the diode's DC current to return to ground. Pins 1,2 and 3 in Fig. 2.7 correspond to the ones indicated in Fig. 2.1(a).

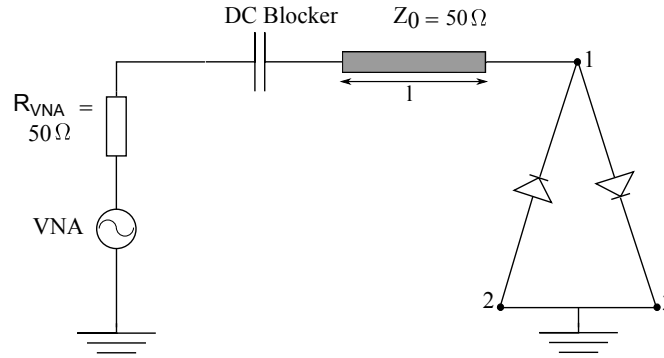


**Figure 2.7.** Setup to measure the impedance of the diode using a Vector Network Analyzer (VNA).

Figures 2.8(a) and 2.8(b) show the real and imaginary parts of the input impedance as a function of frequency at an available power level of  $-15$  dBm.

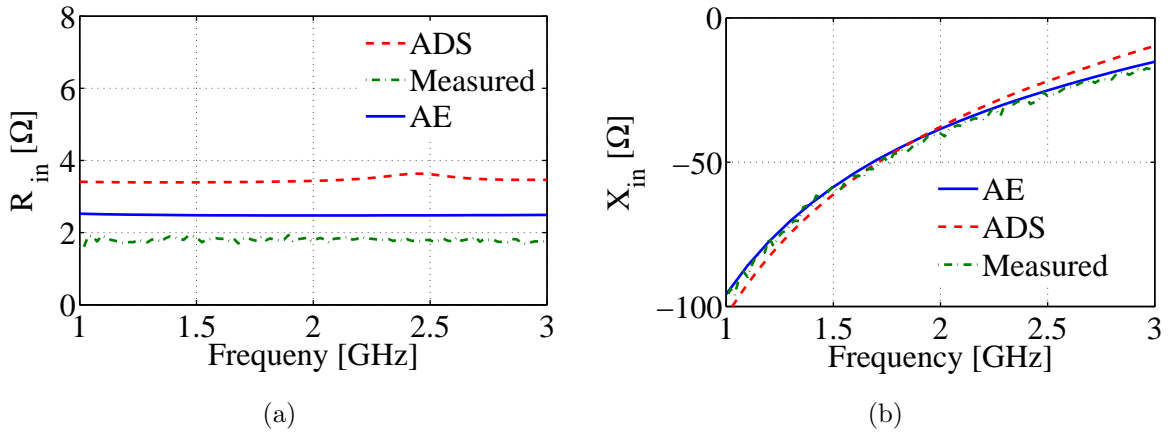


**Figure 2.8.** Real (a) and imaginary (b) parts of the input impedance versus frequency for the diode HSMS-2822 at an available power level of  $-15$  dBm.

Figures 2.9(a) and 2.9(b) show the input impedance as a function of available power level  $P_{in}$  at an operating frequency of 2.45 GHz.

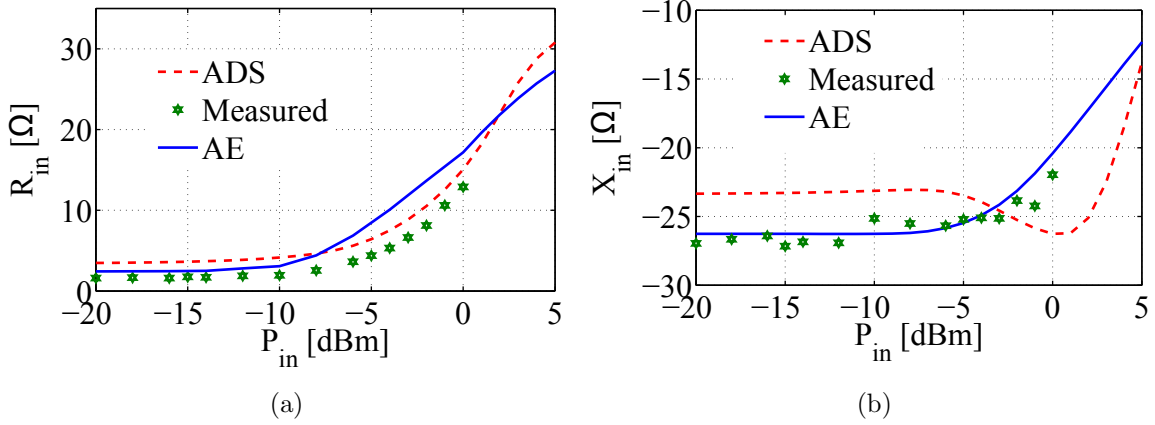


**Figure 2.9.** Real (a) and imaginary (b) parts of the input impedance versus  $P_{in}$  for diode HSMS-2822 at an operating frequency of 2.45 GHz.

It is demonstrated in Figs. 2.8 and 2.9 that the presented analytical expressions as well as Harmonic Balance simulations can predict the impedance behaviour of the diode as a function of frequency (see Fig. 2.8) and as a function of the available power level (see Fig. 2.9). To quantify the agreement between the results of the AE and measurements, the Figure of Merit as a function of input power level is plotted in Fig. 2.10. It is depicted in the figure that the deviations do not exceed the -10 dB threshold, thus validating the accuracy of the analytical expressions with respect to measurements.

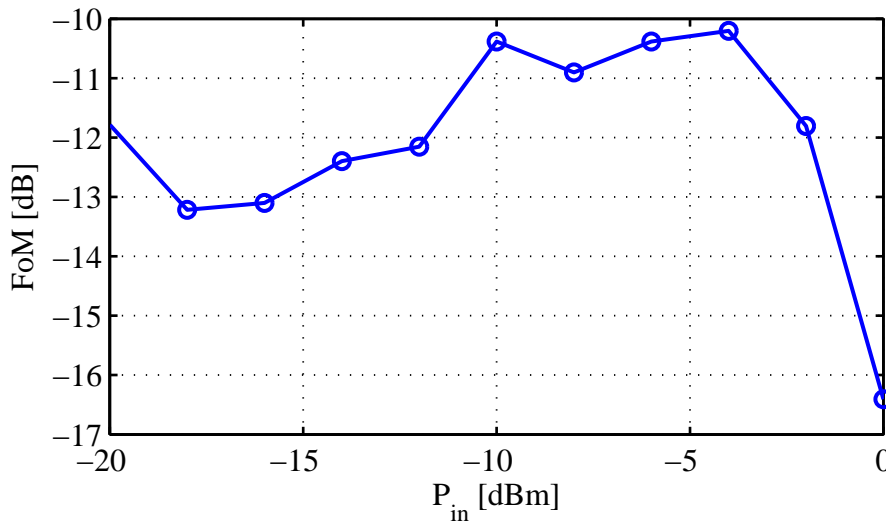


**Figure 2.10.** Figure of Merit versus maximum available power level for the equivalent circuit model and the measurements shown in Fig. 2.9.

## 2.4 Output Voltage of the Rectifier Circuit

In this section we will investigate the DC output voltage as a function of maximum available input power for a single diode. The Ritz-Galerkin averaging method [46] is used to predict the DC output voltage across different resistance values. An implicit equation is obtained for the output voltage as a function of the maximum available input power  $P_{in}$ , the generator resistance  $R_g$ , the saturation current  $I_s$ , the contact resistance  $R_s$  and the load resistance  $R_L$ ,

$$I_0\left(\alpha\sqrt{8R_gP_{in}}\right) = \left(1 + \frac{V_{out}}{R_L I_s}\right) \exp\left(1 + \frac{R_g + R_s}{R_L}\right) \alpha V_{out} \quad (2.10)$$

where  $I_0(\alpha\sqrt{8R_gP_{in}})$  is the zero-order modified Bessel function of the first kind.  $\alpha = \frac{q}{nkT}$ , where  $q$  is the electron charge,  $k$  is Boltzmann's constant,  $T$  is the temperature in Kelvins, and  $n$  is the diode ideality factor. By solving Eq. (2.10) the output voltage for different load resistances is calculated. Note that the generator is not matched to the rectifier and that  $P_{in}$  is the power that would be available if the diode would have the same impedance as that of the generator. Therefore,  $P_{in}$  is the maximum available power. The output voltage of the commercially available diode HSMS-2850 ( $I_s = 3 \mu\text{A}$  and  $R_s = 25\Omega$ ,  $n = 1.03$ ) is calculated and compared to harmonic balance simulation results. Figure 2.11 shows the DC output voltage calculated by the Ritz-Galerkin (RG) method and by Harmonic Balance (HB) simulations for different load resistances.

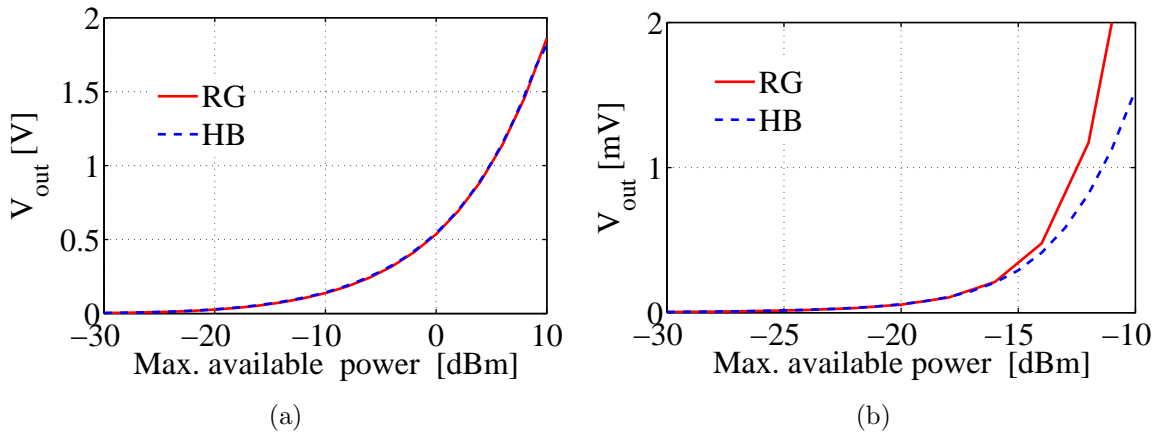


**Figure 2.11.** Output voltage as a function of maximum available input power calculated by Ritz-Galerkin averaging (RG) method and by Harmonic Balance (HB) for a load resistance of (a)  $R_L = 100\text{k}\Omega$ , and (b)  $R_L = 10\Omega$ . The generator impedance  $R_g = 50\Omega$ .

It is shown in the figure that the simulation results calculated by Ritz-Galerkin aver-

aging method can accurately predict the output voltage of the rectifier with a relative difference of less than 5 %, when the load resistance is high (100k $\Omega$ ). On the other hand when the load resistance decreases the relative difference increases to 43 % for  $P_{in} = -12$  dBm. For a 10  $\Omega$  load resistance, the Ritz-Galerkin averaging method is accurate up to  $P_{in} = -15$  dBm (relative difference  $\leq 5\%$ ) as depicted in Fig. 2.11(b).

## 2.5 Investigation of the Diode Parameters on the Output Voltage

The influence of the diode parameters (the junction capacitance  $C_j$  and the contact resistance  $R_s$ ) on the conversion efficiency was first investigated in [47]. In this section we investigate the effect of the contact resistance  $R_s$  and the saturation current  $I_s$  on the output voltage. The Ritz-Galerkin averaging method [46] presented in the previous section is used to calculate the DC output voltage as a function of maximum available input power level for different contact resistance values  $R_s$  and for different saturation current values  $I_s$ . Figure 2.12(a) shows the output voltage of the rectifier as a function of maximum available power for different values of the contact resistance  $R_s$ . Figure 2.12(b) shows the output voltage versus maximum available power for different saturation current values  $I_s$ . The load resistance  $R_L$  is set to 100 k $\Omega$ . The figure shows that the DC output voltage increases with a decreasing value of  $R_s$  and increases with an increasing value of  $I_s$ . These results provide additional selection criteria for choosing commercially available Schottky diodes.

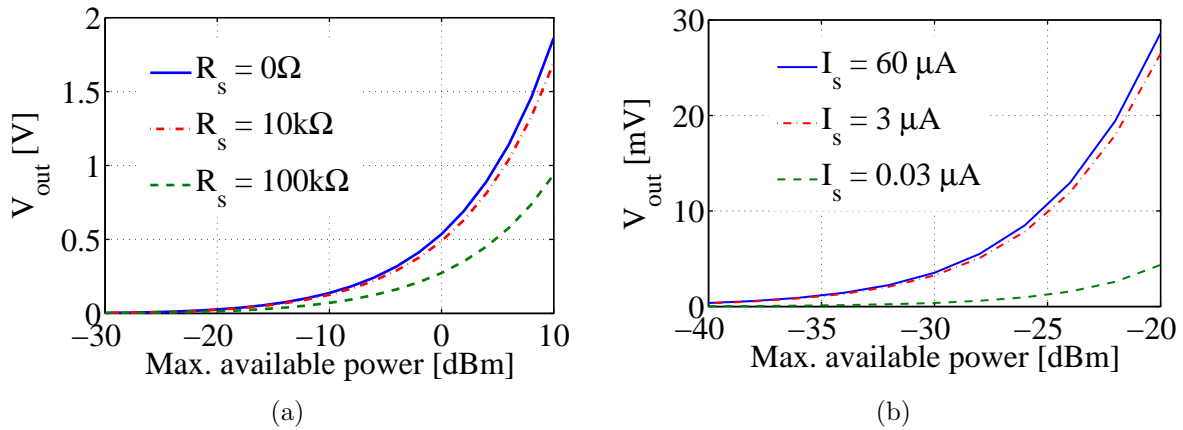


**Figure 2.12.** Influence of the contact resistance (a) and the saturation current (b) on the output voltage as a function of maximum available power.  $R_L = 100$  k $\Omega$ .

Table 2.2 lists the  $I_s$  and the  $R_s$  values of different commercially available Schottky

diodes.

**Table 2.2.**  $I_s$  and  $R_s$  values for commercially available Schottky diodes.

Schottky diode	$I_s$ (A)	$R_s$ ( $\Omega$ )
HSCH-5310	3.00E-10	13
HSCH-5314	3.00E-10	9
HSCH-5340	4.00E-8	13
HBAT-540X	1.00E-7	2.4
HSMS-270X	1.40E-7	0.65
HSMS-280X	3.00E-8	30
HSMS-281X	4.80E-9	10
HSMS-282X	2.20E-8	6
HSMS-285X	3.00E-6	25
HSMS-286X	5.00E-8	6

Figure 2.13 shows the calculated DC output voltage as a function of the load resistance ( $R_L$ ) for two different maximum available power levels, for three chosen Schottky diodes. The figure shows that the Schottky diode HSMS-285X outperforms the two other diodes HSCH-5310 and HSMS-280X with respect to the DC output voltage for the two simulated maximum available power levels. This is due to the higher saturation current.

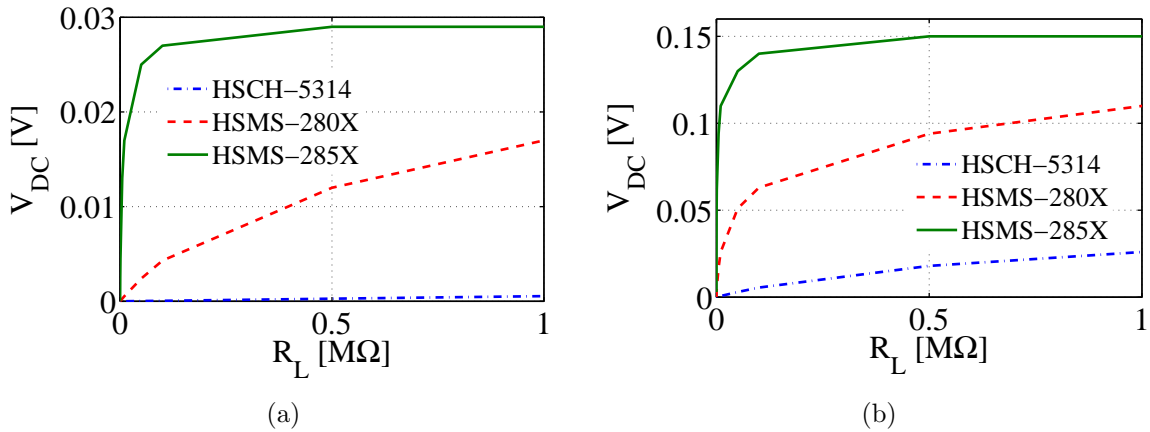


**Figure 2.13.** DC output voltage as a function of load resistance ( $R_L$ ) for different maximum available power levels for three Schottky diodes. (a)  $P_{in} = -20$  dBm, (b)  $P_{in} = -10$  dBm.

The Schottky diode HSMS-285X is characterized by a saturation current that is higher

than that of the other diodes. Since this leads to a higher DC output voltage, this diode is selected for rectenna designs to be discussed in subsequent Chapters.

## 2.6 Voltage Multiplier

At low input power levels, the DC output voltage of the rectifier is well below 1 V. Modern low-power electronics needs at least a voltage in the order of 1 - 1.2 V to operate [48]. To increase the DC output voltage, a voltage multiplier may be employed. A much used configuration is based on a Dickson charge pump circuit [49] and is shown in Fig. 2.14.

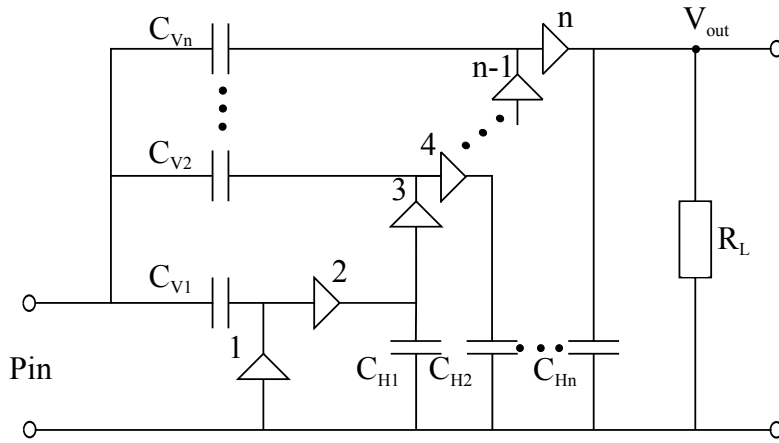


**Figure 2.14.** Voltage multiplier configuration based on a Dickson charge pump circuit.

As an illustration, ADS harmonic balance has been used to simulate the DC output voltage. For an operating frequency of 1 GHz and based on the Schottky diode HSMS 2822, the DC output voltage across  $R_L$  has been simulated as a function of the number of rectifier stages. The results are shown in Fig. 2.15 for two maximum available power levels.

At an input power level of +10 dBm (solid curve), the maximum output voltage is reached after cascading 8 Schottky diodes, while at a power level of -6dBm (dashed curve), the output voltage is saturated after cascading only 4 Schottky diodes. It is clearly shown in Fig. 2.15 that, at a low input power level (e.g. -6 dBm), increasing the number of the rectification stages will eventually result in a lower DC output voltage, and consequently the RF-to-DC power conversion efficiency will decrease.

The saturation point depends on the operating frequency, the input power level, and the load resistance value. In view of this saturation effect, and since this thesis deals with harvesting power at very low input power levels ( $P_{in} = -10$  dBm) a voltage doubler configuration ( $n=2$ , see Fig. 2.14) will be adapted for the designed rectennas in Chapter

3 and in Chapter 5.

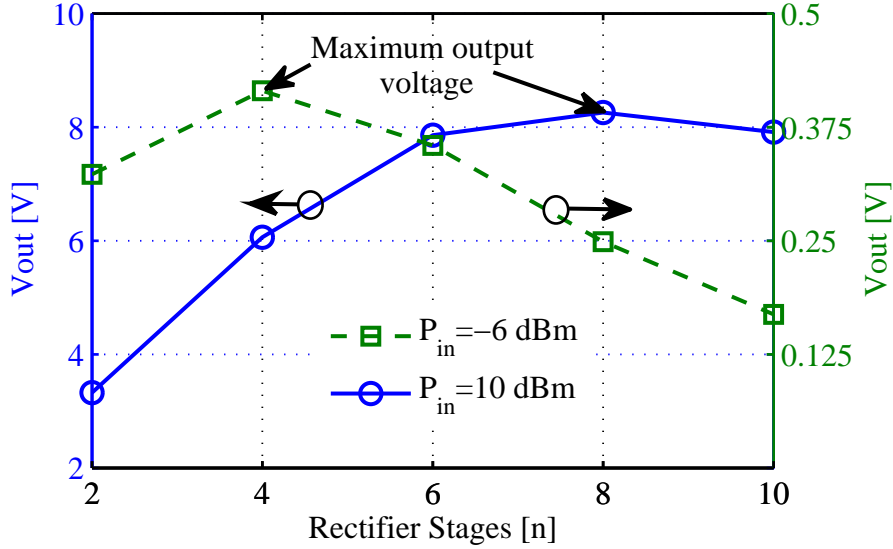


**Figure 2.15.** DC output voltage as a function of the number of multiplier stages (diodes) for two maximum available power levels simulated by ADS. Frequency = 1 GHz,  $R_L = 1\text{M}\Omega$ ,  $C_{V_i} = C_{H_j} = 100\text{ pF}$ ,  $R_g = 50\Omega$ .  $P_{in}$  is the maximum available input power.

After choosing the commercially available Schottky diode HSMS-285X for the design of the rectenna and limiting the multiplier to a voltage doubler, the following section will present the selection of the design frequency and the input power level.

## 2.7 Rectenna Design

Since the rectifier's impedance changes as a function of frequency and as a function of input power level, an operating frequency  $f_0$  and an input power level ( $P_r$ ) should be selected first, before proceeding to the investigation of different rectenna topologies. Based on the two design criteria, operating frequency and assessed input power level ( $f_0$ ,  $P_r$ ), different rectenna topologies will be presented. Figure 2.16 shows a general far-field wireless power transmission system. The rectenna in this system consists of an antenna that is directly complex-conjugate matched to the rectifier.

The power density ( $S$ ) at the receiving side is dictated by the effective isotropic radiated power,  $EIRP = P_t G_t$ , where  $P_t$  is the transmitted power and  $G_t$  is the transmit antenna gain, and by the distance  $R$  between the transmitting and the receiving antennas as shown in Fig. 2.16.

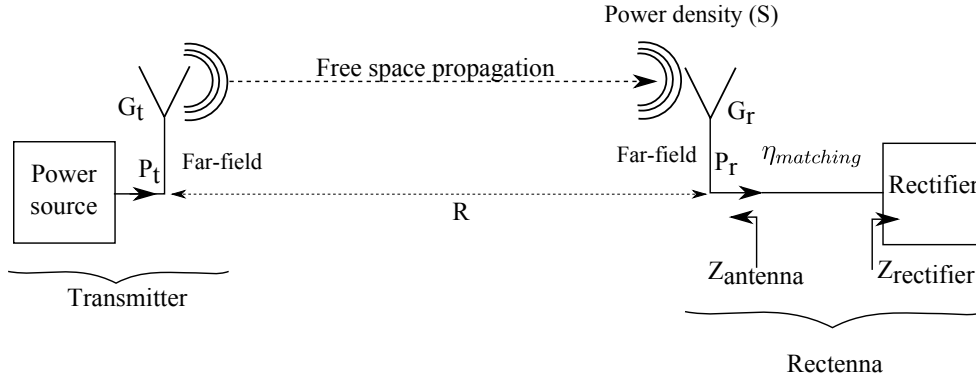


**Figure 2.16.** Far-field wireless power transmission system, where no matching circuit is used at the receiving side.

The power density is obtained by distributing the total power over a spherical surface with area  $4\pi R^2$ :

$$S = \frac{EIRP}{4\pi R^2} = \frac{P_t G_t}{4\pi R^2}. \quad (2.11)$$

The antenna at the receiving side captures part of this power density with an effective aperture  $A_r$ . The received power  $P_r$  (see Fig. 2.16) is given by:

$$P_r = A_r S, \quad (2.12)$$

where  $A_r$  is the effective aperture of the receiving antenna in the direction of the transmitting antenna. According to [50], the effective aperture is related to the antenna gain by

$$A_r = G_r \frac{\lambda_0^2}{4\pi}, \quad (2.13)$$

where  $\lambda_0$  is the wavelength of transmitted signal. Substituting Eq. (2.13) in Eq. (2.12) leads to the Friis transmission equation where the received power at the terminals of the rectifier is expressed as

$$P_r = P_t G_t G_r \left( \frac{\lambda_0}{4\pi R} \right)^2 = P_t G_t G_r \left( \frac{c}{4\pi f_o R} \right)^2, \quad (2.14)$$

where  $c$  is the free-space speed of light and  $f_o$  is the operating frequency of the transmitted signal. The term  $\left( \frac{c}{4\pi f_o R} \right)^2$  is called the free-space path loss. The term path loss may lead to confusion. It gives the impression that, apart from a spherical spreading, a frequency dependent path loss exists. This is not true, since the gain changes with frequency.



### 2.7.1 Operating Frequency

For practical reasons we will aim for a rectenna that is ideally credit-card sized, so that it can be applied in wireless sensors for smart building applications.

Since there are no special regulations for rectenna systems yet, it makes sense to operate these systems in the licence-free Industry-Science-Medical (ISM) frequency bands, see Table 2.3. The frequency bands around 0.9 GHz and 2.4 GHz are of special interest due to our credit card size constraint and due to the relative high EIRP allowed. Adapting a frequency band from 865 to 928 MHz will allow RF power transfer operation both in Europe and North America, and RF harvesting from GSM transmissions on both continents.

After having thus selected the design frequency, the expected input power level will be presented next.

**Table 2.3.** Frequency band allocations and transmit power restrictions for RFID applications as reported in [12].

Frequency Band	Power	Duty Cycle/ Tx type	Channel Spacing / BW	Region
2446 - 2454 MHz	500 mW EIRP 4 W EIRP	Up to 100 $\leq 15\%$	No spacing	Europe*
865.0 - 865.6 MHz	10 mW ERP		200 kHz	Europe
865.6 - 867.6 MHz	2 W ERP		200 kHz	Europe
867.6 - 868.0 MHz	500 mW ERP		200 kHz	Europe
902 - 928 MHz	4 W EIRP	FH ( $\geq 50$ channels) or DSSS		USA Canada
2400-2483.5 MHz	4 W EIRP	FH ( $\geq 75$ channels) or DSSS		USA Canada
2400-2483.5 MHz	10 mW EIRP		1MHz BW	Japan Korea

In Table 2.3, ERP is the Effective Radiated Power, the EIRP is 1.64 times ERP. FH stands for Frequency Hopping. DSSS stand for Direct Sequence Spread Spectrum and BW indicates Band Width. \*Power levels above 500 mW are restricted to use inside the boundaries of a building and the duty cycle of all transmissions shall in this case be  $\leq 15\%$  in any 200 ms period (30 ms on / 170 ms off).

### 2.7.2 Expected Input Power Level

Possible design operating frequencies have been discussed in the previous section. We will settle for a design frequency of 868 MHz. It is indicated in Table 2.3 that at this design frequency, the maximum allowed Effective Radiated Power (ERP) is 500 mW in Europe.

Based on the applications that have been indicated in the previous chapter, including the Smart Building Initiative (SBI), a direct line-of-sight propagation distance ( $R$ ) between 2 meters and 10 meters is expected, being related to the size of a general office, hallway or meeting room. Using the maximum allowed ERP at a frequency of 868 MHz, see Table 2.3, the power density as a function of propagation distance is calculated using Eq. (2.11) and is plotted in Fig. 2.17 (solid curve). It is indicated in the figure that the power density does not exceed  $12 \text{ dBm}/\text{m}^2$ . At a distance of 5 meters away from the transmitting source, the power density drops to  $4 \text{ dBm}/\text{m}^2$ .

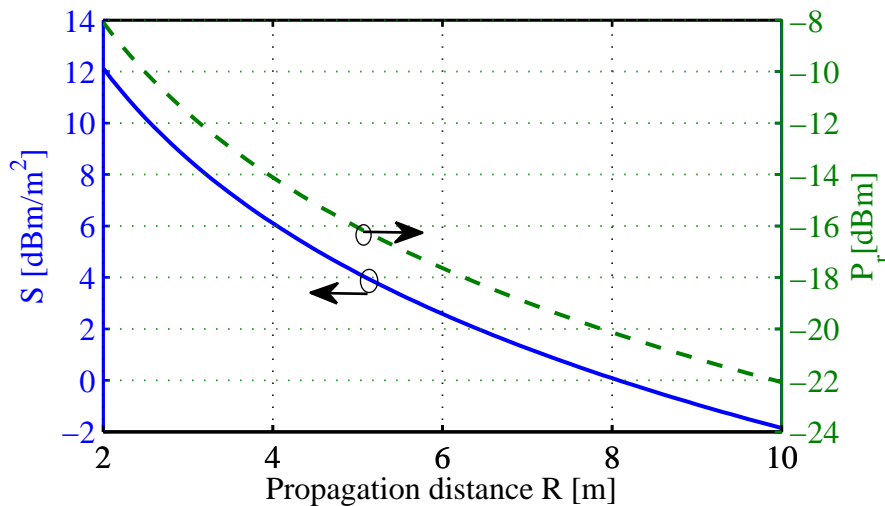


**Figure 2.17.** Power density and received power calculated using Eq. (2.11) and Eq. (2.14) respectively as a function of propagation distance.

To translate the power density into input power levels  $P_r$  (see Fig. 2.16), Eq. (2.14) is used to calculate the input power level, where a receiving antenna gain of  $0 \text{ dBi}$ <sup>1</sup> is used. The received power within the practical propagation distance ( $2 \leq R \leq 10 \text{ m}$ ) is plotted in Fig. 2.17 (dashed curve). It is clearly indicated in the figure that the received power is within  $-8 \text{ dBm} \leq P_r \leq -22 \text{ dBm}$  for the practical propagation distances. Based on this argument it makes sense then to choose an assessed input power level of  $-10 \text{ dBm}$ .

<sup>1</sup>The reason behind choosing  $0 \text{ dBi}$  for the receive antenna gain is the size constraint related to a credit-card size antenna at 868 MHz.

A second reason to choose an input power level around -10 dBm is derived from the results of the input impedance of the Schottky diode as a function of maximum available input power level shown in Fig. 2.9. Since the input impedance of the Schottky diode (both the real and the imaginary part) is almost constant at low input power levels  $\leq -5$  dBm, choosing a low input power level for the design of the rectenna will ensure that the rectenna will be matched for a broad input power-level band.

To further strengthen this power level choice we will look at the antenna matching. To this end, the term matching efficiency denoted by  $\eta_{\text{matching}}$  is introduced. The matching efficiency  $\eta_{\text{matching}}$  describes how well the antenna is matched to the rectifier. Since a matching network is not present (see Fig. 2.16), the antenna is conjugately matched to the rectifier, with an impedance  $Z_{\text{antenna}} = Z_{\text{rectifier}}^*$ , where \* denotes the complex conjugate. The matching efficiency is calculated as a function of received power level  $P_r$ , for an antenna designed to be matched at  $P_r = -10$  dBm and for an antenna designed to be matched at  $P_r = 0$  dBm.

The matching efficiency is expressed as

$$\eta_{\text{matching}} = 1 - S_{11}^2, \quad (2.15)$$

where the power wave reflection coefficient concept [34] [51] is used to calculate the reflection coefficient:

$$S_{11} = \frac{Z_{\text{rectifier}} - Z_{\text{antenna}}^*}{Z_{\text{rectifier}} + Z_{\text{antenna}}}. \quad (2.16)$$

Figure 2.18 shows the matching efficiency as a function of input power level for both antennas.

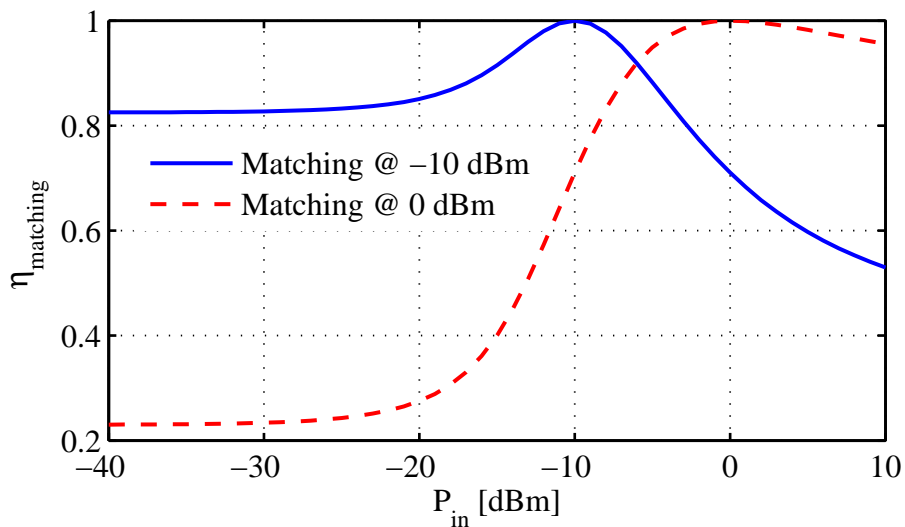


**Figure 2.18.** Matching efficiency as a function of input power level for an antenna designed to be matched at  $P_r = -10$  dBm (solid curve) and for an antenna designed to be matched at  $P_r = 0$  dBm (dashed curve).

The figure shows that, when the rectenna is designed for -10 dBm, a matching efficiency higher than 80 % is calculated for a broad input-power-band,  $-40 \text{ dBm} \leq P_r \leq -3 \text{ dBm}$ . On the other hand, if the rectenna is designed at an input power level of 0 dBm, a matching efficiency higher than 80 % is calculated for an input power band,  $-8 \text{ dBm} \leq P_r \leq 10 \text{ dBm}$ .

It is thus demonstrated that designing a rectenna for an input power level around  $-10 \text{ dBm}$  will result in a rectenna that is matched to broad input power band from  $-40 \text{ dBm}$  up to  $-3 \text{ dBm}$ , which corresponds to the expected input power levels for our applications (see Fig. 2.17 dashed curve).

## 2.8 Conclusion

For a maximum power transfer between the receiving antenna and the rectifier in a rectenna system, the antenna's input impedance should be matched to that of the rectifier circuit. A detailed design method to accurately predict the input impedance and the DC output voltage of a Schottky diode based rectifier is presented in this chapter. The presented method uses circuit analysis to calculate the impedance of a Schottky diode as a function of frequency for different maximum available power levels. The simulation results are validated by measurements. In addition, the influence of the diode's parameters on the output voltage are investigated. It is shown that the highest output DC voltage is achieved for the lowest contact resistance and for the highest saturation current. Thus the commercially available Schottky diode HSMS-285X is selected for the design of a voltage doubler.

In addition, the practical rectenna design criteria with respect to the operating frequency and the input power levels are presented. Based on the possible applications, license free frequency bands and allowed transmit powers, chosen is to design rectennas having small or broad frequency bands around 868 MHz for an input power level of  $-10 \text{ dBm}$  ( $100 \mu \text{ W}$ ).



## CHAPTER THREE

# RF Power Transport Employing Rectennas Using Matching Networks

---

In this chapter a modified Yagi-Uda antenna is introduced. The design is based on a wide-band strip dipole around which a Yagi-Uda structure is formed. The antenna consists of a reflector and a single director placed nearby the driven dipole. The main advantage of the suggested antenna is that, by tuning its geometrical parameters, the antenna can perform as a dual-band, a triple-band or a broad-band antenna. Three prototypes are designed, simulated, fabricated and measured. The simulated results are validated by measurements. The modified Yagi-Uda antenna is then used for RF power transport. A matching network is designed to match the  $50\Omega$  antenna to a voltage-doubler rectifier. The matching circuit and rectifier are characterized as a single unit. The measured Power Conversion Efficiency (PCE) reaches 31.6% and 49.7 % over  $10\text{ k}\Omega$  load resistance at an input power level of -20 dBm and -10 dBm, respectively. Compared to the state-of-the-art published results, the PCE increases by 5 % at -10 dBm and by 10 % at -20 dBm.

The advantage of this rectenna design is that the antenna may be replaced by any  $50\Omega$  antenna having the correct frequency response. The disadvantage is that the matching network introduces additional losses. This disadvantage will be dealt with in a subsequent chapter.

### 3.1 Introduction

The main challenge in far-field energy harvesting is to overcome the power-density decay due to the long distance between the transmitter and the harvesting location. To partly compensate for this so-called path loss, antenna arrays or high gain antennas can be used at the receiving part. Figure 3.1 shows the  $50\ \Omega$  rectenna system investigated in this chapter. The arrows indicate the power flow from the transmitting side to the receiving side to reach the load  $R_L$ .

First, a novel  $50\ \Omega$  modified Yagi-Uda antenna for the transmission and reception of RF power is introduced. Three different prototypes are designed, simulated, manufactured and measured. The first antenna is designed to harvest ambient RF power from Digital TV (DTV) broadcasting stations. The second and the third prototype are a dual-band and a triple-band antenna respectively. The dual band prototype is developed for RF power harvesting at 900 MHz (GSM 900) and 2.45 GHz (ISM). The triple-band prototype adds (GSM 1800) to these two frequency bands.

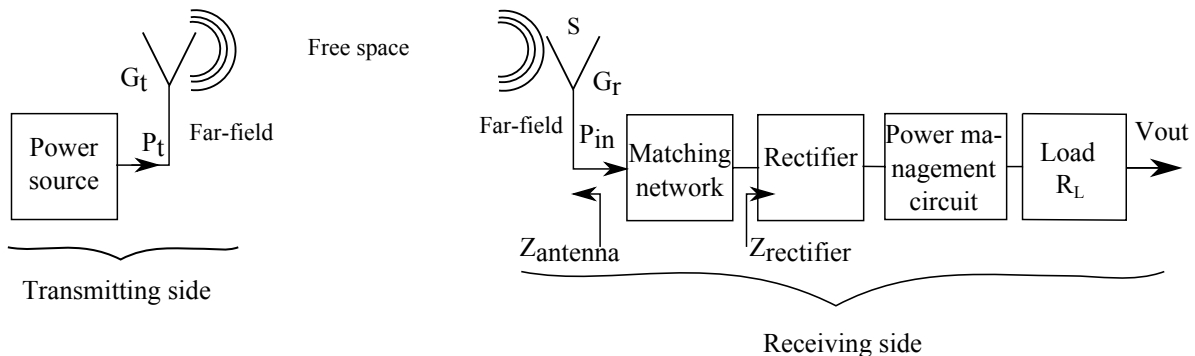


**Figure 3.1.** RF power transport system employing a ( $50\ \Omega$ ) antenna matched to the rectifier using a matching network on the receiving side.

A Schottky diode voltage doubler configuration is used on the receiving side to transform the RF power into DC power. For an improved power transfer, a lumped-element matching network between the  $50\ \Omega$  receiving antenna and the voltage doubler (rectifier) is designed. The main target of the matching network is to transform the impedance of the rectifier ( $Z_{rectifier}$ ) to that of the antenna ( $Z_{antenna}$ ), see Fig. 3.1.

This chapter consists of two parts. In the first part, the design of a novel, modified Yagi-Uda antenna to harvest power from DTV stations is presented. The developed procedure is then employed also to design a dual-band and a triple-band antenna. In the second part, the matching network will be introduced. Using the newly developed antenna, we design one RF power transport prototype system at an operating frequency

of 868 MHz for an input power level of -10 dBm.

For the development of the modified Yagi-Uda antenna, we first need to introduce a wide-band strip dipole antenna that will replace the driven element in a normal Yagi-Uda antenna.

## 3.2 Center-Fed and Step-Shaped-Fed Strip Dipoles

Various types of printed dipoles have been studied in the literature [52,53]. The printed strip dipole antennas are desirable due to their low profile, low production cost and their ease of fabrication. Many attempts have been performed to enlarge the bandwidth of the strip dipole antenna [54]. A printed wide-band dipole antenna with a step-shaped feed gap for DTV signal reception was suggested in [55] and is shown in Fig. 3.2(b). The wide-band characteristics are obtained by two closely-spaced resonances.

Figure 3.2 shows a conventional centre-fed strip dipole (a) and the step-shaped-fed (the feed of the antenna has a shape of a step strip dipole antenna (b) as introduced in [55] and [56].

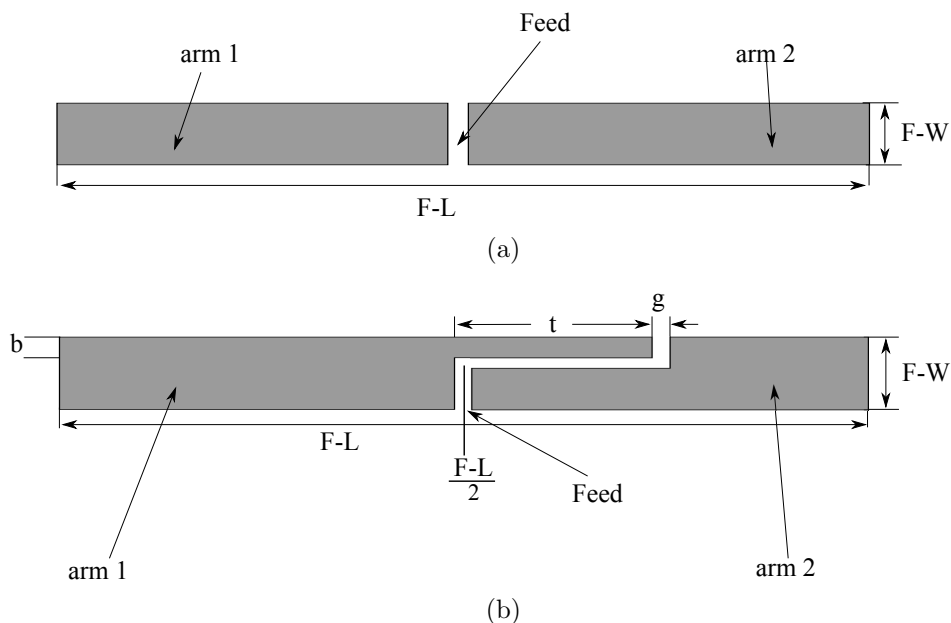


**Figure 3.2.** Centre-fed strip dipole configuration (a) and the step-shaped-fed strip dipole configuration (b) as introduced in [55].

To verify that the suggested antenna in [55] has two resonance modes, Table 3.1 shows the optimized parameters for having the step-shaped-fed strip dipole resonate at 550



MHz. An ordinary, centre-fed strip, dipole is also designed to resonate at the same frequency. The center-fed and the step-shaped-fed dipole antennas are printed on a 1.6 mm thick FR4 substrate with permittivity  $\epsilon_r = 4.4$  and loss tangent  $\tan \delta = 0.025$ . CST Microwave Studio [57] is used to simulate the reflection coefficients as a function of frequency for both the centre-fed and the step-shaped-fed strip dipole.

**Table 3.1.** Optimized parameters for the step-shaped-fed dipole to resonate at 550 MHz. The dimensions are explained in Fig. 3.2.

Parameter	mm
F-L	226
F-W	20
$b$	2.5
$g$	1
$t$	42.5

Figure 3.3 shows the simulated reflection coefficient versus frequency for a centre-fed strip dipole antenna having a length F-L and width F-W (see Table 3.1) and for a step-shaped-fed strip dipole antenna of the same length and width. The dimensions of the feed structure of the latter antenna, i.e.,  $b$ ,  $g$  and  $t$ , are listed in Table 3.1.

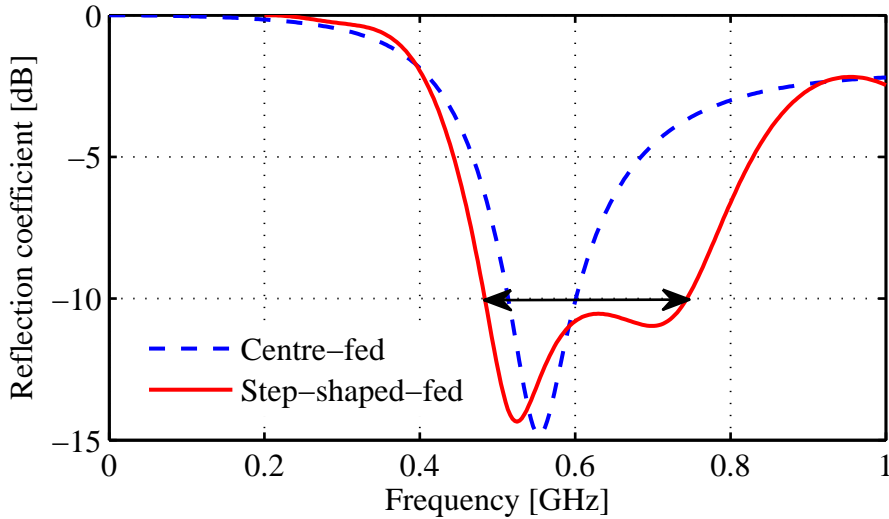


**Figure 3.3.** Reflection coefficient as a function of frequency for the centre-fed strip dipole antenna and the step-shaped-fed strip dipole antenna, having identical total length and identical width and both placed on the same substrate carrier.

It is indicated in the figure that the bandwidth of the step-shaped-fed strip dipole

antenna is increased by more than 120% compared to the standard centre-fed strip dipole antenna. This increase in bandwidth is realized by the two excited resonant modes, one at  $0.5\lambda$  controlled by the antenna length  $F-L$ , and a second one controlled by choosing a proper value of  $t$  (see Fig. 3.2(b)). This additional resonant mode of the antenna is controlled by the total effective length of the antenna comprising its two asymmetric radiators arm 1 and arm 2 [55] (see Fig. 3.2(b)).

The main limitation of this antenna is its restricted gain. Since it is a  $\lambda/2$  dipole antenna, its gain is limited to 2.15 dBi. For a higher antenna gain, other types of antennas are needed.

### 3.3 Printed Yagi-Uda Antenna and Parameter Optimization

The printed Yagi-Uda antenna shown in Fig. 3.4 is a highly directive but narrow-band antenna [58]. The parameters of a quasi Yagi-Uda antenna were optimized for a broadband operation in [59]. The resulting antenna achieves 48% bandwidth for a Voltage Standing Wave Ratio (VSWR)  $< 2$ , but uses a truncated ground plane and a balun structure.

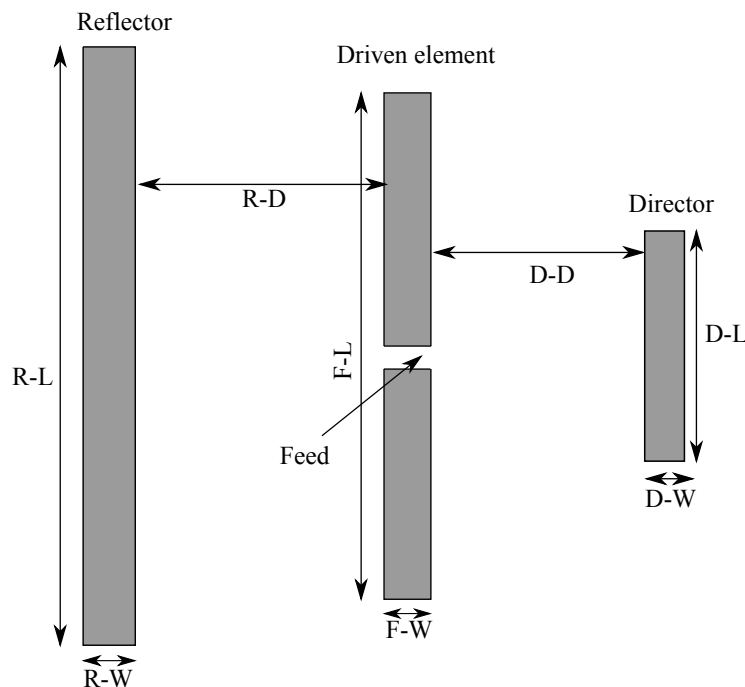


**Figure 3.4.** Conventional printed strip Yagi-Uda antenna configuration.

A design that serves as a wide-band Yagi-Uda antenna or as a multi-band printed dipole

was realized by using parasitic elements in proximity to a dipole that is parallel to a truncated ground plane [60,61]. Recently, the effects of all the antenna parameters for such antennas on the frequency response were investigated in [62].

Table 3.2 shows the optimized parameters for the ‘standard’ Yagi-Uda antenna shown in Fig. 3.4 to resonate in the DTV frequency band between 475 MHz and 794 MHz [63].

**Table 3.2.** Optimized parameters of the conventional Yagi-Uda antenna to cover the DTV frequency bandwidth. The dimensions are explained in Fig. 3.4.

Parameter	mm
F-L	235
F-W	15
R-L	290
R-W	30
D-D, D-L	see Sec. 3.3.1
R-D	see Sec. 3.3.2

The Yagi-Uda antenna parameters including the length of the director (D-L), the distance between the feed and the director (D-D), and the distance between the feed and the reflector (R-D) are optimized to obtain the widest bandwidth possible that can cover the DTV broadcasting frequency bandwidth (475 MHz - 794 MHz). The feed length F-D is set to 235 mm so that the Yagi-Uda antenna resonates in the required frequency band (475 MHz - 794 MHz). The reflector length R-L is set to 290 mm as indicated in Table 3.2.

### 3.3.1 Optimization of the Distance Between Feed and Director (D-D) and the Director Length (D-L)

In this section the distance between feed and director (D-D) and the director length (D-L) are optimized to broaden the frequency response of the conventional printed Yagi-Uda antenna. The distance between the reflector and the feed is fixed to 110 mm and will be optimized in the following section.

Figure 3.5(a) shows the simulated reflection coefficient as a function of frequency for different distances between the feed and the director. It is clear from the figure that, when the director is set close to the feed, a second resonance is generated at a higher frequency which enhances the reflection coefficient bandwidth. This is due to the increased mutual coupling between the feed and the director. Actually the director acts as a resonator of length  $\lambda/4$  when it is close to the driven element.

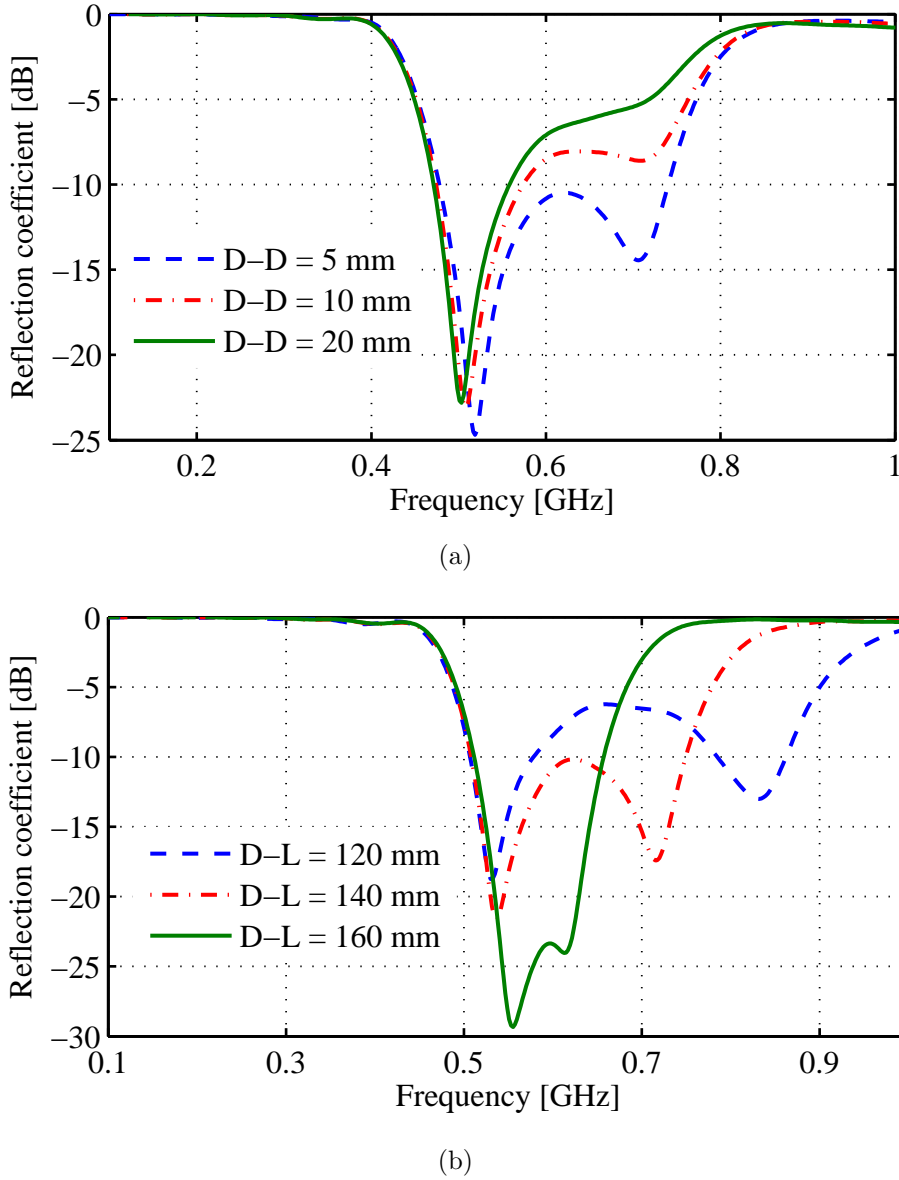


**Figure 3.5.** (a) Reflection coefficient versus frequency for different D-D, D-L = 140 mm, R-D = 110 mm. And (b) reflection coefficient versus frequency for different D-L, R-D = 110 mm, D-D = 5 mm.

To confirm this observation, the distance between the director and the driven element is set to  $D-D = 5$  mm, and the director length is swept between 120 mm and 160 mm. As expected, see Fig. 3.5(b), the reflection coefficient is characterised by two resonances. The low-frequency resonance is due to the feeding length (F-L) designed for 530 MHz, the high-frequency resonance is due to the length of director (D-L). The latter resonance shifts toward the lower frequency resonance when the length of the director is increased. This behaviour makes it possible to bring the two resonances together, which results in an improved reflection coefficient over an extended frequency band.

### 3.3.2 Optimization of the Distance Between Feed and Reflector (R-D)

Based on the parameters in Table 3.2, the optimization of the distance between the feed and the reflector (R-D) is presented in this section.

Figure 3.6 shows the reflection coefficient as a function of frequency for different distances between the feed and the reflector.

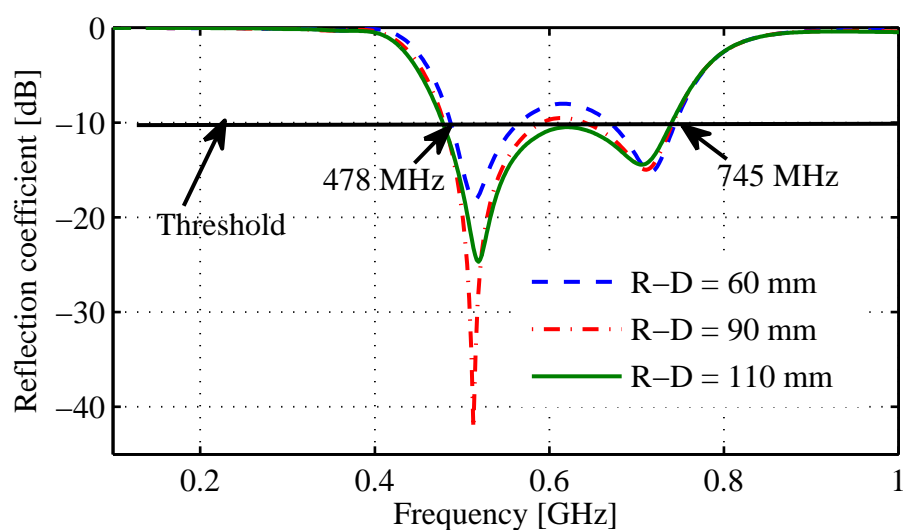


**Figure 3.6.** Simulated results of the reflection coefficient as a function of frequency for different distances between the reflector and the feed. D-L = 140 mm, D-D = 5 mm.

It is clear from the simulation results that the operating antenna bandwidth is not strongly affected by the distance between the feed and the reflector. However, an increased reflection coefficient exceeding the threshold of -10 dB (dashed curve, R-D = 60 mm), is observed when the reflector is placed nearby the feed. When the distance between the feed and the director is enlarged, the absolute value of the reflection coefficient decreases as illustrated by the solid curve for R-D = 110 mm.

After all the Yagi-Uda antenna parameters have been optimized, it is shown by the solid curve in Fig. 3.6 that the maximum achievable bandwidth is 267 MHz (478 MHz - 745 MHz) which does not meet the full bandwidth requirements (475 - 794 MHz).

## 3.4 Modified Yagi-Uda antenna

To further broaden the frequency band and at the same time preserve the radiation characteristics, a novel broadband modified Yagi-Uda antenna is introduced in this sec-

tion.

As was shown in Sec. 3.2, the step-shaped-fed strip dipole is characterized by two resonant modes, the first one being due to the strip length and the second one due to the total effective length of the antenna comprising its two asymmetric radiator arms 1 and 2 [55] (see Fig. 3.3). We have also seen that by carefully placing the parasitic elements in a 3-elements Yagi-Uda antenna, a dual resonance may be obtained. In this section the driven element in Fig. 3.4 will be replaced by the step-shaped-fed strip dipole antenna shown in Fig. 3.2(b). The resulting configuration is shown in Fig. 3.7.

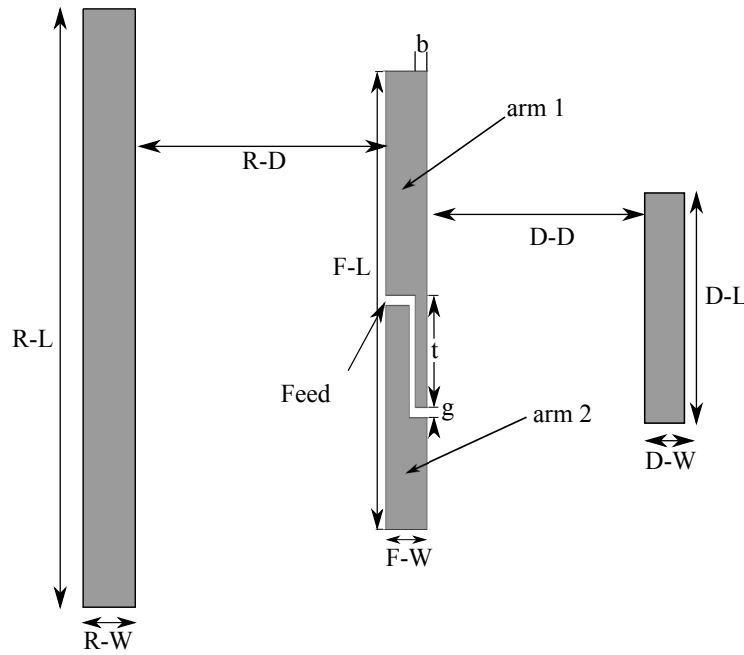


**Figure 3.7.** Modified Yagi-Uda antenna with a step-shaped-fed driven element.

It is expected that this modified configuration will be characterized by three resonant modes, one due to the feed length ( $F-L$ ), a second one due to the director length ( $D-L$ ) and a third one due to the total effective length of the feed comprising its two asymmetric radiators arms 1 and 2 ( $0.5F-L + t$ ). The main advantage of this configuration will be that it offers three additional parameters  $b$ ,  $t$  and  $g$  (see Fig. 3.2(b) and Fig. 3.7) for resonance frequency tuning. By optimizing these additional parameters the frequency bandwidth will be widened to cover the complete DTV band (475 MHz - 794 MHz).

To validate that the modified Yagi-Uda antenna is characterized by three different resonant modes, that can be tuned independently, CST Microwave Studio is used to simulate the reflection coefficient versus frequency. The previously designed Yagi-Uda antenna is used as a starting point. The dimensions are summarized in Table 3.3. Only

the parameters,  $D-L$ ,  $b$  and  $t$  will be sequentially optimized.

**Table 3.3.** Optimized parameters of the modified Yagi-Uda antenna to cover the DTV frequency band.

Parameter	mm
F-L	235
F-W	15
R-L	290
R-W	30
R-D	110
D-D	5
$g$	1
$D-L$	see Sec. 3.4.1
$b$	see Sec. 3.4.2
$t$	see Sec. 3.4.3

### 3.4.1 Modified-Yagi: Three Resonant Modes

In this section the director length is optimized to demonstrate that the modified Yagi-Uda is characterized by three resonant modes. Figure 3.8 shows the reflection coefficient as a function of frequency for different director lengths ( $D-L$ ). The parameters shown in Table 3.3 are used for simulations.

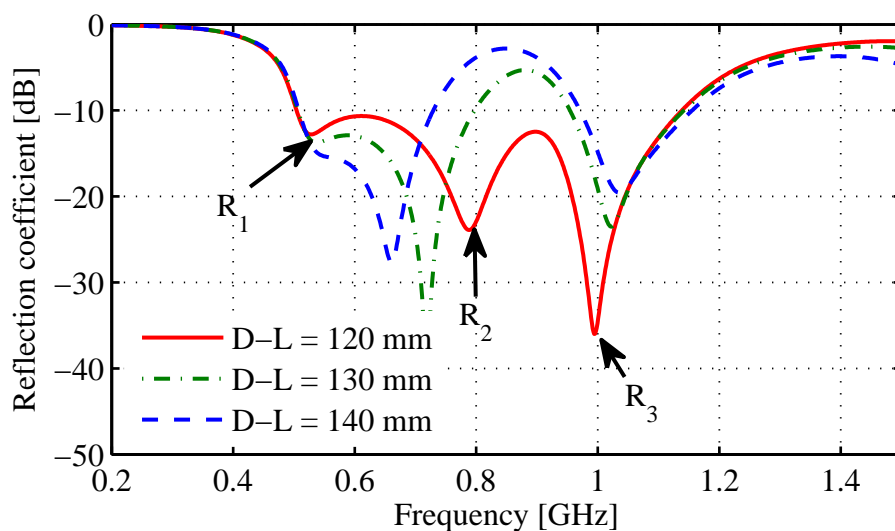


**Figure 3.8.** Optimization of the novel broad band Yagi-Uda antenna parameter  $D-L$ . Simulated results of the reflection coefficient as a function of frequency.  $b = 1$  mm,  $t = 35$  mm,  $g = 1$  mm,  $R-L = 235$  mm.

As expected, the figure indicates that the modified Yagi-Uda antenna is characterised by three resonance frequencies,  $R_1$ ,  $R_2$  and  $R_3$ . The first resonance frequency band around  $R_1$  is due to the driven element length F-L. The second resonance  $R_2$  is due to the length of the director D-L and shifts toward the first resonance when the length of the director increases. The third resonance  $R_3$  is due to the effective length of the feed that is controlled by the arm width  $b$  and the step length  $t$ .

Possessing three resonant modes that can be tuned independently, the modified Yagi-Uda antenna is potentially a broad-band antenna if these three resonant frequencies are close enough. If the three resonant frequencies are separated, the modified Yagi-Uda antenna operates as a triple-band antenna. If two of the three resonant frequencies are close enough the antenna operates as a dual-band antenna.

### 3.4.2 Optimization of the Arm Width $b$

In this section the effect of the parameter  $b$  is discussed. The arm width is swept between 3 mm and 7 mm since the strip width F-W (see Fig.3.7) is fixed to 15 mm. Figure 3.9 shows the reflection coefficient as a function of frequency for the different arm widths  $b$ .

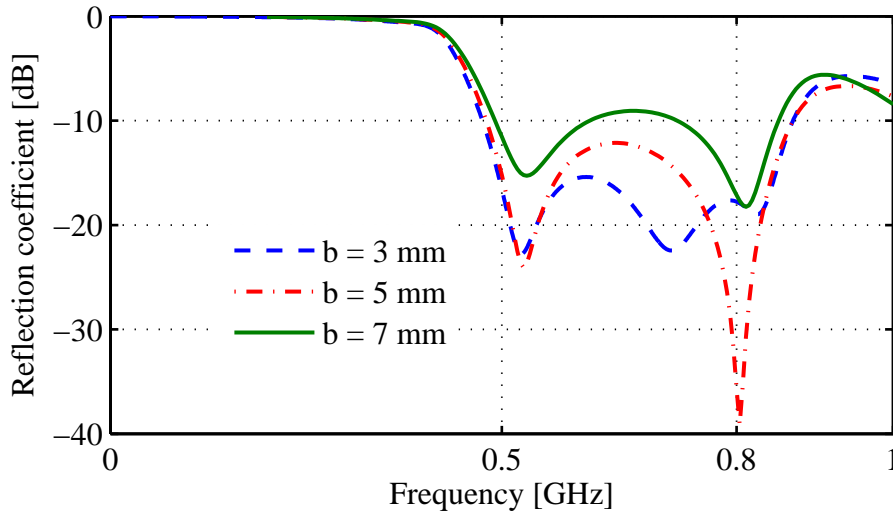


**Figure 3.9.** Optimization of the novel broad band Yagi-Uda antenna parameter  $b$ . Simulated results of the reflection coefficient as a function of frequency for different values of  $b$ .  $g = 1$  mm,  $t = 45$  mm, D-L = 130 mm.

It is observed that  $b$  has a strong effect on the reflection coefficients. It is shown in the figure that a smaller width  $b$  will lead to a lower reflection coefficient. When  $b$  increases, the absolute value of the reflection coefficient increases to surpass the -10dB threshold for  $b = 7$  mm. Thus, we decide to fix  $b$  at 3 mm.



### 3.4.3 Optimization of the Step Length $t$

In this section, the step length  $t$  is sequentially optimized so that the frequency bandwidth of the modified Yagi-Uda antenna covers the required DTV frequency band. Figure 3.10 shows the simulated reflection coefficient as a function of frequency for different step lengths  $t$ . As expected, the parameter  $t$  has a low impact on the lower resonance position ( $R_1$ ). The higher resonance mode ( $R_3$ ) is clearly affected and is shifted towards the lower frequency resonance  $R_2$ , when the step length  $t$  increases.

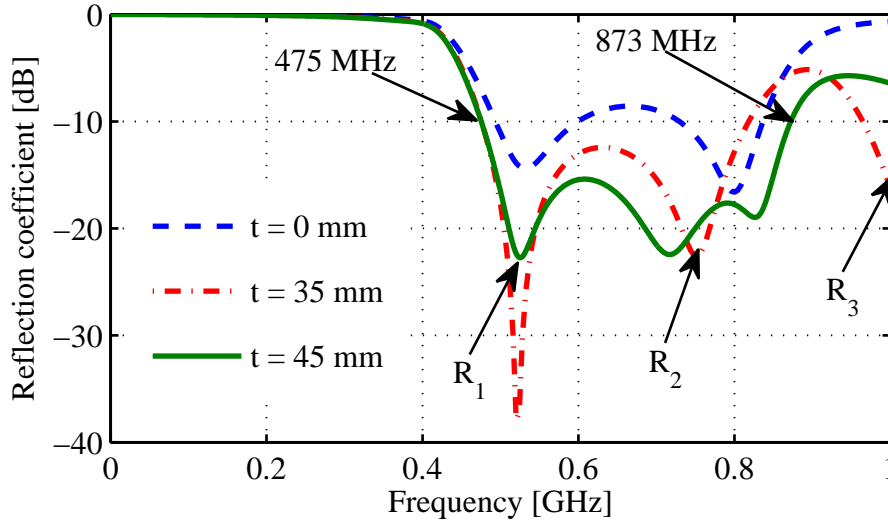


**Figure 3.10.** Simulated results of the reflection coefficient as a function of frequency for different step length values  $t$ .  $g = 0.5$  mm,  $b = 3$  mm,  $D-L = 130$  mm.

As a result, a wide bandwidth is achieved when  $t$  is set to 45 mm. When compared to a standard centre fed Yagi-Uda antenna (dashed curve,  $t = 0$  mm) which is characterized by only two resonances, the reflection coefficient of the novel antenna does not exceed the -15 dB level between 595 and 850 MHz, while the reflection coefficient of the standard Yagi-Uda antenna reaches -8.7 dB at a frequency of 680 MHz.

The sequentially optimized parameters for covering the DTV bandwidth are as follows: gap width  $g = 1$  mm, step length  $t = 45$  mm, arm width  $b = 3$  mm and director length  $D-L = 130$  mm. For these parameters, the antenna impedance bandwidth reaches 398 MHz (475 MHz - 873 MHz) or about 61 % in 2.0:1.0 VSWR centered at 650 MHz, compared to 50 % in 2.5:1.0 VSWR for the wide-band strip dipole antenna in [55].

The gain and the front-to-back ratio as a function of frequency of the optimized antenna are shown in Fig. 3.11.

The novel antenna shows a gain above 4.3 dBi in the operating bandwidth. The front-to-back ratio is less than 9.6 dB to reach the DTV broadcasting range. Above 810 MHz the front-to-back ratio degrades, and reaches 5.2 dB at a frequency of 875 MHz.

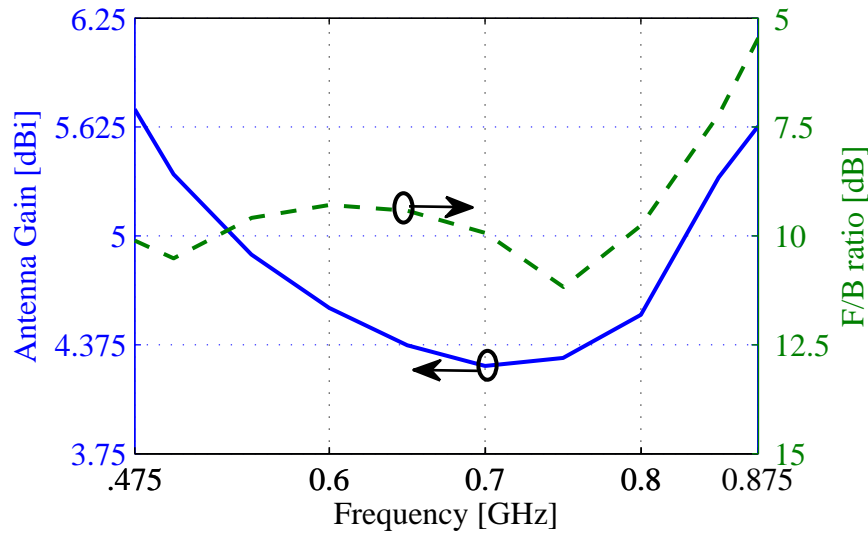


**Figure 3.11.** Simulated antenna gain and front-to-back ratio as a function of frequency for the novel broad-band Yagi-Uda antenna,  $b = 3$  mm,  $t = 45$  mm,  $D-L = 130$  mm. Other parameters are listed in Table.3.3.

The antenna gain for the new configuration has almost doubled with respect to the step-shaped-fed strip dipole antenna investigated in Sec. 3.2, which makes the newly proposed antenna well suitable for RF energy harvesting from DTV broadcast signals. In Table. 3.4 the comparison between the performances of a standard Yagi-Uda antenna and the modified Yagi-Uda antenna are presented.

**Table 3.4.** Comparison between a standard Yagi-Uda antenna and the modified broadband Yagi-Uda antenna.

	Standard Yagi-Uda (See Fig. 3.5(a)-solid curve)	Modified Yagi-Uda [This work]
Gain	5.7 dBi	4.2 dBi
F/B ration	10 dBi	5.2 dB
Bandwidth	80 MHz	398 MHz
Antenna size	290 mm x 295 mm	290 mm x 190 mm

Compared to a standard printed Yagi-Uda antenna (See Sec. 3.3) where the bandwidth around the resonance frequency is limited to 80 MHz (See Fig. 3.5(a)-solid curve), the novel antenna operating bandwidth is increased by a factor of four. The antenna gain over the wide band is only reduced by an average of 1.5 dBi. The front-to-back ratio

for a standard Yagi-Uda antenna is 5 dB lower, which makes the standard Yagi-Uda antenna more directive. However, the novel antenna (290 mm x 190 mm) is 35 % smaller when compared to a standard Yagi-Uda antenna (290 mm x 295 mm). The antenna gain of the novel broadband Yagi-Uda antenna can be improved at the expense of the antenna bandwidth and size.

### 3.4.4 Fabricated Antenna

Based on the previous results, an antenna is fabricated as shown in Fig. 3.12.

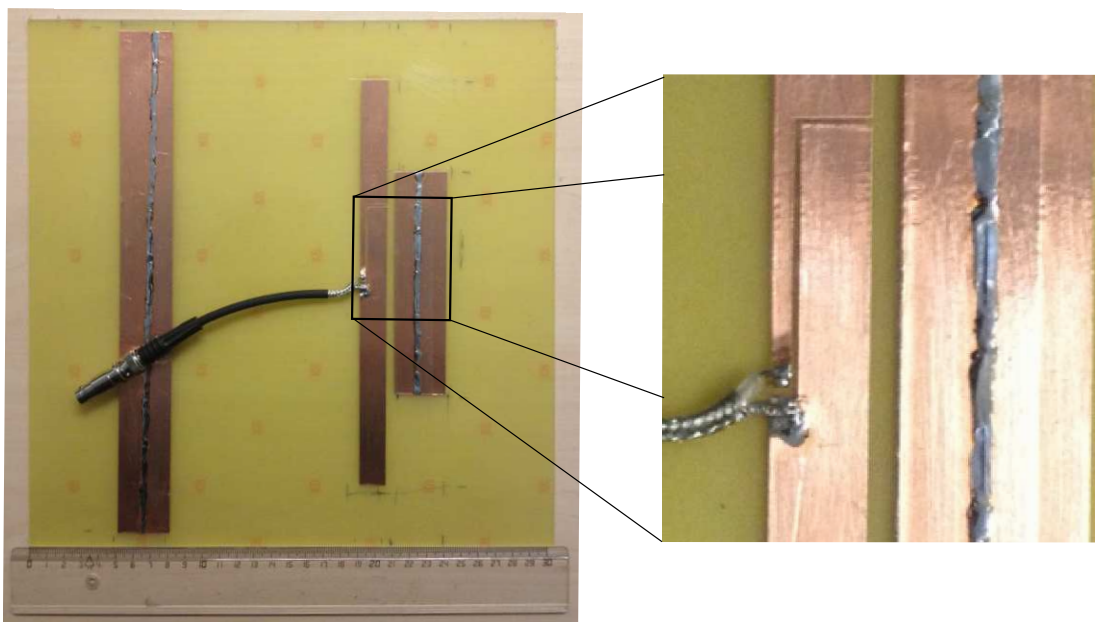


**Figure 3.12.** Fabricated antenna on a 1.6 mm thick FR4 substrate.

The antenna is printed on a 1.6 mm thick FR4 substrate. The reflection coefficient of the fabricated antenna is measured between 10 MHz and 1 GHz with the aid of the PNA-X Network Analyser [45]. The measured reflection coefficient as a function of frequency is shown in Fig. 3.13. It is clear from the figure the measured results of the reflection coefficients are lower than -10 dB for the frequency band between 475 MHz and 950 MHz which validates the broadband characteristics for the novel antenna.

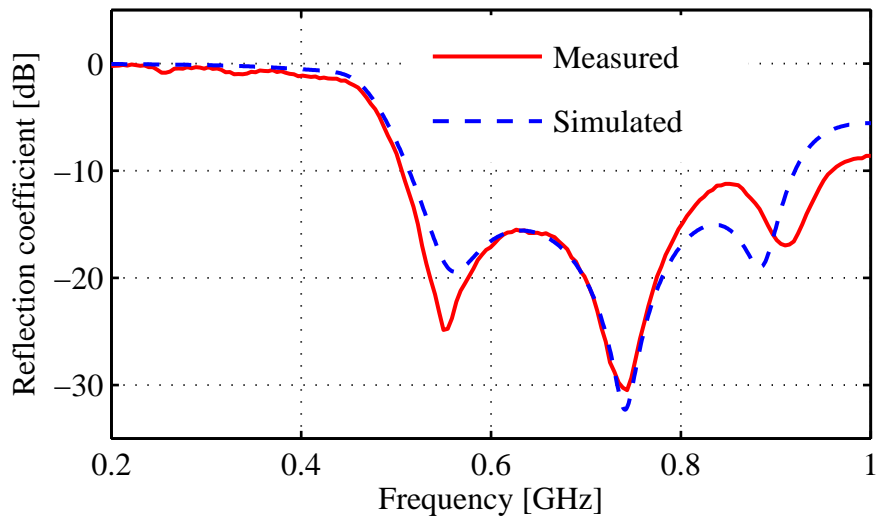


**Figure 3.13.** Simulated and measured reflection coefficient as a function of frequency.

Radiation diagrams in the E-plane of the fabricated prototype are measured at three different frequencies, 470 MHz, 650 MHz and 800 MHz. The E-plane and H-plane are indicated in Fig. 3.14.

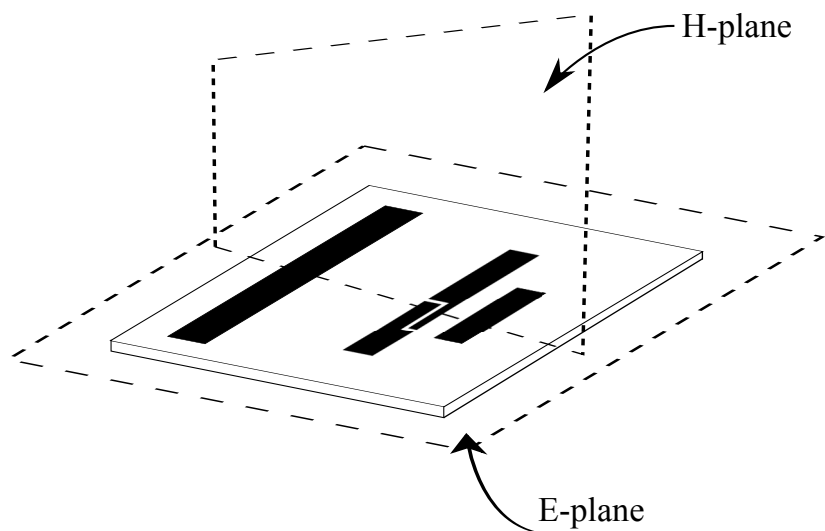


**Figure 3.14.** E-plane and H-plane.

Figure 3.15 shows the simulated and the measured radiation diagrams in the E-plane at the three different frequencies. The solid curve represents the simulated radiation diagrams while the dashed curve represents the measured ones. It is clearly indicated in the figure that the simulated radiation diagrams are validated by measurements with less than 0.5 dB difference in the direction of the main beam between  $\theta = 330^\circ$  and  $\theta =$

$30^\circ$  at 470 MHz and 650 MHz. At 800 MHz, the difference increases to 2.5 dB at  $30^\circ$ , but note that both in simulations and measurements the main beam has been tilted to the left.

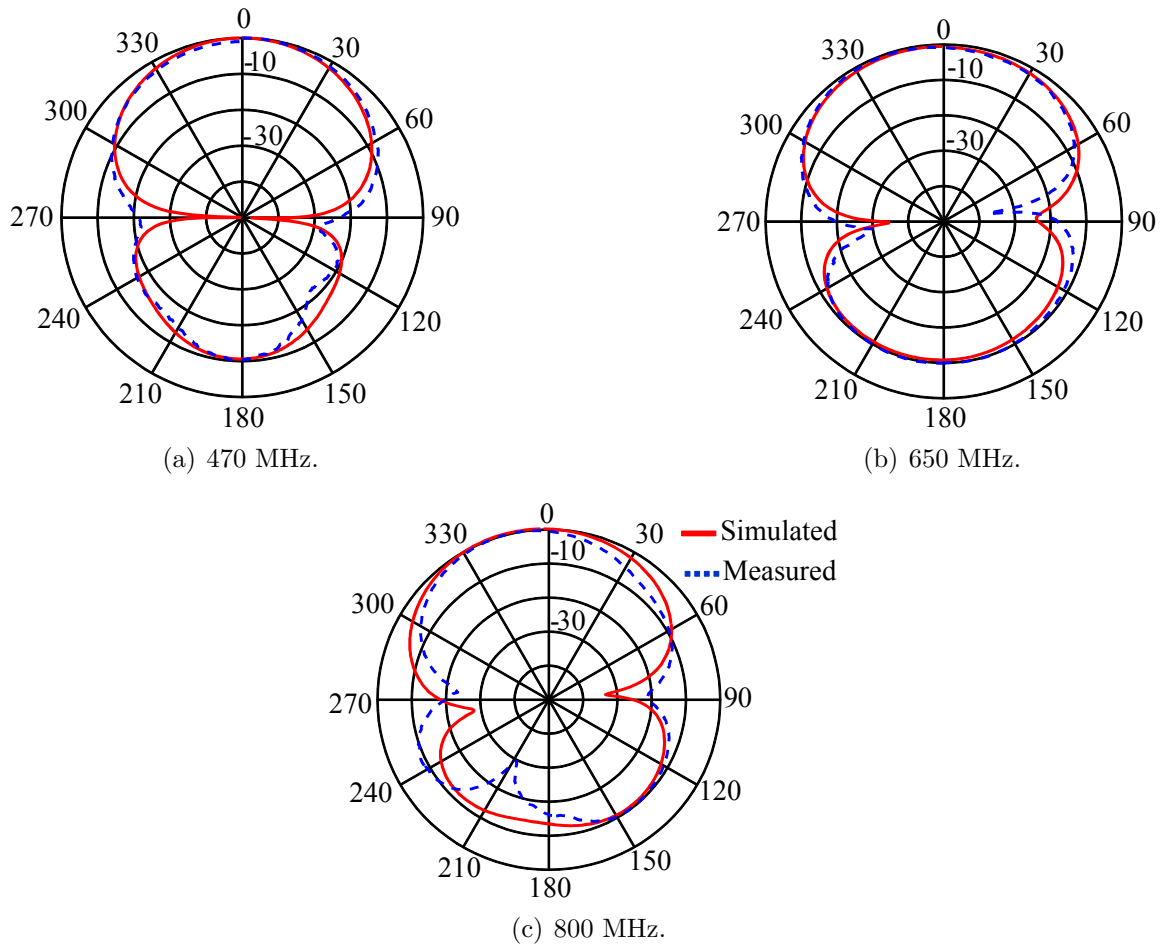


**Figure 3.15.** Simulated and measured normalized radiation diagrams in the E-plane of the broad-band Yagi-Uda antenna.

### 3.5 Triple-Band Modified Yagi-Uda Antenna

The exponential increase in the usage of wireless communication devices, especially mobile phones, increases the presence of electromagnetic radiation in the environment. The dominant communication systems are as follows: GSM (890-910 MHz), DCS/PCS/UMTS (1800-2100 MHz) and WiFi (2.446 - 2.454 GHz). RF energy harvesting from these transmitting sources has gained a lot of attention recently. A multi-band RF power harvesting system was introduced in [64]. In this section, the triple-band antenna suggested in [64] to have the possibility to harvest RF power at three different frequencies (900 MHz, 1800 MHz and 2.45 GHz), is presented.

Using the same design procedures as in the previous section, the antenna parameters can be optimized to produce a triple-band or a dual-band antenna. This section introduces a triple-band modified Yagi-Uda antenna. The following section introduces a dual-band modified Yagi-Uda antenna. The optimized parameters (see Fig. 3.7) for the triple-band antenna prototype are shown in the first two columns of Table 3.5.

**Table 3.5.** Optimized parameters for the triple-band and for the dual-band prototypes. The antenna is fabricated on a 1.6 mm thick FR4 substrate.

Parameter	Triple-band (mm)	Dual-band (mm)
D-L	42	38
F-L	130	119
F-W	10	10
R-L	170	160
R-W	5	5
R-D	20	20
D-D	6	5
D-W	8	5
g	1.2	0.5
b	1.35	2
t	13	11

The triple-band antenna (see column 1 and 2 in Table 3.5) is designed, simulated and manufactured on a 1.6 mm thick FR4 substrate. The simulated (solid curve) and the measured (dashed curve) reflection coefficients as a function of frequency are shown in Fig. 3.16.

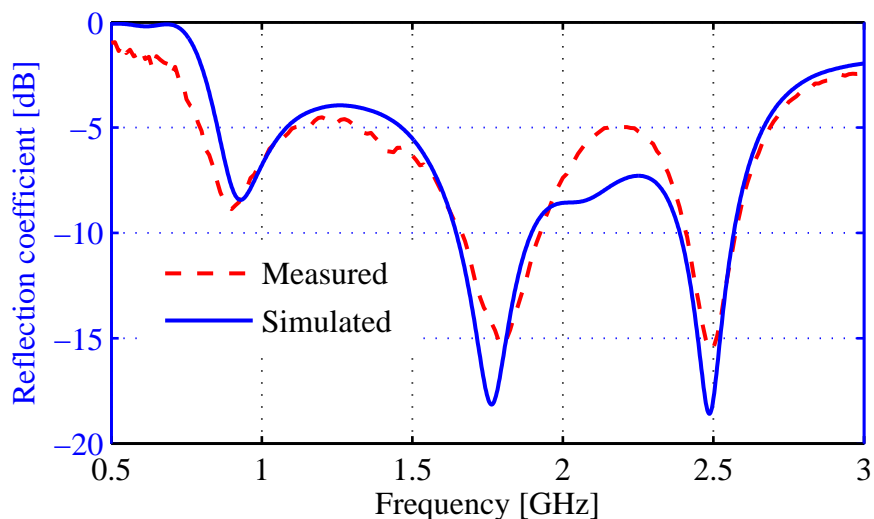


**Figure 3.16.** Measured and simulated reflection coefficients versus frequency of the triple-band Yagi-Uda antenna

It is observed in the figure that the measured reflection coefficients agree well with the simulated ones. The differences between the simulated and the measured results are less than 1 dB at 900 MHz, the difference increase to less than 3 dB at 1800 MHz and 2.45 GHz. The measured reflection coefficient is -8.6 dB, -16 dB and -13.25 dB at 900 MHz, 1800 MHz and 2.45 GHz respectively. This validates the triple-band characteristics for the antenna.

The normalized power radiation diagrams in the E-plane (see Fig. 3.14) have been simulated and measured at the three desired frequencies and are shown in Fig. 3.17.

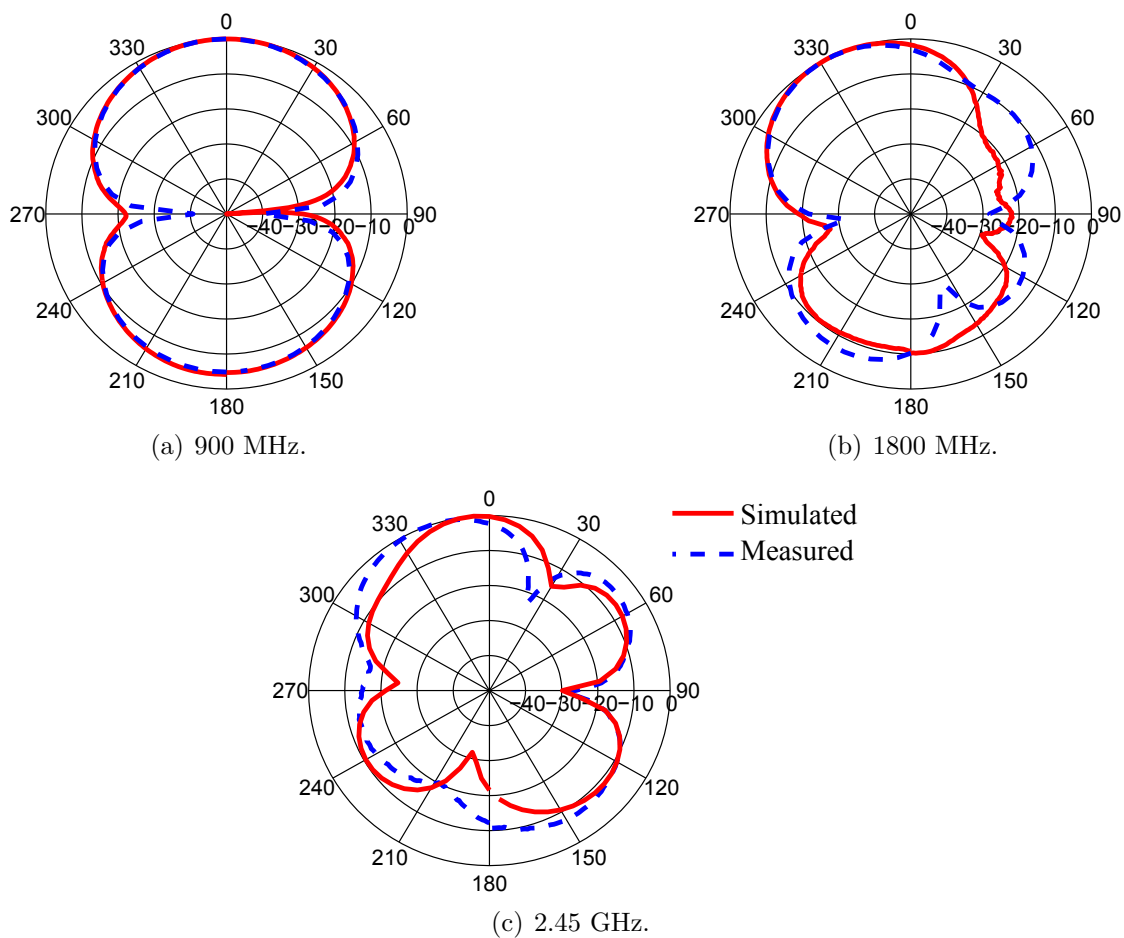


**Figure 3.17.** Simulated and measured normalized power radiation diagrams in the E-plane of the triple-band modified Yagi-Uda antenna.

Figures 3.17(a), 3.17(b) and 3.17(c) show the simulated and the measured normalized power radiation diagrams at 900 MHz, 1800 MHz and at 2.45 GHz respectively. It is shown that the simulated and the measured results agree well with less than 0.5 dB difference in the direction of the main beam between  $\theta = 330^\circ$  and  $\theta = 30^\circ$  at 900 MHz. It should be mentioned that the direction of the maximum propagation is shifted 30

degrees at 1800 MHz and at 2.45 GHz. This shift is due to the asymmetry in the driven element for the modified Yagi-Uda antenna (see Fig. 3.7). In the direction of the shifted main beam at 1800 MHz, between  $\theta = 300^\circ$  and  $\theta = 0^\circ$ , the difference between the simulated radiation diagram and the measured one is 1 dB at 1800 MHz.

At 2.45 GHz, in the direction of the main beam  $\theta = 330^\circ$ , the difference increases to 3 dB. Here the radiation pattern is more complex, showing multiple lobes explaining the higher differences.

### 3.6 Dual-Band Modified Yagi-Uda Antenna

To demonstrate the reconfigurability of the novel antenna geometry, a third prototype is presented in this section. The antenna here is designed to be a dual-band antenna resonating at 900 MHz and at 2.45 GHz. The optimized parameters for the novel dual-band antenna are listed in Table 3.5 (column 1 and 3).

Figure 3.18 shows the simulated (solid curve) and the measured (dashed-dotted curve) reflection coefficient versus frequency as well as the simulated antenna gain (dashed curve) as a function of frequency.

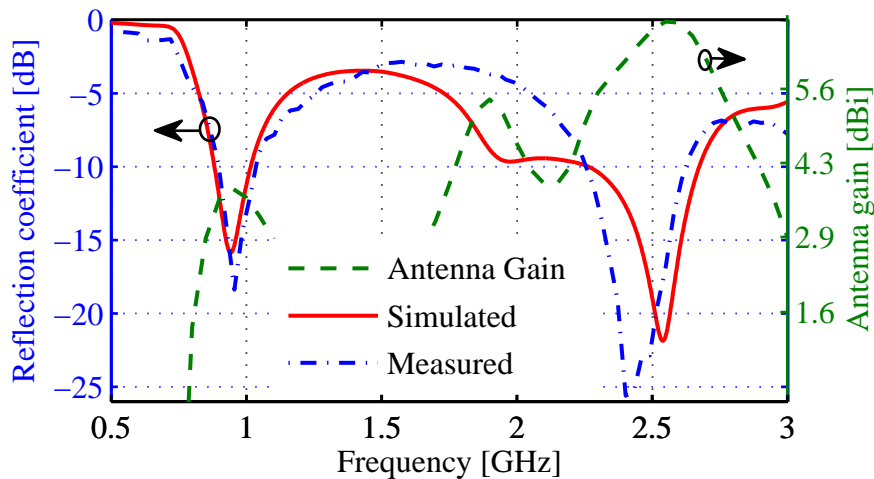


**Figure 3.18.** Simulated and measured results of the reflection coefficient and antenna gain as a function of frequency for the dual band antenna.

It is shown in the figure that a frequency shift of 100 MHz is present between the simulated and the measured reflection coefficients at the second resonance. This shift is due to fabrication tolerances due to the narrow gap width  $g$  of 0.5 mm. The simulated antenna gain reaches 3.2 dBi at 900 MHz and 6.45 dBi at 2.45 GHz.

The radiation diagrams in the E-plane have been simulated and measured for the dual-



band modified Yagi-Uda antenna. Figures 3.19 and 3.20 show the simulated and the measured normalized power radiation diagrams in the E-plane at the frequencies 900 MHz and 2.45 GHz respectively. The differences between simulations and measurements are less than 1 dB in the direction of the main beam between  $\theta = 330^\circ$  and  $\theta = 30^\circ$  at 900 MHz and at 2.45 GHz.

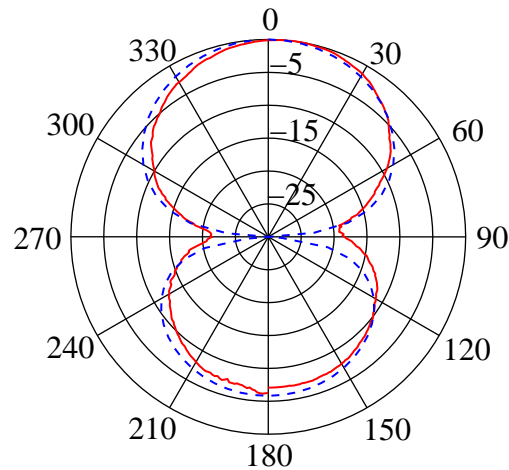


**Figure 3.19.** Simulated (dashed curve) and measured (solid curve) normalized power radiation diagrams in the E-plane of the dual-band modified Yagi-Uda antenna at 900 MHz.

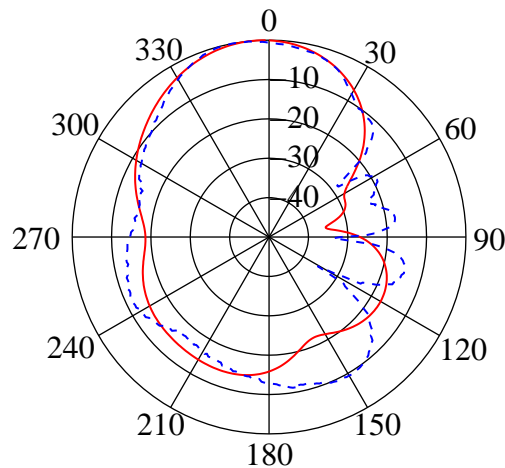


**Figure 3.20.** Simulated (dashed curve) and measured (solid curve) normalized power radiation diagrams in the E-plane of the dual-band modified Yagi-Uda antenna at 2.45 GHz.

## 3.7 RF Power Transport at 868 MHz

In this section, the receiving part of the RF power transport system is discussed. Design and measurement results will be described. The DC output voltage and the power conversion efficiency are measured for different values of the load resistance and for different input power levels.

### 3.7.1 Lumped-Element Matching Network

As is apparent from Fig. 3.1, a rectifier is needed to transform the RF input power into DC power. For a maximum power transfer between the antenna and the rectifier, an impedance matching network is designed, simulated, manufactured, and measured. Commercially available, discrete Schottky diodes HSMS-2852 [43] are used for power rectification.

Figure 3.21 shows a voltage doubler configuration.  $C_1$  and  $C_2$  are set to 100 pF. This value of  $C_1$  and  $C_2$  is not critical for the voltage doubler functioning. The capacitors need to function as ‘DC-blockers’.  $R_L$  is set to 10 k $\Omega$ . The main reason behind choosing  $R_L = 10$  k $\Omega$  is that the measured power conversion efficiency peaks around 10 k $\Omega$ . Moreover, this value is around the optimum input impedance of the power management circuit [65] that will follow the rectifier part (see Fig. 3.1).  $Z_{rectifier}$  is the input impedance of the voltage doubler.

The diode is a nonlinear device and its impedance changes as a function of frequency and as a function of input power level. A fixed input power level and a fixed operating frequency are chosen. Based on the results from previous chapters, we choose  $P_{in} = -10$  dBm and the operating frequency  $f = 868$  MHz (see Sec. 2.7). A lumped-element matching network is designed to match the input impedance of the rectifier to the input impedance of the antenna (50  $\Omega$ ).

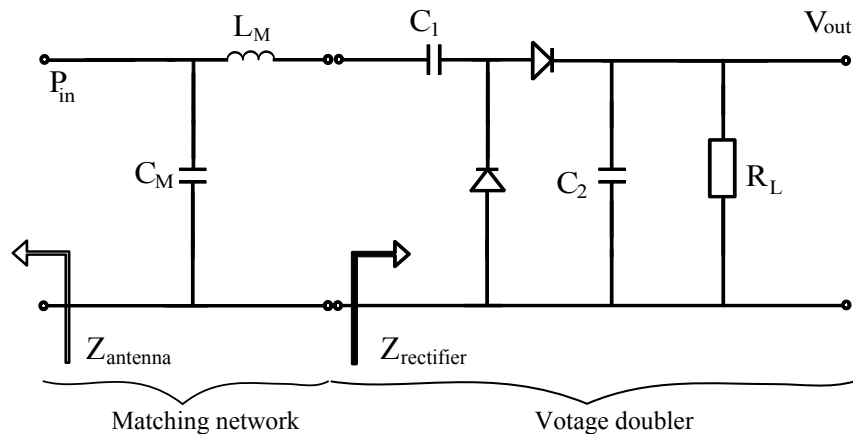


**Figure 3.21.** Voltage doubler configuration used to rectify the RF power harvested.

Agilent ADS [44] harmonic balance is used for impedance simulations. Figure 3.22 shows the Printed Circuit Board (PCB) footprint layout of the voltage doubler and the lumped-elements matching network. The components used to realize the circuit are summarized in Table 3.6. The circuit is printed on a 1.6 mm thick FR4 substrate.

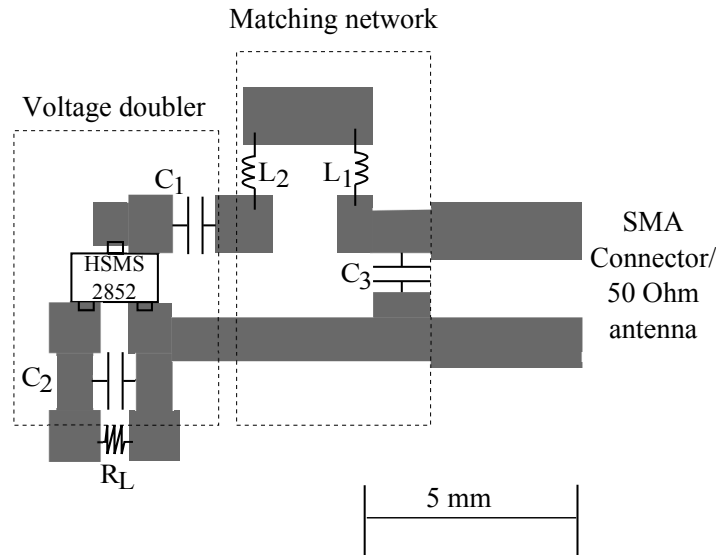


**Figure 3.22.** Layout of the PCB footprint of the voltage doubler and the matching network.

**Table 3.6.** Used lumped elements components.

Reference	Value	Manufacturer Ref.
$C_3$	0.7 pF	AVX SQCFVA 0R7BAT1A\500
$C_2, C_1$	100 pF	AVX 08052U101J
$L_1, L_2$	16 nH	JOHANSON TECHNOLOGY L- 15W16NJV4E
$R_L$	Variable resistor decade box	TENMA 72720
HSMS 2852	-	AVAGO TECHNOLOGIES HSMS-2852-TR1G

The reflection coefficient as a function of frequency for the realized network is measured for different input power levels, and the results together with the simulated ones are plotted in Fig. 3.23.

From the figures, it is observed that the simulated results agree reasonably well with the measured ones with a difference less than 3 dB between the simulated and the measured results. The designed matching networks match the impedance of the rectifier at 868 MHz for different power levels. At 868 MHz and using a  $10\text{ k}\Omega$  load the measured reflection coefficients are equal to  $-9.2\text{ dB}$ ,  $-11.9\text{ dB}$ ,  $-13.9\text{ dB}$  and  $-28.9\text{ dB}$  at  $-20\text{ dBm}$ ,  $-15\text{ dBm}$ ,  $-10\text{ dBm}$  and at  $-5\text{ dBm}$ , respectively. From the Figures, it is clear that the rectifier is matched to the antenna for the input power range  $-15\text{ dBm} \leq P_{in} \leq -5\text{ dBm}$  with a measured reflection coefficients less than  $-10\text{ dB}$ .

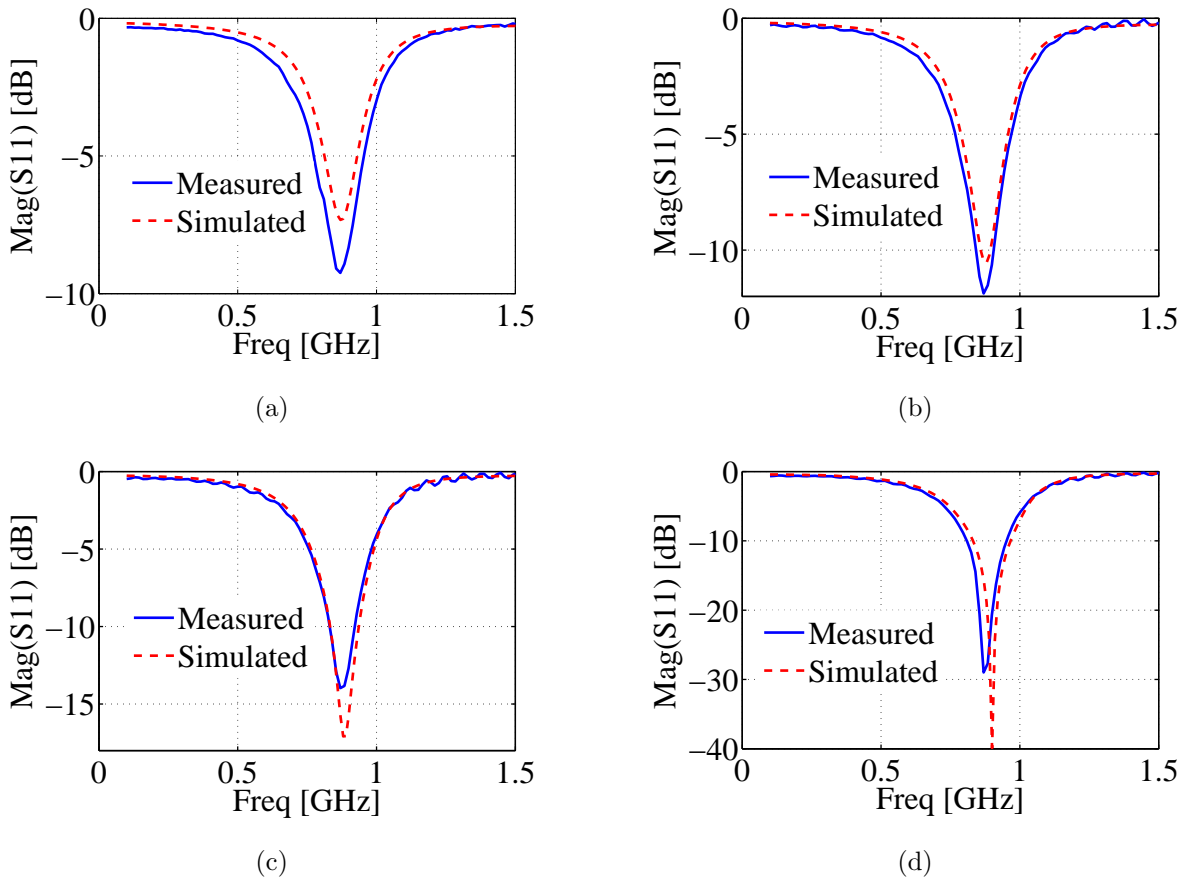


**Figure 3.23.** Reflection coefficients versus frequency for different input power levels.  $R_L = 10\text{ k}\Omega$ . (a)  $P_{in} = -20\text{ dBm}$ . (b)  $P_{in} = -15\text{ dBm}$ . (c)  $P_{in} = -10\text{ dBm}$ . (d)  $P_{in} = -5\text{ dBm}$ .

### 3.7.2 RF Power Transport Measurement Results

For RF power transport, a system as shown in Fig. 3.1 is being used. In this section, we describe how the rectenna is used for wireless RF power transfer. The power

transfer measurement setup is shown in Fig. 3.24. The setup is calibrated by using two antennas with a known gain,  $G_r$  and  $G_t$  (see Fig. 3.24) at 868 MHz separated by 1 meter. With the choice of the antenna, we ensure that far-field conditions are satisfied for both antennas. The power density ( $S$ ) at the receiving side is dictated by the effective isotropic radiated power,  $EIRP = P_t G_t$ , where  $P_t$  is the transmitted power and  $G_t$  is the transmit antenna gain, and by the distance  $R$  between the transmitting and the receiving antennas.

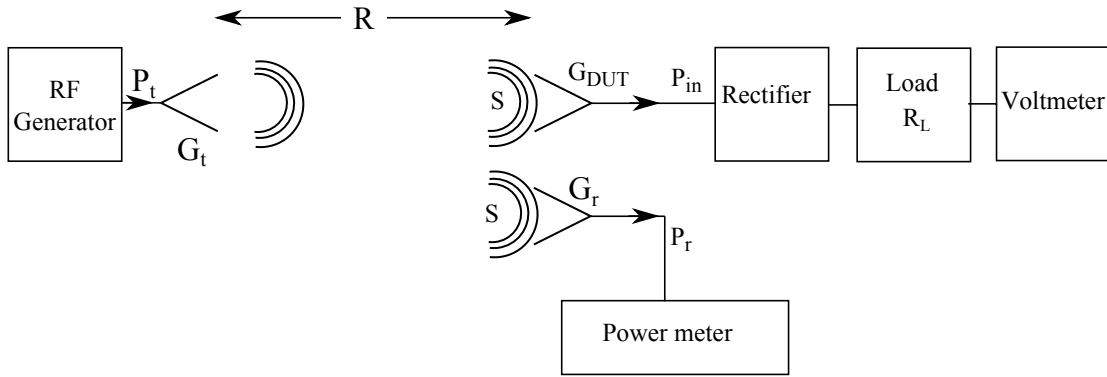


**Figure 3.24.** Power transfer measurement setup.

The power density is calculated by

$$S = \frac{EIRP}{4\pi R^2} = \frac{P_t G_t}{4\pi R^2}. \quad (3.1)$$

The antenna at the receiving side captures part of this power density with an effective aperture  $A_r$ . The received power  $P_r$  (see Fig. 3.24) is given by:

$$P_r = A_r S, \quad (3.2)$$

where  $A_r$  is the effective aperture of the receiving antenna in the direction of the transmitting antenna. According to [50], the effective aperture is related to the antenna gain by

$$A_r = G_r \frac{\lambda_0^2}{4\pi}, \quad (3.3)$$

where  $\lambda_0$  is the wavelength of transmitted signal. Substituting Eq. (3.3) in Eq. (3.2) in Eq. (3.1) leads to the Friis transmission equation where the received power at the

terminals of the power meter is expressed as

$$P_r = P_t G_t G_r \left( \frac{\lambda_0}{4\pi R} \right)^2 = P_t G_t G_r \left( \frac{c}{4\pi f_0 R} \right)^2, \quad (3.4)$$

where  $c$  is the free-space speed of light and  $f_0$  is the operating frequency of the transmitted signal.

A power meter is used to measure the received RF power  $P_r$ . The measured power  $P_r$  is then compared to the theoretically calculated value based on Eq. (3.4). The measured power appeared to be within  $\pm 0.5$  dB agreement with the theoretically calculated power, which ensures an accurate measurement setup. The rectenna is then placed for wireless power transport. The antenna gain of the rectenna is denoted by  $G_{DUT}$  as shown in Fig. 3.24.  $G_{DUT}$  is simulated with the aid of CST Microwave Studio. The input power level  $P_{in}$  at the clamps of the rectifier (see Fig. 3.24) is then calculated from

$$P_{in} = P_t G_t G_{DUT} \left( \frac{c}{4\pi f_0 R} \right)^2, \quad (3.5)$$

so that

$$P_{in} = \frac{P_r G_{DUT}}{G_r}. \quad (3.6)$$

The receiving rectenna system is connected to a variable load resistor  $R_L$ . The DC output voltage is measured with the aid of a voltmeter for different load resistances and for different input power levels.

The antenna of the receiving rectenna system shown in Fig. 3.24 consists of the modified Yagi-Uda antenna introduced in the previous section. The antenna is optimized to resonate at 868 MHz [37]. Then the antenna is connected to the rectifier through the impedance matching network and to a variable load resistor  $R_L$ . The DC output voltage is measured for different load resistances at three different input power levels -20 dBm, -10 dBm and -5 dBm calculated according to Eq. (3.6).

Figure 3.25 shows the measured output voltage versus load resistance at the three input power levels at an operating frequency  $f_0$  of 868 MHz. The solid curve represents the output voltage as a function of  $R_L$  at an input power level of -20 dBm. The dashed curve and the dotted-dashed curve represent the measured output DC voltage at -10 dBm and -5 dBm respectively. The system output voltage reaches 0.17 V, 0.7 V and 1.3 V over a 10 k $\Omega$  load resistance at an input power level of -20 dBm, -10 dBm and -5 dBm, respectively.

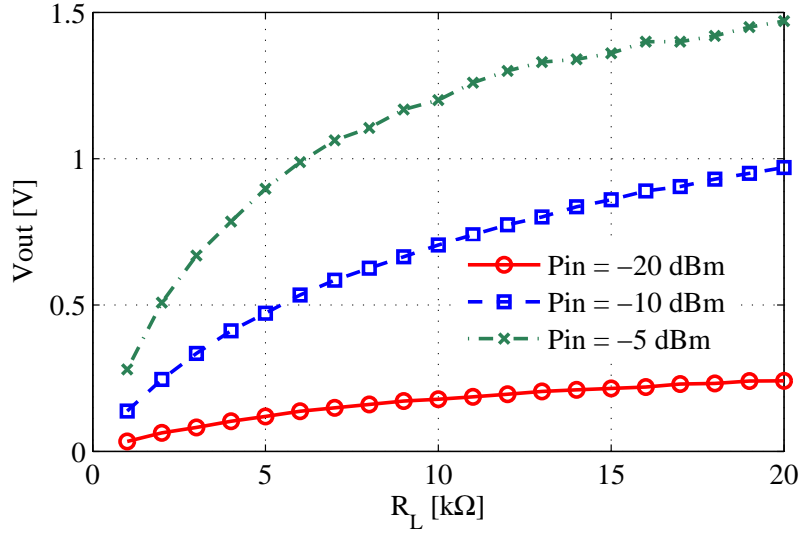


**Figure 3.25.** Measured DC output voltage versus load resistance  $R_L$  for different input power levels. Operating frequency  $f_0 = 868$  MHz.

The measured power conversion efficiency (PCE) is calculated using the following equation:

$$\text{PCE (\%)} = \frac{P_{load}}{P_{in}} = \frac{V_{out}^2}{R_L P_{in}} \quad (3.7)$$

The PCE is calculated for different input power levels from Eq. (3.7) and the results are plotted in Fig. 3.26.

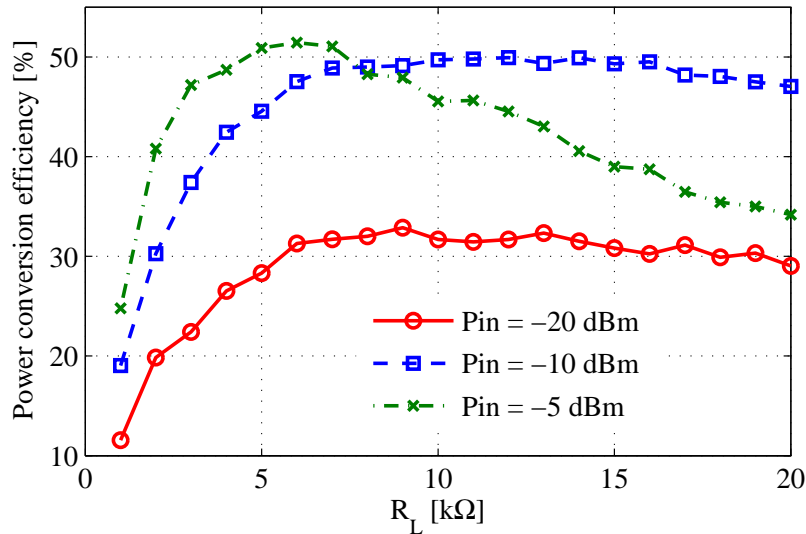


**Figure 3.26.** Measured power conversion efficiency (PCE) as a function of load resistance  $R_L$  for different input power levels. Operating frequency  $f_0 = 868$  MHz.

The system PCE reaches 31.6% and 49.7 % over a 10 k $\Omega$  load resistance at an input power level of -20 dBm and -10 dBm, respectively. The PCE decreases to 45.5 % at an input power level of -5 dBm across the same load resistance. Table 3.7 compares the presented results in this section to the state-of-the-art reported results [19, 66–68] that use commercially available discrete rectifiers.

**Table 3.7.** Comparison of rectenna systems in literature that uses commercially available discrete rectifiers

Reference	Pin [dBm]	Frequency [MHz]	Resistive Load k $\Omega$	Discrete rectifier	Power Conversion Efficiency
[66]	-10	866.5	3	HSMS285C	24*%
[19]	-10 -20	1800	2.4	HSMS2850	38*% 15*%
[67]	-10	830	10 <sup>4</sup>	HSMS286Y	44%
[68]	-20	850 1850	-	SMS7630	14*% 13*%
This work	-10 -20	868	10	HSMS2852	49.7% 31.6%

\*calculated from figure

The authors in [66] and [19] use the same Schottky rectifier as was used in this section. The peak measured power conversion efficiency is 24 % across a 3 k $\Omega$  load in [66] and is 38% across a 2.4 k $\Omega$  load in [19] which is lower than the 49.7 % achieved by using the suggested matching network.

In [67], the authors use the commercial rectifier HSMS-286Y in combination with an impedance matching circuit and a resonant circuit. The maximum measured PCE at 830 MHz and at -10 dBm is 44 %. Compared to the results reported in Fig. 3.26, the system suggested in this chapter is 5 % more efficient. It is clearly indicated in Table 3.7 that the rectenna presented in this chapter shows a higher efficiency performance at -20 dBm and at -10 dBm.

## 3.8 Conclusion

A novel modified Yagi-Uda antenna is presented in this chapter. The main advantage of the presented antenna is that, by tuning its parameters, the antenna can be reconfigured to behave as either a broad-band, triple-band or dual-band antenna. Three prototypes are designed to validate the reconfigurability of the antenna. The antennas are simulated, manufactured and measured. The simulated results are in line with the



measured ones. Agilent ADS harmonic balance simulations are used to design a voltage doubler and a matching network to match the impedance of the rectifier to  $50\Omega$ .

The DC output voltage and the power conversion efficiency as a function of load resistance at three input power levels are measured for a frequency of 868 MHz. The system output voltage reaches 0.17 V, 0.7 V and 1.3 V over a  $10\text{ k}\Omega$  load resistance at an input power level of -20 dBm, -10 dBm and -5 dBm respectively. The system PCE reaches 31.6 % and 49.7 % over a  $10\text{ k}\Omega$  load resistance at an input power level of -20 dBm and -10 dBm, respectively.

The  $50\Omega$  rectenna system presented in this chapter exhibits an increased PCE of at least 5 % at -10 dBm and at least 10 % at -20 dBm, compared to the reported state-of-the-art results.

# Compact and Conjugate-Matched Antenna Design

---

In this chapter we investigate different antenna topologies. These are the strip dipole, the folded strip dipole and a modified loop antenna. Novel, simple and accurate empirical expressions are introduced to calculate the input impedance of a strip dipole antenna. Next these expressions are employed to calculate the input impedance of a strip folded dipole antenna. A modified rectangular loop antenna with additional geometrical structures is introduced. The additional geometrical structures will make it possible to tune the antenna input impedance to the complex conjugate of that of a rectifier.

## 4.1 Introduction

To design an antenna with a specific input impedance, the geometry of the antenna should have enough parameters to be able to tune the input impedance. One such antenna is the strip-folded dipole array antenna shown in Fig. 4.1(a) [69]. This antenna is characterised by its broad bandwidth when the resonant frequencies of the individual elements are close together. If used for RFID applications and RF power harvesting, the strip folded-dipole array antenna has enough geometrical features to tune its input impedance. Another antenna that has ample geometrical features is the modified loop antenna shown in Fig. 4.1(b). Horizontal inner strips are added to the loop to tune the antenna input impedance. The main advantage of this modified loop antenna is its compact size compared to the strip-folded-dipole-array antenna.

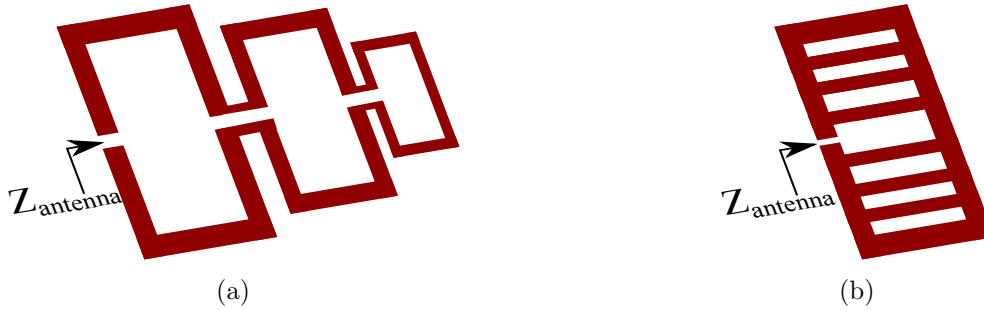


**Figure 4.1.** (a) Strip folded-dipole array antenna configuration and (b) the suggested modified loop antenna configuration.

The core of a strip folded-dipole array antenna is the folded dipole antenna. It is worthwhile therefore to put some effort into calculating the characteristics of the strip folded dipole antenna with a high degree of accuracy, without resorting to full-wave methods. The core of a folded dipole antenna is a dipole antenna. In this chapter, new empirical equations are introduced to calculate the input impedance of a strip dipole antenna. The proposed design equations are very accurate and can be easily implemented in standard computing tools, e.g. Matlab. The simulation results are validated by measurements. Next, updated analytical equations are presented to calculate the input impedance of an asymmetric strip folded dipole antenna. In addition, a novel and compact modified loop antenna configuration is introduced for which the antenna impedance can be tuned independently from its radiation efficiency. The impedance tuning ability eliminates the need for a matching network between the antenna and the rectifier which makes the rectenna system more compact, power-efficient, and cheaper to produce. The modified loop antenna will be used in Chapter 5 for RF power transport applications.

## 4.2 Strip Dipole Antenna

The basic element of the folded dipole antenna is the single dipole antenna [70]. A folded dipole antenna is commonly analyzed by recognizing a transmission line mode and a dipole antenna mode. The strip folded dipole antenna will be investigated in Sec. 4.3. In this section we present a strip dipole antenna analysis, using accurate and easy-to-use design equations to calculate the input impedance.

The input impedance of a dipole antenna can be calculated using full-wave analysis techniques, e.g. the method of moments (MoM) [71], and the finite integration technique (FIT) [72]. These methods are potentially very accurate for solving the Maxwell equations without a-priori approximations, but in general are time consuming. An alternative way is to use dedicated analytical-equation methods. Analytical equations may be derived by employing, among other methods, the induced EMF method, Hallén's

integral equation (HIE) method, and the King-Middleton second-order method [70]. While the resulting equations are easy-to-use, they appear to be insufficiently accurate to design antennas with a specific non-standard input impedance, especially when the radius of the cylindrical dipole antenna increases as shown in Appendix A. In this section, we present a simple but highly accurate analysis method that improves upon the known analytical expressions.

From a realization perspective, strip dipole antennas are more convenient than cylindrical wire dipole antennas. Strip dipole antennas may be implemented on foil, e.g. for RFID tags and even on-chip realizations are feasible.

A printed dipole antenna of width  $W$  can be analyzed by treating it as an equivalent cylindrical dipole antenna with a radius  $r = \frac{W}{4}$  [73].

### 4.2.1 Equivalent Radius of a Strip Dipole Antenna

Cylindrical and strip dipole configurations are shown in Fig. 4.2(a).

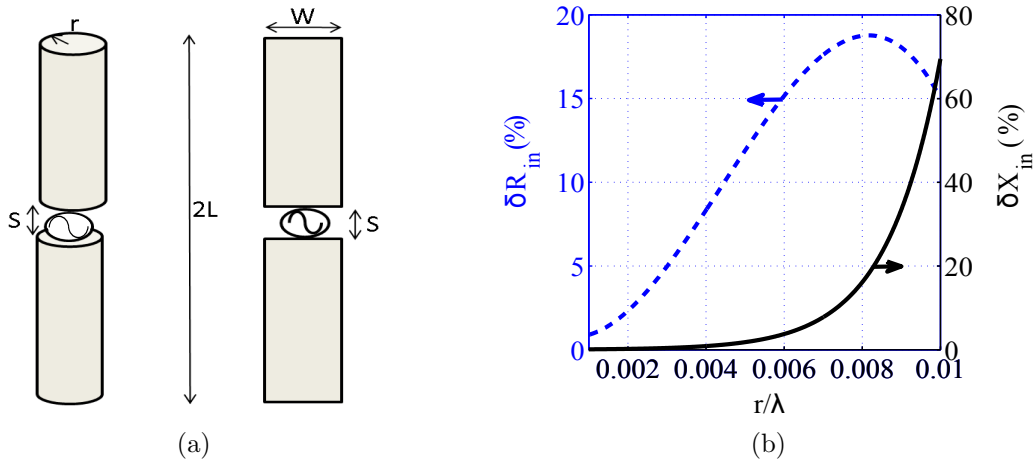


**Figure 4.2.** (a) Cylindrical and strip dipole configuration and (b) relative difference between the real and imaginary parts of the input impedance as a function of dipole radius over wavelength.  $L = 237$  mm,  $S = 2$  mm.  $\lambda = 1$  m.

To investigate the accuracy of the equivalence  $r = \frac{W}{4}$ , the radius  $r$  of the cylindrical dipole is set to a quarter of the strip dipole width  $W$ , and CST Microwave Studio [57] is used to calculate the input impedance of the strip dipole and its equivalent cylindrical dipole. The feeding gap  $S$  is set to  $0.002\lambda$  for the cylindrical dipole and for the strip dipole. This procedure is repeated for different dipole radii. Figure 4.2(b) shows the relative difference errors  $\delta R_{in} = (R_{Cylindrical} - R_{Strip}) / R_{Cylindrical}$  (dashed curve) and  $\delta X_{in} = (X_{Cylindrical} - X_{Strip}) / X_{Cylindrical}$  (solid curve) as a function of dipole

radius. It is shown in the figure that, for larger dipole radii, the deviation increases, which makes the quasi-static approach ( $r = \frac{W}{4}$ ) not accurate especially for larger dipole radii. Therefore, it should be used only for very thin cylindrical radii ( $\frac{r}{\lambda} \leq 0.004$  for  $\epsilon_{\delta R_{in}, X_{in}} \leq 10\%$ ). It should be mentioned that the frequency solver employed by CST Microwave Studio has been used for simulations which proved to be the most accurate compared to measurements.

## 4.2.2 Input Impedance of a Strip Dipole Antenna

Since the quasi-static approach ( $r = \frac{W}{4}$ ) is not accurate enough to calculate the input impedance of a practical strip dipole, a new analytical solution to calculate the impedance of a strip dipole of length  $2L$  and a width of  $W$  as shown in Fig. 4.2(a) is derived. The input impedance of the strip dipole antenna is calculated for different lengths and widths at a frequency of 300 MHz. Figure 4.3 shows the simulated results of the real (a) and imaginary (b) parts of the input impedance for  $1.0 \leq \left(\frac{2\pi L}{\lambda}\right) \leq 2.0$  and  $0.003 \leq \left(\frac{W}{\lambda}\right) \leq 0.04$  at an operating frequency of 300 MHz.

Different data fitting methods, using polynomial models, exponential models, Fourier series and power series have been investigated to best fit the results shown in Fig. 4.3. It has been found that the polynomial models match the simulated results with the lowest relative errors (less than 10 %). Matlab has been used to investigate the optimum fitting method. Since the strip dipole antenna has two parameters: the width  $W$  and the half-length length  $L$ , a two dimensional fitting expression is needed. Performing surface fitting on the full-wave calculated real and imaginary parts of the input impedances shown in Fig. 4.3, results in

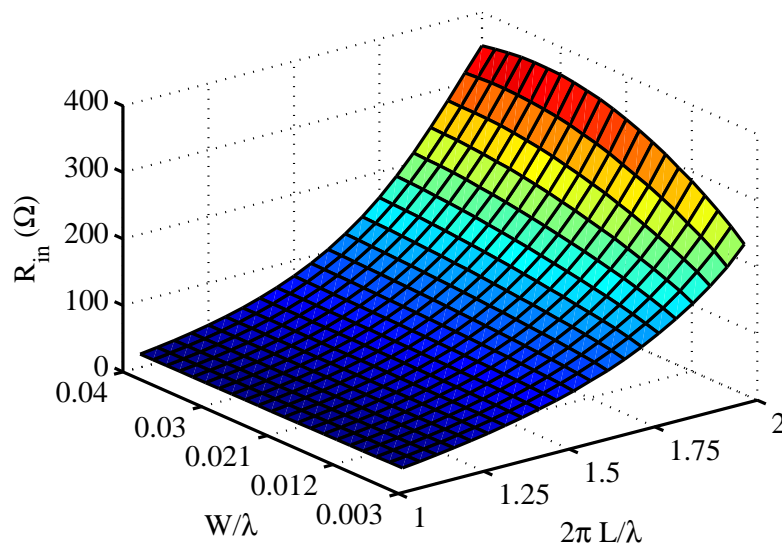
$$R_{in} \left( \frac{L}{\lambda}, \frac{W}{\lambda} \right) = \sum_{m=0}^5 \sum_{n=0}^5 R_{mn} \left( \frac{L}{\lambda} \right)^m \left( \frac{W}{\lambda} \right)^n, \quad (4.1)$$

$$X_{in} \left( \frac{L}{\lambda}, \frac{W}{\lambda} \right) = \sum_{m=0}^5 \sum_{n=0}^5 X_{mn} \left( \frac{W}{\lambda} \right)^m \left( \frac{L}{\lambda} \right)^n, \quad (4.2)$$

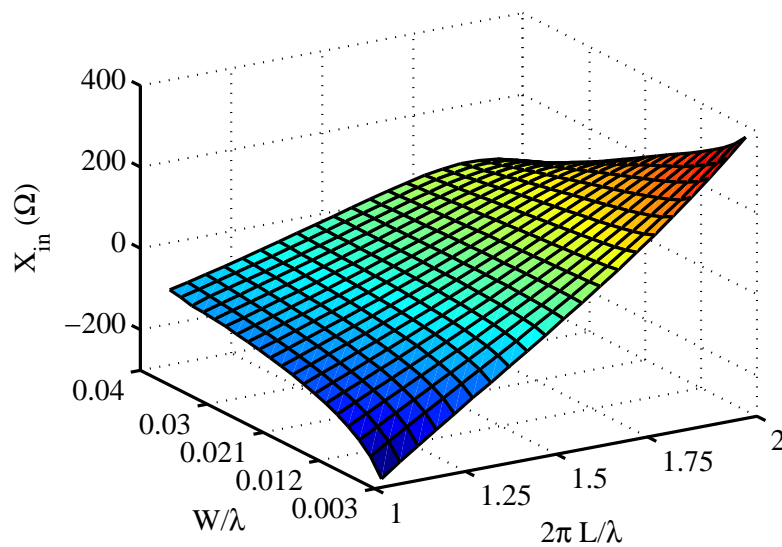
where the coefficients  $R_{mn}$  and  $X_{mn}$  are listed in Table 4.1 and Table 4.2, respectively.

The width of the feeding gap  $S$  is set to  $0.002\lambda$ . The effect of the feeding gap is limited and will be discussed in detail in Sec. 4.2.3. The impedance equations are valid for  $1.0 \leq \left(\frac{2\pi L}{\lambda}\right) \leq 2.0$  and  $0.003 \leq \left(\frac{W}{\lambda}\right) \leq 0.04$ , where they show a relative error less than 10 % for both real and imaginary parts. Compared to King-Middleton second-order fitting equations as described in Appendix A [70], which are valid only for  $1.3 \leq \left(\frac{2\pi L}{\lambda}\right) \leq 1.7$  and  $0.001 \leq \left(\frac{W}{\lambda}\right) \leq 0.01$ , the novel expressions are valid for longer

and wider strip dipole antennas, as will be shown in Sec. 4.2.3. These equations can be used for a feeding gap width  $S$  in the range of  $0.001\lambda$  to  $0.005\lambda$ .



(a)



(b)

**Figure 4.3.** Real (a) and imaginary (b) parts of the input impedance of a strip dipole antenna as a function of antenna half-length ( $L$ ) and antenna width ( $W$ ) calculated by the Finite Integration Technique (FIT).  $\lambda = 1$  m.

**Table 4.1.**  $R_{mn}$  coefficients used in Eq. (4.1) to calculate the input resistance of a strip dipole.

$m \backslash n$	0	1	2	3	4	5
0	211.4	-3.456e4	7.96e5	-5.796e6	2.535e7	2.089e8
1	-1486	5.072e5	-9.993e6	4.49e7	-2.478e8	0
2	-1.544e4	-2.582e6	4.235e7	-5.274e7	0	0
3	2.047e5	4.834e6	-6.439e7	0	0	0
4	-7.511e5	-1.251e6	0	0	0	0
5	9.655e5	0	0	0	0	0

**Table 4.2.**  $X_{mn}$  coefficients used in Eq. (4.2) to calculate the input reactance of a strip dipole.

$m \backslash n$	0	1	2	3	4	5
0	1022	-4.528e4	4.563e5	-2.015e6	4.277e6	-3.472e6
1	4.256e4	4.843e5	-6.868e6	2.478e7	-3.084e7	0
2	-4.147e6	2.13e7	-2.259e7	5.027e6	0	0
3	9.215e7	-3.885e8	2.088e8	0	0	0
4	-8.8e8	2.709e9	0	0	0	0
5	1.873e9	0	0	0	0	0

Figure 4.4 shows the real (a) and imaginary (b) parts of the input impedance of a strip dipole as a function of frequency calculated using the finite integration technique (FIT) and the analytical equations for strip dipoles (AE). The electrical length of the dipole is set to  $\frac{2\pi L}{\lambda} = 1.5$  ( $L = 11.93$  cm), the width  $W$  is set to  $0.003\lambda$  ( $W = 1.5$  mm). It is clear from Fig. 4.4(a) and Fig. 4.4(b) that the results obtained by the new empirical equations overlap the results obtained by the electromagnetic simulation software, which shows the accuracy of these fitting equations.

For this example, the relative difference error is calculated for both the real and imaginary parts. For the real part, the highest relative difference error occurs at a frequency of 800 MHz and it is equal to 8 %. For the imaginary part the highest relative difference error occurs at a frequency of 400 MHz and it is equal to 6 %. These equations have been verified for different strip widths and for different strip lengths as a function of frequency within the validity range. They show a relative error less than 10 % for both real and imaginary parts.

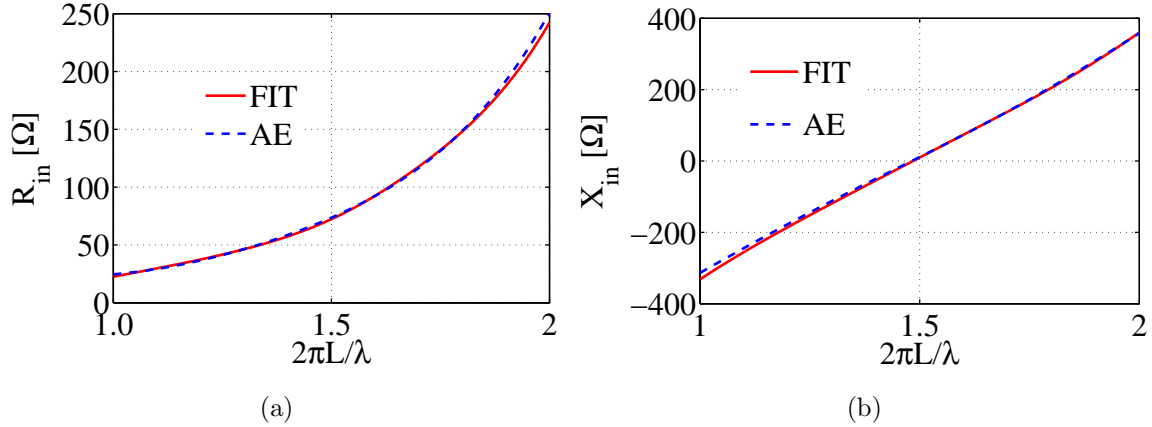


**Figure 4.4.** Real (a) and imaginary (b) parts of the input impedance of a strip dipole antenna as a function of frequency calculated by the Finite Integration Technique (FIT) and by the novel Analytical equations (AE).  $L = 11.93$  cm,  $W = 1.5$  mm,  $S = 1$  mm.

### 4.2.3 Feeding Gap $S$ Dependence

The presented equations are developed for a fixed feeding width  $S$  of  $0.002\lambda$  but may be valid over a range of  $S$ -values. The  $0.002\lambda$  constraint may be too specific for general use. To investigate the effect of the feeding width, the FIT is used to calculate the reflection coefficients and the input impedance of two strip dipole antennas A1 and A2 with a length  $L_1 = 225$  mm and a width  $W_1 = 20$  mm for antenna A1. The length and width for antenna A2 are  $L_2 = 115$  mm and  $W_2 = 10$  mm, respectively.

Figures 4.5(a) and 4.5(b) show the reflection coefficients relative to  $50\Omega$  as a function of frequency for different feeding width values  $S$  for antennas A1 and A2, respectively. It is shown in the figures that the antenna resonance is shifted when the feeding width is changed. However, for practical values ( $0.001\lambda - 0.005\lambda$ ) the change in the reflection coefficient is negligible (see Figs. 4.5(a) and 4.5(b)). Consequently, for these practical values, the change in the impedance may be neglected.

To calculate the deviations between the input impedance calculated by the Analytical Equations (AE) and calculated by the Finite Integration Technique (FIT), the Figure of Merit (FoM) introduced in Sec. 1.6 is used. Using the FoM, the validity of the presented formulas for different feeding widths  $S$  are expressed in a single number having the characteristics of a power wave reflection coefficient. The input impedance of a strip dipole is calculated from the presented empirical expressions and by using the FIT for different feeding width values  $S$ . The FoM accounts for the mismatch due to feed gap errors in the analytical calculations.

Figure 4.6 shows the FoM for the analytical equations as a function of feeding gap width  $S$  referred to the outcome of the FIT analysis for antennas A1 (solid curve) and antenna



A2 (dashed curve). It is clear from the figure that the presented expressions are valid for a feeding width up to  $0.02\lambda$  (Threshold  $\leq -10$  dB), which validates the accuracy of the novel empirical expressions for the practical values of the feeding gap ( $0.001\lambda - 0.005\lambda$ ) with a FoM  $\leq -20$  dB.

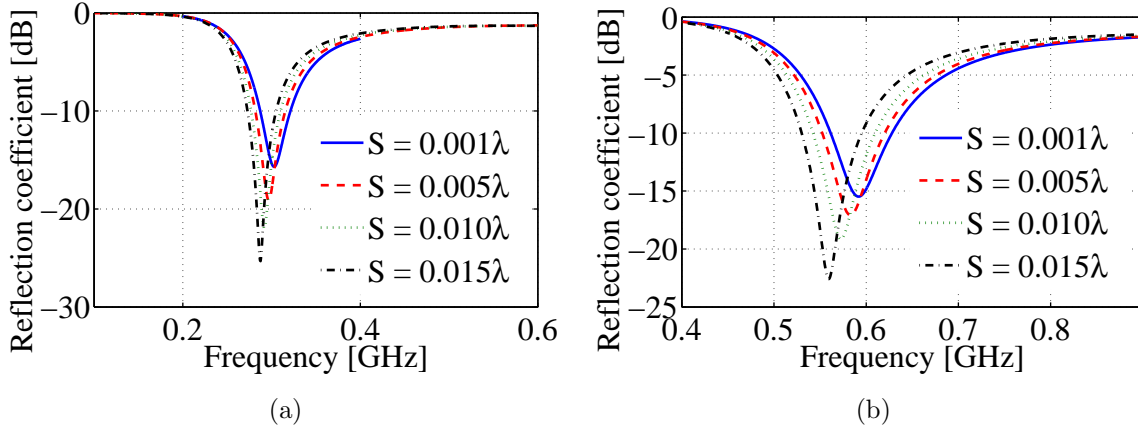


**Figure 4.5.** Reflection coefficients relative to  $50\Omega$  as a function of frequency for different feeding width  $S$  for antenna A1 (a) and antenna A2 (b).  $L_1 = 225$  mm,  $W_1 = 20$  mm,  $\lambda_1 = 1$  m.  $L_2 = 115$  mm,  $W_2 = 10$  mm,  $\lambda_2 = 0.5$  m

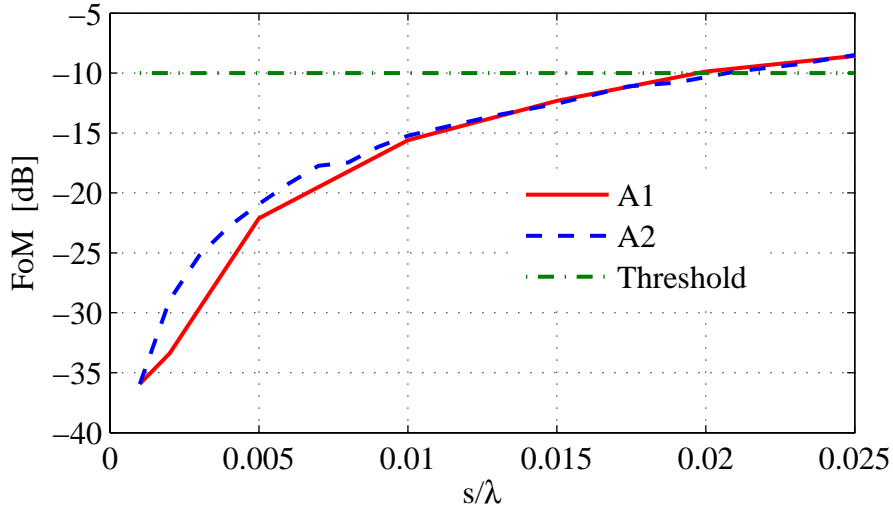


**Figure 4.6.** Figure of Merit (FoM) to calculate the deviations between the presented equations and the FIT for different feeding width for antenna A1 and antenna A2.

#### 4.2.4 Fabricated Antenna

So far, we have used the results of CST Microwave Studio as a reference. To verify the real accuracy of the novel empirical equations, a strip dipole antenna is designed, simulated using AE and FIT, manufactured and tested. The antenna is designed to cover the GSM900 frequency bands: 890-915 MHz (uplink) and 935-960 MHz (downlink) [74]. The designed length and width of the strip dipole are  $2L = 15$  cm,  $W = 1$  cm. Figure 4.7 shows the simulated (AE & FIT) and the measured reflection coefficients as a function of frequency. It is clear from the full-wave analysis results and the measurement results that the novel empirical equations can predict the input impedance behavior and the resonance of the strip dipoles with less than 2 dB difference in the reflection coefficients in the specified GSM900 frequency bands.

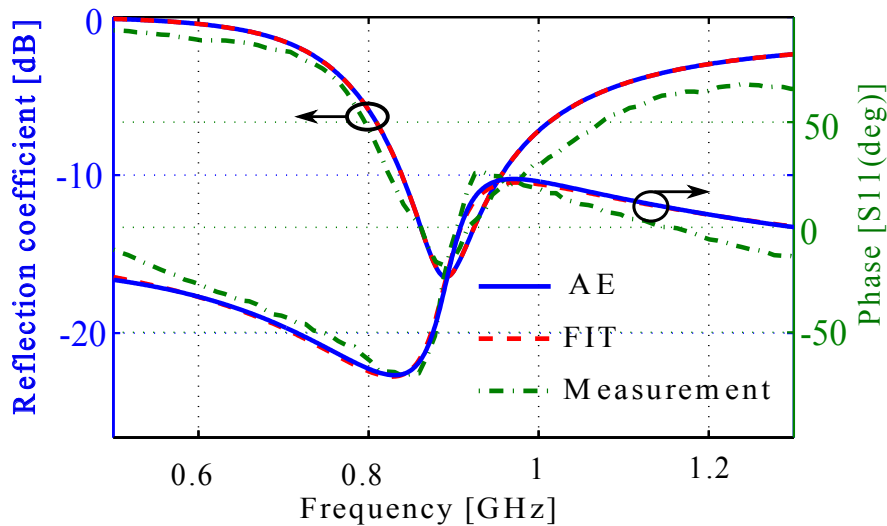


**Figure 4.7.** Simulated and measured reflection coefficients as a function of frequency.

### 4.3 Folded-Strip Dipole Antenna

The main limitation of the strip dipole antenna investigated in the previous section is its restricted number of geometrical features. This will make it hard to directly conjugate impedance match the antenna to a complex impedance. The impedance tuning ability of the strip dipole antenna depends only on the strip width  $W$ , the strip length  $2L$  and - to a lesser extent - the feed gap width  $S$  (see Fig. 4.2(a)). Another antenna with more geometrical features that can be used for RF power harvesting applications is the strip folded dipole antenna [75] shown in Fig. 4.8(a). The strip folded dipole antenna may

be regarded as an evolution of the strip dipole antenna.

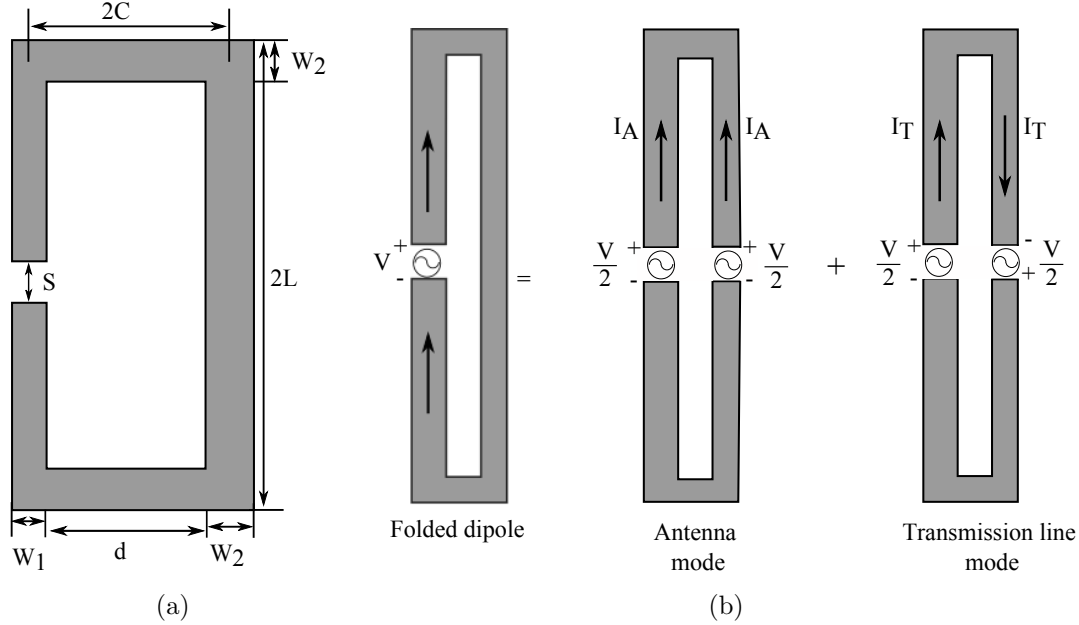


**Figure 4.8.** Strip folded dipole antenna configuration (a) and the decomposition of the current distribution into an antenna mode and a transmission line mode(b).

The main advantage of the strip folded dipole antenna over the strip dipole antenna is that it introduces two additional geometrical features,  $W_2$ , the width of the parallel, short-circuited dipole, and  $d$ , the inter-element distance between the CoPlanar Strips (CPS), (see Fig. 4.8(a)).

In this section we will discuss an updated design procedure to calculate the input impedance of an asymmetric strip folded dipole antenna. Compared to the state of the art [76, 77], the design procedure in this section does not use the equivalence between a strip and a circular cross section wire to calculate the input impedance of a strip dipole. Instead it directly uses the empirical equations (Eq. (4.1) and Eq. (4.2)) for the strip dipole antenna introduced in the previous section.

The folded dipole antenna analysis by Thiele and Ekelman [75] will be followed. The currents in the folded dipole are decomposed into two fundamental modes: the transmission-line mode and the antenna mode as visualized in Fig. 4.8(b), where  $I_A$  is the antenna current flowing on the surface of the dipole and  $I_T$  is the transmission line current.

### 4.3.1 Input Impedance of a Strip Folded Dipole

Figure 4.8(a) shows the configuration of an asymmetric strip folded dipole antenna in free space. By decomposing the current into two modes, the input impedance of the strip folded dipole has become a function of three variables, the input impedance of the strip dipole, the input impedance of the coplanar strip transmission line stubs that may be recognized in the antenna configuration and the step-up impedance ratio [78,79] accounting for the difference in strip widths. The input impedance of the folded dipole antenna is then found to be [33]:

$$Z_{in} = \frac{2(1+q)^2 Z_D Z_T}{(1+q)^2 Z_D + 2Z_T}, \quad (4.3)$$

where  $Z_D$  is the input impedance of a strip dipole antenna with length  $2L$  and width  $W_1$ .  $Z_T$  is the input impedance of the asymmetric coplanar strip transmission line stub of length  $L$ . The CPS line widths are  $W_1$  and  $W_2$ , respectively, and  $(1+q)^2$  is the step-up impedance ratio [75].  $q$  will be specified in the next subsection.

### 4.3.2 Transmission Line Analytical Equations

The input impedance of a short circuited length of coplanar strip transmission line  $Z_T$  is calculated from the general transmission line theory as [80]:

$$Z_T = jZ_C \tan\left(\frac{\beta L}{2}\right), \quad (4.4)$$

where  $Z_C = \left[\frac{120\pi}{\sqrt{\epsilon_r}} \frac{K(k)}{K'(k)}\right]$  is the characteristic impedance of the CPS transmission line [76].  $K(k)$  is the complete elliptic function of the first kind where  $K'(k) = K(k')$  and  $k'^2 = 1 - k^2$ . The ratio of the complete elliptic functions  $\frac{K(k)}{K'(k)}$  may be approximated by [81],

$$\frac{K(k)}{K(k')} \approx \begin{cases} \frac{1}{2\pi} \ln \left[ 2 \frac{\sqrt{1+k} + \sqrt[4]{4k}}{\sqrt{1+k} - \sqrt[4]{4k}} \right] & \text{for } 1 \leq \frac{K}{K'} \leq \infty, \quad \frac{1}{\sqrt{2}} \leq k \leq 1 \\ \frac{2\pi}{\ln \left[ 2 \left( \frac{\sqrt{1+k'} + \sqrt[4]{4k'}}{\sqrt{1+k'} - \sqrt[4]{4k'}} \right) \right]} & \text{for } 0 \leq \frac{K}{K'} \leq 1, \quad 0 \leq k \leq \frac{1}{\sqrt{2}} \end{cases} \quad (4.5)$$

The argument  $k$  is given by [78,79],

$$k = \frac{\left(\frac{d}{2}\right) \left(1 + e \left(\frac{d}{2} + W_1\right)\right)}{\left(\frac{d}{2}\right) + W_1 + e \left(\frac{d}{2}\right)^2}, \quad (4.6)$$

and

$$e = \left[ \frac{W_1 W_2 + \frac{d}{2} (W_1 + W_2) - \sqrt{W_1 W_2 (d + W_1) (d + W_2)}}{\left(\frac{d}{2}\right)^2 (W_1 - W_2)} \right], \quad (4.7)$$

where  $W_1$  is the width of the strip dipole,  $W_2$  is the width of the parallel, short circuited dipole and  $d$  is the distance between the CPS strips as shown in Fig.4.8(a). The step-up impedance ratio  $(1 + q)^2$ , is calculated from [78],

$$q = \left[ \frac{\ln \left\{ 4C + 2\sqrt{(2C)^2 - \left(\frac{W_1}{2}\right)^2} \right\} - \ln \{W_1\}}{\ln \left\{ 4C + 2\sqrt{(2C)^2 - \left(\frac{W_2}{2}\right)^2} \right\} - \ln \{W_2\}} \right], \quad (4.8)$$

where  $2C$  is the distance from the middle of the strip dipole to the middle of the parallel dipole as shown in Fig.4.8(a). ( $C = \frac{d}{2} + \frac{W_1}{4} + \frac{W_2}{4}$ ). Now, we will follow the existing analysis for the strip folded dipole antenna and replace the dipole input impedance with the newly derived expressions.

### 4.3.3 Validation of the New Analytical Procedures

To verify the accuracy of the updated analytical expressions, the real and imaginary parts of the input impedance of a strip folded dipole are calculated using CST Microwave Studio (FIT). These results are compared to the results of the proposed analytical expressions (AE). Figure 4.9 shows the input impedance (real and imaginary parts) as a function of frequency for a strip folded dipole calculated by both the FIT and the AE. The strip widths are  $W_1 = 8$  mm, and  $W_2 = 4$  mm, the separation between strips is  $d = 16$  mm, the strip folded dipole length is  $2L = 16$  cm and the feeding width is  $S = 2$  mm.

It is clear from the figure that the results obtained by the AE deviate from the results obtained by the FIT. Both curves (for the real and imaginary parts) show more or less the same behavior, but a frequency shift is visible as well as a change in the impedance level. To investigate possible sources of errors in the analytical expressions, the surface current distribution is simulated with the aid of CST Microwave Studio. Figure 4.10 shows the surface current distribution on a strip folded dipole antenna for two different separation distances,  $d = 16$  mm and  $d = 32$  mm, at an operating frequency of 1.2 GHz.

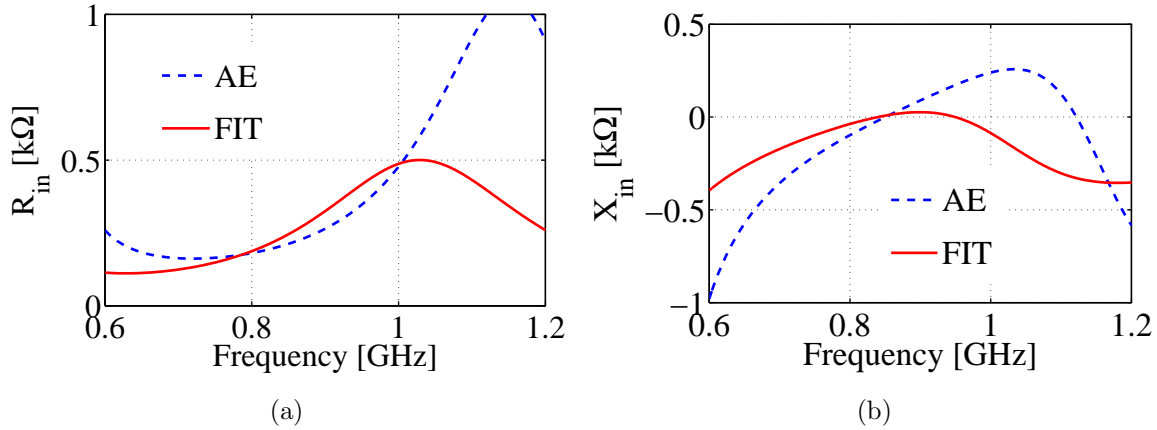


**Figure 4.9.** Real (a) and imaginary (b) parts of the input impedance versus frequency for an asymmetric strip folded dipole antenna calculated using the Finite Integration Technique (FIT) and the Analytical Equations (AE).  $W_1 = 8$  mm,  $W_2 = 4$  mm,  $d = 16$  mm,  $2L = 16$  cm.

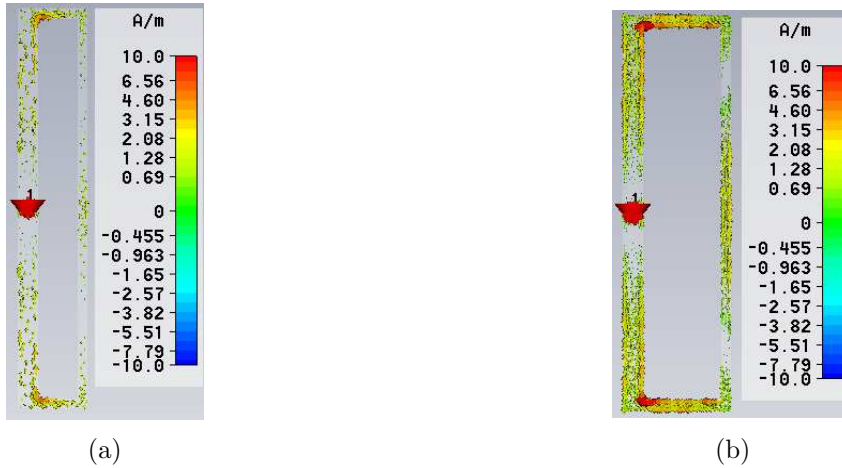


**Figure 4.10.** Surface current distribution on a strip folded dipole antenna for a separation between strips of (a)  $d = 16$  mm and of (b)  $d = 32$  mm.  $W_1 = 8$  mm,  $W_2 = 4$  mm,  $2L = 16$  cm. Frequency = 1.2 GHz

It is observed in Fig. 4.10 that a considerable amount of current flows along the short-horizontal strips. Moreover it is shown that when the separation distance is increased to  $d = 32$  mm (Fig. 4.10(b)) the surface current density in these strips increases.

When the input impedance of the coplanar strip transmission line  $Z_T$  is calculated, it is assumed that the coplanar strip lines are connected with an infinitely thin horizontal strip, but in reality they are interconnected with a strip that has the same width as the transmission line  $W_2$ . Consequently, the deviations shown in Fig. 4.9 are assumed

to be due to the connecting strips of length  $d$ . In order to compensate for the distance between the CPS and the current flowing in the connecting strips, a correction to the transmission line length is required.

To derive the correction factor analytically, the input impedance of the antenna is calculated and compared to the results obtained by FIT. Then the length of the transmission line in the transmission line mode is increased until the resonance frequency of the AE coincides with that of the FIT. This procedure is repeated for different separation widths  $d$ .

The correction to the transmission line length  $L_T$  is calculated as:

$$L_T = 2L + \Phi(d) \lambda d, \quad (4.9)$$

where the correction factor  $\Phi(d)$  for the separation width is found to be

$$\Phi(d) = (0.06243d^{(-1.038)} + 3.071). \quad (4.10)$$

The results after using this correction factor are shown in Fig. 4.11. It is shown in the figure that when the correction factor is used, the proposed analytical equations can predict the impedance behavior of the strip folded dipole antenna within reasonable accuracy as will be explained in the following.

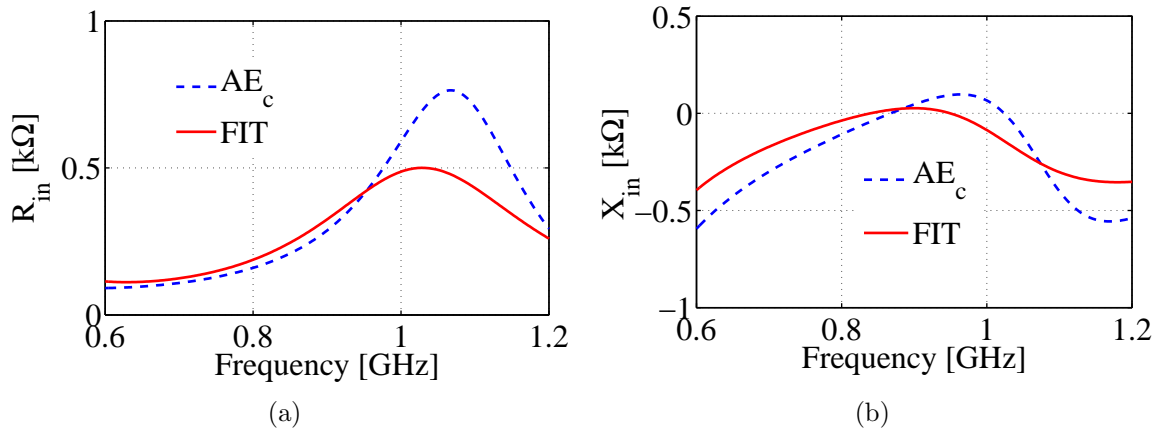


**Figure 4.11.** Real (a) and imaginary (b) parts of the input impedance versus frequency for the same asymmetric strip folded dipole antenna as analyzed in Fig. 4.9. The correction factor for the transmission line length is introduced in the analytical expressions.

To quantify the improvement of using the correction factor in terms of a single Figure of Merit, Eq.(1.2) is used to transform the deviations into power reflection coefficients. Using the suggested Figure of Merit, the deviations between the input impedance calculated by the FIT and by AE without a correction factor (Fig. 4.9) and when the

correction factor is employed (Fig. 4.11) are casted into a single plot. The higher the deviations between FIT and AE are, the higher the reflection coefficients (FoM) will be.

Figure 4.12 shows the Figure of Merit as a function of frequency for the two simulations. The dashed curve represents the FoM for the uncorrected Analytical Expressions (AE), while the solid curve represents the FoM for the corrected Analytical Expressions ( $AE_c$ ). It is shown in the figure that, when the correction factor is used, the validity range of the corrected analytical expressions (0.75 GHz - 1.05 GHz) is extended by approximately 50 % compared to a validity range of the uncorrected analytical expressions (0.75 GHz - 0.95 GHz). The validity range is determined by a FoM not exceeding -10 dB. Two more validation examples, one for an antenna resonant at 300 MHz and one for an antenna resonant at 1.5 GHz, are presented in [82], and are shown in Appendix A.

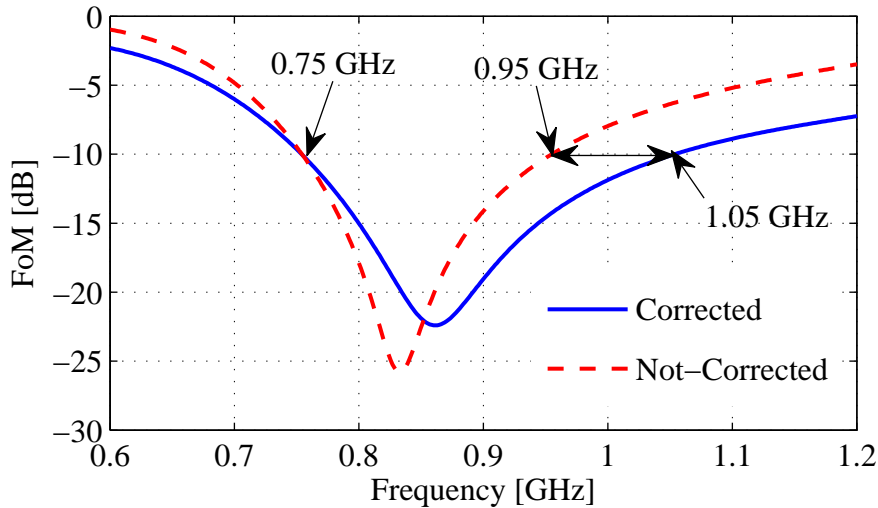


**Figure 4.12.** FoM as a function of frequency for the AE and corrected AE

The analytical expressions for the folded strip dipole antenna are valid within the range  $1.3 \leq \left(\frac{2\pi L}{\lambda}\right) \leq 1.7$  ensuring a  $FoM \leq -10$  dB. The validity range of these expressions is also limited for  $d$ , being less than 1/20th of a wavelength.

Although we now have an antenna type with more possibilities to tune its input impedance than a strip dipole antenna, the tuning possibility may still be too limited for a practical use. Moreover, the size of the antenna (about half a wavelength long) might be too large for some applications, especially for Smart Building Integration (SBI). The following section therefore introduces a compact modified rectangular loop antenna.



## 4.4 Modified Rectangular Loop Antenna

In this section, a novel and compact antenna configuration is introduced to be conjugately matched to the impedance of the rectifier. The antenna is a modified rectangular loop antenna. The modification consists of adding additional arms to control its input impedance. The suggested antenna configuration is shown in Fig. 4.13 and consists of metal printed on a substrate. The radiation characteristics (radiation efficiency and radiation pattern) of the antenna are dictated by the outer antenna length and width  $L_1$  and  $L_2$ , respectively, while adding additional arms to the antenna allows tuning its input impedance without affecting the radiation characteristics much. The width of each arm  $W_1$  to  $W_n$  and the distance between the arms  $E_1$  to  $E_n$  are fine tuned to obtain the exact desired input impedance.

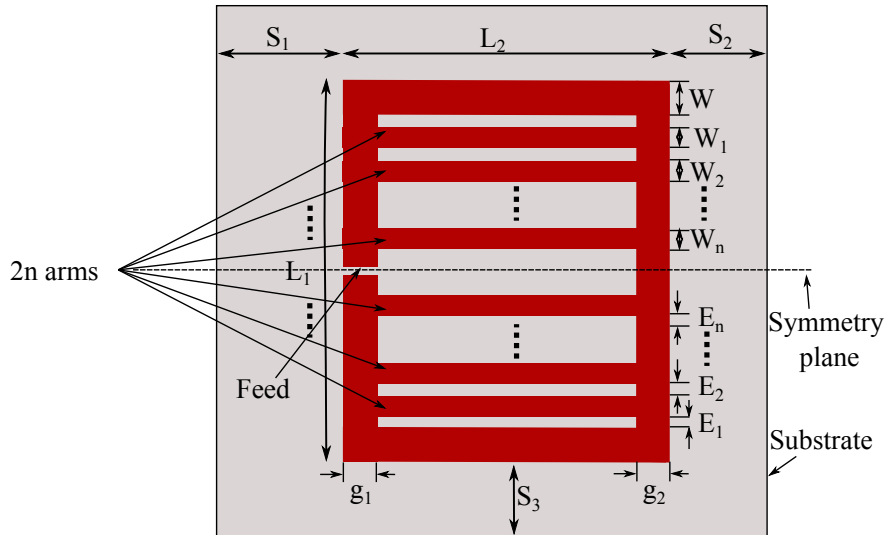


**Figure 4.13.** Compact antenna topology and dimensional parameters.

In order to understand the physical behavior of the suggested antenna, CST Microwave Studio is used to simulate the surface current density for four different antenna configurations that possess the same outer dimensions  $L_1$  and  $L_2$  (see Fig. 4.13). The parameters of the four simulated antennas denoted by A1, A2, A3 and A4 are listed in Table. 4.3.

**Table 4.3.** Antenna parameters used to calculate the input impedance and the radiation efficiency. All dimensions are in millimeters.

$W_1, W_2, W_3, E_1, E_2$	$E_3$	$W, g_1, g_2$	$L_2$	$L_1$	$S_1$	$S_2$	$S_3$
3	4	5	32	54	10	7	8

The first simulated antenna (A1) is a loop antenna without any additional arm see Fig. 4.14(a). The outer dimensions of the loop antenna are  $L_1$  and  $L_2$ . The width of the strips are  $W$ ,  $g_1$  and  $g_2$ . The second simulated antenna (A2), with  $n = 1$ , has exactly the same outer dimensions as antenna A1 but with two additional arms added as shown in Fig. 4.14(b). The additional needed parameters to simulate antenna A2 are  $W_1$  and  $E_1$ . In the same way the third antenna (A3) and the fourth antenna (A4) are designed and simulated. Antenna (A3) with  $n = 2$ , possesses the same outer characteristics as antenna A1 but has four additional arms while antenna A4 ( $n = 3$ ) has 6 additional arms compared to antenna A1.

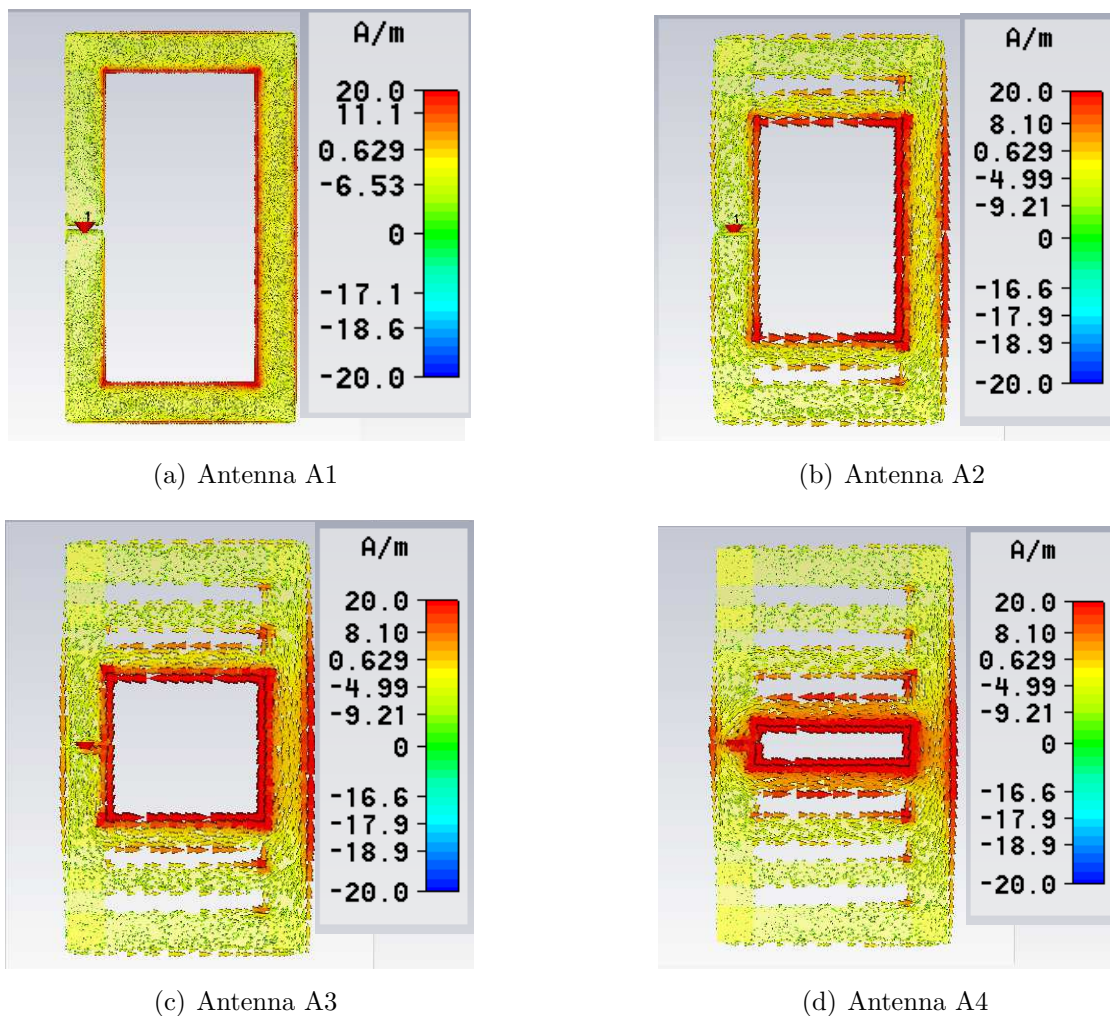


**Figure 4.14.** Surface current density on the suggested compact loop antenna for different numbers of additional arms. Frequency = 868 MHz.

Figure 4.14(a) shows the surface current density for antenna A1. It is clear from the figure that the surface current density is distributed along the loop. When two

arms are added to antenna A1 to form antenna A2, the maximum current density is concentrated in the inner loop as shown in Fig. 4.14(b). Similarly, when more internal arms are added to the loop, the maximum current density is drawn by the inner loops as shown in Fig. 4.14(c) and Fig. 4.14(d). Using the suggested configuration, the antenna input impedance and its radiation efficiency can be tuned separately. Since the surface current density is concentrated in the inner loop, consequently the inner loop dictates the input impedance of the antenna, while the outer loop dimensions  $L_1$  and  $L_2$  determine the antenna radiation efficiency. The arms between the inner loop and the outer loop are used to fine tune the antenna input impedance.

#### 4.4.1 Impedance Tuning Capability

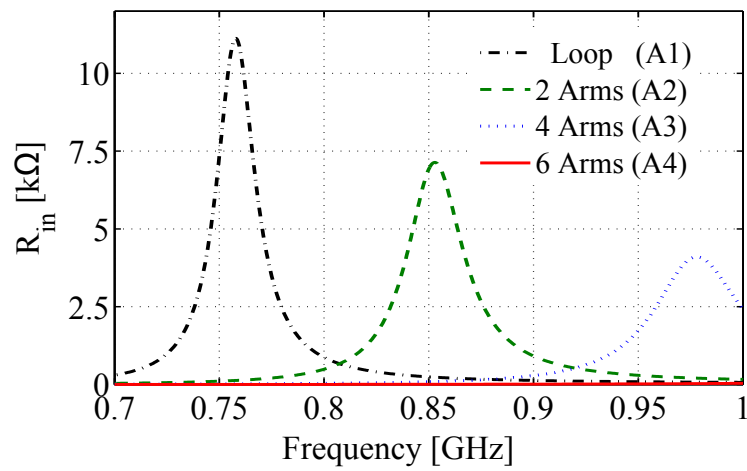
To verify the tuning capability of the suggested antenna configuration, the antenna input impedance and the radiation efficiency are simulated using CST Microwave Studio for the antennas A1, A2, A3 and A4. Figure 4.15 shows the real (a) and imaginary (b) parts of the input impedance as well as the radiation efficiency (c) as a function of frequency for the four simulated antennas. We see, as we expected, that the inner loop dominates the impedance and we see that the resonance shifts toward higher frequencies with the addition of more internal arms. Since the outer arms do draw currents but these currents are much smaller than those in the inner loop, we only observe a slight variation in the radiation efficiency. This demonstrates the impedance-tuning ability of the suggested compact-modified-loop antenna by tuning the variables  $E_i$  and  $W_i$ , where  $i = 1, 2, \dots, n$ , without deteriorating the radiation efficiency of the antenna much. The in-between arms are needed to fine tune the required input impedance.

Table 4.4 summarizes the input impedances and the radiation efficiencies of the four simulated antennas at the design frequency of 868 MHz.

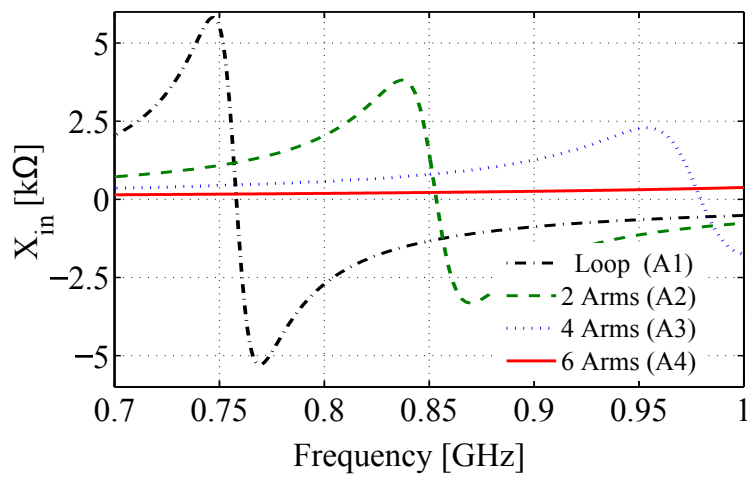
**Table 4.4.** Simulated input impedance and radiation efficiency at an operating frequency of 868 MHz.

Antenna	A1	A2	A3	A4
$R_{in}(\Omega)$	187.2	3945	129.7	7.08
$X_{in}(\Omega)$	-112.4	-3294	922.3	239.9
$Radiation_{eff}(\%)$	71.51	73.14	74.1	70.7

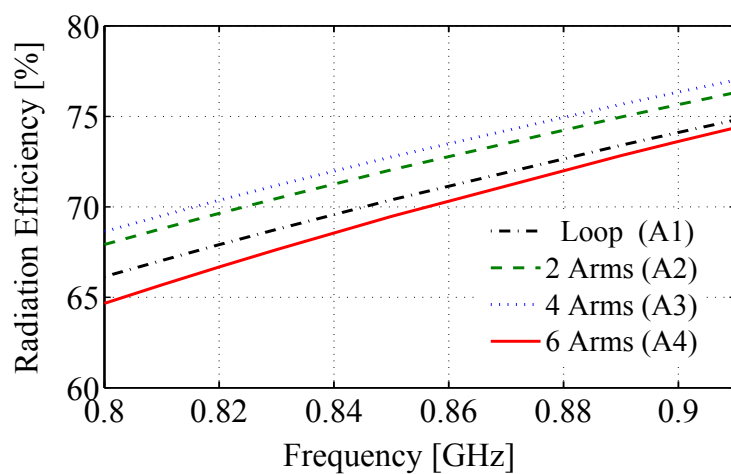
The table shows a large change in the real and imaginary parts of the input impedance when inner arms are added, while the radiation efficiency difference is less than 3.4% over all configurations. In Subsection 4.4.3 we will further discuss the radiation efficiency simulation results.



(a)



(b)



(c)

**Figure 4.15.** Real (a) and imaginary (b) parts of the input impedance and the radiation efficiency (c) as a function of frequency of the four simulated antennas.

The main benefits of the suggested novel antenna topology are its compact size ( $0.16\lambda \times 0.093\lambda \times 0.0046\lambda$ ) and the ability to tune its input impedance while maintaining a constant radiation efficiency.

#### 4.4.2 Validation of the Simulation Results

To cross-verify the simulation results two different simulation software packages have been employed: CST Microwave Studio [57] and Empire XCcel [83] that use two different computational methods. CST uses the Finite Integration Technique (FIT) [72] and Empire XCcel uses the Finite Difference Time Domain Method (FDTD) [84]. Antenna A4 (Fig. 4.14(d)) is selected for simulation. The simulated real and imaginary parts of the input impedance are plotted versus frequency in Fig. 4.16. It is shown in the figure that the two different simulation methods converge to almost identical values in the shown frequency range. At a frequency of 868 MHz, the input impedances are found to be:  $Z_{in, FDTD, 868 \text{ MHz}} = 8.49 + j237\Omega$  and  $Z_{in, FIT, 868 \text{ MHz}} = 7.08 + j239.9\Omega$ . The power wave reflection coefficient is calculated using the figure of merit (FoM) introduced in Sec. 1.6. The FoM results in -13.8 dB power reflections at 868 MHz ensuring accurate simulation results.

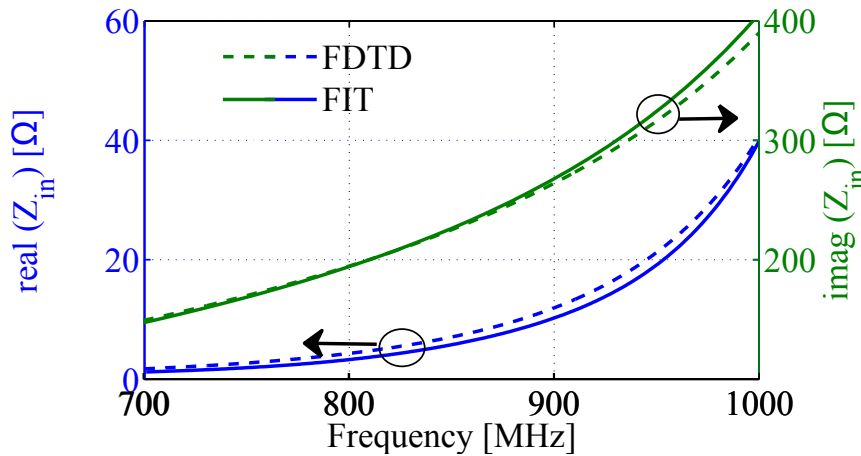


**Figure 4.16.** Real (a) and imaginary (b) parts of the input impedance as a function of frequency simulated using the Finite Difference Time Domain (FDTD) method and the Finite Integration Technique (FIT).

To verify the simulated results by measurements, a monopole version of the antenna has been fabricated by cutting the antenna through its symmetry plane (see Fig.4.13), and soldering this monopole to a large ground plane as shown in Fig. 4.17. In this way, the antenna can be measured using a single-ended (SMA) connection, which matches with the use of a standard Vector Network Analyser (VNA). The input impedance of the fabricated antenna is measured and compared to the simulated results. Figure 4.18 shows the simulated and measured real (Fig. 4.18(a)) and imaginary (Fig. 4.18(b)) parts

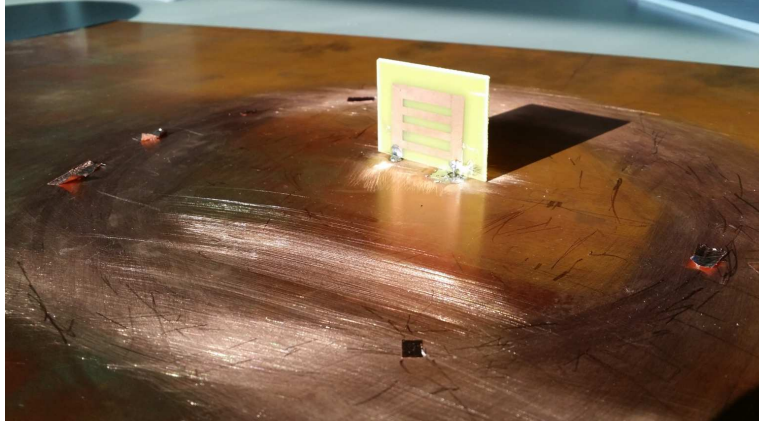


**Figure 4.17.** Fabricated monopole prototype for impedance measurements.

of the input impedance as a function of frequency. The measured values are multiplied by two to give results that apply for the actual antenna. It is shown in the Figure that the measurement results verify the simulated ones.

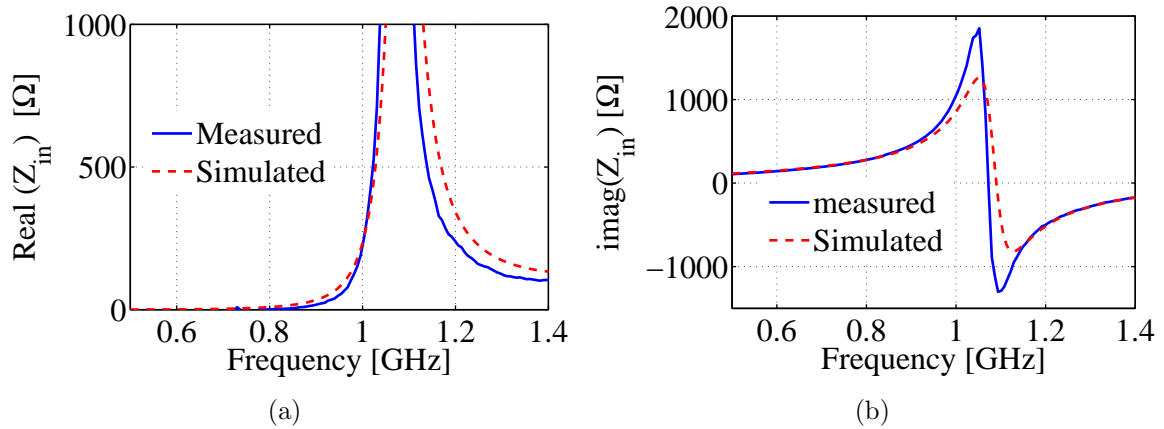


**Figure 4.18.** Simulated and measured real (a) and imaginary (b) parts of the input impedance of the fabricated prototype antenna versus frequency.

### 4.4.3 Radiation Efficiency and Radiation Pattern

The antenna radiation efficiency  $\eta$  is defined as [50]:

$$\eta = \frac{R_{rad}}{R_{rad} + R_{loss}}, \quad (4.11)$$

where  $R_{rad}$  is the radiation resistance and  $R_{loss}$  is the loss resistance.

The Wheeler cap method [85, 86] enables separate measurements of the radiation resistance ( $R_{rad}$ ) and loss resistance ( $R_{loss}$ ) by enclosing the antenna with a radiation shield.

The radiation shield is a conducting sphere enclosing the near-field of the antenna at a radius  $r = \lambda/2\pi$  [85] as shown in Fig. 4.19(b).

The input impedance of the antenna ( $Z_{in}$ ) is first measured as indicated in the previous section and illustrated in Fig. 4.19(a).

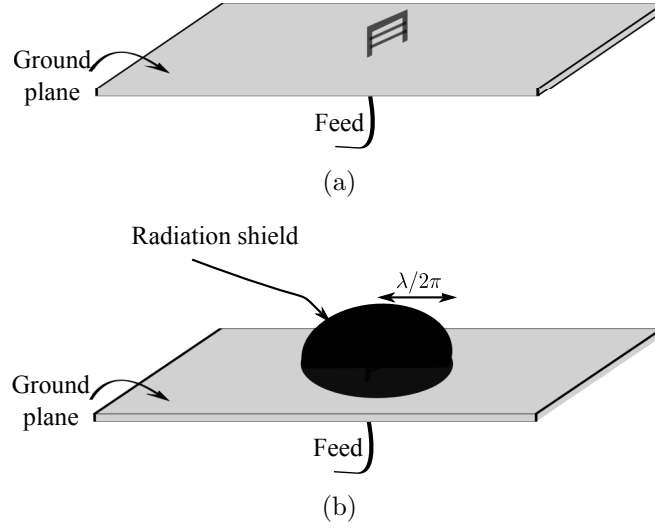


**Figure 4.19.** Input impedance measurement setup (a) and Wheeler cap measurement setup (b).

The real part of the input impedance is expressed as:

$$Re\{Z_{in}\} = R_{rad} + R_{loss}. \quad (4.12)$$

By placing the radiation shield over the antenna, the radiation resistance ( $R_{rad}$ ) can be eliminated and consequently the Wheeler cap input impedance ( $Z_{wc}$ ) can be measured where the real part is expressed as:

$$Re\{Z_{wc}\} = R_{loss}. \quad (4.13)$$

Substituting Eqs. (4.13) and (4.12) in Eq. (4.11), the antenna radiation efficiency is expressed as:

$$\eta = \frac{R_{rad}}{R_{rad} + R_{loss}} = \frac{Re\{Z_{in}\} - Re\{Z_{wc}\}}{Re\{Z_{in}\}} \quad (4.14)$$

The shape of the cap is not critical and need not be spherical [87], [88] and [89]. In this section, a cylindrical cap with a radius of 10.5 cm and a height of 7.5 cm will be used to measure the radiation efficiency of the manufactured prototype. The cylindrical cap

measurement setup is shown in Fig. 4.20. During the measurements, the lid in Fig. 4.20 is placed to enclose the near field of the antenna.



**Figure 4.20.** Radiation efficiency measurement setup using a cylindrical cap.

The simulated and the measured radiation efficiencies are plotted in Fig. 4.21. It is shown in the figure that the measured results exhibit two major resonances around 1.1 GHz and 1.8 GHz. These resonances are due to the cutoff frequencies of the  $TM_{01}$  (1.12 GHz) and  $TE_{01}$  (1.78 GHz) propagating modes of the used cylindrical waveguide [80].

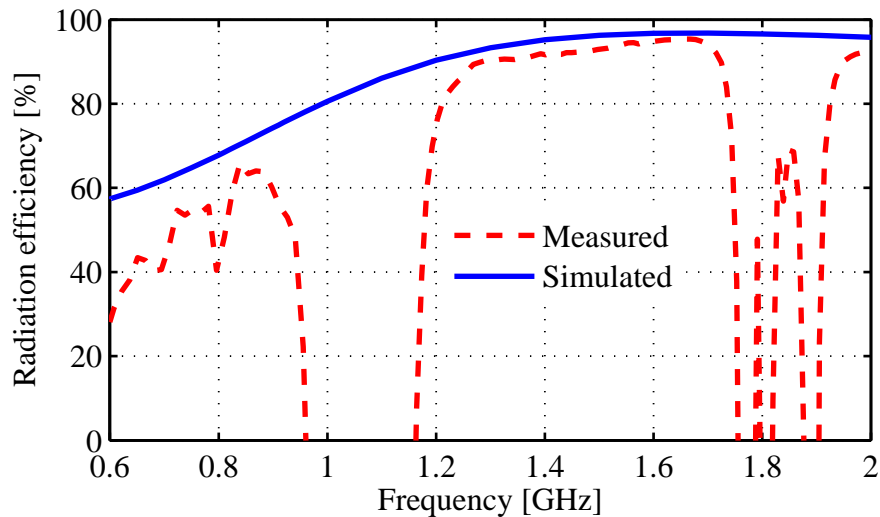


**Figure 4.21.** Simulated and measured radiation efficiency as a function of frequency using the Finite Integration Technique (simulation) and the Wheeler cap method (measurement).

It should be mentioned that for frequencies below 1 GHz, the height of the cylindrical



cap (7.5 cm) does not satisfy the radian sphere criterion ( $r = \lambda/2\pi$ ) and consequently an extension of the cap height is needed. The cap height is extended by 5 cm using a 5 mm-thick copper plate. The measured radiation efficiency as a function of frequency below 1 GHz using the extended cap is shown in Fig. 4.21. It is clearly indicated in the figure that the deviations between the simulated and the measured radiation efficiencies increase at low frequencies. The deviations are less than 2 % at 1.6 GHz, while they are almost 30% at 0.6 GHz. This behaviour is mainly due to the small value of the input resistance at low frequencies as shown in Fig. 4.16. At low frequencies ( $\leq 1$ GHz) accurate small input resistance measurement is quite a challenge due to the imperfections of the calibration standards used which leads to higher deviations in the measured radiation efficiency [90]. Another source of errors at lower frequencies is the non-perfect galvanic contact of the extension of the cylindrical cap.

Excluding the resonant modes of the cylindrical cap, the radiation efficiency has been measured between 1.3 GHz and 1.6 GHz for antennas A1, A2, and A4 (see Fig. 4.14). The simulated and the measured radiation efficiency as a function of frequency are shown in Fig. 4.22. It is indicated in the figure that the deviations between the simulated and the measured radiation efficiency do not exceed 5 % in the measured frequency band. The simulated radiation efficiency has been verified also by employing full-wave Wheeler cap simulations [91].

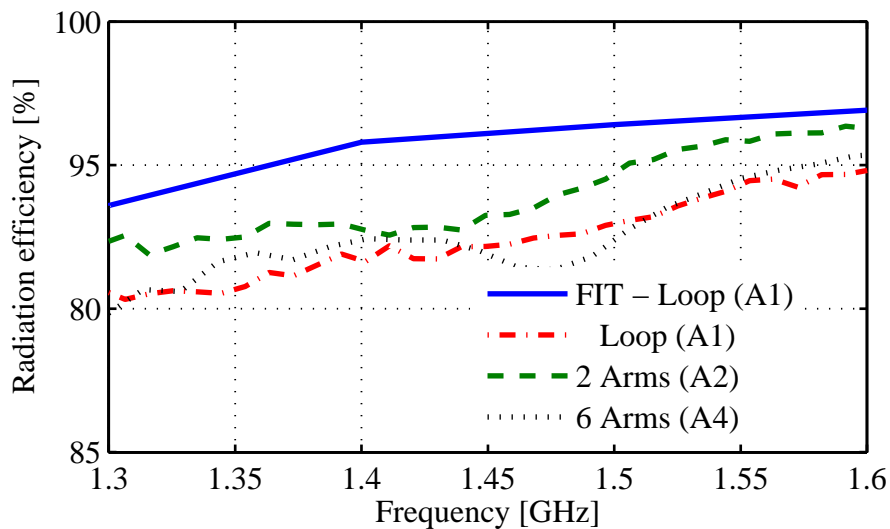


**Figure 4.22.** Simulated and measured radiation efficiency as a function of frequency for antennas A1, A2 and A4.

The antenna radiation efficiency reaches 70.7 % at the design frequency (868 MHz), see Fig. 4.21. This radiation efficiency can be increased by using a thinner and a lower-loss substrate. The substrate optimization will be presented in the following chapter.

The rectifier is connected on the top side of the antenna, directly to the antenna feeding points, see Fig. 4.23 for the rectifier layout. Figure 4.23 shows the 3D directivity pattern, where the rectifier is placed in the direction of the maximum directivity ( $\theta = -90^\circ$ ,  $\phi = 0^\circ$ ). It is clear from the figure that the layout position of the rectifier does not visibly affect the 3D radiation pattern of the antenna. The directivity  $D_r$  and the radiation efficiency  $\eta_{radiation}$  determine the antenna gain  $G_r$ .  $G_r = \eta_{radiation}D_r$ , with  $D_r = 1.74$  dBi and  $\eta_{radiation} = 0.707$ , the simulated antenna gain is  $G_r = 0.23$  dBi.

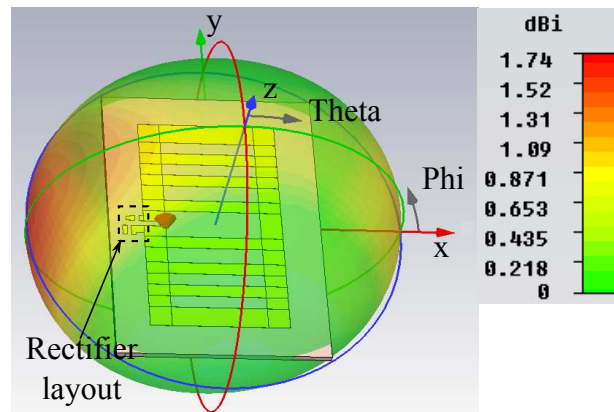


**Figure 4.23.** 3D directivity pattern at an operating frequency of 868 MHz, simulated using CST Microwave Studio.

As the input impedance of the modified compact loop antenna can be tuned to satisfy the conjugate complex design criterion (i.e. be the complex conjugate of the rectifier input impedance), and the presence of the rectifier does not affect the radiation characteristics of the antenna, this antenna topology will be used in the following chapter to harvest RF power and convert it to usable DC power.

## 4.5 Conclusion

In this chapter, new design expressions and updated analytical procedures are introduced to calculate the input impedance of strip dipoles and strip folded dipole antennas. The development is driven by the necessity to match the input impedance of the rectifier in a rectenna for maximum power transfer. Simulation and measurement results have shown that the proposed equations satisfy the Figure of Merit criterion and are easily implementable in standard computing tools. Compared to the state-of-the-art analytical solutions, the validity range for the dipole length is extended by 150 % which allows for the modeling of longer strip dipole antennas.

In addition, a novel and compact modified loop antenna configuration has been intro-

duced. The modification consists of adding additional horizontal arms to the loop antenna, which results in a higher degree of freedom to tune the antenna's input impedance. The main advantage of the introduced antenna topology is that the antenna impedance can be tuned without affecting its radiation efficiency much. The simulation results of the input impedance are validated by measurements.

# RF Power Transport Using Conjugate-Matched Rectenna System

---

In this chapter, the modified compact loop antenna introduced in the previous chapter is tuned to eliminate the commonly used matching network between the antenna and the rectifier, since this antenna will be conjugately matched to the rectifier. Two rectenna prototypes are presented in this chapter. The first prototype consists of a rectenna using commercially available, discrete rectifiers. At an incident RF power level of -20 dBm, the Power Conversion Efficiency (PCE) reaches 33.8 % for a resistive load of 10 k $\Omega$ . The PCE increases to 54.7 % for a power level of -10 dBm. Compared to the state-of-the-art, the PCE is at least 10 % higher for the same input power levels.

For the second prototype, an integrated 5 stage cross-connected bridge rectifier with a capacitor bank, implemented in standard 90-nm CMOS technology has been used. The PCE reaches 30 % at an input power level of -20 dBm and it increases to 36.6 % at an input power level of -17 dBm over a 0.33 M $\Omega$  resistive load. Measurements show a -27 dBm sensitivity for 1 V DC output. At an input power level of -20 dBm, the peak output voltage is measured at an operating frequency of 855 MHz reaching 1.73 V. The suggested prototype is smaller in size than those reported in the literature.

## 5.1 Introduction

Figure 5.1 shows the configuration of the wireless power transmission system being used in this chapter.

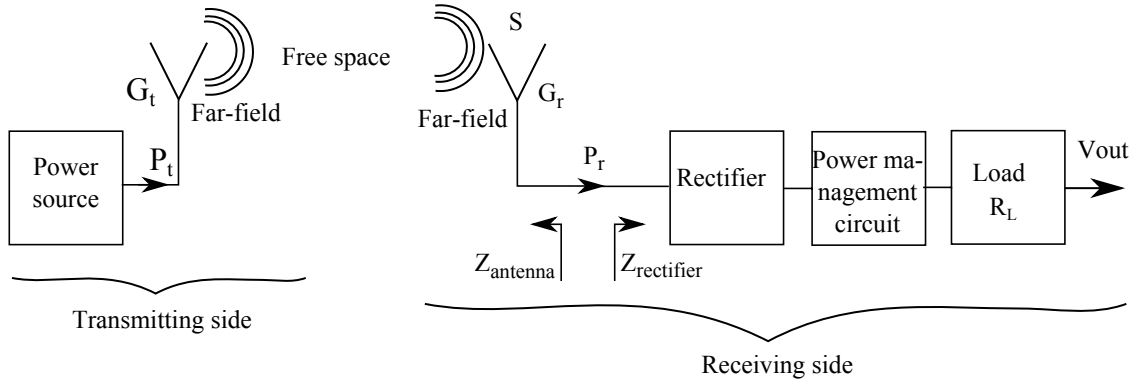


**Figure 5.1.** Wireless power transmission system.

The system consists of a transmitter that transmits RF power and a receiver that collects part of the transmitted power.

When the transmitter is not dedicated for wireless power transmission, e.g. a TV broadcasting or a GSM base station, the power collection and conversion is defined as wireless power *harvesting* [22], [92]. When the power is intentionally transmitted using a dedicated source, this is defined as wireless power *transport* [93], [94]. For both, the receiving side consists of a *rectenna* (*rectifying antenna*) which is an antenna connected to a rectifier and a load. The load can be an ultra-low power sensor. A power management circuit between the rectifier and the load is needed to transfer and store the DC power. In order to achieve a compact rectenna system, the commonly employed impedance matching network between the antenna and the rectifier is removed as shown in Fig. 5.1 and the antenna is conjugately matched to the rectifier ( $Z_{\text{antenna}} = Z_{\text{rectifier}}^*$ ). The compact antenna configuration introduced in the previous chapter is used to capture part of the transmitted RF power.

## 5.2 Design Methodology

In this section<sup>1</sup>, a design methodology is presented to optimize the power transfer between the antenna and the rectifier [95]. The optimal impedance matching network with

<sup>1</sup>This section is based on the work by Hubregt J. Visser that is published in [95]. For the completeness of the work, this section is included in the thesis.

respect to power efficiency, rectifier input voltage maximization and rectifier sensitivity improvement is investigated. It should be mentioned that the impedance matching may be accomplished by a (discrete) lumped-element matching network and by a distributed network integrated into the antenna. Figure 5.2 shows the equivalent circuit model of a generalized rectenna system.

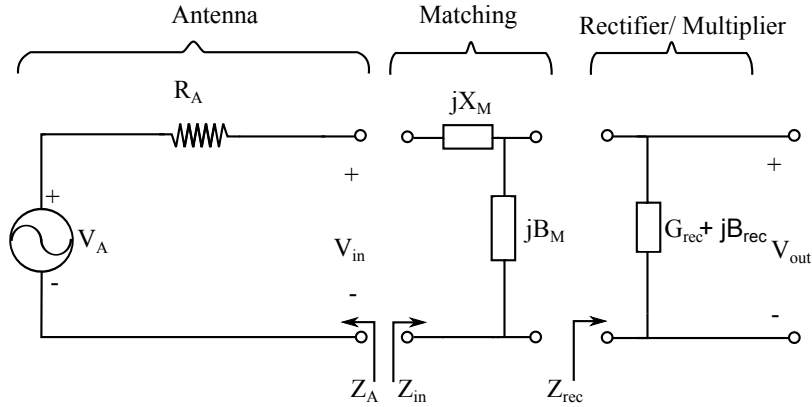


**Figure 5.2.** Equivalent circuit model of a rectenna system.

The antenna in the figure is represented by its Thévenin equivalent circuit of a voltage source  $V_A$ , with an internal resistance  $R_A$ . The Thévenin equivalent voltage  $V_A$  is:

$$V_A = \sqrt{8R_A P_{in}}, \quad (5.1)$$

where  $P_{in}$  is the maximum power available at the clamps of the antenna.

For the generalized rectenna system shown in Fig. 5.2, an ‘L-network’ impedance matching is introduced between the antenna and the rectifier/multiplier.

The input power  $P_{in}$  at the input of the matching network is described as

$$P_{in} = \frac{1}{2} |V_{in}|^2 \Re \{Y_{in}\}, \quad (5.2)$$

where  $Y_{in} = \frac{1}{Z_{in}}$  is the input admittance as indicated in Fig. 5.2. The function  $\Re \{x\}$  denotes the real part of  $x$ .  $V_{in}$  is the voltage across the input impedance  $Z_{in}$  see Fig. 5.2.  $V_{in}$  is calculated as

$$V_{in} = \left( \frac{Z_{in}}{Z_{in} + R_A} \right) V_A = \left( \frac{1}{1 + Y_{in} R_A} \right) V_A. \quad (5.3)$$

Substituting Eq. (5.3) in Eq. (5.2) results in

$$P_{in} = \frac{1}{2} \left| \frac{1}{1 + Y_{in} R_A} \right|^2 V_A^2 \Re \{ Y_{in} \}. \quad (5.4)$$

The output power  $P_{out}$  across the rectifier terminals is given by

$$P_{out} = \frac{1}{2} |V_{out}|^2 \Re \{ Y_{rec} \}, \quad (5.5)$$

where  $Y_{rec}$  is the input admittance of the rectifier  $Y_{rec} = G_{rec} + jB_{rec} = \frac{1}{Z_{rec}}$  and  $V_{out}$  is the output voltage across the rectifier terminals.  $V_{out}$  and  $Z_{rec}$  are indicated in Fig. 5.2.

### 5.2.1 Antenna Matched to the Rectifier

The ‘L-network’ shown in Fig. 5.2 is used to conjugately match the antenna impedance to that of the rectifier. If a lossless network is assumed, the output power  $P_{out}$  is equal to input power  $P_{in}$  and, consequently, the voltage gain  $G_v$  is given by

$$G_v = \frac{|V_{out}|}{|V_A|} = \frac{1}{2} \sqrt{\frac{\Re \{ Y_{in} \}}{\Re \{ Y_{rec} \}}}. \quad (5.6)$$

The input impedance  $Z_{in}$  is calculated using the network model shown in Fig. 5.2 as

$$\begin{aligned} Z_{in} &= jX_M + \frac{1}{G_{rec} + j(B_M + B_{rec})} \\ &= \frac{G_{rec}}{G_{rec}^2 + (B_M + B_{rec})^2} + j \left( X_M - \frac{B_M + B_{rec}}{G_{rec}^2 + (B_M + B_{rec})^2} \right). \end{aligned} \quad (5.7)$$

In order to conjugately match the antenna to the rectifier, the following conditions apply

$$R_A = \frac{G_{rec}}{G_{rec}^2 + (B_M + B_{rec})^2}, \quad (5.8)$$

$$X_M = \frac{B_M + B_{rec}}{G_{rec}^2 + (B_M + B_{rec})^2}. \quad (5.9)$$

From Eqs. (5.7) and (5.9), the real part of the input admittance is calculated as

$$\Re\{Y_{in}\} = \frac{G_{rec}^2 + (B_M + B_{rec})^2}{G_{rec}}, \quad (5.10)$$

and, since  $Y_{rec} = G_{rec} + jB_{rec}$ , the real part of the rectifier's admittance is

$$\Re\{Y_{rec}\} = G_{rec}. \quad (5.11)$$

Substituting Eq. (5.10) and Eq. (5.11) in Eq. (5.6) leads to the voltage gain

$$G_v = \frac{|V_{out}|}{|V_A|} = \frac{1}{2} \sqrt{\frac{\Re\{Y_{in}\}}{\Re\{Y_{rec}\}}} = \frac{1}{2} \sqrt{1 + \left(\frac{B_M + B_{rec}}{G_{rec}}\right)^2} = \frac{1}{2} \sqrt{1 + (Q)^2}, \quad (5.12)$$

where  $Q = \frac{B_M + B_{rec}}{G_{rec}}$  is the quality factor at the output of the matching circuit.

$G_{rec}$  and  $B_{rec}$  are defined by the rectifier's impedance. Eq. (5.12) leaves the impression that, by a proper choice of the matching network susceptance  $B_M$ , one can choose the output voltage  $V_{out}$  and then design the antenna having an impedance  $R_A$  and take  $X_M$  as dictated by Eq. (5.8) and Eq. (5.9), respectively.

The error made in this reasoning is that it is implicitly assumed that  $V_A$  and  $R_A$  can be chosen independently, while in fact they are related through the available power from the antenna as specified in Eq. (5.1).

## 5.2.2 Maximizing the Output Voltage

Assuming a lossless network, one can express the available power from the antenna by using Eq. (5.1)

$$P_{in} = \frac{V_A^2}{8R_A}. \quad (5.13)$$

By the substitution of Eq. (5.8) in Eq. (5.13),  $V_A$  is expressed as

$$V_A = \sqrt{8R_A P_{in}} = 2 \sqrt{2P_{in} \frac{G_{rec}}{G_{rec}^2 + (B_M + B_{rec})^2}}. \quad (5.14)$$



The output voltage is calculated by substituting Eq. (5.14) in Eq. (5.12), which results in

$$V_{out} = G_v V_A = \sqrt{\frac{2P_{in}}{G_{rec}}}. \quad (5.15)$$

As described in Eq. (5.15), the output voltage is thus dictated by the available power from the antenna and the real part of the input admittance of the rectifier/multiplier.

$G_{rec}$  is the real part of the rectifier admittance as shown in Fig. 5.2.

$$\begin{aligned} G_{rec} &= \Re\{Y_{rec}\} \\ &= \frac{R_{rec}}{R_{rec}^2 + X_{rec}^2}. \end{aligned} \quad (5.16)$$

After substituting Eq. (5.16) in Eq. (5.15), the output voltage is described in terms of the input impedance of the rectifier as follows:

$$V_{out} = \sqrt{2P_{in} \frac{R_{rec}^2 + X_{rec}^2}{R_{rec}}}. \quad (5.17)$$

To maximize the output voltage  $V_{out}$  (i.e. the sensitivity) and the power transfer between the antenna and the rectifier, Eq. (5.17) should be satisfied. The real part of the input impedance should be as high as possible while the imaginary part should be as low as possible or the other way around. Since most Schottky diodes show an input impedance having a low resistance in series with a high capacitance we choose for the latter method. Figure 5.3 shows the DC output voltage for different input power levels for different rectifier impedances following Eq. (5.17). Figure 5.3(a) shows the output voltage for different values of the real part of the rectifier impedance while the rectifier reactance is set to 300  $\Omega$ . Figure 5.3(b) shows the output voltage for different values of the imaginary part of the rectifier impedance while the rectifier resistance is set to 10  $\Omega$ .

It is clear from the figure that when  $X_{rec} \gg R_{rec}$ , the voltage decreases with increasing real part of the rectifier's input impedance. A voltage of 0.5 V is generated at an available power level of -9 dBm (dotted-dashed curve) when  $R_{rec}$  is set to 100  $\Omega$ . The same output voltage is generated at an available power level of -18.5 dBm (solid curve) when  $R_{rec}$  is decreased to 10  $\Omega$ , which results in a 8.5 dB sensitivity improvement. Figure 5.3(b) clearly indicates that the output voltage increases with increasing reactive part of the input impedance when the real part is set to 10  $\Omega$ .

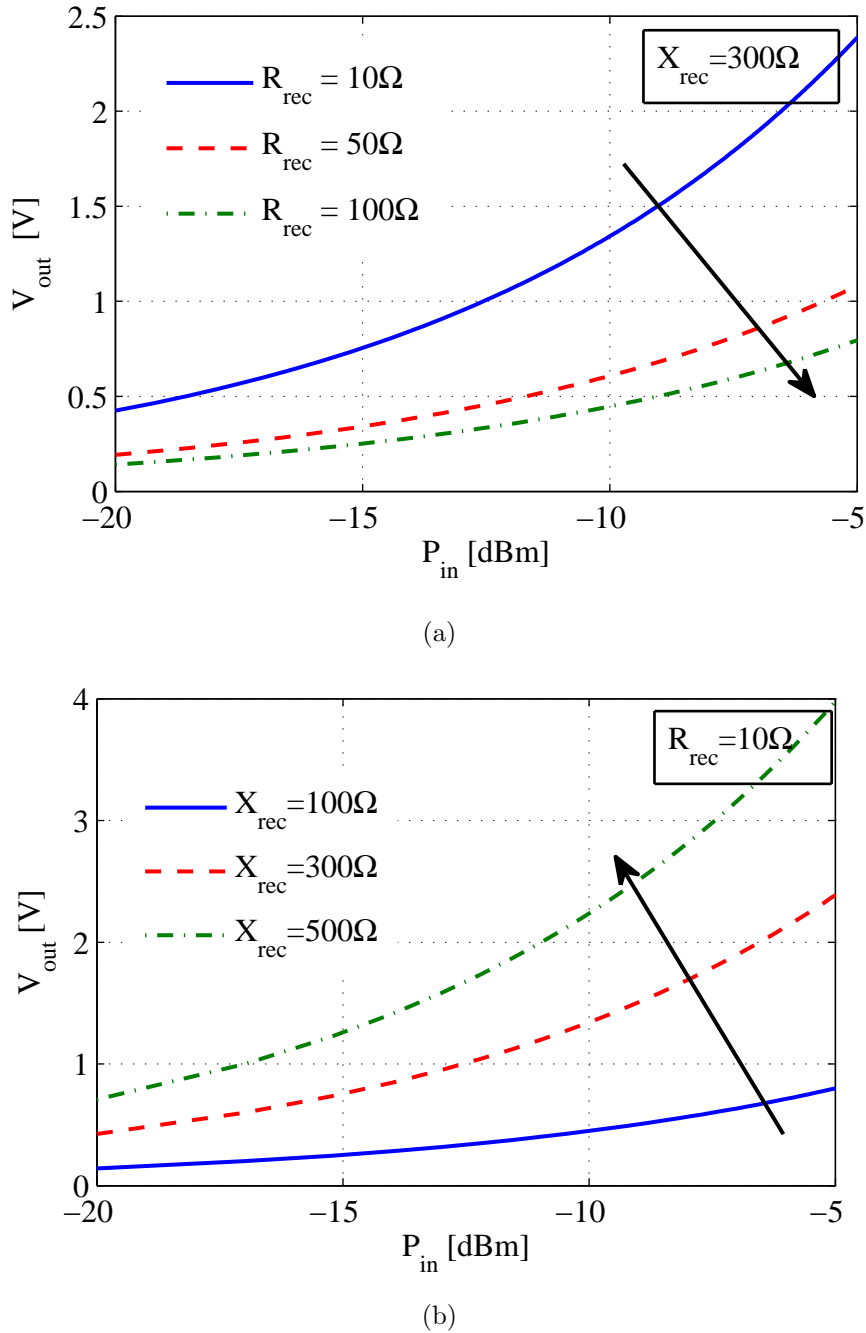


**Figure 5.3.** Output voltage for different input power levels  $P_{in}$  for different rectifier impedances. (a)  $X_{rec} = 300\Omega$ , (b)  $R_{rec} = 10\Omega$ .

A voltage of 0.7 V is generated at an available power level of -6 dBm (solid curve) when  $X_{rec}$  is set to 100  $\Omega$ . The same output voltage is generated at an available power level of -20 dBm (dotted-dashed curve) when  $X_{rec}$  is increased to 500  $\Omega$ , which results in a 14 dB sensitivity improvement. This knowledge will be used in Sec. 5.4 where a 5 stages rectifier implemented in TSMC 90-nm CMOS technology with an input impedance of

$Z_{in} = 7.6 + j418$  has been designed, realized and measured.

Through the presented analysis and our results for a compact loop antenna, it has been shown that the steps to maximize the output voltage and thus improve the rectifier's sensitivity for a given low power level are:

- conjugate match the antenna to the rectifier;
- design the rectifier circuit for a minimum real part and maximum absolute value of the imaginary part  $|X_{rec}| \gg R_{rec}$ ;
- use antenna miniaturization up to a level that the radiation resistance still dominates the loss resistance;
- use a small loop antenna as a basis.

## 5.3 Power Transport Using Commercially Available Diodes

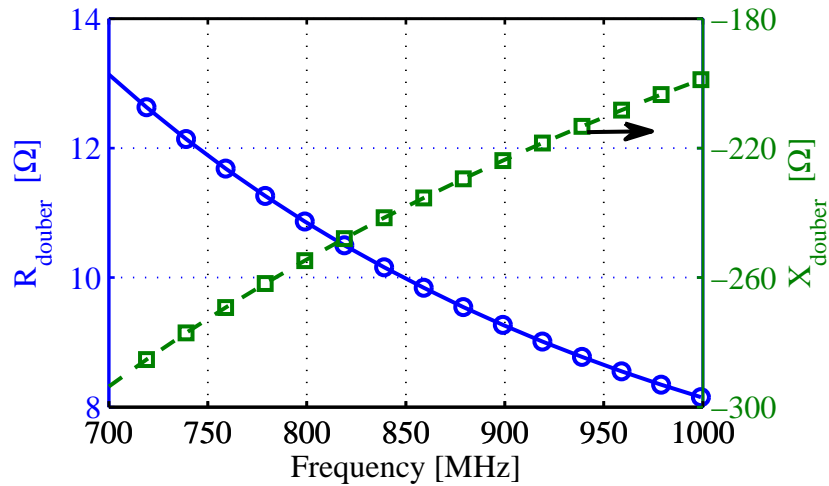
In this section, the modified loop antenna introduced in the previous chapter is combined with commercially available diodes. A voltage doubler rectifier is used. The output voltage is measured for different input power levels at an operating frequency of 868 MHz.

### 5.3.1 Rectenna Design

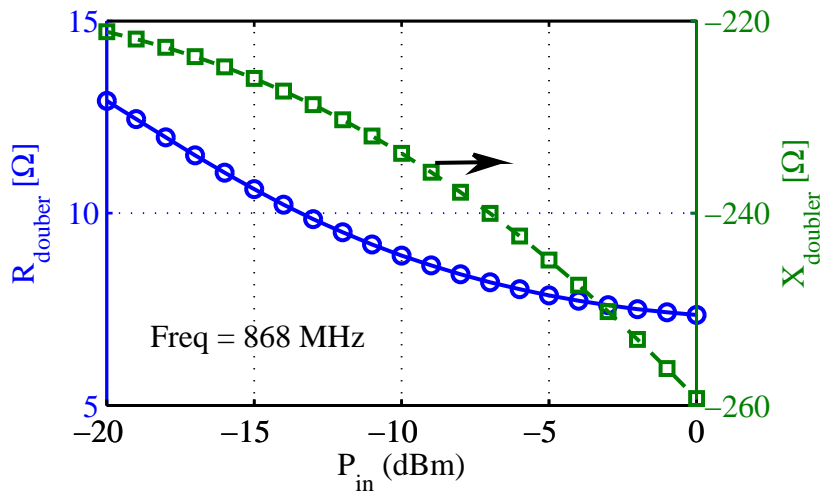
The design frequency and the design input power level have been investigated in Sec. 2.7.1 and Sec. 2.7.2, respectively. The output voltage and the input impedance of a single rectifier (Schottky diode) have been investigated in [41] and have been presented in Chapter 2. In this section we will investigate the input impedance of the voltage doubler (see Fig. 3.21) as a function of frequency for different RF input power levels. The main reason to choose a voltage doubler is that it provides a higher DC output voltage than the single rectifier and it eliminates the need for a return-current coil. In addition, it provides a compact size due to the commercially available double-packaged-diodes. ADS harmonic balance and Momentum [44] have been used for simulations.

For a voltage doubler circuit made with an Avago HSMS-2852 [43] Schottky-diode pair, the input impedance is calculated as a function of frequency and as a function of input power level. Figures 5.4(a) and 5.4(b) show the real and imaginary parts of the input impedance as a function of frequency and as a function of input power level, respectively. For Fig. 5.4(a), the input power level is set to -10 dBm while for Fig. 5.4(b) the operating frequency is 868 MHz. It is observed in the figure that the

impedance of the voltage doubler changes as a function of frequency and as a function of input power level. At the design frequency (868 MHz) and input power level (-10 dBm) the input impedance of the voltage doubler is  $Z_{doubler} = 8.9 - j234 \Omega$ .



(a)



(b)

**Figure 5.4.** Simulated real and imaginary parts of the input impedance of the voltage doubler based on the AVAGO HSMS-2852 as a function of frequency for an input power level of -10 dBm (a) and as a function of input power level at an operating frequency of 868 MHz (b).

The modified compact loop antenna introduced in the previous chapter is tuned, so that its input impedance is equal to the conjugate complex of that of the voltage

doubler, at an input power level of -10 dBm, and an operating frequency of 868 MHz. Figure 5.5 shows the real (a) and imaginary parts of the input impedance as a function of frequency for the voltage doubler and for antenna A4 introduced in Sec. 4.4. It is shown in the figure that the real parts of the input impedance for the antenna and the rectifier intersect around 868 MHz. The imaginary parts of the input impedance for the antenna and the voltage doubler are plotted in Fig. 5.5(b). It is indicated in the figure that  $\text{imag}(Z_{\text{rectifier}}) = -\text{imag}(Z_{\text{antenna}})$  around 868 MHz.

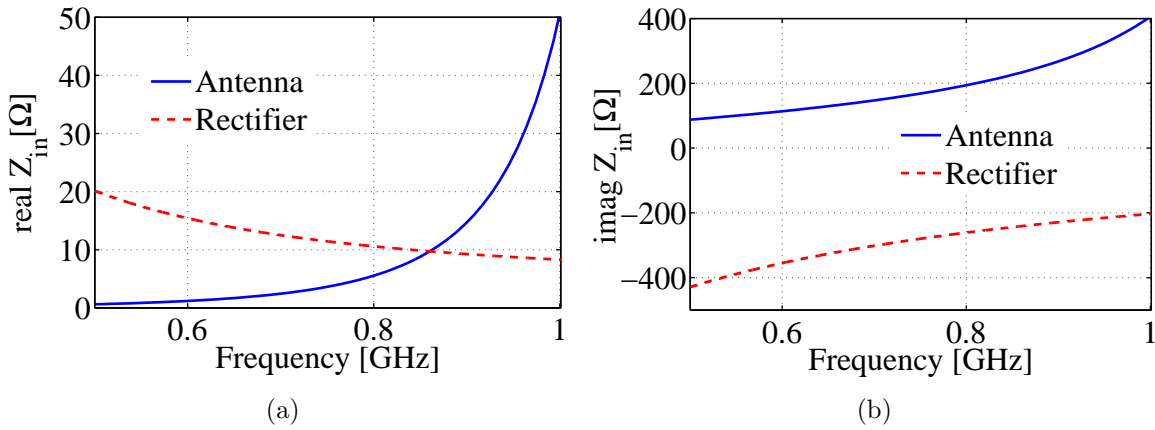


**Figure 5.5.** Simulated real (a) and imaginary (b) parts of the input impedance of the voltage doubler as well as the antenna as a function of frequency, for  $P_{in} = -10$  dBm.

To investigate the complex conjugate matching, the power wave reflection coefficient concept [34] [51] introduced in Sec. 1.6 is used to calculate the power reflection coefficient between the input impedance of the rectifier and the input impedance of the antenna.

$$\text{FoM} = 20 \log \left| \frac{Z_{\text{rectifier}} - Z_{\text{antenna}}^*}{Z_{\text{rectifier}} + Z_{\text{antenna}}} \right|, \quad (5.18)$$

where \* denotes the complex conjugate of the input impedance. Figure 5.6 shows the power wave reflection coefficient (FoM) as a function of frequency calculated using Eq. 5.18. The figure shows that the antenna is matched to the rectifier with  $S_{11} = -16$  dB at the design frequency 868 MHz.

At the design frequency (868 MHz) and at the design input power level (-10 dBm), the input impedance of the voltage doubler is conjugately matched to that of the antenna, which results in a power wave reflection coefficients of -16 dB as indicated in Fig. 5.6. A first rectenna prototype is realized on a 1.6 mm thick FR4 substrate. A photograph of the fabricated rectenna is shown in Fig. 5.7.

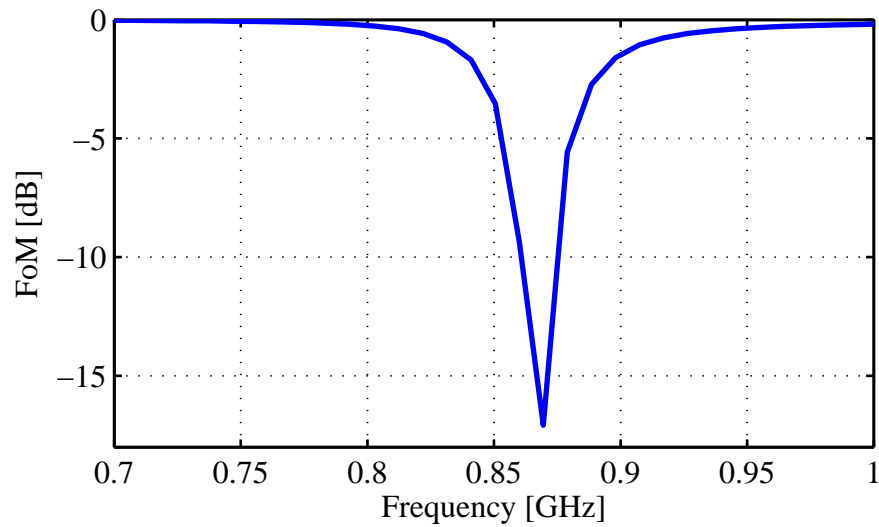


**Figure 5.6.** Power wave reflection coefficient as a function of frequency calculated using the input impedance of the voltage doubler and the input input impedance of the antenna.

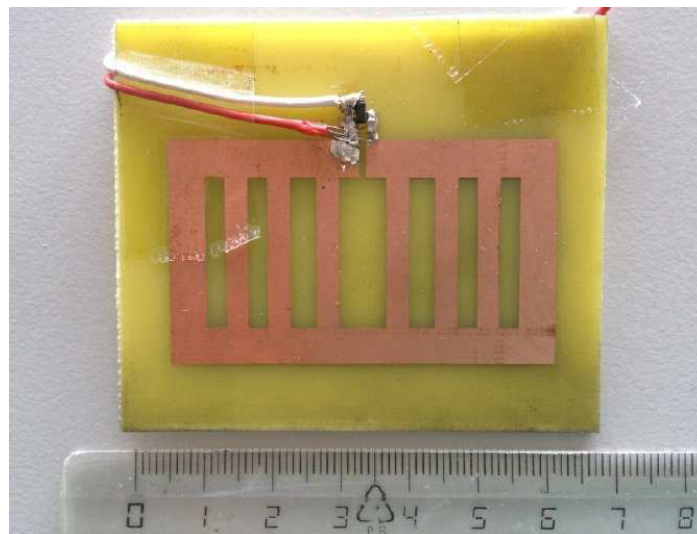


**Figure 5.7.** Photograph of the fabricated rectenna.

### 5.3.2 RF Power Transport Measurement Results

For RF power transport, a system as shown in Fig. 3.1 is being used. In this section, we describe how the rectenna is used for wireless RF power transfer. The power transfer measurement setup is shown in Fig. 5.8. The setup is calibrated using two antennas with a known gain,  $G_r$  and  $G_t$  (see Fig. 5.8), at 868 MHz separated by a distance  $R$ .

$R$  is chosen to ensure that far-field conditions are satisfied for both antennas. The power density ( $S$ ) at the receiving side is dictated by the effective isotropic radiated power,  $EIRP = P_t G_t$ , where  $P_t$  is the transmitted power and  $G_t$  is the transmit antenna gain, and by the distance  $R$  between the transmitting and the receiving antennas.

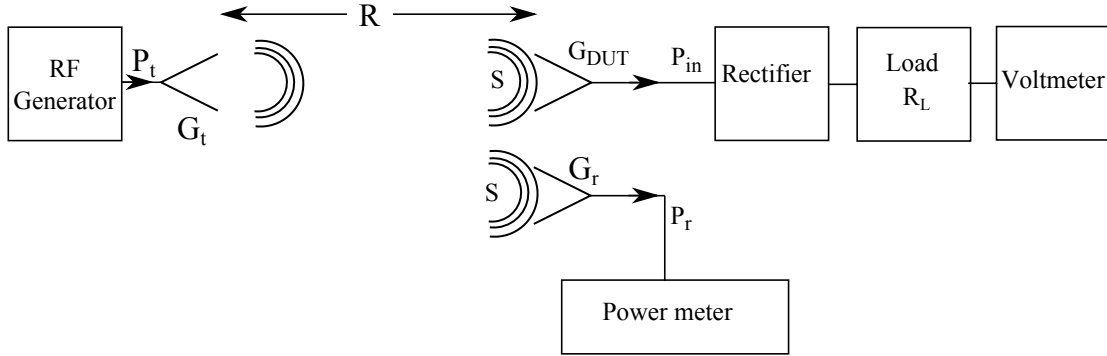


**Figure 5.8.** Power transfer measurement system.

Using the same procedures as introduced in Sec. 3.7.2 in Chapter 3, the received power at the terminals of the power meter is expressed as

$$P_r = P_t G_t G_r \left( \frac{\lambda_0}{4\pi R} \right)^2 = P_t G_t G_r \left( \frac{c}{4\pi f_0 R} \right)^2, \quad (5.19)$$

where  $c$  is the free-space speed of light and  $f_0$  is the operating frequency of the transmitted signal. A power meter is used to measure the received RF power  $P_r$ . The measured power  $P_r$  is compared to the theoretically calculated value based on Eq. (5.19). The measured power appeared to be within  $\pm 0.5$  dB agreement with the theoretically calculated power, which ensures an accurate measurement setup. The rectenna is then placed at the position of the test receiving antenna for wireless power transport. The antenna gain of the rectenna is denoted by  $G_{DUT}$  as shown in Fig. 5.8. The input power level  $P_{in}$  at the clamps of the rectifier (see Fig. 5.8) is then calculated as

$$P_{in} = \frac{P_r G_{DUT}}{G_r}. \quad (5.20)$$

The receiving rectenna system is connected to a variable load resistor  $R_L$ . The DC output voltage is measured using a voltmeter for different load resistances and for different input power levels using a voltmeter.

The antenna of the receiving rectenna system shown in Fig. 5.8 consists of the modified loop antenna shown in Fig. 5.7. This antenna is connected to the rectifier having a variable load resistor  $R_L$ . The DC output voltage is measured for different load resistances

at three different input power levels -20 dBm, -10 dBm and -5 dBm calculated according to Eq. (5.20).

The output voltage is first measured as a function of frequency at an input power level  $P_{in}$  (see Fig.5.8) of -10 dBm where a  $1\text{ M}\Omega$  load resistance is used to terminate the rectenna. Figure 5.9 shows the measured output voltage versus frequency. It is clear from the measurement results that the system output voltage peaks at 868 MHz and reaches 1.36 V. Centered at 868 MHz, the -3dB voltage bandwidth is approximately 30 MHz as indicated in the same figure.

The Power Conversion Efficiency (PCE) is calculated as:

$$\text{PCE (\%)} = \frac{P_{load}}{P_{in}} = \frac{V_{out}^2}{R_L} \frac{1}{P_{in}}. \quad (5.21)$$

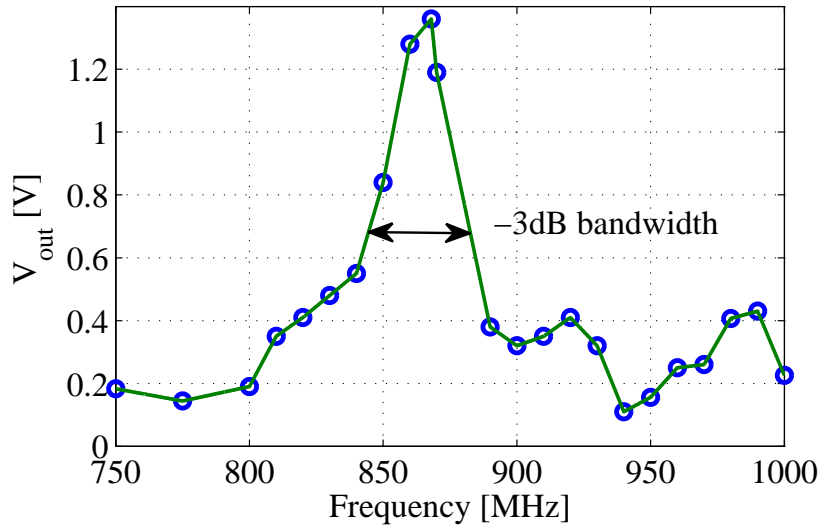


**Figure 5.9.** Measured output voltage ( $V_{out}$ ) over a  $1\text{ M}\Omega$  load resistance as a function of frequency at an input power level  $P_{in}$  of -10 dBm.

To measure the power conversion efficiency (PCE), the output voltage is measured over different load resistances and for different input power levels; the results are shown in Fig. 5.10. Over a  $10\text{ k}\Omega$  resistive load, the DC output voltage reaches 0.19 V at an input power level of -20 dBm.  $V_{out}$  increases to 0.76 V and 1.41 V at an input power level of -10 dBm and -5 dBm, respectively.



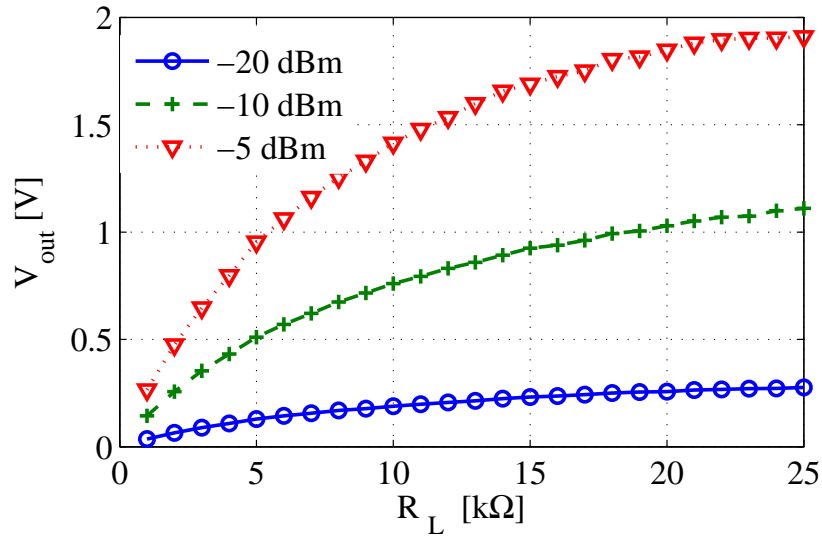


**Figure 5.10.** Measured output voltage ( $V_{out}$ ) for different input power levels ( $P_{in}$ ) versus  $R_L$ .

Figure 5.11 shows the measured PCE as a function of  $R_L$  for different input power levels ( $P_{in}$ ) at the design frequency, 868 MHz.

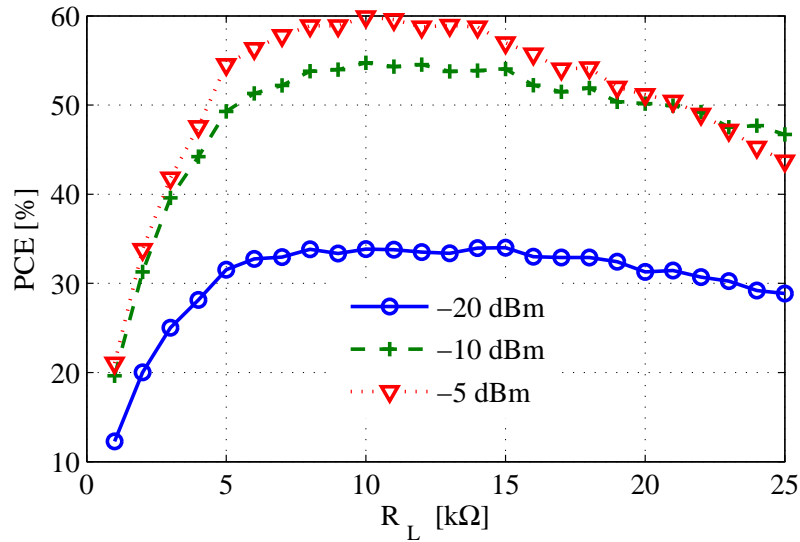


**Figure 5.11.** Measured power conversion efficiency (PCE) for different input power levels ( $P_{in}$ ) versus  $R_L$ .

At an input power level of -20 dBm, the PCE reaches 33.8 % for a resistive load for 10  $k\Omega$ . For the same load resistance, the PCE increases to 54.7 % and 60 % at an input power level of -10 dBm, and -5 dBm, respectively.

Table 5.1 gives a short overview of the state of the art reported for rectennas in the literature that use commercially available rectifiers for RF to DC power conversion.

**Table 5.1.** Overview of rectenna performances from literature.

Reference	Pin [dBm]	Frequency [MHz]	Load $R_L$ [ $\Omega$ ]	$\frac{Size}{\lambda^2}$	Power Conversion Efficiency (PCE)
[19]	-10 -20	1800	$2.4 \times 10^3$	-	38*% 15*%
[67]	-10	830	$1 \times 10^7$	0.027	44 %
[96]	-20	550	$2 \times 10^3$	0.035	18* %
[20]	0*	1960	460	0.192	54 %
This work	-10 -20	868	$10 \times 10^3$	0.028	54.7% 33.8%

\*calculated from figure

Compared to [67], where a 4 stage rectifier has been used, the presented rectenna in this paper is more efficient at the same input power level and has approximately the same size. At an input power level of -20 dBm, the measured PCE in [96] is 18 %. At the same input power level, the measured PCE of the rectenna presented in this paper reaches 34%. When compared to the measured PCE in [20], our rectenna shows approximately the same performance at an input power level that is 10 times lower. In addition, the rectenna in this chapter is more than five times as compact and operates at a lower frequency. Thus, through a co-design of the antenna and the rectifier, we are able to significantly improve the performance compared to the state of the art.

## 5.4 Five Stage CMOS Rectifier with a Control Loop

In the previous section a voltage doubler using commercially available diodes has been used to convert the RF incident power into DC power. To further increase the output voltage, a 5 stage rectifier<sup>2</sup> implemented in TSMC 90-nm CMOS technology is designed and realized and the rectifier output voltage and sensitivity are measured.

### 5.4.1 Design and Implementation

The CMOS rectifier to be presented has been first introduced in [98] and is optimized to harvest power at low input power levels, around -20 dBm. Fig. 5.12 shows the principle

<sup>2</sup>This section is the result of the cooperation between Holst Centre/imec and Delft University of Technical (TUD). The 5 stage CMOS rectifier with the control loop was designed, developed and realized by Mark Stoopman from TUD. The antenna design as well as the connector layout are realized by Shady Keyrouz from TU/e. The reported results in this section are published in [97].

of the multi-stage RF harvester as introduced in [98].

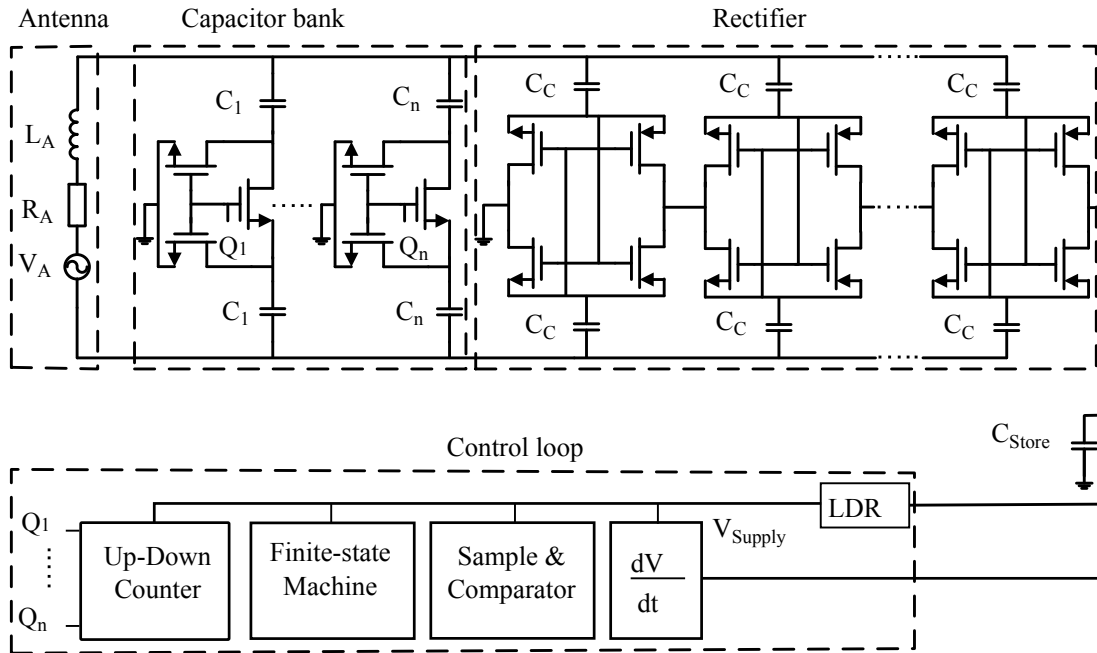


**Figure 5.12.** Multi-stage RF harvester implemented using CMOS technology.

The harvester consists of a 5 stage cross-connected bridge rectifier. For maximizing the output voltage, the rectifier is connected to a purely capacitive load  $C_{Store}$ . A control loop is added to maximize the output voltage on the capacitive load by tuning the reactive part of the rectifier's input impedance such that it is conjugately matched to the antenna. The antenna is connected to a capacitor bank that is controlled by an up-down counter. The 7-bit capacitor bank consists of 128 capacitor switches where  $C_{max} = 256$  fF and  $C_{min} = 116$  fF. By using the control loop, the input impedance of the rectifier as seen from the antenna can be tuned between  $C_{min}$  and  $C_{max}$  to be conjugately matched to that of the antenna, provided that the real parts of the antenna and rectifier are identical.

The control loop implementation in combination with the multi-stage rectifier is also shown in Fig. 5.12. The harvester initially charges the storage capacitor to the turn-on voltage of the control loop. Then the energy transfer to the off-chip capacitor ( $C_{Store}$ ) is optimized by maximizing the slope of the load voltage. The slope information is obtained by using a differentiating network. Then the slope information is compared with the previous sample using the sample and comparator stage that determines whether the slope has increased or decreased. Consequently, the finite-state machine determines if the up-down counter should keep counting or change the count direction.

In this realized first prototype, the control loop is implemented off chip by using a micro-

controller. Once the loop is calibrated, it can be turned off so that it is not loading the rectifier for very low input power levels. The input impedance seen from the antenna is found to be  $Z_{in,0} = 7.6 - j418 \Omega$  for  $C_{min}$  and  $Z_{in,1} = 4.3 - j310 \Omega$  for  $C_{max}$ . This self-calibrating RF rectifier has been implemented in [39] where the rectifier was printed on a FR4 substrate connected to the modified square loop antenna introduced in the previous chapter. In this section, the substrate material and the substrate thickness are optimized for maximum antenna radiation efficiency. A prototype realized on a low-loss and thin substrate will be presented.

### 5.4.2 Antenna Optimization and Chip Integration

The same antenna topology as introduced in Sec. 4.4 is used for realizing a rectenna based on the just discussed rectifier. In this design the antenna reactance part  $X_{Antenna}$ , should be between  $310 \Omega$  and  $418 \Omega$ . Then, the control loop will optimize the rectifier impedance to be conjugately matched to the antenna. The real part should be a fixed value between  $4.3 \Omega$  and  $7.6 \Omega$ . So an exact, critical value of the reactive part of the antenna impedance is not required. This gives another degree of freedom in maximizing the antenna radiation efficiency.

The antenna radiation efficiency is improved by choosing a thin and a low-loss substrate instead of the so far used lossy FR4 PCB material. Figure 5.13 shows the simulated antenna radiation efficiency versus frequency for different substrate materials for the structure shown in Fig. 5.15.

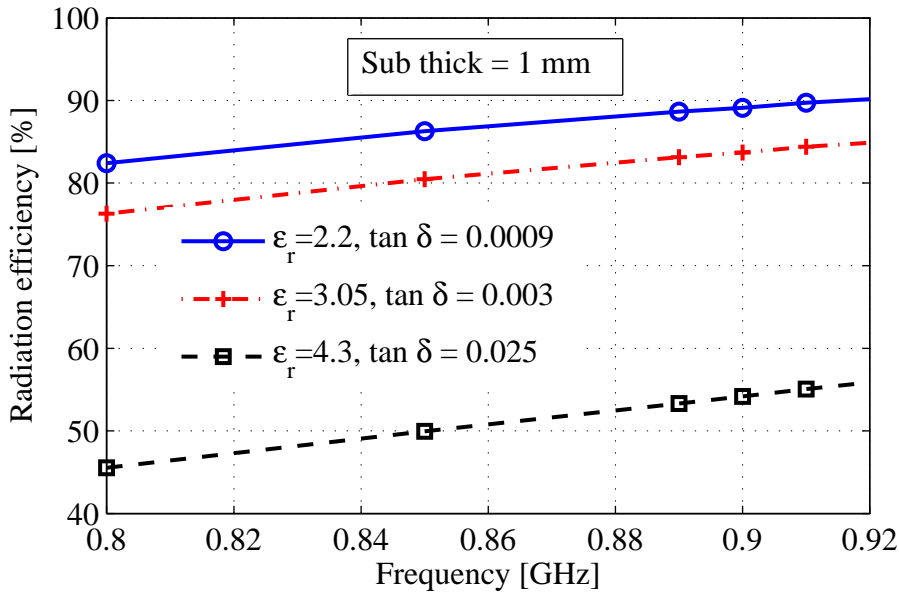


**Figure 5.13.** Antenna radiation efficiency versus frequency for different substrate materials. Substrate thickness is 1 mm.

In this Figure the substrate height is set to 1mm and the radiation efficiency is simulated for three different substrate materials, FR4 dashed curve ( $\epsilon_r = 4.3$ ,  $\tan \delta = 0.025$ ), GML 1000 dashed-dotted curve ( $\epsilon_r = 3.05$ ,  $\tan \delta = 0.003$ ) and Rogers RT-5880 solid curve ( $\epsilon_r = 2.2$ ,  $\tan \delta = 0.0009$ ). It should be mentioned that the antenna size is kept constant for the three simulations. It is shown in the figure that the radiation efficiency increases when the substrate loss ( $\tan \delta$ ) decreases.

Figure 5.14 shows the antenna radiation efficiency as a function of frequency for varying substrate thickness. In this figure the substrate material is chosen to be GML 1000. The figure shows that a thinner substrate has a limited effect on the radiation efficiency and will result in a slightly higher radiation efficiency. The antenna radiation efficiency is improved by less than 4% when choosing a 0.5 mm thick substrate instead of a 1.5 mm thick substrate.

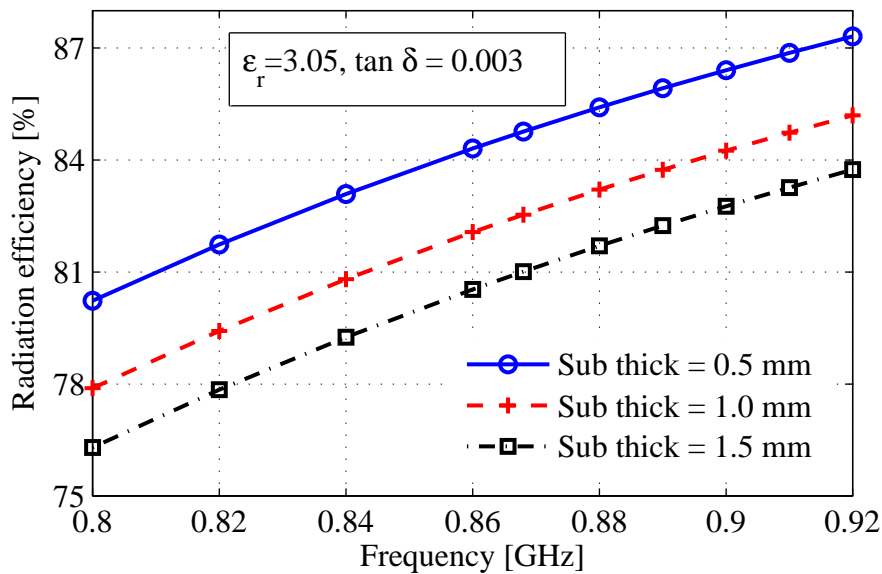


**Figure 5.14.** Antenna radiation efficiency as a function of frequency for different substrate thickness.

For the prototype realized in this section using the 5 stage CMOS rectifier, a 0.5 mm thick GML 1000 substrate is chosen. At the design frequency, the simulated radiation efficiency is presented in the solid curve of Fig. 5.14. At an operating frequency of 868 MHz, the antenna radiation efficiency is 84.7 %.

The real part of the antenna should be a fixed value between  $4.3 \Omega$  and  $7.6 \Omega$ . Based on the rectenna design criterion presented in Sec. 5.2.2, the real part of the input impedance of the rectifier is chosen to be  $4.4 \Omega$ . After optimizing all the antenna parameters (see Fig. 4.13), an antenna with one short-circuited arm ( $n = 1$ ) having an input impedance

of  $Z_{Antenna} = 4.4 + j328\Omega$  is chosen. The geometrical parameters of the designed antenna (see Fig. 4.13) are listed in Table 5.2.

**Table 5.2.** Optimized antenna parameters for the suggested antenna prototype. All dimensions are in mm.

$n$	$W, W_1$	$g_1, g_2$	$E_1$	$L_1$	$L_2$	$S_1$	$S_2$	$S_3$
1	5	3	2	34	35.25	13.75	2	4.5

The front and the back sides of the designed antenna are shown in Fig. 5.15.

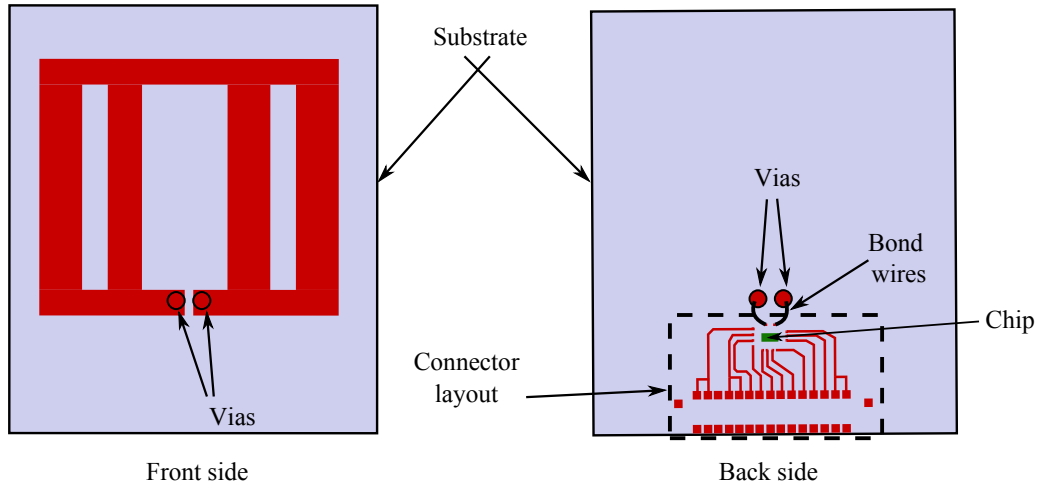
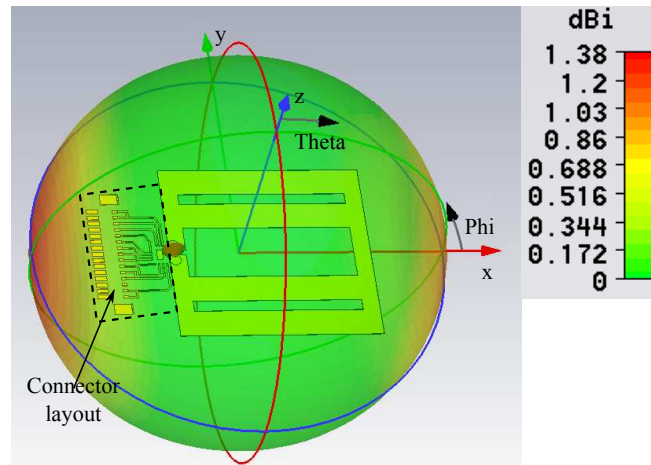


**Figure 5.15.** Front and back sides of the designed compact antenna structure, including the five stage CMOS chip and the connector layout.

For a proof of principle, the control loop is connected to the chip and antenna using the connector layout shown in Fig. 5.15. The chip is integrated on the backside of the antenna. It should be mentioned that the antenna parameters are optimized in the presence of the connector layout, vias and bond wires. The rectifier inputs are bonded to the vias (2 mm in diameter) that connect to the antenna feeding points. The bond wires are modeled using CST Microwave Studio and are having a length of 2.1 mm and a radius of  $25\ \mu\text{m}$ .

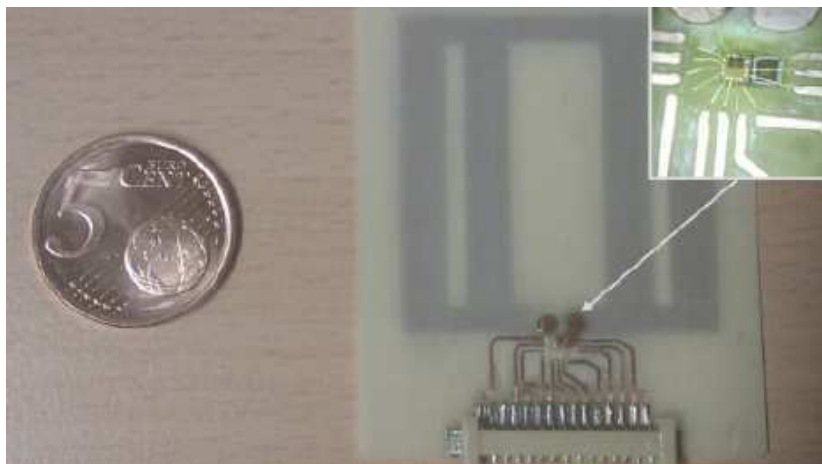
Due to the self-calibrating capability of the circuit and the low real part of the input impedance ( $R_{in}$ ), the antenna size of the prototype presented in this section is reduced to  $21.9\ \text{cm}^2$  compared to  $34.3\ \text{cm}^2$  for the first prototype presented in Sec. 5.3.1. Once the external control loop is completely integrated on chip, the connector is no longer required and the antenna board size can be scaled down further without introducing a significant performance loss.

Figure 5.16 shows the simulated 3D directivity pattern of the prototype antenna. The directivity  $D_r$  and the radiation efficiency  $\eta_{radiation}$  determine the antenna gain  $G_r$ .  $G_r = \eta_{radiation} D_r$ , with  $D_r = 1.3$  dBi and  $\eta_{radiation} = 0.85$ , the simulated antenna gain is  $G_r = 0.6$  dBi.



**Figure 5.16.** 3D directivity pattern of the prototype antenna at an operating frequency of 868 MHz, simulated using CST Microwave Studio.

Figure 5.17 shows a photograph of the manufactured prototype.



**Figure 5.17.** Photograph of the manufactured prototype antenna with the integrated circuit. The inset shows the bonded chip in more detail.

### 5.4.3 Measurement Results

The output voltage and the power conversion efficiency have been measured for different load resistances and for different RF input power levels ( $P_{in}$ ) at the design frequency (868 MHz).

Figure 5.18 shows the measured DC output voltage ( $V_{out}$ ) as a function of frequency for a load resistance of 1 M $\Omega$  at an input power level of -20 dBm.

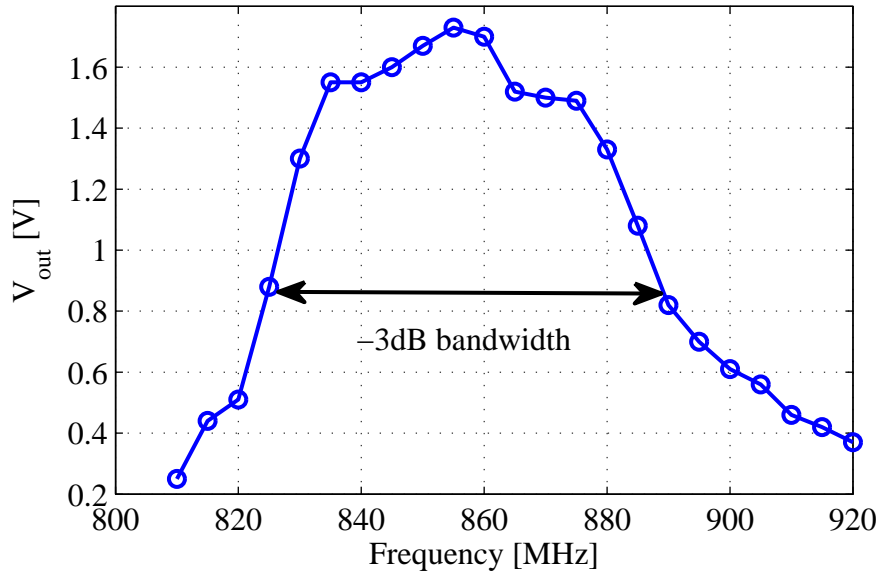


**Figure 5.18.** Measured output voltage versus frequency for  $R_L = 1M\Omega$  and  $P_{in} = -20$  dBm

The peak output voltage is measured at an operating frequency of 855 MHz and reaches 1.73 V. The -3 dB voltage bandwidth is approximately 60 MHz. Compared to the output voltage (measured at  $P_{in} = -10$  dBm) of the first fabricated prototype, where commercial diodes have been used (see Fig. 5.9), it is clear that this prototype rectenna generates a higher output voltage even at an input power level that is ten times lower (-20 dBm). In addition, the -3dB voltage bandwidth of this prototype rectenna has almost doubled. This increase in the output voltage was expected and is due to the lower real part and higher imaginary part of the input impedance of the designed CMOS rectifier ( $Z_{CMOS-Rectifier} = 4.4 + j328\Omega$ ) as compared to the input impedance of the discrete diode voltage doubler used for the prototype introduced in the previous section ( $Z_{Doubler} = 8.5 + j237\Omega$ ).

Next, the output voltage has been measured as a function of input power level for different load resistances at 868 MHz; the result is shown in Fig. 5.19. The open circuit output voltage is represented by the dashed-dotted curve in the figure, where the rectenna is able to generate 1 V at an input power level on -27.5 dBm.



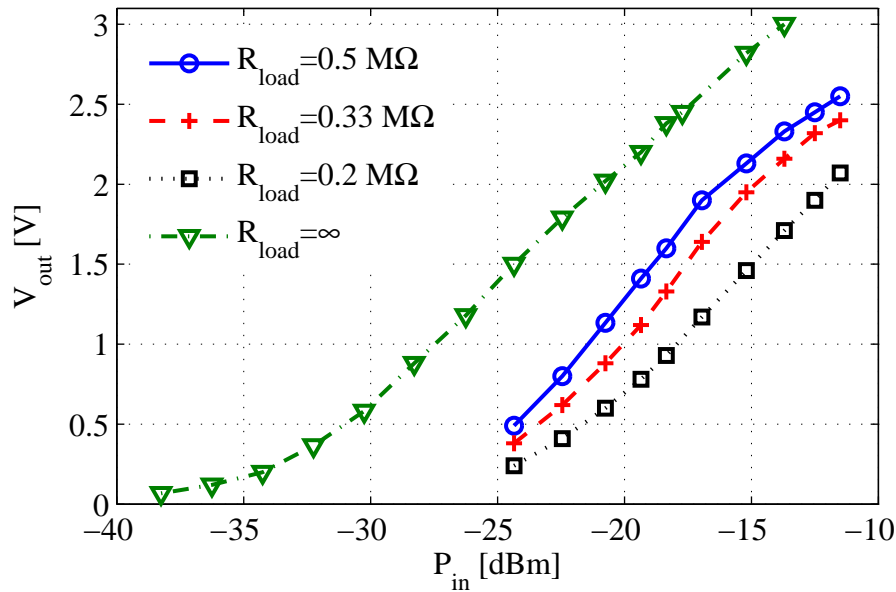


**Figure 5.19.** Measured output voltage as a function of input power level for different resistive load values.

Based on these voltage levels, and on the simulated antenna gain of 0.6 dBi ( $D_r = 1.3$  dBi,  $\eta_{\text{radiation}} = 0.85$ ), the Power Conversion Efficiency (PCE) is calculated from Eq. (5.21) and plotted in Fig. 5.20 as a function of  $P_{in}$  for different load resistance values.

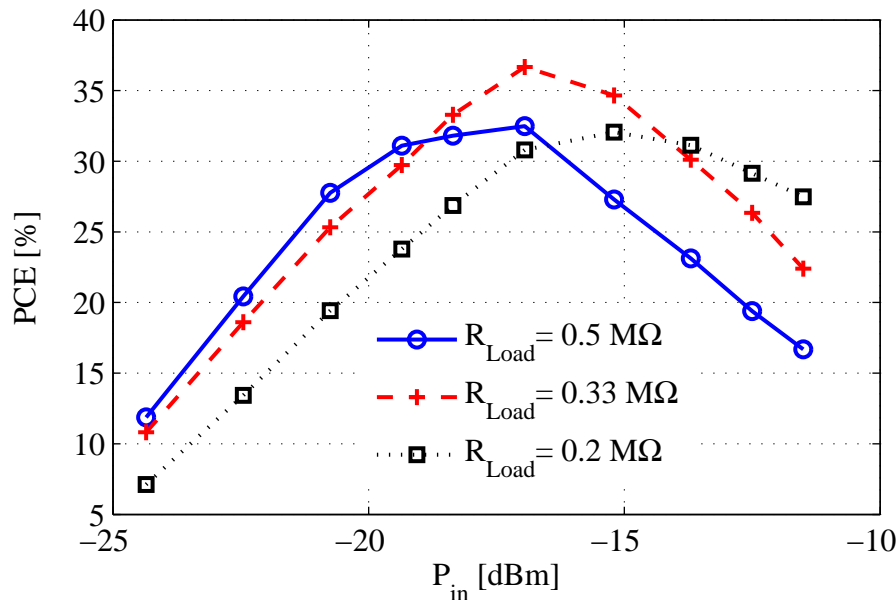


**Figure 5.20.** Measured power conversion efficiency versus input power level for different resistive load values. Operating frequency = 868 MHz

The power conversion efficiency reaches 30 % at an input power level of -20 dBm and increases to 36.6 % at an input power level of -17 dBm over a 0.33 M $\Omega$  resistive load. Compared to the recently reported results in [99, 100], the presented rectenna in this paper has a lower sensitivity and is more compact. Compared to [101] and [102], the proposed rectenna is 70% and 37% more compact respectively. Table 5.3 compares the performances achieved in this work to the state of the art as published in the open literature.

**Table 5.3.** Overview of rectennas performance with CMOS rectifier in literature.

Ref.	This work	[101]	[102]	[103]
Technology	90 nm	0.18 $\mu$ m	250 nm	90 nm
Frequency	868 MHz	970 MHz	906 MHz	915 MHz
Sensitivity	-27 dBm @ 1 V	-17.7 dBm @ 0.8 V	-22.6 dBm @ 2 V	-24 dBm @ 1 V
Peak PCE (%)	36.6 @ -17 dBm	37* @ -18.7 dBm	30* @ -8 dBm	11 @ -18.83 dBm
$\frac{Size}{\lambda^2}$	0.018	0.039	0.027	n.a
Measured distance	27 meters @ 1.78 w	n.a.	15meters @ 4 w	n.a.

\*calculated from the graph

The suggested co-designed antenna-CMOS rectifier is smaller in size than those reported in other publications. Once the control loop is integrated on chip, the size can be even further reduced. Thus, through the co-design of the 5 stage CMOS rectifier and the antenna and following the design criterion from Sec. 5.2.2 we were able to significantly increase the performance of the rectenna with respect to the DC output voltage, power conversion efficiency, sensitivity and size compared to the state of the art.

## 5.5 Conclusion

A compact rectenna has been presented in this chapter. The design strategy is based on designing an antenna with a input impedance equal to the complex conjugate of that of the rectifier. This allows removing the matching network, which results in a more compact and efficient rectenna system. Two prototypes have been designed, manufactured, and measured. The first prototype consists of a rectenna that uses commercially available diodes, while in the second prototype a CMOS rectifier is used to convert the RF power into DC power.

In the first prototype, a voltage doubler is used that is conjugately matched to the

antenna. At an available power level of -20 dBm, the PCE reaches 33.8 % for a resistive load of 10 k $\Omega$ . The PCE increases to 54.7 % when the RF input power level is increased to -10 dBm. The measured results showed an improved performance compared to recently reported results in literature.

For the second prototype, a 5 stage cross-connected bridge rectifier with a capacitor bank implemented in standard 90-nm CMOS technology has been used. A control loop is used to optimize the matching between the antenna and the rectifier. Compared to the output voltage of the voltage doubler of the first fabricated prototype, where commercially available diodes have been used, the 5 stages bridge rectifier generates a higher output voltage even at an input power level that is ten times lower. In addition, the -3 dB voltage bandwidth of the second prototype is almost doubled. Measurements show a sensitivity of -27 dBm for a 1 V DC output.

At an input power level of -20 dBm, the peak output voltage is measured at an operating frequency of 855 MHz and reaches 1.73 V. The radiation efficiency reaches 30 % at an input power level of -20 dBm and it increases to 36.6 % at an input power level of -17 dBm over a 0.33 M $\Omega$  resistive load. Compared to the state of the art published results, a better performance of the rectenna has been achieved with respect to the DC output voltage, power conversion efficiency and sensitivity. Moreover the suggested rectenna is smaller in size than those reported in previous publications.

## RF Power Transfer - Complete Rectenna System

---

In this chapter a complete rectenna system, i.e. the receiving part of the RF power transfer system, is described. The system consists of a signal generator connected to a matching network and a rectifier. The signal generator replaces the receiving antenna to ensure an accurate and repeatable signal injection. A commercially available power management circuit is then used to boost the DC voltage and to store the captured energy in a capacitor. The power management circuit is connected to a dynamic load to emulate different radio systems behaviour. The system's DC average output power and the system's power conversion efficiency are measured and compared to those of a commercially available rectenna system.

## 6.1 System Concept and Measurement Setup

In this section, the matching network and the voltage doubler introduced in Sec. 3.7.1 are combined with the power management circuit TI BQ25570 [104] and a dynamic load that emulates the behaviour of a radio system. The measurement system<sup>1</sup> is shown in Fig. 6.1.

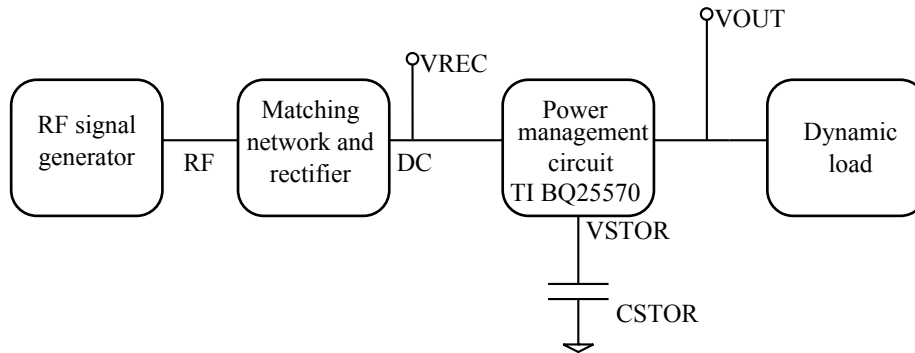


**Figure 6.1.** Measurement setup using a power management circuit and a dynamic load.

The RF signal generator in this setup replaces the ( $50\Omega$ ) antenna, so that a stable and repeatable measurement setup is created. Since the DC output voltage of the rectifier stage VREC (see Fig. 6.1) is limited and changes with input power level, a power management circuit is needed to store and regulate the system output energy. For our system, the power management circuit TI BQ25570 is used. The connections to the TI BQ25570 are shown in Fig. 6.2. A complete schematic and explanation of the evaluation board used are presented in [105].

The integrated boost controller in the chip amplifies the DC input voltage ( $V_{IN\_DC}=V_{REC}$ ) and controls its output voltage ( $V_{STOR}$ ). The boost controller stops when  $V_{STOR}$  reaches a threshold level that is set with the external resistor network shown in Fig. 6.2. The energy is stored in a (super)-capacitor or a rechargeable battery. The integrated buck converter (see Fig. 6.2) is powered from  $V_{STOR}$  and regulates the output voltage to drive different applications. To emulate different radio systems behaviour a dynamic load is connected to the VOUT pin of the evaluation board. This dynamic load will be discussed in more detail in the remainder of this chapter.

The amount of energy stored in a capacitor  $C$ , when the voltage increases from  $V_1$  to

<sup>1</sup>The measurement setup as well as the measurement results presented in this chapter were performed at the Holst Centre/imec by Hans Pflug.

$V_2$  is:

$$W = \frac{1}{2}C (V_2^2 - V_1^2). \quad (6.1)$$

The minimum capacitance value,  $C_{\min}$ , depends on the power drawn by the dynamic load  $P_L$  during a discharge time  $T_p$  when the capacitor voltage drops from  $V_2$  to  $V_1$  and is given by:

$$C_{\min} \geq \frac{P_L T_p}{0.5 (V_2^2 - V_1^2)}. \quad (6.2)$$

For example, suppose 60 mW of power is drawn for 40 ms, resulting in a voltage drop from 4.2 V to 1.8 V. This system will have a  $C_{\min} \geq 333 \mu\text{F}$ . To ensure sufficient storage capacitance, a 1000  $\mu\text{F}$  (CSTOR) capacitor is connected to the VSTOR-pin of the TI chip.

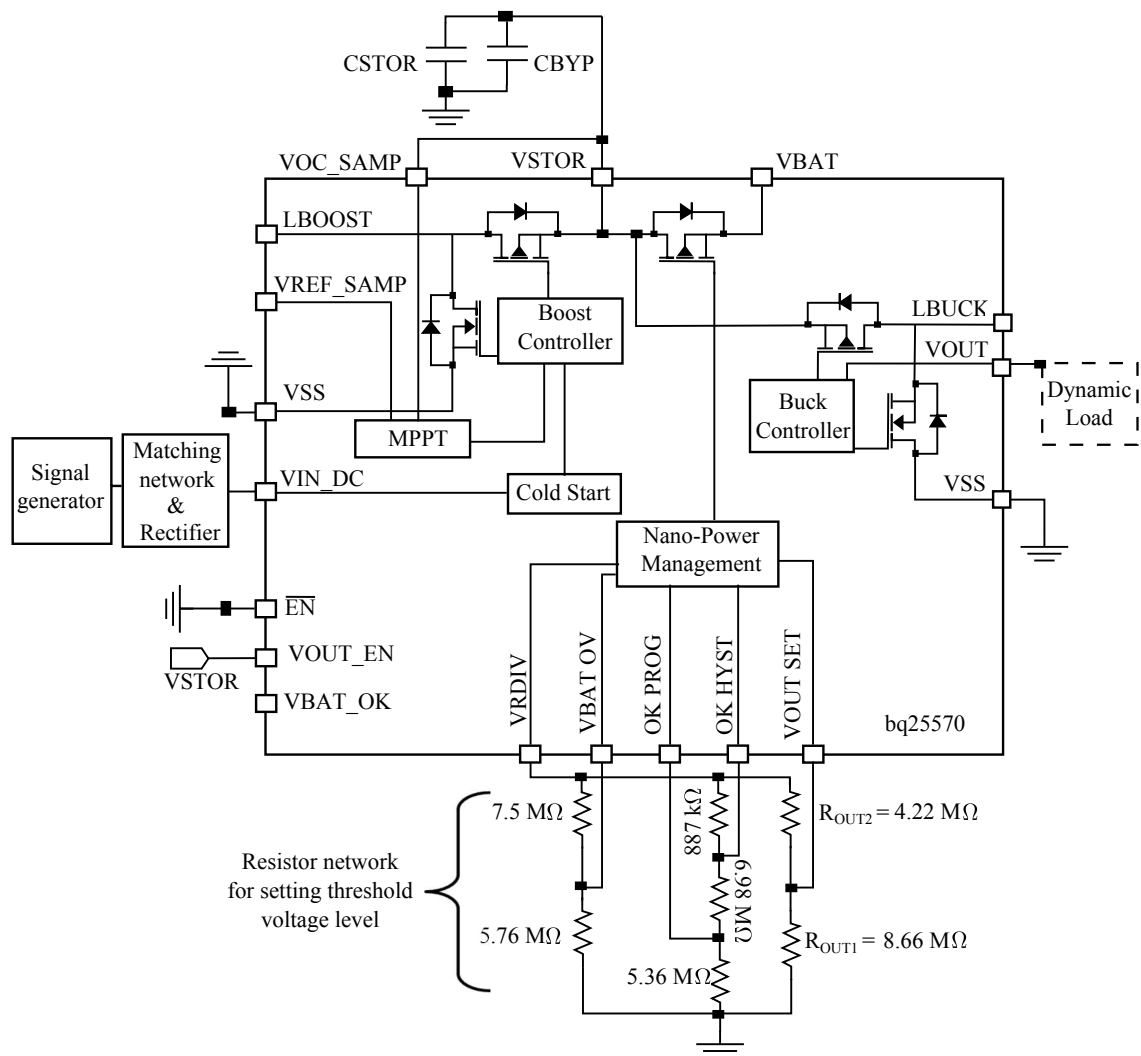


**Figure 6.2.** Schematic connection to the TI BQ25570 evaluation board.

The integrated boost controller provides 4.2 V at the VSTOR-pin. The buck controller regulates the output voltage VOUT (see Fig. 6.2) at 1.8 V for the chosen values of the resistor network shown in Fig. 6.2. A dynamic load is connected at the VOUT-pin of the TI chip.

The schematic of the dynamic load is shown in Fig. 6.3. It consists of an array of load resistors connected to BJTs that are operated as switches. The switches are controlled by an Arduino Mega board [106] with the ATmega2560 Atmel micro-controller. So, the load resistance and the on-time ( $T_P$ ) and off-time ( $T_i$ ) are at the users disposal.

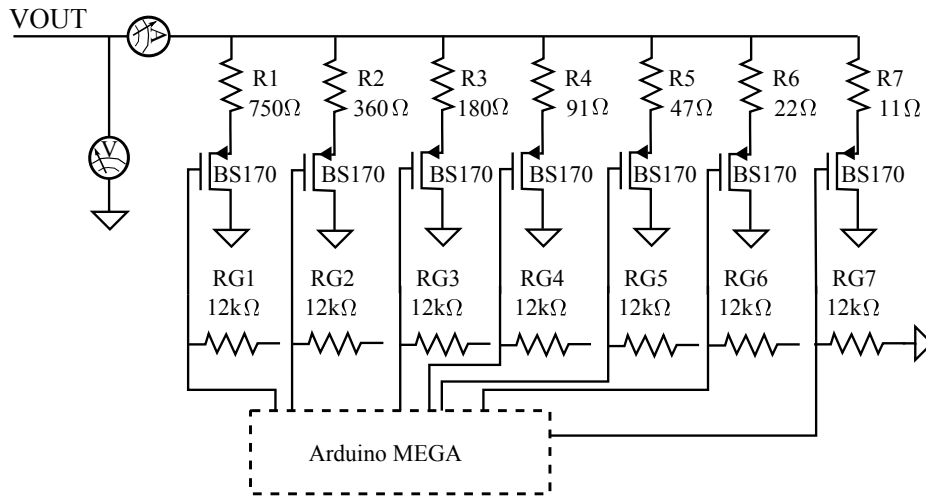


**Figure 6.3.** Schematic of the used dynamic load connected to the VOUT-pin of the TI BQ25570 chip.

## 6.2 Measurement Results

The system's average DC output voltage and the system's efficiency are measured, and the results are presented in this section. For the presented measurements,  $T_P$  is the pulse duration corresponding to a transmission of a frame and is set to 10 ms.  $T_i$  is the time between two consecutive bursts required to recharge the storage capacitor (CSTOR).

The efficiency,  $\eta_{\text{system}}$ , of the complete harvesting system is expressed as:

$$\eta_{\text{system}} = \frac{P_{\text{out}}}{P_{\text{RF}}}, \quad (6.3)$$

where  $P_{\text{RF}}$  is the RF power provided by the signal generator, and  $P_{\text{out}}$  is the average

DC output power.  $P_{\text{out}}$  is calculated as:

$$P_{\text{out}} = \frac{T_p}{T_p + T_i} P_L. \quad (6.4)$$

The system output voltage is  $V_{\text{OUT}}=1.8$  V and 55 mW ( $P_L = 55\text{mW}$ ) of power is drawn by the dynamic load. A commercially available rectenna system [107] has been measured under the same conditions.

Figure 6.4 shows the average DC output power as a function of RF input power level for the commercially available rectenna system and for the presented system. The figure shows that the DC output power of the presented system outperforms that of the commercially available rectenna system, especially at lower input power levels ( $\leq -6\text{dBm}$ ). The presented system is able to generate  $10 \mu\text{W}$  on average at an RF input power level of  $-12$  dBm, while the commercially available rectenna system generates the same output power at an input power level of  $-6$  dBm, which results in 6 dB sensitivity improvement for this average DC output power level.

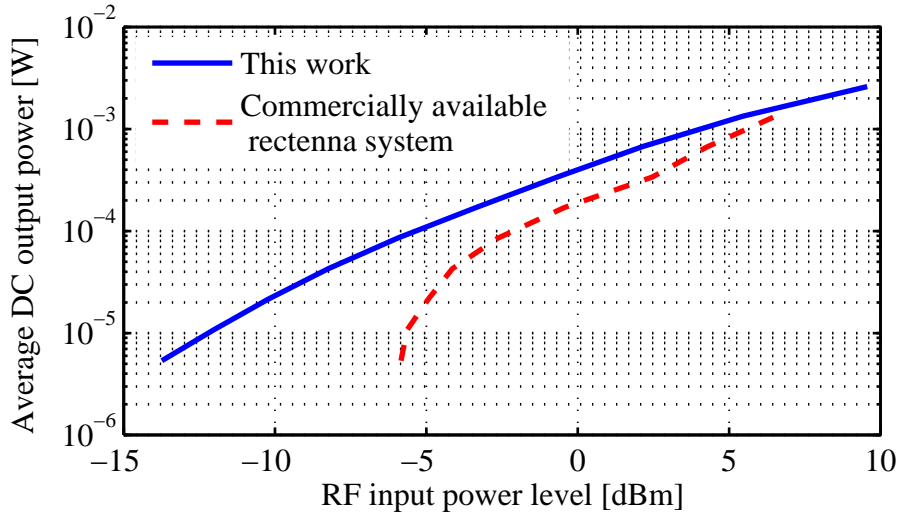


**Figure 6.4.** Average DC output power as a function of RF input power level using the harvesting system developed in this thesis and the commercially available rectenna system.  $P_L=55\text{mW}$ ,  $T_p = 10\text{ms}$ ,  $T_i$  varies.

The system's RF to DC conversion efficiency is calculated using Eqs.(6.3) and (6.4) and the results for both systems are plotted in Fig. 6.5. The figure shows that the power conversion efficiency of the presented system is higher than that of the commercially available system in the shown RF power level band. The efficiency of the presented system reaches 23 % at an input power level of  $-10$  dBm, while at the same input power level the commercially available system fails to operate.

At an input power level of  $0$  dBm, the power conversion efficiency of the commercially



available system is 19 %, while the power conversion efficiency of the presented system reaches 40 % resulting in more than 20 % improvement in power conversion efficiency.

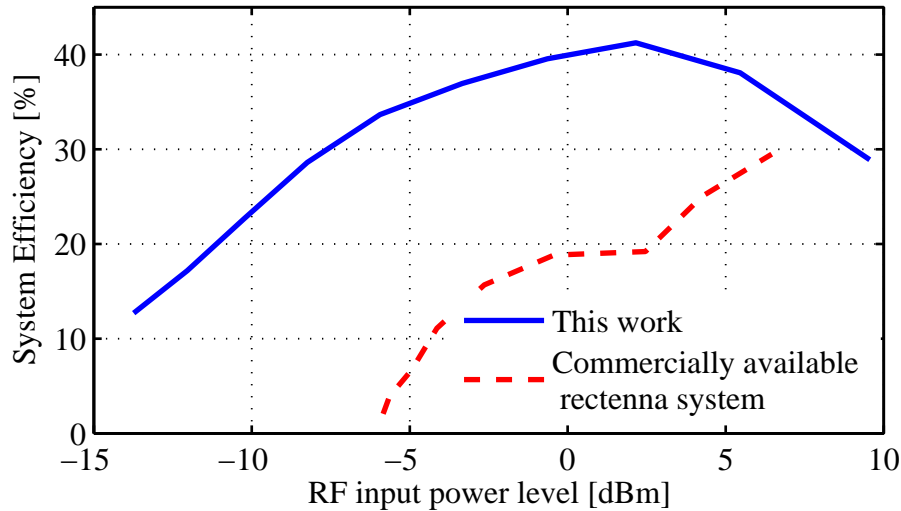


**Figure 6.5.** System's RF to DC conversion efficiency as a function of RF input power level using the harvesting system developed in this thesis and the commercially available rectenna system.  $PL=55\text{mW}$ ,  $T_p = 10\text{ms}$ ,  $T_i$  varies.

Using the measured system efficiency (solid curve in Fig. 6.5), the average DC output power is calculated as a function of rectenna's distance from a 2 W Effective Radiated Power (ERP) source at 868 MHz. Figure 6.6 shows the calculated average DC output power as a function of propagation distance when using a 1 dBi and a 6 dBi receiving antenna.

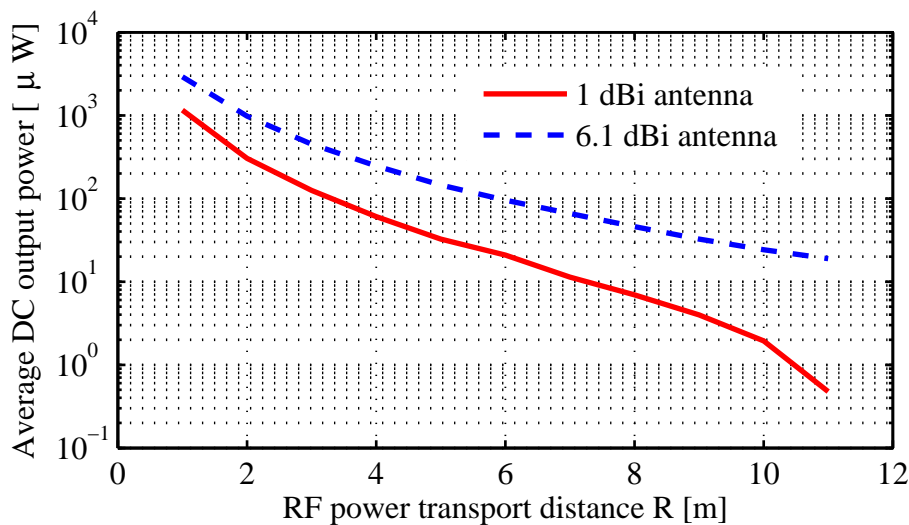


**Figure 6.6.** Average DC output power as a function of RF power transport distance (R) using a 1 dBi and a 6 dBi receiving antenna.

Figure 6.6 indicates that for an average DC output power of  $20 \mu\text{W}$ , the RF power transport distance increases from 6 meters to 10.5 meters when using a 6.1 dBi gain antenna instead of 1 dBi gain antenna. An average DC output power of  $20 \mu\text{W}$ , having a  $P_L$  of 55 mW and a burst time  $T_p = 10\text{ms}$  results in an off-time of  $T_i = 27$  seconds.

As a practical application, the commercially available humidity and temperature sensor, Cresta WX688 [108] is used. The Cresta sensor is shown in Fig. 6.7. The sensor uses a 433 MHz transmitter to send data to the main station. The (two AA 1.5 V) batteries of the sensor are removed and the power lines are extended as shown in Fig. 6.7, and connected to the VOUT pin of the TI BQ25570 chip (see Fig. 6.2).



**Figure 6.7.** Cresta humidity and temperature sensor.

To provide 3.0 V at the VOUT-pin of the TI BQ25570, the resistor network is modified where  $R_{OUT2}$  and  $R_{OUT1}$  (see Fig. 6.2) are set to  $7.5 \text{ M}\Omega$  and  $5.1 \text{ M}\Omega$  respectively. The sensor transmits a burst containing the temperature and the humidity information to the main station every 45 seconds ( $T_i = 45$  seconds). The burst duration is 823 ms, ( $T_p = 823$  ms). The voltage variation on the storage capacitor (CSTOR) is 844 mV (3.844 V to 3.0 V). The energy stored in the capacitor is calculated using Eq. (6.1) and is 2.89 mJ. This results in a 3.5 mW power drawn by the sensor and an average DC output power, using Eq. (6.4), of  $62.9 \mu\text{W}$ .

The sensor operated at different RF input power levels. The minimum RF input power level that operates the sensor was  $-5 \text{ dBm}^2$ . It should be mentioned that the sensor

---

<sup>2</sup>The system efficiency is 35 % at  $-5\text{dBm}$  for drawing 55 mW during 10 ms (see Fig. 6.5). The system efficiency is expected to decrease if 3.5 mW are drawn during 823 ms. Since the minimum RF input power level that operated the sensor was  $-5 \text{ dBm}$  ( $316 \mu\text{W}$ ), and the average DC power drawn by the sensor is  $62.9 \mu\text{W}$ , this results in a system efficiency of 20 % for powering the Cresta humidity and temperature sensor, which is consistent with our expectations.

is not developed for RF power transport applications, but the sensor was used in this experiment as a proof of concept.

### 6.3 Conclusion

In this chapter, a complete rectenna system was presented. The system encompasses a matching network, a voltage doubling rectifier, a commercially available power management circuit, a 1000  $\mu\text{F}$  storage capacitor and a dynamic load. The average DC output power and the system's RF to DC conversion efficiency are measured, and compared to those measured for a commercially available rectenna system operated under the same conditions. It has been shown that the commercially available rectenna system fails to operate at low power levels ( $\leq -6\text{dBm}$ ) while the presented system can operate at an RF input power level as low as  $-13\text{ dBm}$ . This means that for example, 55 mW of DC power can be drawn for 10 ms every 27.5 seconds on a distance of about 10 m from a 2 W ERP source at 868 MHz using a 6.1 dBi receiving antenna.

At an input power level of 0 dBm, the power conversion efficiency of the commercially available system does not exceed 19 %, while the power conversion efficiency of the presented system reaches 40 %, resulting in more than 20 % improved power conversion efficiency.

# A Frequency Selective Surface for RF Energy Harvesting

---

In this chapter, a novel implementation and application of Frequency Selective Surfaces (FSS) is presented. The novel FSS design can harvest power from arbitrarily polarized incident electromagnetic waves. The design does not involve a matching network, which results in a simple (polarization-independent) power harvester. An equivalent circuit model to predict the transmission and reflection characteristics of a gridded square loop FSS loaded with diodes is employed. The design method is validated for different incident angles, through full-wave analysis and measurements. To that end, the addition of lumped elements (R,L,C) in a metallic conductive grid of a non-harvesting FSS is investigated. Waveguide simulator measurements and full-wave simulations are employed to validate the derived analytical equations. A  $3 \times 3$  and a  $5 \times 5$  RF harvesting FSS have been designed, fabricated and measured. An RF to DC conversion efficiency of 25% for the  $3 \times 3$  RF harvester and 16% for the  $5 \times 5$  RF harvester are measured at an incident power density of  $3.2 \mu\text{W}/\text{cm}^2$ .

## 7.1 Introduction

In the previous chapters the developed rectennas are designed to harvest linearly polarized waves. In this chapter a practical and efficient way to harvest RF waves that may be polarized in any direction is proposed. The technique can be used to produce RF power harvesting glass, or RF power harvesting wall paper. Figure 7.1 shows a photograph of two RF power harvesting glass prototypes using two different Frequency Selective Surfaces (FSS): the gridded square FSS and the gridded cross FSS. In the final design, transparent conductive film [109, 110] could be implemented on glass for the realization of optically transparent harvesting grids.



**Figure 7.1.** RF power harvesting glass using frequency selective surfaces.

The main advantages of the suggested RF harvester in comparison to conventional rectenna array configurations, (i.e. wherein each element is connected to a rectifier and wherein the DC-signals are combined) are as follows.

- In a conventional rectenna array configuration, RF combining networks or/and DC combining circuits are needed e.g. [111]. In the FSS-based rectenna, the combining circuits are absent. The DC output voltage is collected using only two DC connections to the structure, which simplifies the design of the RF harvester.
- The matching networks used in conventional rectennas and rectenna arrays are in general narrow-band and therefore enable power harvesting in most cases in a single frequency band only e.g. [112]. In the FSS harvesters presented in this chapter, impedance matching networks are not present. They form an integral part of the FSS structure, which eliminates the losses that would be introduced

by a separate matching network. In addition, the suggested design allows power harvesting from a dual frequency band, more specifically: the FSS transmission and reflection frequency bands.

- To maximize the harvested power, polarization matching between the transmitter and the receiver is crucial. Consequently, dual linearly, or circularly polarized rectennas are designed e.g. [113]. In this chapter, a polarization independent FSS is presented, which allows to harvest power from arbitrary polarized waves by decomposing the polarization of the incident wave into two orthogonal linear polarizations and rectifying them independently.
- Array rectennas (i.e. array antennas connected to a diode) exhibit a relatively high directivity and thus need to be positioned in the direction of the source for an optimal power transfer. The suggested FSS harvester that is a rectenna array (i.e. combination of radiators, each one connected to a rectifier) is less sensitive to angles of incidence and can harvest RF power efficiently at angles away from broadside.

The FSS rectenna discussed in this chapter consists of a metallic grid with inner square loops of conductors disposed in a periodic fashion as shown in Fig. 7.2(a).

The grid is loaded with Schottky diodes for current rectification. After rectification, the DC power is collected at the top-left and bottom-right corners as shown in Fig. 7.2(a). The physical principles of operation were first discussed in [114] and are shown in Figs. 7.2(b) and 7.2(c). For our FSS configuration, the labels U (up), D (down), R (Right) and L (Left) indicate the direction of the induced current in the grid. To start with, a vertically polarized incident wave  $\vec{E}_V$  is considered, see Fig.7.2(b). The induced current will flow from the diodes  $d_{V1}$  toward diodes  $d_{V2}$  in the U-direction. Diodes  $d_{H1}$  and  $d_{H2}$  are unbiased, and consequently they will prevent the current from flowing in the R-direction. Similarly, when a horizontally polarized incident wave  $\vec{E}_H$  hits the FSS surface, see Fig.7.2(c), this time diodes  $d_{H1}$  and  $d_{H2}$  draw the current in the L-direction from  $d_{H1}$  toward  $d_{H2}$ . Diodes  $d_{V1}$  and  $d_{V2}$  are unbiased, and consequently they will prevent the current from flowing in the D-direction. When an elliptically polarized wave hits the FSS surface, the vertical and the horizontal components of the electric field will drive the induced current to flow in the U and L-directions. Consequently the induced current can be collected at the top left corner by using the DC collection lines as shown in Fig.7.2(a). With this configuration the grid acts as a half-wave rectifier, making the FSS capable of rectifying the signal from arbitrarily polarized waves.

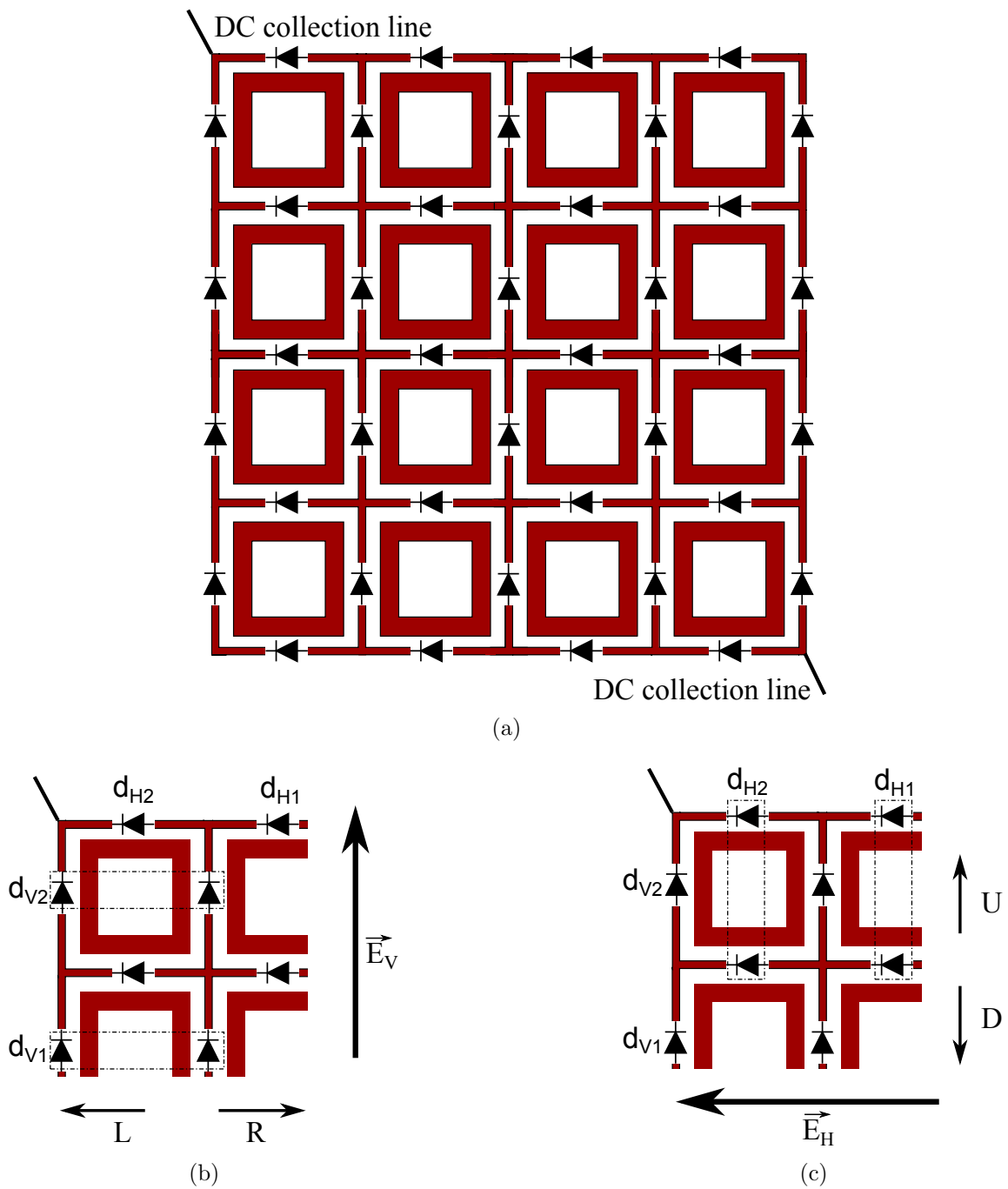


**Figure 7.2.** Suggested RF FSS harvester (a) and its physical principal of operation for an incident vertical electric Field ( $E_V$ ), (b) and an incident horizontal electric Field ( $E_H$ ), (c).

## 7.2 Square Loop FSS

The square loop FSS has been reported in the literature by several authors [115, 116] and is shown in Fig. 7.3(a).

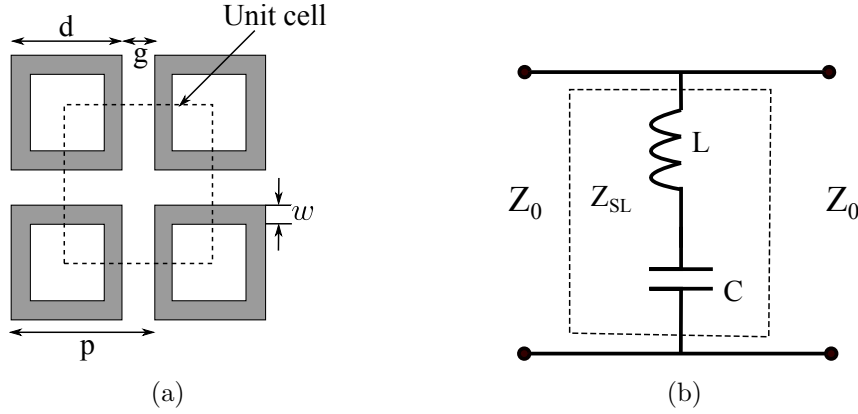


**Figure 7.3.** Square Loop (SL) frequency selective surface (FSS) configuration (a) and its unit-cell equivalent electric circuit model (b).

It consists of a periodic array of identical conducting strip square loops.  $g$  is the gap between neighboring elements,  $w$  is the width of the loop strip,  $d$  is the length of the square side and  $p = (d + g)$  is the periodicity of the unit cell. The unit cell is the structure that is periodically repeated in the two orthogonal planar directions. Several choices can be made, the results are identical. The equivalent circuit model of the unit cell is shown in Fig. 7.3(b) and is a series  $LC$  circuit, shunt-positioned in a segment of transmission line carrying a plane incident wave, where  $L$  represents the inductance due to the vertical (horizontal) metal conductor and  $C$  is the capacitance between the horizontal (vertical) conductors.

The impedance of the unit cell (dashed box in Fig. 7.3(a)), is given by:

$$Z_{fss} = j \left( X_L - \frac{1}{B_C} \right), \quad (7.1)$$

where  $X_L$  and  $B_C$  are derived as presented in [117]:

$$X_L = Z_0 \left( \frac{d}{p} \right) F(p, 2w, \lambda), \quad (7.2)$$

$$B_C = \frac{4}{Z_0} \left( \frac{d}{p} \right) F(p, g, \lambda). \quad (7.3)$$



$Z_0$  is the characteristic impedance of free space,  $Z_0 = \sqrt{\frac{\mu_0}{\epsilon_0}}$  and  $\lambda$  is the free-space wavelength. The function  $F(p, g, \lambda)$  is given in [118] and [119]:

$$F_{TE}(p, w, \lambda) = \Upsilon \left[ \ln \csc \left( \frac{\pi w}{2p} \right) + G(p, w, \lambda, \theta) \right], \quad (7.4)$$

$$F_{TM}(p, w, \lambda) = \Phi \left[ \ln \csc \left( \frac{\pi w}{2p} \right) + G(p, w, \lambda, \varphi) \right], \quad (7.5)$$

$$F_{TE}(p, g, \lambda) = \Psi \left[ \ln \csc \left( \frac{\pi g}{2p} \right) + G(p, g, \lambda, \theta) \right], \quad (7.6)$$

$$F_{TM}(p, g, \lambda) = \Omega \left[ \ln \csc \left( \frac{\pi g}{2p} \right) + G(p, g, \lambda, \varphi) \right], \quad (7.7)$$

where  $\Upsilon = (p \cos \theta) / \lambda$ ,  $\Phi = (p \sec \varphi) / \lambda$ ,  $\Psi = (p \sec \theta) / \lambda$  and  $\Omega = (p \cos \varphi) / \lambda$ . Herein,  $\theta$  and  $\varphi$  are the angles of incidence of a TE and TM polarized wave, respectively. The FSS is supposed to be positioned in the xy-plane of a rectangular xyz coordinate system.  $G$  is the first-order correction term for both TE-wave and TM-wave incidence, and has been given in [118] and [120]. The correction factor  $G$  is presented in Appendix B. To account for the influence of the supporting dielectric layer, the results derived in [121] and [122] are used and presented in Sec. 7.2.2. The absolute value in dB of the transmission and reflection coefficients is derived from the normalized impedance of the unit cell [120]:

$$|T|_{dB} = 20 \log_{10} \left[ \frac{2Z_{fss}}{1 + 2Z_{fss}} \right], \quad (7.8)$$

$$|R|_{dB} = 20 \log_{10} \left[ \frac{-1}{1 + 2Z_{fss}} \right]. \quad (7.9)$$

### 7.2.1 Model Verification

To demonstrate the accuracy of these Analytical Expressions (AE), the reflection and the transmission coefficients are calculated and compared to the results obtained by

the Finite Integration Technique (FIT) [72] as implemented in CST Microwave Studio. Table 7.1 summarizes the dimensions for different array configurations that are investigated here.  $t$  is the substrate thickness and  $\epsilon_r$  is the substrate permittivity.

**Table 7.1.** Analyzed Square Loop Array Configurations. Dimensions are explained in Fig. 7.3(a).

Square Loop Array #	$\mathbf{p}$ (mm)	$\mathbf{d}$ (mm)	$\mathbf{g}$ (mm)	$\mathbf{w}$ (mm)	$\mathbf{t}$ (mm)	$\epsilon_r$
1	10.0	8.75	1.25	0.625	0.0	1.0
2	36	31.0	5	3.0	0.25	2.2
3	22.0	21.0	1.0	3.0	see Sec. 7.2.2	2.2
4	32.25	31.0	1.25	3.0	0.25	see Sec. 7.2.2

Figure 7.4 shows the magnitude (a) and the phase (b) of the transmission and the reflection coefficients for FSS #1 in Table 7.1 as a function of frequency calculated by the Analytical Expressions (AE) and by the Finite Integration Technique (FIT) using CST Microwave Studio, demonstrating the validity of the AE.

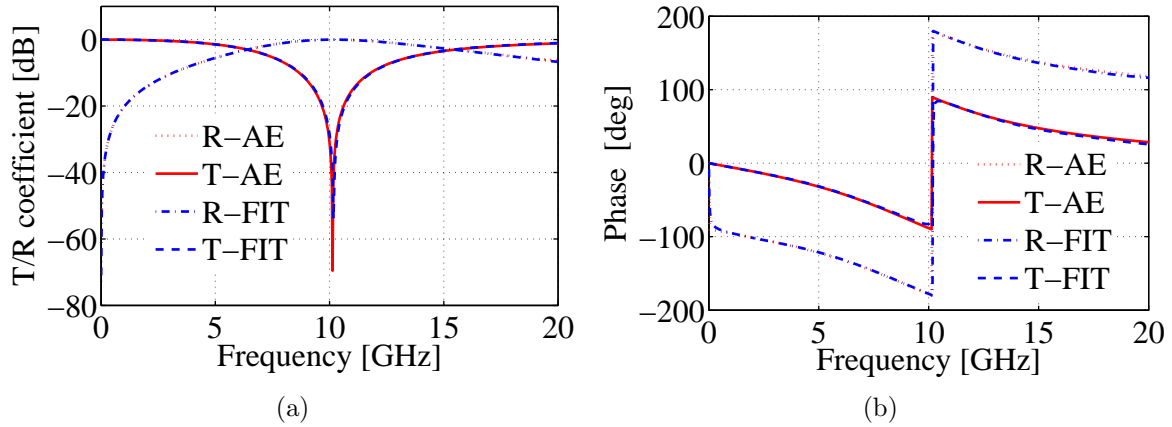


**Figure 7.4.** Magnitude (a) and phase (b) of reflection (R) and transmission (T) coefficients as a function frequency for the square loop Array #1 of Table 7.1 at normal incidence,  $\theta = \varphi = 0^\circ$ .

The frequency response of the FSS is affected by the polarization of the incident plane wave (TE, TM) and by its angle of incidence ( $\theta$ ,  $\varphi$ ). The main advantage of the presented equivalent circuit model is that it offers the capability of deriving expressions for predicting the behavior of the reflection/transmission coefficients for different polarizations and for an oblique angle of incidence, up to an angle of incidence of 45 degrees [119]. To demonstrate that the equivalent circuit model can accurately predict

the reflection and the transmission coefficients for different angles of incidence and for different polarizations, the square loop array # 2 presented in Table 7.1 is investigated. The frequency response is calculated with the aid of the presented analytical expressions and is compared to the results obtained by CST Microwave studio. Figure 7.5 shows the magnitude (a) and phase (b) of the reflection (R) and transmission (T) coefficients as a function frequency for the square loop Array #2 of Table 7.1, for a TE incidence with  $\theta = 15^\circ$ ,  $\varphi = 0^\circ$ . The results for the same FSS are also calculated for a TM wave incidence with  $\theta = 0^\circ$ ,  $\varphi = 15^\circ$  and are plotted in Fig. 7.6, again demonstrating the validity of the AE.

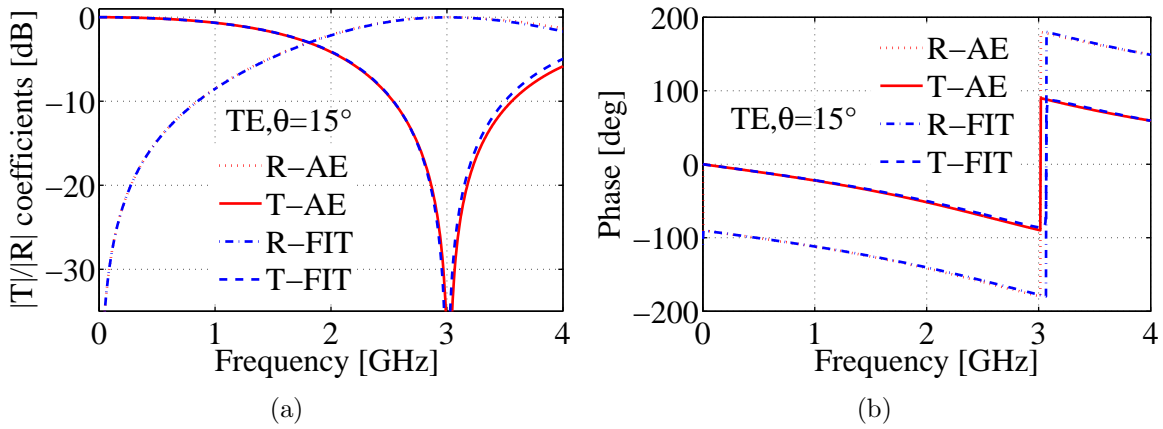


**Figure 7.5.** Magnitude (a) and phase (b) of reflection (R) and transmission (T) coefficients as a function frequency for the square loop Array #2 of Table 7.1,  $\theta = 15^\circ$ ,  $\varphi = 0^\circ$ .

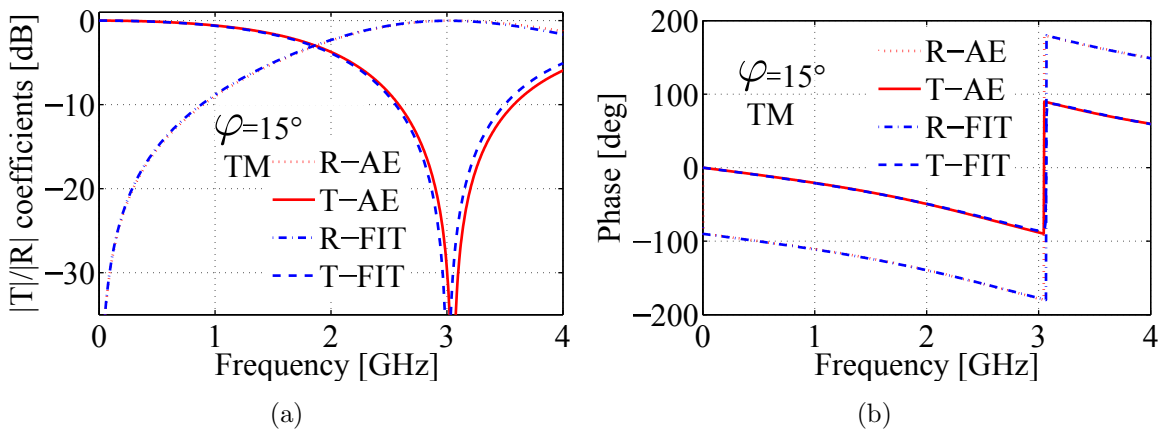


**Figure 7.6.** Magnitude (a) and phase (b) of reflection (R) and transmission (T) coefficients as a function frequency for the square loop Array #2 of Table 7.1,  $\theta = 0^\circ$ ,  $\varphi = 15^\circ$ .

We conclude with a final example, wherein we look at the FSS #2 in Table 7.1 for an

angle of incidence,  $\theta = 45^\circ$ , and  $\varphi = 0^\circ$ . The reflection and the transmission coefficients are calculated using the equivalent circuit model and are compared with the results obtained by the FIT with the aid of CST Microwave Studio. Figure 7.7 shows the magnitude (a) and phase (b) of reflection (R) and transmission (T) coefficients as a function frequency for the square loop Array #2 of Table 7.1 at  $\theta = 45^\circ$ , and  $\varphi = 0^\circ$ .

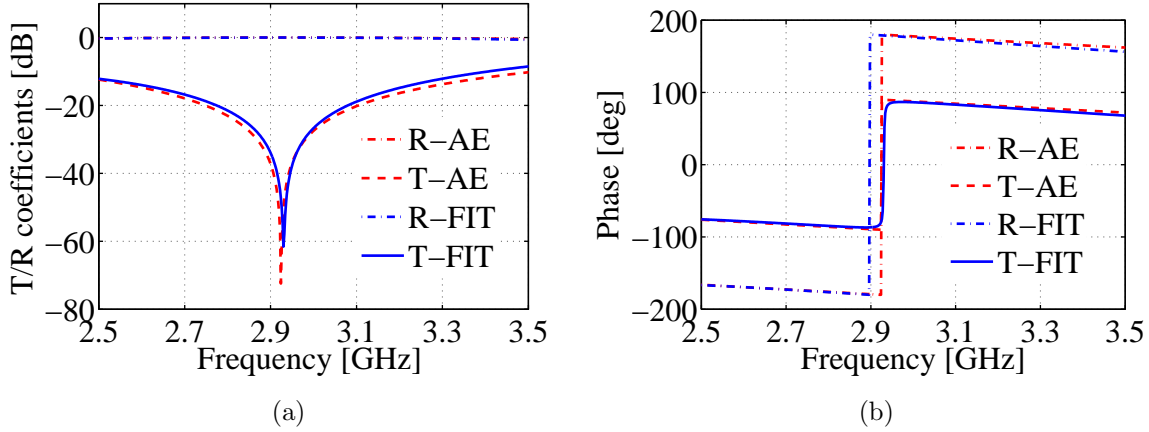


**Figure 7.7.** Magnitude (a) and phase (b) of reflection (R) and transmission (T) coefficients as a function frequency for the square loop Array #2 of Table 7.1 at  $\theta = 45^\circ$ , and  $\varphi = 0^\circ$ .

It is observed from Figs. 7.4-7.7 that the equivalent circuit model can predict the reflection and the transmission coefficients for a square loop FSS for different polarization and for different angles of incidence, with a frequency shift in the transmission and reflection coefficients less than 5%.

## 7.2.2 Effect of the Supporting Dielectric Substrate

The effect of the dielectric substrate that is carrying the array elements was discussed in [121–123]. For thin dielectric layers the value of the unit-cell capacitance, see Fig. 7.3(b), varies as a function of dielectric thickness  $t$ . A value of the effective permittivity  $\varepsilon_{eff}$ , which will be used instead of the substrate permittivity  $\varepsilon_r$ , is calculated via an iterative procedure for thin dielectric substrates in [121]. The expression depends on both  $\varepsilon_r$  and  $t$  and the resulting effective permittivity can be included in the equivalent circuit model by multiplying the susceptance  $B_C$  (Eq. (7.3)) by this effective permittivity. The expression of the effective permittivity ( $\varepsilon_{eff}$ ) is obtained as:

$$\varepsilon_{eff} = \varepsilon_r + (\varepsilon_r - 1) \cdot \left[ \frac{-1}{e^{x \cdot N}} \right], \quad (7.10)$$

where

$$x = 10 \cdot t/p. \quad (7.11)$$

$t$  is the thickness of the substrate,  $p$  is the periodicity and  $N$  is an exponential factor that depends on the geometry of the unit cell. For square loop arrays,  $N$  is approximately 1.8 [121]. For the square loop FSS the value of the susceptance is, therefore, modified as:

$$B_C = 4 \cdot \varepsilon_{eff} \cdot \frac{1}{Z_0} \left( \frac{d}{p} \right) F(p, g, \lambda). \quad (7.12)$$

To investigate the effect of the dielectric substrate, the resonant frequency ( $f_0$ ), which is the transmission resonance frequency, is calculated by the equivalent circuit model and by FIT. The results are plotted as a function of thickness variation in Fig. 7.8(a) and as a function of substrate permittivity in Fig. 7.8(b).

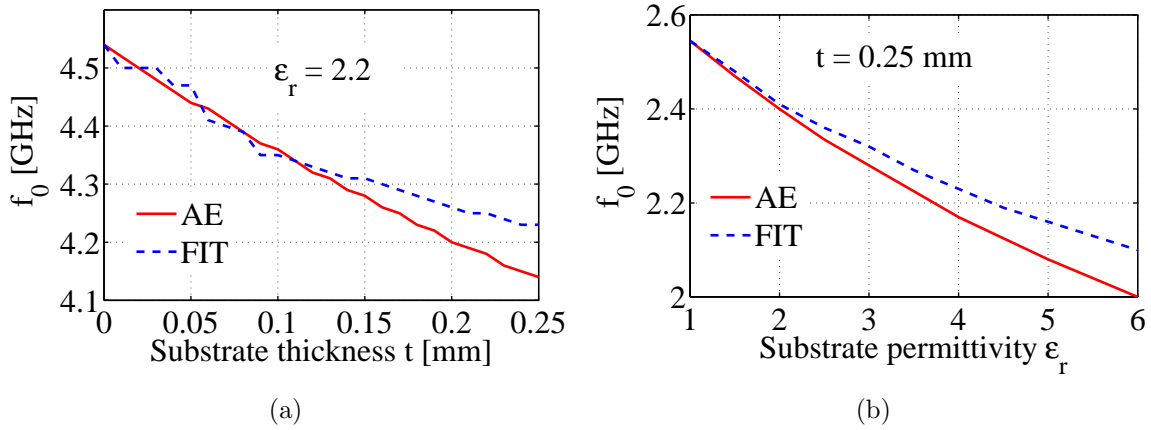


**Figure 7.8.** (a) Transmission resonance frequency as a function of substrate thickness  $t$  for the square loop Array #3 of Table 7.1. (b) Transmission resonant frequency as a function of substrate permittivity  $\varepsilon_r$  for the square loop Array #4 of Table 7.1. Both curves are calculated using the analytical equations (AE) and the Finite Integration Technique (FIT) at normal incidence.  $\theta = \varphi = 0^\circ$ .

It is shown in the figures that the deviations between the presented analytical expressions and the Finite Integration Technique increases with increasing the substrate thickness (see Fig. 7.8(a)) and with increasing the substrate permittivity (see Fig. 7.8(b)). The relative difference error in the resonant frequency ( $f_0$ ) between FIT and AE is calculated for a substrate thickness of 0.25 mm and  $\varepsilon_r = 2.2$  (see Fig. 7.8(a)) and for a substrate permittivity of  $\varepsilon_r = 6$  and a substrate thickness of 0.25 mm (see Fig. 7.8(b)) as are 2.12 % and 4.7 %, respectively.

Since the relative difference in the the resonant frequency ( $f_0$ ) between FIT and AE less than 5%, then the results of the analytical expressions are considered to be accurate for a substrate thickness less than 0.25 mm and substrate permittivity  $\varepsilon_r$  between  $1 \leq \varepsilon_r \leq 6$ .

Since the equivalent circuit model is most accurate for a thin and low permittivity sub-

strate, for the fabricated RF power harvester a substrate thickness of 0.125 mm with a relative permittivity equal to 3.0 is chosen.

Having established the validity of the analytical expressions, we now proceed with the investigation of a gridded square-loop FSS. The addition of the grid to the loops is crucial for RF power harvesting since the diodes will be integrated in the grid.

## 7.3 Gridded Square Loop FSS

The frequency selective surface that will be used to harvest RF power is the gridded square-loop FSS (see Fig. 7.2(a)). A grid is added to the square-loop FSS introduced in the previous section. The main advantage of this structure is that, when it is loaded with rectifiers, the grid will direct the DC current to the collection point. Moreover, it provides additional physical parameters (width of the grid and grid-loop separation) that can be tuned to control the response of the FSS.

### 7.3.1 Equivalent Circuit Model

The equivalent circuit model introduced in the previous section is extended for the grid to predict the transmission and the reflection band behaviour for a Gridded Square-Loop (GSL) FSS. The FSS unit cell of the GSL-FSS is shown in Fig. 7.9(a).

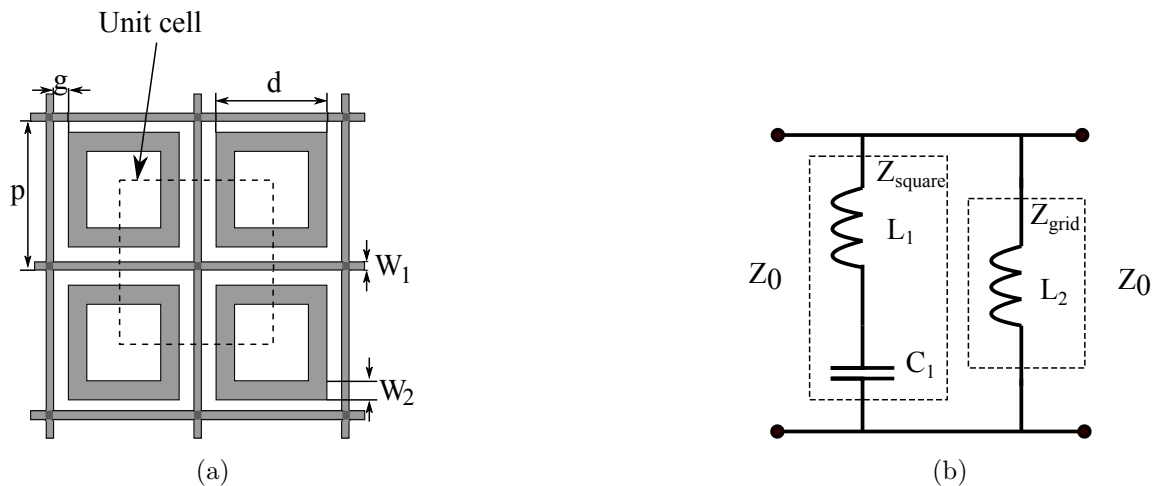


**Figure 7.9.** Unloaded (i.e. without diodes) gridded square loop configuration (a) and its unit cell equivalent circuit model (b).

In Fig. 7.9(a),  $p$  is the periodicity,  $g$  is the gap width between the grid and the square loop,  $W_1$  is the strip width of the grid and  $W_2$  and  $d$  are the strip width and the

length of the square loop, respectively. The equivalent electric circuit model introduced in [119, 124] is shown in Fig. 7.9(b).  $Z_{fss}$  is the equivalent FSS unit cell impedance and is derived by considering two impedances in parallel:

$$Z_{fss} = \frac{Z_{grid} Z_{square}}{Z_{grid} + Z_{square}}. \quad (7.13)$$

$Z_{square}$  is the square-loop impedance and is given by:

$$Z_{square} = j \left( X_1 - \frac{1}{B_1} \right), \quad (7.14)$$

$Z_{grid}$  is the grid impedance given by:

$$Z_{grid} = jX_2, \quad (7.15)$$

where [119]

$$X_1 = 2Z_0 \left( \frac{X_2 X_3}{X_2 + X_3} \right), \quad (7.16)$$

$$X_2 = Z_0 F_{TE, TM}(p, W_1, \lambda), \quad (7.17)$$

$$X_3 = Z_0 \frac{d}{p} F_{TE, TM}(p, 2W_2, \lambda), \quad (7.18)$$

$$B_1 = \frac{2}{Z_0} \cdot \epsilon_{eff} \cdot \left( \frac{d}{p} \right) F_{TE, TM}(p, g, \lambda). \quad (7.19)$$

$F_{TE, TM}(p, g, \lambda)$  is a function of the incident angles  $\theta$  and  $\varphi$  and depends on whether a TE incidence or TM incidence or if a combination of the two occurs.  $F_{TE, TM}(p, g, \lambda)$  is calculated by using Eq. (7.4) to Eq. (7.7). Again, The FSS is supposed to be positioned in the xy-plane of a rectangular xyz coordinate system.

### 7.3.2 Model Verification and Waveguide Simulator Measurements

In this section, the equivalent circuit model presented in the previous section is tested by full-wave simulations and by measurements. The reflection and the transmission coefficients of a Gridded Square-Loop (GSL) FSS possessing the following dimensions:  $p = 5.05$  mm,  $d = 3.7$  mm,  $g = 0.6$  mm,  $W_1 = 0.15$  mm,  $W_2 = 0.15$  mm, are calculated by using the equivalent circuit model and the Finite Integration Technique. The GSL-FSS is positioned on a 0.027 mm thick substrate ( $t = 0.027$  mm) having a relative

permittivity of  $\epsilon_r = 3.0$ . Fig. 7.10 shows the magnitude (a) and the phase (b) of the reflection (R) and transmission (T) coefficients as a function frequency for the gridded square-loop array calculated by the FIT and by the Analytical Expressions (AE) for a TE incidence with  $\theta = 0^\circ$ , and  $\varphi = 0^\circ$ .

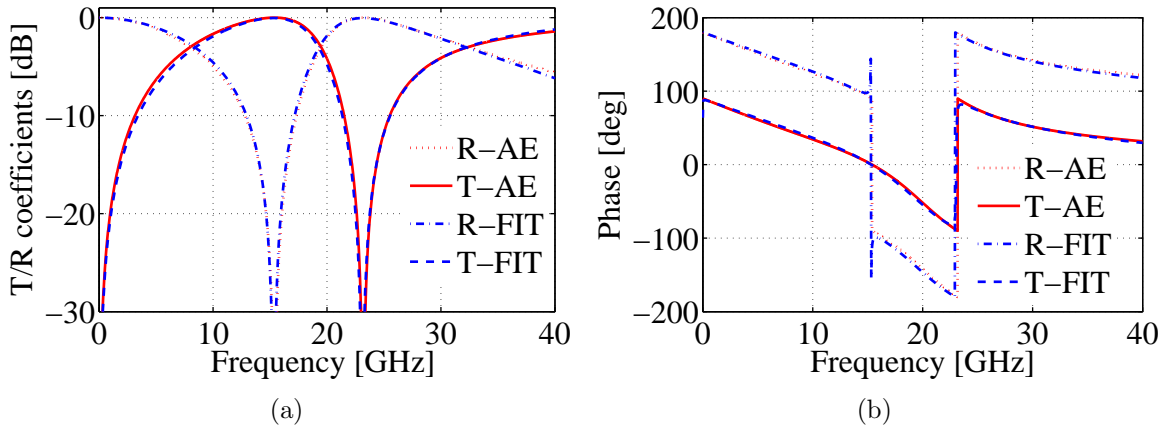


**Figure 7.10.** Magnitude (a) and phase (b) of reflection (R) and transmission (T) coefficients as a function frequency for a gridded square loop array with  $p = 5.05$  mm,  $d = 3.7$  mm,  $g = 0.6$  mm,  $W_1 = 0.15$  mm,  $W_2 = 0.15$  mm,  $t = 0.027$  mm,  $\epsilon_r = 3.0$ . TE incidence with  $\theta = 0^\circ$ , and  $\varphi = 0^\circ$ .

To validate the accuracy of the analytical expressions with measurements, the waveguide-simulator technique is used [125]. The reflection and transmission coefficients versus frequency for a GSL-FSS unit cell with  $d = 31$  mm,  $g = 2$  mm,  $W_1 = 1$  mm,  $W_2 = 4$  mm are calculated and compared to waveguide simulator measurements. The chosen dimensions of the FSS unit cell are dictated by the waveguide aperture used for measurements, see Fig. 7.11.

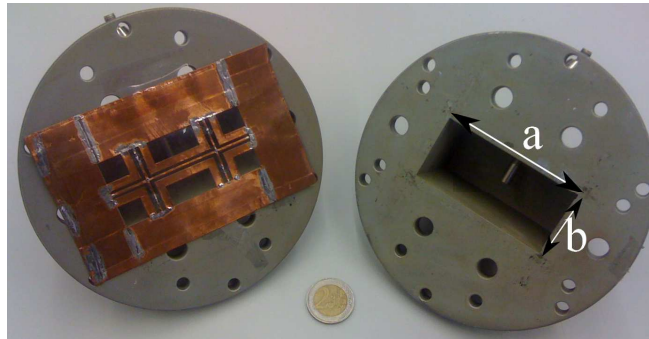


**Figure 7.11.** Waveguide used for measurements and the fabricated two unit cells matching the waveguide aperture.



The rectangular waveguide (SIVERS-LAB PM 7325 S-04) has side lengths  $a = 71.5$  mm and  $b = 34$  mm. The waveguide aperture contains two GSL-FSS unit cells. The lower and the higher cut-off frequencies of the waveguide are 2.5 GHz and 3.9 GHz, respectively. The FSS unit cell was designed to create a reflection band around 3.2 GHz.

The waveguide simulator reproduces the behaviour of an infinite array by exploiting the symmetry of a unit cell. The walls of the waveguide act like periodic boundary conditions around the elements [125]. The decomposition of the  $TE_{10}$  mode into two plane waves in a rectangular waveguide having the widest dimension  $a$  as introduced in [126] is shown in Fig. 7.12.

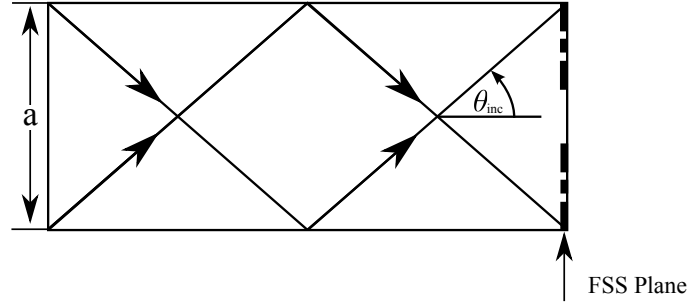


**Figure 7.12.** Decomposition of the  $TE_{10}$  mode into two plane waves in a rectangular waveguide having the widest dimension  $a$  as introduced in [126].

The incident angle  $\theta_{inc}$  on the FSS plane, of the fundamental  $TE_{10}$  mode, traveling inside the waveguide, depends on: the operating frequency  $f$ , the widest dimension of the rectangular waveguide  $a$ , and the free-space speed of light  $c$ . The angle of incidence is calculated from the following expression [127]:

$$\theta_{inc} [\text{degrees}] = \frac{180}{\pi} \cos^{-1} \left( \frac{\sqrt{\left(\frac{2\pi f}{c}\right)^2 - \left(\frac{\pi}{a}\right)^2}}{\frac{2\pi f}{c}} \right). \quad (7.20)$$

From Eq. (7.20), at a frequency of 3.2 GHz, using  $a = 71.5$ mm, the incident angle on the FSS surface is  $\theta_{inc} = 41^\circ$ . It should be mentioned that, in order to fit the two fabricated unit cells in the waveguide aperture, a slight asymmetry in the fabricated unit cell is introduced. Fig. 7.13 shows the waveguide simulator setup and specifies this asymmetry.

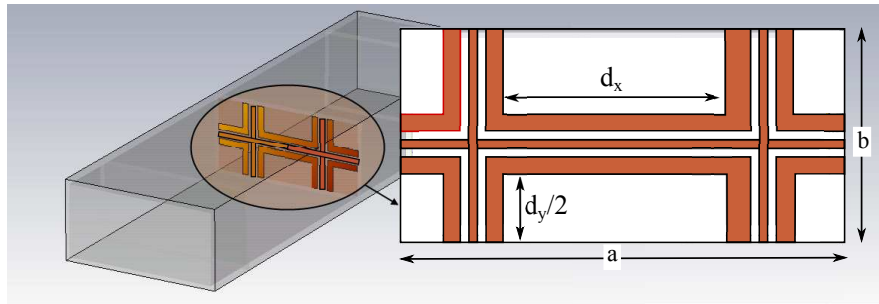


**Figure 7.13.** Waveguide simulator setup of two unit cells of a GSL-FSS array.  $d_x = 31$  mm,  $d_y = 30$  mm.

Referring to Fig. 7.13, the dimensions chosen for the fabricated GSL-FSS are  $d_y = 30$  mm and  $d_x = 31$  mm. With the introduction of the small asymmetry in the unit cell, the elements are now matching the waveguide aperture.

Figure 7.14 shows the simulated and measured magnitudes of the transmission (a) and reflection (b) coefficients as a function of frequency at an angle of incidence of  $\theta_{inc} = 41^\circ$ .

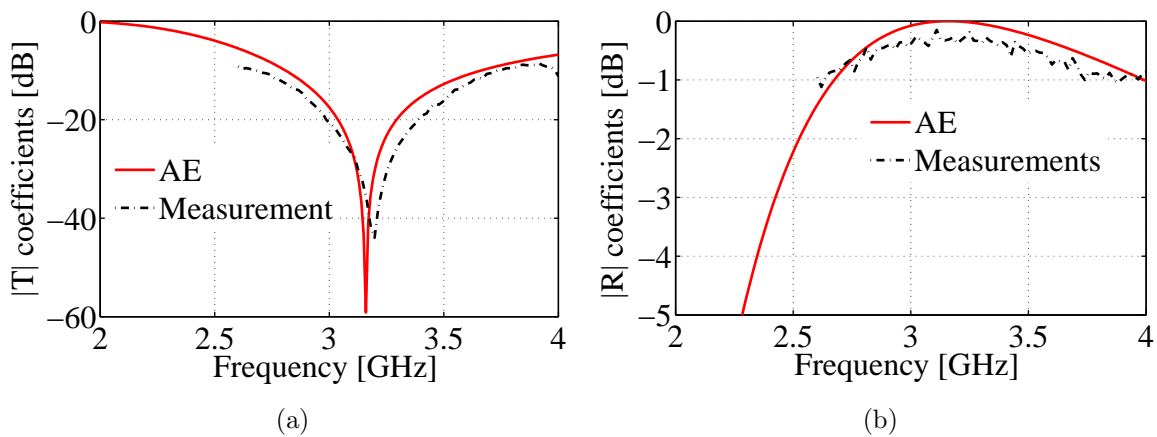


**Figure 7.14.** Magnitude of the transmission (a) and reflection (b) coefficients versus frequency for a GSL-FSS unit-cell with  $d = 31$  mm,  $g = 2$  mm,  $W_1 = 1$  mm,  $W_2 = 4$  mm. TE with  $\theta_{inc} = 41^\circ$ , as simulated with AE and measured using a waveguide simulator.

As depicted in the figure, a frequency offset exists between the measurement results and the simulated results. This frequency offset is believed to be due to the asymmetry introduced by the fabricated two unit cells in order to match the waveguide aperture. It should be mentioned that the two waveguide adapters (see Fig. 7.11) are tightly fastened to create a good galvanic contact between the unit cell edges and the waveguide walls. Referring to Fig. 7.14(a), the resonance frequency for the measured transmission

coefficient is  $F_{T_{measured}} = 3.197$  GHz, while the resonance frequency for the transmission coefficients calculated by the equivalent circuit model is  $F_{T_{AE}} = 3.16$  GHz, which results in an offset of 37 MHz. The relative difference frequency offset  $\delta$  (%) is calculated as follows:

$$\delta (\%) = 100 \left( \frac{F_{T_{measured}} - F_{T_{AE}}}{F_{T_{measured}}} \right), \quad (7.21)$$

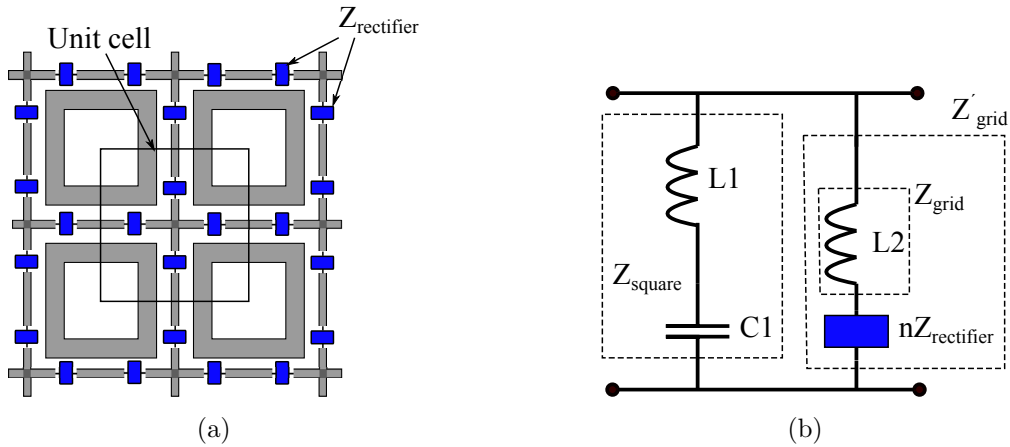
which is equal to 1.15 %. Since the relative difference frequency offset  $\delta$  (%) is less than 5 %, the equivalent circuit model is considered to be accurate and will be extended in the following section for the insertion of lumped elements.

## 7.4 Loaded Gridded Square-Loop FSS

The basic principle of creating a RF frequency selective surface harvester is to insert diodes in the grid. By resonating the FSS and rectifying the resonating RF currents, DC power is obtained. The harvested DC current is collected at the DC collection lines as shown in Fig. 7.2(a). In this section, the equivalent circuit model introduced in the previous section will be extended to account for the rectifiers (Schottky diodes) that are inserted to the grid.

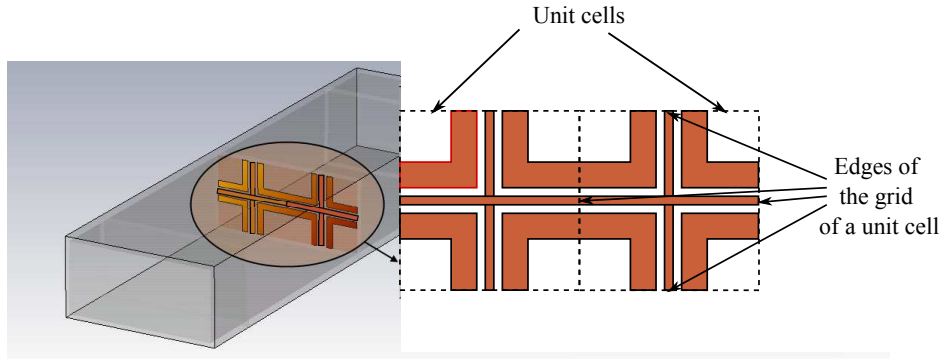
### 7.4.1 Equivalent Circuit Model

Figure 7.15(a) shows a loaded unit-cell configuration. The reason for having two rectifiers for each polarization in the unit cell as indicated in the figure will be explained further on.



**Figure 7.15.** Loaded gridded square loop configuration (a) and its unit cell equivalent electric circuit model (b).

Since the rectifiers will be integrated to the grid, the equivalent impedance of the rectifier  $Z_{rectifier}$  is placed in series with the grid impedance  $Z_{grid}$  in the equivalent unit-cell circuit, see Fig. 7.15(b). Combined, the grid impedance  $Z_{grid}$  and the rectifier's impedance  $nZ_{rectifier}$  are denoted by  $Z'_{grid}$ .  $n$  is the number of lumped elements (Schottky diodes) in the unit cell for each polarization. For the unit cell shown in Fig. 7.15(a), two lumped elements for each polarization are shown, consequently  $n$  is set to 2. It should be mentioned that in the final design one rectifier per unit cell will be used for each polarization. The reason for having two rectifiers (Schottky diodes) has to do with the practical implementation of measuring a unit cell in a waveguide simulator. The unit-cell as implemented in the waveguide simulator is indicated in Fig. 7.15(a) and is chosen in this way to prevent the creation of a lumped element between the edges of the grid and the waveguide walls. Using a single rectifier would result in needing half a rectifier in the waveguide simulator at the edges of the grid of a unit cell as indicated in Fig. 7.16.



**Figure 7.16.** Two unit cells fitting the aperture of the waveguide simulator.

It has been demonstrated in Sec. 2.2 that the equivalent impedance of a diode, at an operating frequency below 3 GHz (see Figs. 2.2, 2.3 and 2.8) and at an input power level between -20 dBm and -5 dBm (see Fig. 2.9), may be modeled (linearized) as a series R-C circuit.

For a FSS loaded with an R-C series circuit, the FSS equivalent unit-cell impedance  $Z_{fss}$  is calculated from Eq.(7.13), where the grid impedance is extended to

$$Z'_{grid} = jX_2 + nZ_{rectifier} \quad (7.22)$$

$$= n \left[ R_{rectifier} + j \left( \frac{X_2}{n} - \frac{1}{B_{rectifier}} \right) \right], \quad (7.23)$$

where  $B_{rectifier} = \omega C_{rectifier}$ ,  $\omega$  being the angular frequency. With expression 7.23 an FSS having a grid loaded with any combination of R, L and C can be analysed.

### 7.4.2 FSS Loaded with Capacitors

We start with a unit cell that is loaded with two capacitors in series with the grid inductance  $L_2$  (see Fig. 7.15(b)). Figures 7.17 and 7.18 show the transmission and reflection coefficients versus frequency respectively, for the thus loaded FSS for different capacitance values.

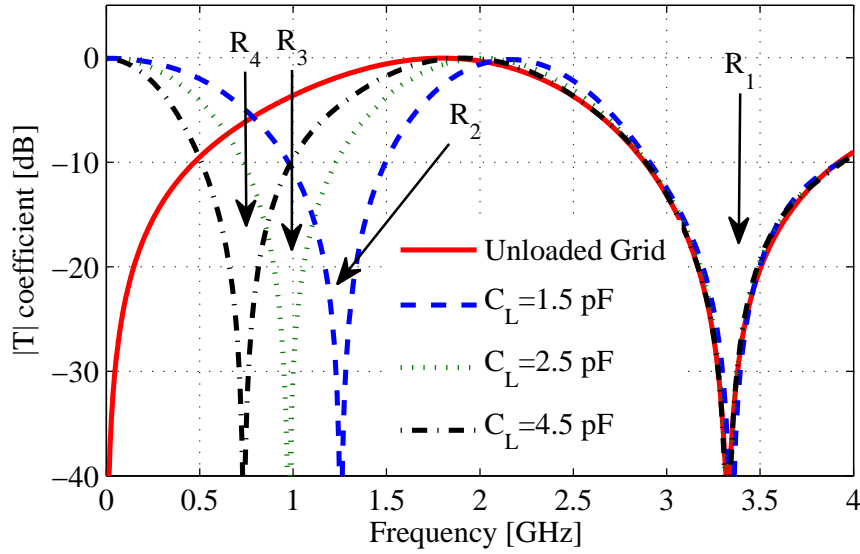


**Figure 7.17.** Magnitude of the transmission coefficients versus frequency for a gridded-square-loop unit-cell with  $d = 31$  mm,  $g = 2$  mm,  $W_1 = 1$  mm,  $W_2 = 4.5$  mm. TE with  $\theta_{inc} = 0^\circ$ .

In Fig. 7.17, the ‘Unloaded Grid’ label represents the gridded square loop investigated in Sec. 7.3. It is shown in the figure that for the unloaded grid (solid curve), only one reflection band is observed. The centre of the reflection band is indicated with  $R_1$ . This single reflection band is due to the capacitor  $C_1$  placed in series with the inductor  $L_1$  (see Fig. 7.15(b)), which creates a resonance at  $R_1$ . However, when the grid is loaded with a capacitor, for instance 1.5 pF (dashed curve) a second reflection band is generated around  $R_2 = 1.25$  GHz. Consequently the loaded FSS is characterized by two reflection bands centered around  $R_1$  and  $R_2$ . When the capacitance value is increased to 2.5 pF (dotted curve) and to 4.5 pF (dashed-dotted curve) two new reflection bands centered around  $R_3$  and  $R_4$  are created. Increasing the capacitance value thus results in a shifting of the additional reflection band to the lower frequencies. The created second resonance  $R_2$  is due to the capacitor  $C_2$  placed in series with the inductor  $L_2$  (see Fig. 7.15(b)).

From the reflection coefficients shown in Fig. 7.18, it is observed that the unloaded grid (solid curve) resonates around 1.65 GHz ( $T_1$ ). When a 1.5 pF capacitor is inserted

in the grid, the transmission band is shifted to the right to form a shifted-reflection band  $T_2$ . If the capacitance value is further increased to 2.5 pF and to 4.5 pF, the transmission band shifts back to the left toward  $T_3$  (dotted curve) and  $T_4$  (dashed-dotted curve). It is clear from the transmission and reflection bands that, when the capacitance value is further increased to a relatively high value, the loaded FSS will behave like the unloaded one, since high-valued capacitances will behave like a short circuit at the considered frequencies.

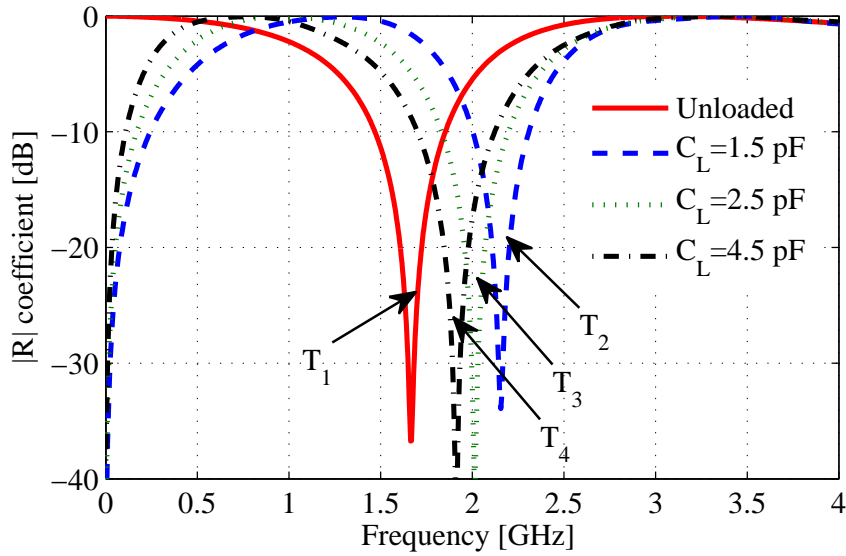


**Figure 7.18.** Magnitude of the reflection coefficients versus frequency for a gridded-square-loop unit-cell with  $d = 31$  mm,  $g = 2$  mm,  $W1 = 1$  mm,  $W2 = 4.5$  mm. TE with  $\theta_{inc} = 0^\circ$ .

A capacitively loaded GSL-FSS prototype is designed, simulated, manufactured as two slightly asymmetric unit-cells and measured. The gridded square loops are printed on a 0.125 mm thick substrate having a relative permittivity  $\epsilon_r = 3.0$  and are loaded with four 0.47 pF capacitors in total positioned in the vertical direction. Fig. 7.19 shows the calculated and the measured transmission (Fig.7.19(a)) and reflection (Fig. 7.19(b)) coefficients as a function of frequency.

It is shown in Fig. 7.19(a) that the first resonance in the transmission coefficients around the centre of the reflection band  $R_1$  is predicted by the analytical expressions. A slight deviation is observed between the results of the analytical expressions and the measured results, which is believed to be due to the asymmetry introduced in the manufactured unit cells to fit the waveguide aperture. However, for the second resonance centered around  $R_2$ , which is due to the capacitive load introduced in the grid, a large difference is observed in the centre frequency between the simulated and

the measured results for a capacitive load of 0.47 pF. A similar shift is observed in the transmission resonance shown in Fig. 7.19(b). This difference in the centre frequency of the measured responses is within the tolerance of the capacitor used for measurements ( $\pm 0.25$ pF) [128]. Within the tolerance value of the measured capacitor, it is shown in the same figures that for a capacitive load of 0.57 pF, the results of the analytical expressions match the measured results more closely.

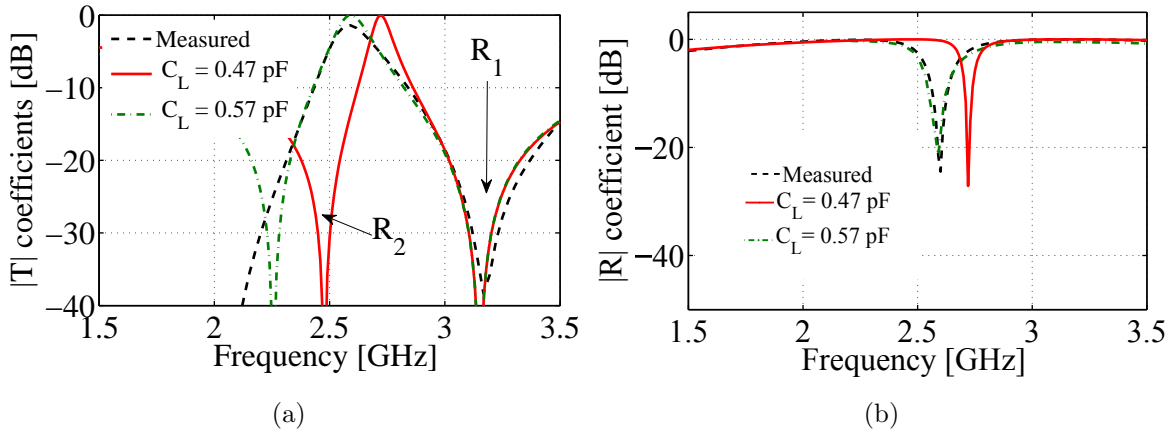


**Figure 7.19.** Magnitude of the transmission (a) and reflection (b) coefficients versus frequency for a capacitively loaded GSL-FSS simulated using the presented analytical expressions and measured using the waveguide simulator.  $d = 31$  mm,  $g = 2$  mm,  $W_1 = 1$  mm,  $W_2 = 4$  mm. TE with  $\theta_{inc} = 41^\circ$ ,  $C_L = 0.47$  pF.

With the design strategy and the analytical expressions considered to be sufficiently validated, we now proceed to the design of a RF power harvesting FSS.

## 7.5 FSS Power Harvesting - Final Design

For the validation of the new concept, only harvesting power from a vertically polarized wave is considered since this simplifies the measurement setup. Consequently, the Schottky diodes are only placed in the vertical direction. At an operating frequency of 1GHz, the impedance of the diode is calculated for different  $P_{in}$  from the analytical expressions presented in Sec. 2.2. This impedance corresponds to an equivalent series circuit of a resistor and a capacitor. For an input power level  $P_{in}$  between  $-14$  dBm  $\leq P_{in} \leq -5$  dBm the real part  $R$  of the input impedance and the capacitive part  $C$  are shown in Table 7.2.

**Table 7.2.** Real and capacitive parts of the HSMS-2820 Schottky diode as a function of input power level. The operating frequency is 1 GHz.

$P_{in}$ [dBm]	$R$ [ $\Omega$ ]	$C$ [pF]
-14	5.66	1.17
-11	6.322	1.18
-8	10.85	1.19
-5	39.73	1.21

The rectifier's equivalent impedance is used in the equivalent circuit model introduced in the previous section to predict the reflection and the transmission behavior as a function of frequency. The reflection and the transmission bands will be used as the RF power harvesting bands. The parameters of the GSL-FSS are optimized for the new reflection band introduced by the loading ( $R_2$  see Fig. 7.20(a)) to resonate around 1 GHz. Figure 7.20 shows the magnitude of the transmission (a) and reflection (b) coefficients as a function of frequency for the final GSL-FSS design for different RF input power levels. For every input power level the corresponding rectifier's impedance as stated in Table 7.2 is used. The equivalent circuit model is used for simulations.

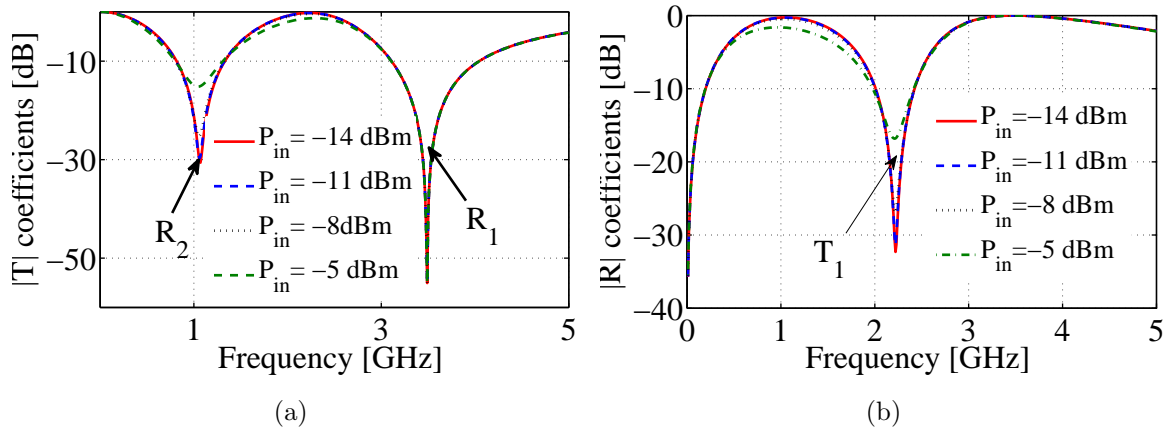
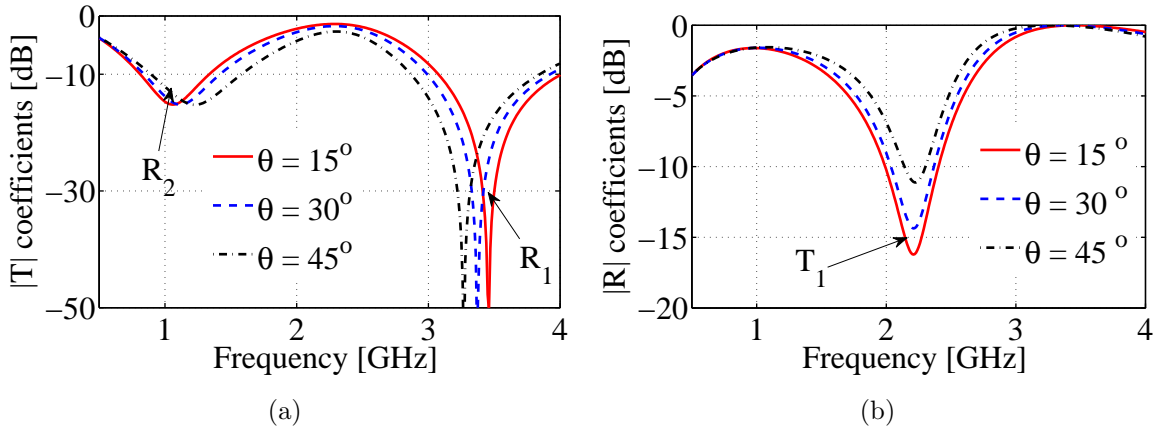


**Figure 7.20.** Magnitude of the transmission (a) and reflection (b) coefficients versus frequency for different  $P_{in}$ , TE incident wave  $\theta_{inc} = 0^\circ$ . The optimized parameters (see Fig. 7.9(a)) are  $d = 31$  mm,  $g = 2.5$  mm,  $W_1 = 2$  mm, and  $W_2 = 5$  mm.

The Figures (Figs. 7.20(a) and 7.20(b)) show that for an input power level increasing from  $-14$  dBm to  $-5$  dBm the amplitudes of the transmission and reflection coefficient at resonances decrease a bit. Up to  $-8$  dBm the values stay more or less constant. This is due to the large increase of the real part of the rectifier's impedance at higher power levels, see Table 7.2. The centre of frequency bands  $R_1$  and  $R_2$ , do not shift for both transmission and reflection bands, which makes the system more robust for different power levels. The main reason for choosing the commercially available Schottky diode



HSMS 2820 is its low resistive part of the input impedance at low input power levels. To investigate the effect of the direction of arrival (DoA) of the incident wave, the equivalent circuit model for the loaded GSL-FSS unit cell is used to calculate the reflection and the transmission coefficients for different angles of incidence for a TE polarized wave. The input impedance of the rectifier (see Table 7.2) at an input power level of  $-5$  dBm ( $R = 39.73\Omega$ ,  $C = 1.21$  pF) is used in the simulations. Figures 7.21(a) and 7.21(b) show the reflection and the transmission coefficients as a function of frequency for different angles of arrival.



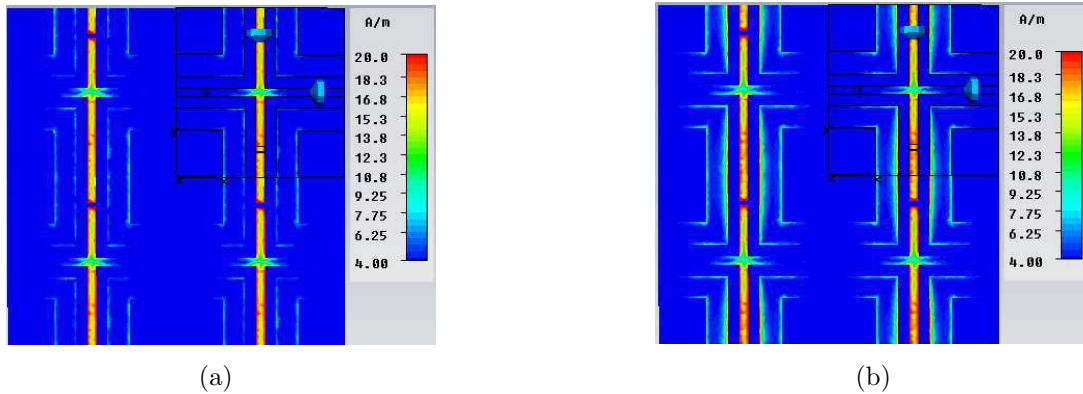
**Figure 7.21.** Magnitude of the transmission (a) and reflection (b) coefficients versus frequency for different incident angles for  $P_{in} = -5$  dBm. The optimized parameters (see Fig. 7.9(a)) are  $d = 31$  mm,  $g = 2.5$  mm,  $W_1 = 2$  mm, and  $W_2 = 5$  mm.

Figure 7.21(a) shows that the centre of first reflection band ( $R_1$ ) shifts to the left (lower frequencies) when the incident angle increases, while the centre of the second reflection band ( $R_2$ ) shifts to the right. Fig. 7.21(b) shows that the magnitude of the transmission coefficients increases when the angle of incidence increases. Considering  $-10$  dB as a threshold for the reflection and the transmission coefficients amplitude, one can conclude from the figures that for an incident angle less than  $45^\circ$ , the reflection and the transmission resonance frequencies stay within the required threshold. Thus for the Schottky diode (HSMS-2820), and for an input power level increasing from  $-15$  dBm to  $-5$  dBm, the reflection and the transmission frequency bands are robust (i.e. will not be affected) for different angles of incidence.

### 7.5.1 FSS Current Density

To visualize the resonance phenomena, Figs. 7.22(a) and 7.22(b) show the magnitude of the surface current distribution at the centre of the reflection frequency band (1 GHz) (a) and at the centre of transmission frequency band (2.2 GHz) (b), simulated with CST

Microwave Studio. It is clear that for a normal incident, TE polarized wave ( $\theta_{inc} = 0^\circ$ ), the current density is concentrated in the grid and not in the loops, which is desired for power harvesting since the diodes are integrated in this grid. We will validate the possibility to harvest power at the centre of the reflection band ( $R_2 = 1$  GHz).



**Figure 7.22.** Magnitude of the surface current distribution at the centre of the reflection band  $R_2 = 1$  GHz (a) and at the centre of the transmission band  $T_1 = 2.2$  GHz (b). The GSL FSS dimensions are:  $d = 31$  mm,  $g = 2.5$  mm,  $W_1 = 2$  mm and  $W_2 = 5$  mm. TE with  $\theta_{inc} = 0^\circ$

Since, for the designed GSL-FSS, the maximum surface current density is concentrated in the grid, and the simulations indicate that the GSL-FSS is robust for different input power levels and for different angles of incidence (see Figs. 7.20 and 7.21), two gridded square loop frequency selective surfaces have been manufactured and tested. The first prototype is a  $3 \times 3$  gridded square-loop FSS. The second prototype is a  $5 \times 5$  gridded square-loop FSS. Both prototypes are shown in Fig.7.23.

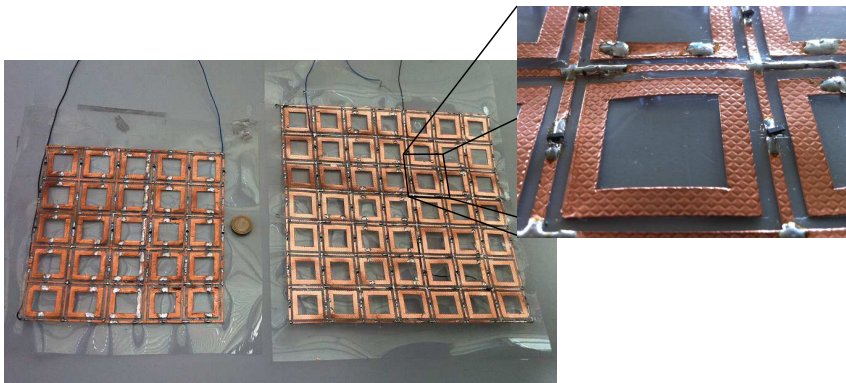


**Figure 7.23.** Manufactured  $3 \times 3$  and  $5 \times 5$  prototypes with  $d = 31$  mm,  $g = 2.5$  mm,  $W_1 = 2$  mm and  $W_2 = 5$  mm. Inset showing the soldered diodes in more detail.

As is shown in the figure, both designs are surrounded by a ring of unloaded unit cells to preserve the FSS properties i.e. the coupling between the elements. Both prototypes are printed on a 0.125 mm thick substrate having a relative permittivity equal to 3.0.

## 7.5.2 RF-Power Transport Measurement Results

The manufactured prototypes are loaded with Schottky diodes, 12 Avago HSMS-2820 [43] diodes for the  $3 \times 3$  FSS and 30 diodes for the  $5 \times 5$  FSS. The diodes are placed in the vertical direction to harvest power from TE polarized incident waves. The DC output voltage is measured across an open circuit ( $R_L = \infty$ ) and across a  $1 \text{ k}\Omega$  resistor ( $R_L = 1 \text{ k}\Omega$ ) connected to the top-left and bottom-right corners with the aid of the DC collection lines as shown in Fig. 7.2(a).

The power density  $S_{RF}$  available at a distance  $R$  from a transmitter with a transmitted power  $P_t$  and antenna transmit gain  $G_t$  is:

$$S_{RF} = \frac{P_t G_t}{4\pi R^2} \quad (7.24)$$

The RF power captured by the FSS surface  $P_{RF}$  is assessed using the following equation,

$$P_{RF} = S_{RF} A_{Physical}, \quad (7.25)$$

where  $A_{Physical}$  is the physical area of the manufactured prototypes. Actually  $P_{RF} = S_{RF} A_e$ , where  $A_e$  is the effective area of the FSS. The physical area will in general be larger than the effective one. By approximating  $A_e$  by  $A_{Physical}$ , we will ensure a conservative assessment of the RF-to-DC power conversion efficiency. The physical area is calculated as follows:  $A_{Physical} = ((M + 1)p + g + W_1)^2$  (see Fig. 7.9(a)), where  $M$  is the number of active cells in the grid.  $M = 3$  for the  $3 \times 3$  FSS and  $M = 5$  for the  $5 \times 5$  FSS.

The RF-to-DC Power Conversion Efficiency (PCE) is then defined as:

$$\eta_{RF/DC} = \frac{V_{out}^2}{R_L} \cdot \frac{1}{P_{RF}}, \quad (7.26)$$

where  $V_{out}$  is the measured output voltage across the load resistance  $R_L$ . Figure 7.24 shows the open-circuit output voltage (a) and the output voltage across a  $1 \text{ k}\Omega$  load (b) as a function of power density available at the FSS surface. It is observed from Fig. 7.24 that both prototypes ( $3 \times 3$  and  $5 \times 5$ ) are able to produce an open-circuit output voltage higher than 1V at an available power density larger than  $1 \mu \text{ W/cm}^2$ .

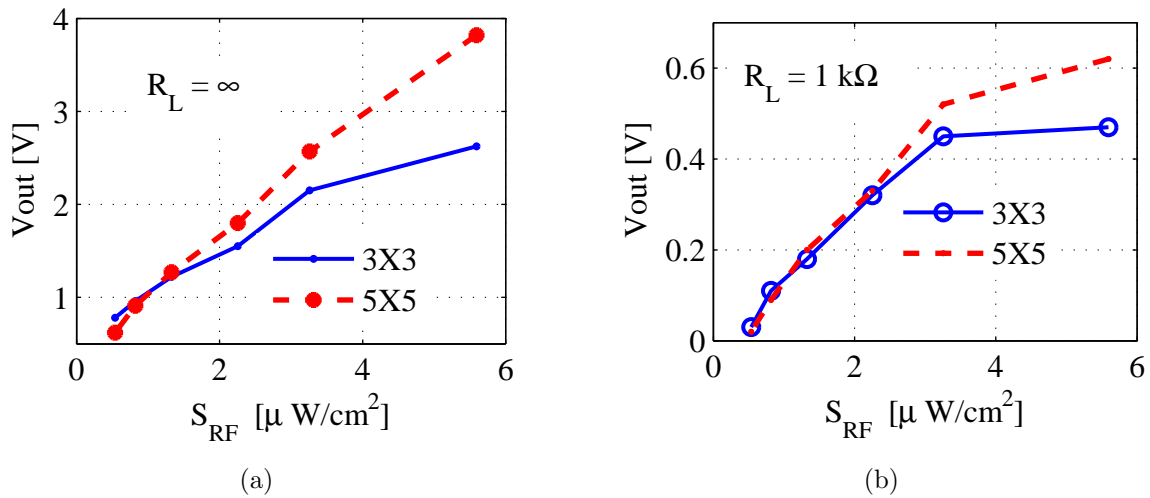


**Figure 7.24.** Measured open circuit output voltage (a), and output voltage across  $1\text{ k}\Omega$  load (b) as a function of the power density  $S_{RF}$ .

Figure 7.25 finally shows the calculated RF-to-DC power conversion efficiency as a function of the input power density. It is shown in the figure that the  $3 \times 3$  fabricated FSS prototype is more efficient than the  $5 \times 5$  fabricated FSS prototype. The maximum RF-to-DC conversion efficiency for both prototypes is found at an available power density of  $3.2\text{ }\mu\text{W}/\text{cm}^2$ , and is equal to 25% for the  $3 \times 3$  prototype and to 16% for the  $5 \times 5$  prototype. This is believed to be due to the larger losses and due to the diode cascading saturation effect as previously noticed in Chapter 2 (see Fig. 2.15).

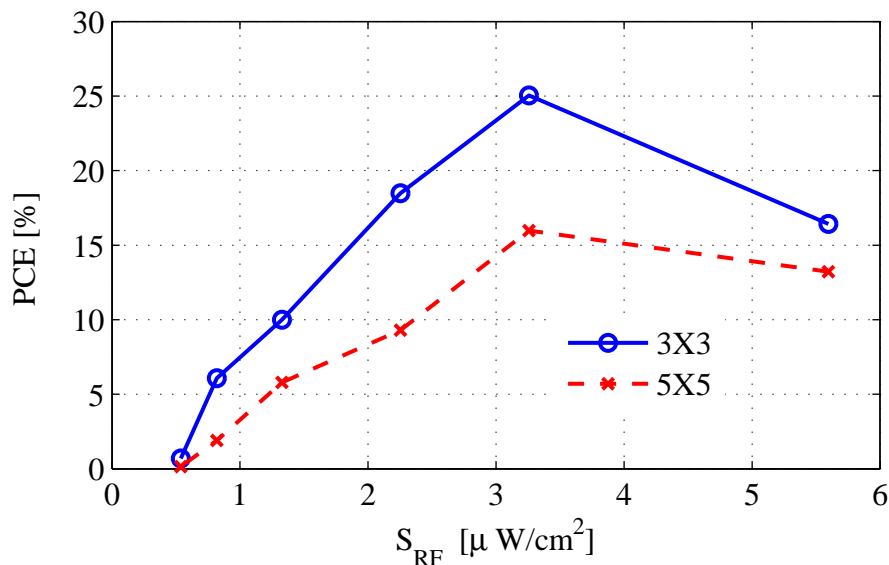


**Figure 7.25.** RF-to-DC Power Conversion Efficiency (PCE) versus the available power density ( $S_{RF}$ ).

## 7.6 Conclusions

The concept, modeling, design, realization and measurement of frequency selective surfaces to harvest RF power is demonstrated in this chapter. The resulting harvester can potentially capture arbitrarily polarized waves, at two different frequency bands, namely the transmission and the reflection bands. A simple and easy-to-implement equivalent circuit model, extended for the insertion of linear lumped components, is investigated, validated and employed for the design. A maximum RF-to-DC power conversion efficiency of 25% at  $3.2\mu\text{ W/cm}^2$  available power density is measured for a  $3 \times 3$  elements harvester. When the size of the FSS is increased to  $5 \times 5$  elements, the maximum RF-to-DC power conversion efficiency at the same power density decreases to 16 %, the reason for the decrease in the power conversion efficiency is currently under investigation. This effect is assumed to be due to the the diode cascading saturation effect. The main potential of the novel RF harvester is that it can be implemented for large area RF power harvesting applications. The novel application is suitable for an energy-harvesting glass that can be used in buildings. It could also be implemented in wall papers.

## Conclusions and Recommendations

---

This thesis addresses the analysis and design of far-field RF power harvesting devices. The potential application of this technology is envisaged in powering wireless sensors that are used in smart buildings. The ‘smartness’ is found in measuring parameters like e.g. light, temperature and presence of people and acting upon the gathered information (switching off light, turning down heating) thus saving energy consumption. Powering these sensors wirelessly is a challenge due to the restricted transmit power levels allowed. Therefore a highly efficient rectenna design is crucial. It is then important to develop accurate and easy to implement design models for rectenna subsystems, including the rectifier and the antenna. In addition, it is essential to develop a design strategy that copes with the low power density constraint.

A new design strategy has been developed. It is found that we need to optimize a rectenna for a low input power level (-10 dBm), conjugate match the antenna to the rectifier and design the rectifier circuit for a minimum real part and maximum imaginary part  $|X_{rec}| \gg |R_{rec}|$ . In implementing this design strategy, it has been found that the antenna can be miniaturized up to a level that the radiation resistance still dominates the loss resistance. Consequently, a compact and highly efficient rectenna system that is matched for a broad input power band can be designed.

An analytical model to determine the input impedance and the output voltage of a high-frequency, rectifying Schottky diode is discussed. Based on this model, the influence of the contact resistance and the saturation current on the DC output voltage is analyzed. It has been shown that a higher saturation current and/or a lower contact resistance will result in a higher output voltage. Based on these observations, the commercially available Schottky diode HSMS-2852 has been selected for the rectenna design.

## 8.1 Conclusions

The first rectenna system presented in this thesis is a  $50\ \Omega$  rectenna system, where a modified  $50\ \Omega$  Yagi-Uda antenna is introduced to realize a reasonable gain (4 dBi) over a frequency bandwidth covering the Digital Television broadcasting frequency bands (475 MHz - 794 MHz). The modified Yagi-Uda antenna is implemented in the rectenna design, using a lumped-element matching network to match the antenna impedance to the complex input impedance of a voltage doubling rectifier. The suggested  $50\ \Omega$  rectenna system shows an increased power conversion efficiency compared to state-of-the-art results reported in the open literature, see Table 8.1.

**Table 8.1.** Comparison of the  $50\ \Omega$  rectenna system with results published in the open literature that are based on commercially available discrete diodes.

Ref.	Pin [dBm]	Frequency [MHz]	Resistive Load $k\Omega$	Discrete rectifier	PCE (%)
[66]	-10	866.5	3	HSMS285C	24%
[19]	-10 -20	1800	2.4	HSMS2850	38% 15%
[67]	-10	830	$10^4$	HSMS286Y	44%
[68]	-20	850 1850	-	SMS7630	14% 13%
This work ( $50\ \Omega$ rectenna)	-10 -20	868	10	HSMS2852	49.7% 31.6%

The second rectenna system presented in this thesis deals with antenna structures intended for a direct conjugate matching to the rectifier, thus omitting an impedance matching network, that will lead to a higher power conversion efficiency (less loss) and a more compact design (fewer lumped elements). For this reason, different antenna structures are investigated that are capable of being tuned to the required complex impedance by changing some geometrical features. The validity range (length and width) of the expression for the impedance of a strip dipole antenna has been extended by deriving new fitting equations. Next, the accuracy of an existing strip-folded dipole antenna has been improved by using the improved strip-dipole antenna model. Evolving from this latter antenna, a new, electrically small antenna type has been invented that allows for tuning the complex input impedance and the radiation efficiency independently.

The new modified loop antenna is used for a rectenna design, and is co-designed with a commercially available Schottky diode based rectifier and with an integrated custom-made rectifier. Both realized rectennas demonstrate characteristics better than the state

of the art as reported in the open literature, see Tables 8.2 and 8.3.

Table 8.2 gives a short overview of the state-of-the-art results for rectennas as reported in the literature that use commercially available diodes for RF-to-DC power conversion.

**Table 8.2.** Overview of rectenna performances with commercially available diodes in the literature.

Ref.	Pin [dBm]	Frequency [MHz]	Load $R_L$ [ $\Omega$ ]	$\frac{Size}{\lambda^2}$	PCE (%)
[19]	-10 -20	1800	$2.4 \times 10^3$	-	38% 15%
[67]	-10	830	$1 \times 10^7$	0.027	44 %
[96]	-20	550	$2 \times 10^3$	0.035	18 %
[20]	0	1960	460	0.192	54 %
This work (Conjugate-complex rectenna)	-10 -20	868	$10 \times 10^3$	0.028	54.7% 33.8%

Table 8.3 gives an overview of the state-of-the-art results for rectennas as reported in the literature that use custom-made integrated rectifiers.

**Table 8.3.** Overview of rectenna performance with custom-made integrated rectifiers as reported in the literature.

Ref.	This work (Conjugate-complex rectenna)	[101]	[102]	[103]
Technology	90 nm	0.18 $\mu\text{m}$	250 nm	90 nm
Frequency	868 MHz	970 MHz	906 MHz	915 MHz
Sensitivity	-27 dBm @ 1 V	-17.7 dBm @ 0.8 V	-22.6 dBm @ 2 V	-24 dBm @ 1 V
Peak PCE (%)	36.6 @ -17 dBm	37 @ -18.7 dBm	30 @ -8 dBm	11 @ -18.83 dBm
$\frac{Size}{\lambda^2}$	0.018	0.039	0.027	-
Measured distance	27 meters @ 1.78 w	-	15meters @ 4 w	-

As a proof of principle, a complete rectenna system is presented where a commercially available power management circuit is used to power a temperature and humidity sensor. The average DC output power and the system's RF to DC conversion efficiency are measured, and compared to those measured for a commercially available rectenna



system operated under the same conditions. It is shown that the commercially available rectenna system fails to operate at low power levels ( $\leq -6$  dBm) while the presented system can operate at an RF input power level as low as  $-13$  dBm. At an input power level of  $0$  dBm, the power conversion efficiency of the commercially available system does not exceed  $19\%$ , while the power conversion efficiency of the presented system reaches  $40\%$ , resulting in more than  $20\%$  improved power conversion efficiency.

Finally, for large-area RF power harvesting applications, the concept, modeling, design, realization and measurement of frequency selective surfaces equipped with Schottky diodes to harvest RF power is demonstrated. A simple and easy-to-implement equivalent circuit model, extended for the insertion of linear lumped components, is investigated, validated and employed for the design. A  $3 \times 3$  and a  $5 \times 5$  RF harvesting FSS have been designed, fabricated and measured. An RF to DC conversion efficiency of  $25\%$  for the  $3 \times 3$  RF harvester and  $16\%$  for the  $5 \times 5$  RF harvester are measured at an incident power density of  $3.2 \mu\text{W}/\text{cm}^2$ . The novel application is suitable for an energy-harvesting glass that can be used in buildings. It could also be implemented in wall papers.

## 8.2 Recommendations

In this thesis different rectenna topologies and different methods to match the impedance of the rectifier to that of the antenna have been reported. In addition, harvesting RF power for large areas using frequency selective surfaces was introduced. Possible directions for future research include:

- **Power and data transfer:** The introduced rectenna topologies collect the RF power and convert it into DC power. From a system perspective, a second antenna is needed for communication purposes, i.e. transfer of data. A dual port antenna [129] can be used for data and power transfer, one port can be used for communication purposes and the second port can be used for RF power harvesting. Also the rectifier can be used as a matching element for the communication port [130].
- **Environment independent rectennas:** The developed antennas in this thesis are characterized for a free-space environment. However, when the antenna is brought close to a metallic ground plane, its input impedance will deteriorate due to the coupling with the antenna image. Consequently, the matching between the antenna and the rectifier will deteriorate and the power conversion efficiency will decrease. To overcome this negative effect, Metamaterial (MTM) structures can be employed to design environment independent rectennas. Adding an MTM layer between the existing antenna and the metal object may maintain the antenna matching, and enhance the radiation characteristics. The properties of the

electromagnetic band gap (EBG) will make it possible to keep the dimensions of this layer small [131].

- **RF power harvesting using Frequency Selective surfaces:** We have experimentally verified in Chapter 7 that the use of Frequency Selective Surfaces to harvest RF power is feasible. We do need to investigate the relation between size and power conversion efficiency. Further, for the RF power harvesting glass application, optical transparency is needed. An optically transparent conductive film manufactured with a silver grid layer (AgGL) is used in [109] where an antenna with a radiation efficiency better than 85% is designed and measured. The reported optical transparency is 81.3%. The same technology could be used to develop the transparent RF power harvesting glass. Ideally, printed diodes should be available to fully exploit these advantages.



# King-Middleton Second Order Method Investigation

---

## A.1 King-Middleton Second-Order Method

The King-Middleton method is an approximate solution procedure for the second order Hallen's integral equation [70]. This method introduces two empirically found fitting expressions to calculate the input impedance of a cylindrical dipole antenna. The input resistance and the input reactance are calculated using Eq. (A.1) and Eq. (A.2), respectively.

$$R(kL, \frac{a}{\lambda}) = \sum_{m=0}^4 \sum_{n=0}^4 a_{mn} (kL)^m \left(\frac{a}{\lambda}\right)^{-n}, \quad (\text{A.1})$$

$$X(kL, \frac{a}{\lambda}) = \sum_{m=0}^4 \sum_{n=0}^4 b_{mn} (kL)^m \left(\frac{a}{\lambda}\right)^{-n}, \quad (\text{A.2})$$

where  $a_{mn}$  and  $b_{mn}$  are the coefficients shown respectively in Tables A.1 and A.2 corrected as indicated in [132]. These equations are valid for:

- $1.3 \leq kL \leq 1.7$ , where  $k$  is the wave number and  $L$  is the half-length of the dipole.
- $0.0016 \leq \frac{a}{\lambda} \leq 0.01$ , where  $a$  is the dipole radius and  $\lambda$  is the wavelength.

**Table A.1.**  $a_{mn}$  coefficients to be used in Eq. (A.1) to calculate the input resistance of a cylindrical dipole antenna.

m \ n	0	1	2	3	4
0	0.484315e4	-0.475502e2	+0.237406	-0.517831e-03	0.387125e-6
1	-0.137680e5	0.134736e3	-0.671429	0.146303e-2	-0.109502e-5
2	0.147939e5	-0.144272e3	0.717576	-0.156154e-2	0.116801e-5
3	-0.716807e4	0.699523e2	-0.346901	0.753029e-3	-0.562448e-6
4	0.134303e4	-0.130631e2	0.644693e-1	-0.139347e-3	0.103804e-6

**Table A.2.**  $b_{mn}$  coefficients to be used in Eq. (A.2) to calculate the input reactance of a cylindrical dipole antenna.

m \ n	0	1	2	3	4
0	-0.644754e4	0.767385e2	-0.360563	0.709234e-3	-0.488904e-6
1	0.189983e5	-0.237542e3	0.110722e1	-0.218661e-2	0.151517e-5
2	-0.209803e5	0.267034e3	-0.124666	0.247753e-2	-0.172674e-5
3	0.102804e5	-0.131818e3	0.619050	-0.123956e-2	0.869298e-6
4	-0.188863e4	0.245077e2	-0.115922	0.233996e-3	-0.161550e-6

### A.1.1 Verification of the King-Middleton Equations by the Finite Integrating Technique

To verify the accuracy of the King-Middleton equations, CST Microwave Studio is used to calculate the impedance of a cylindrical dipole of half-length =  $L = 0.2\lambda$  and for different cylindrical radii. The results are compared with the results of the King-Middleton expressions. Fig. A.1 shows the input impedance of the cylindrical dipole antenna for a radius of 2 mm ( $\frac{a}{\lambda} = 0.002$ ,  $\lambda = 1m$ ).

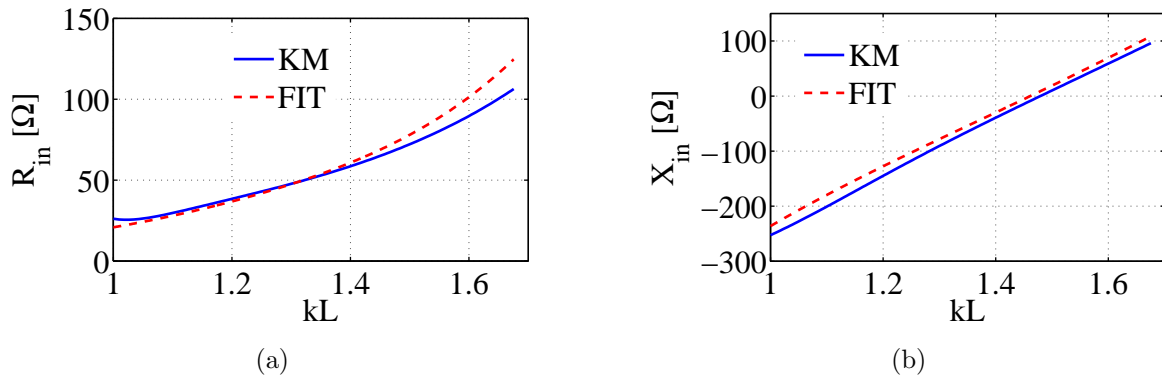


**Figure A.1.** Real (a) and imaginary (b) parts of the input impedance of a cylindrical dipole antenna calculated by the King-Middleton (KM) second order equations and by the Finite Integration Technique (FIT). Cylindrical radius = 0.002 m, ( $\frac{a}{\lambda} = 0.002$ ,  $\lambda = 1m$ ).

It is clearly indicated in the figure that the King-Middleton equations can accurately predict the impedance of a thin cylindrical dipole with less than 10 % difference between the results calculated using the presented expressions and the results calculated using the FIT.

The radius of the cylindrical dipole is increased to 6 mm ( $\frac{a}{\lambda} = 0.006$ ) and 10 mm ( $\frac{a}{\lambda} = 0.01$ ) and the input impedance is calculated using the King-Middleton equations and the Finite Integration technique. The results are plotted in Fig. A.2 for the radius of 6 mm and in Fig. A.3 for the radius of 10 mm. It is clear from the figures that when the radius of the cylindrical dipole increases, the deviations between the results of the FIT and the results of the KM expressions increase, which validates that the King-Middleton equations are most accurate for thin cylindrical dipoles ( $\frac{a}{\lambda} < 0.005$ ).

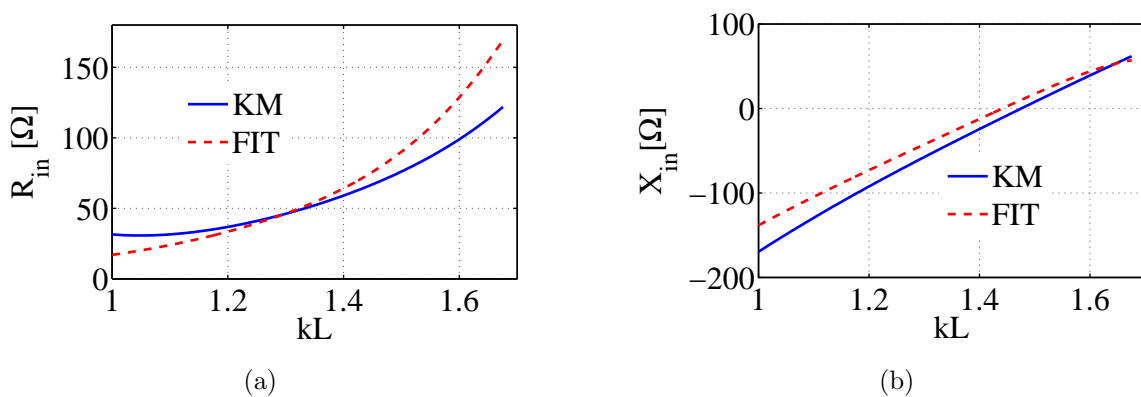


**Figure A.2.** Real (a) and imaginary (b) parts of the input impedance of a cylindrical dipole antenna calculated by the King-Middleton (KM) second order equations and by the Finite Integration Technique (FIT). Cylindrical radius = 0.006,  $\lambda = 1m$ .

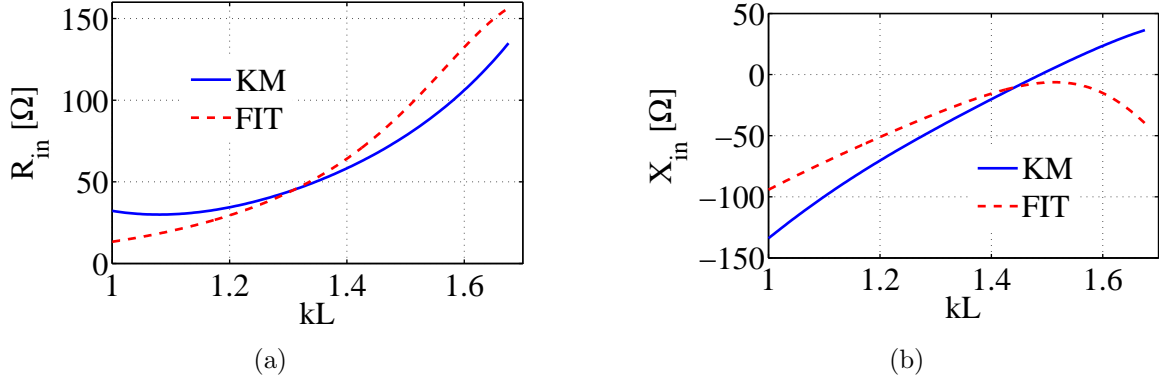


**Figure A.3.** Real (a) and imaginary (b) parts of the input impedance of a cylindrical dipole antenna calculated by the King-Middleton (KM) second order equations and by the Finite Integration Technique (FIT). Cylindrical radius = 0.01,  $\lambda = 1$ m.

## A.2 Modified King-Middleton Equations

To accurately calculate the impedance of a cylindrical dipole correction factors are introduced into the King-Middleton equations. One for both the real part and one for the imaginary part of the input impedance. The corrections are based on fitting FIT results for an antenna of different radius and length at a frequency of 300 MHz.

### A.2.1 Modified King-Middleton Equations - Real Part

The correction factor of the real part of the input impedance of a cylindrical dipole is expressed by:

$$RC(kL, \frac{a}{\lambda}) = \begin{cases} \alpha e^{\beta(\frac{a}{\lambda})} (\sum_{m=0}^4 \sum_{n=0}^4 a_{mn} (kL)^m (\frac{a}{\lambda})^{-n}) & \text{for } a < 0.008\lambda \\ \frac{1}{\gamma e^{\delta(kL)}} (\sum_{m=0}^4 \sum_{n=0}^4 a_{mn} (kL)^m (\frac{a}{\lambda})^{-n}) & \text{for } a \geq 0.008\lambda \end{cases} \quad (\text{A.3})$$

$$\text{where } \begin{cases} \alpha = 0.9204e^{(0.08023(kL))} + 2.565 \cdot 10^{-7}e^{(7.498(kL))}, \\ \beta = 35.16 \sin(3.393(kL) + 8.036), \\ \gamma = 3.657 \sin(168.7(\frac{a}{\lambda}) + 0.02044), \\ \delta = 1.004 \sin(189.8(\frac{a}{\lambda}) + 3.063). \end{cases}$$

The coefficients  $a_{mn}$  are shown in Table A.1. These modified equations have the same validity ranges as the King-Middleton equations. Fig. A.4 shows the real part of the input impedance as a function of the electrical half-length  $kL$ , for a cylindrical dipole

of half-length 0.237 m ( $L = 0.237\lambda$ ) for different dipole radii. The resistive part of the input impedance is calculated using the King-Middleton (KM) equations (solid curve), the corrected King-Middleton ( $KM_c$ ) equations (dashed-dotted curve) and the Finite Integration Technique (FIT) (dashed curve). It is clearly indicated in the figures that the results of the KM equations deviate from the result of the FIT especially when the electrical length of the cylindrical dipole increases. Moreover, it is shown that when the correction factor is introduced to the the KM equations, the results of the corrected KM ( $KM_c$ ) equations match the results of the FIT.

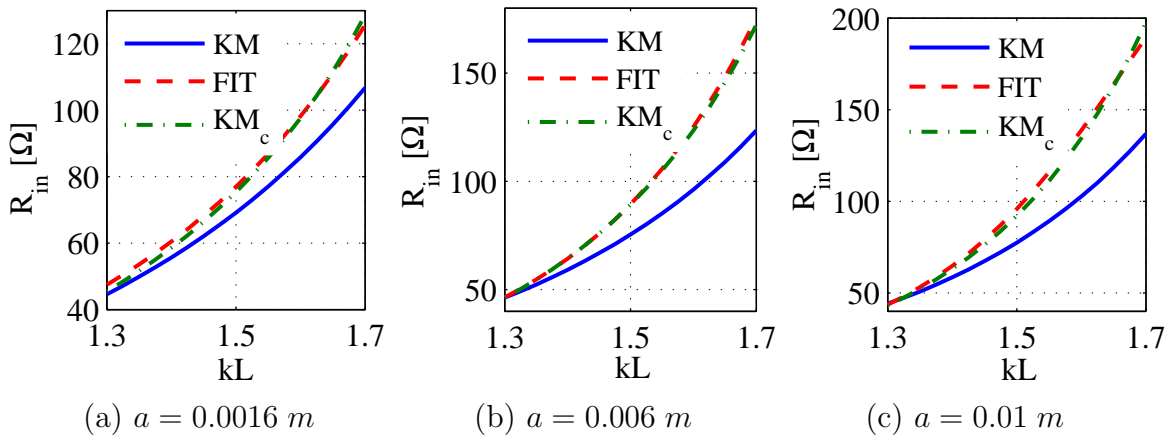


**Figure A.4.** Real part of the input impedance of a cylindrical dipole of length 0.237 m for different dipole radii calculated using the King-Middleton (KM) Method, the Finite Integration Method (FIT) and the corrected King-Middleton ( $KM_c$ ).

## A.2.2 Modified King-Middleton Equations - Imaginary Part

The modified imaginary part of the King-Middleton equation is represented in Eq. (A.4).

$$XC(kL, \frac{a}{\lambda}) = \left( \sum_{m=0}^4 \sum_{n=0}^4 b_{mn} (kL)^m \left(\frac{a}{\lambda}\right)^{-n} \right) + p_0 + p_1 \left(\frac{a}{\lambda}\right) + p_2 \left(\frac{a}{\lambda}\right)^2 \quad (\text{A.4})$$

$$\text{where } \begin{cases} p_0 &= -0.01716e^{(4.445(kL))} + 9.986e^{(0.2436(kL))}, \\ p_1 &= 9.107 \cdot 10^{+9} e^{(-12.47(kL))} + 0.6792e^{(5.894(kL))}. \\ p_2 &= -27.13e^{(6.616(kL))}. \end{cases}$$

The coefficients  $b_{mn}$  are shown in Table A.2. The imaginary parts of the input impedance of the same cylindrical dipole investigated in the previous section, for different dipole radii as a function of electrical length, are shown in Fig. A.5.

It is shown in the figure that the results of the corrected  $KM_c$  expressions overlap the results of the Finite Integration Technique, while the results of the KM expressions



clearly deviate from the results of the FIT especially for large radius cylindrical dipole. To quantify the deviations between the FIT and the KM equation in terms of power wave reflection coefficients, the Figure of Merit introduced in Sec. 1.6 will be used in the following section.

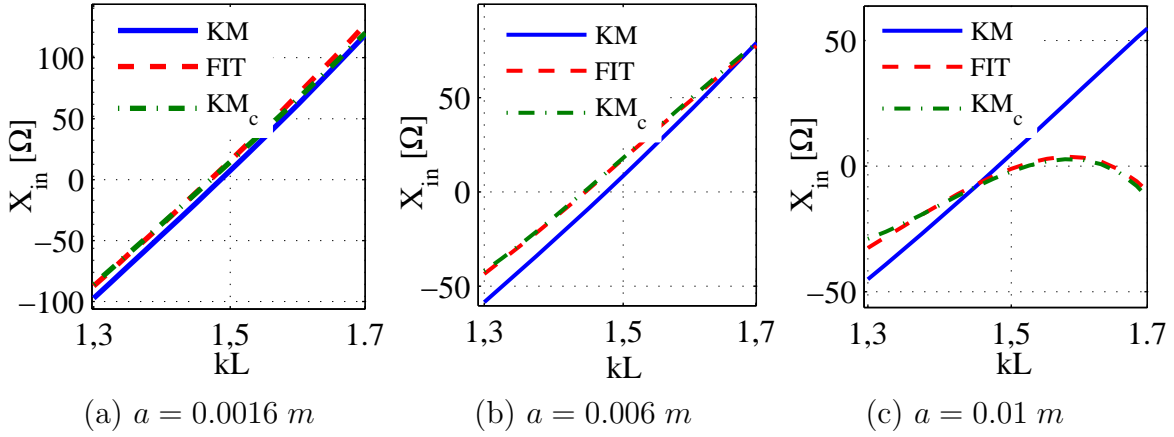


**Figure A.5.** Imaginary part of the input impedance of the dipole antenna for different dipole radii using the King-Middleton (KM) Method, Finite Integration Method (FIT) and the corrected King-Middleton ( $KM_c$ ).

### A.2.3 Comparison Between KM and Corrected KM

From Eq. (1.2), the power wave reflection coefficients due to the deviation between KM equations and FIT is calculated. Using the same equation, the deviations between the corrected  $KM_c$  and the FIT are also calculated for the results shown in Fig. A.4 and Fig. A.5. The Figure of Merit (FoM) results are shown in Fig. A.6.

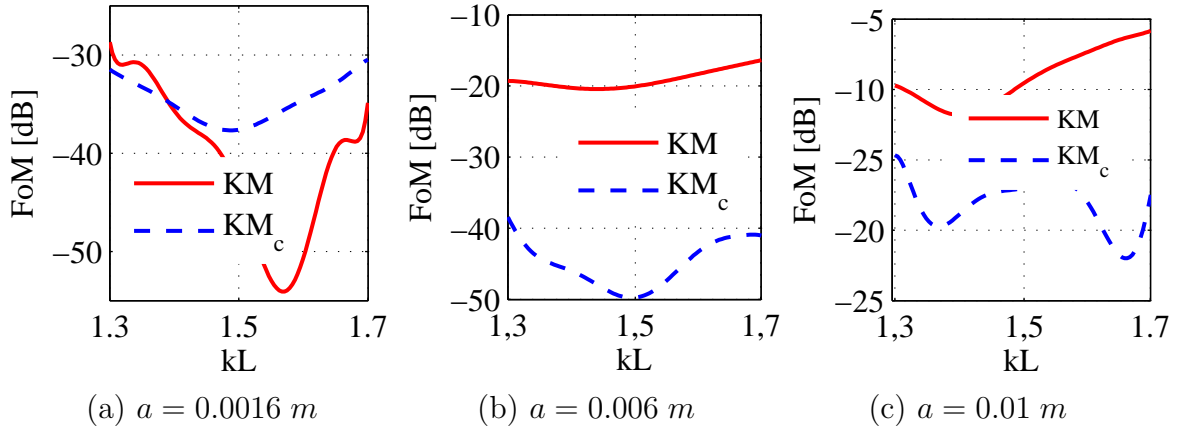


**Figure A.6.** Figure of Merit (FoM) to calculate the deviations between KM and FIT and between  $(KM_c)$  and FIT as a function of the electrical length for different dipole radii.

It is shown in the figures that the results of the  $KM_c$  expressions when compared to the results of the FIT are at least 10 dB more accurate than the KM expressions when compared to the same results (FIT) for larger dipole radii ( $a = 0.006 \text{ m}$  and  $a = 0.01 \text{ m}$ ). To validate the modified King-Middleton ( $KM_c$ ) expressions for different half-lengths, three different cylindrical dipoles are investigated where the input impedance is calculated using the KM expressions, the  $(KM_c)$ , and the FIT. Fig. A.7 shows the real and imaginary parts of the input impedance of a cylindrical dipole of half-length of 0.119 m and a radius of 2.5 mm. It is shown in the figure that the results of the  $(KM_c)$  match the results of the FIT. The same behaviour is shown in Fig. A.8 and in Fig. A.9. In Fig. A.8, the half-length is set to 8 cm, and the cylindrical radius is set to 2.5 mm. The half-length and the radius of the cylindrical dipole are decreased to 5.5 cm and 1 mm and the results of the input impedance are plotted in Fig. A.9. It is shown in the figures that the modified KM ( $KM_c$ ) expressions can accurately predict the impedance of a cylindrical dipole.

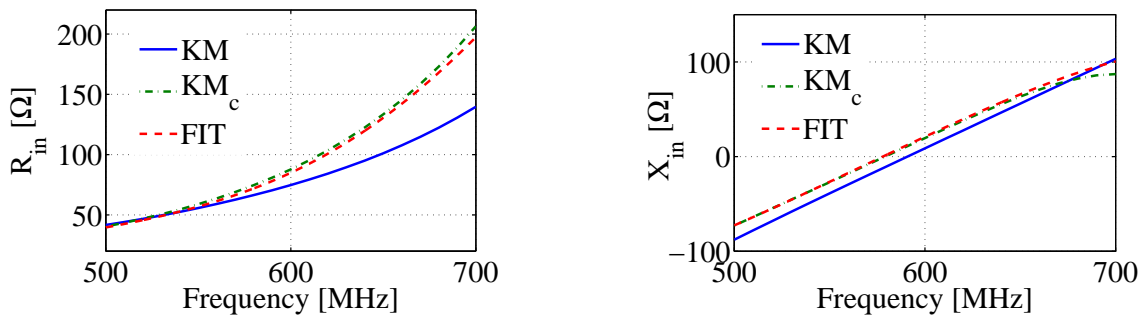


**Figure A.7.** Real and Imaginary parts of the input impedance, using King-Middleton (KM), corrected King-Middleton ( $KM_c$ ) and the Finite Integration Technique (FIT). Cylindrical length = 11.9 cm, cylindrical radius = 2.5 mm.

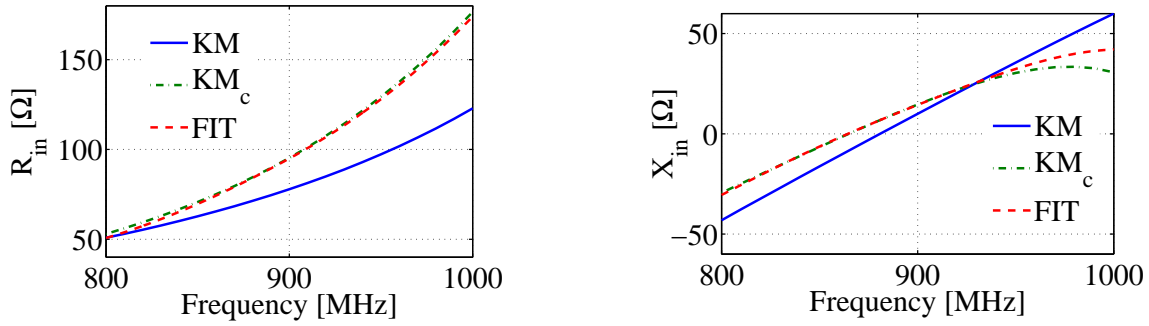


**Figure A.8.** Real and imaginary parts of the input impedance, using King-Middleton (KM), corrected King-Middleton ( $KM_c$ ) and the Finite Integration Technique (FIT). Cylindrical length = 8 cm, cylindrical radius = 2.5 mm.

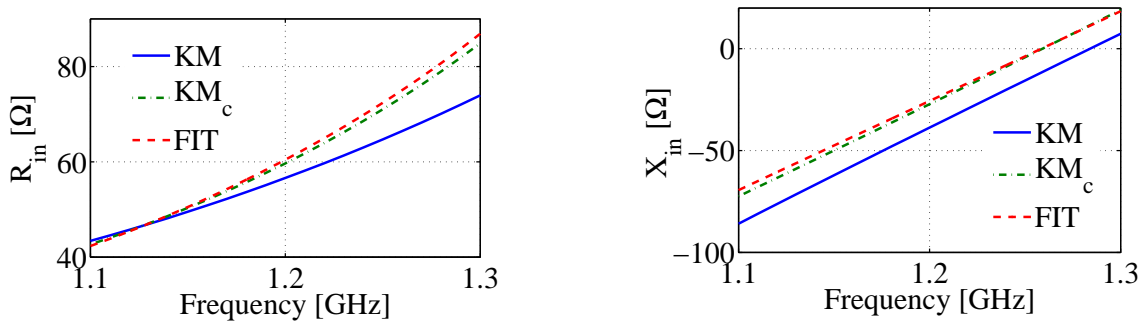
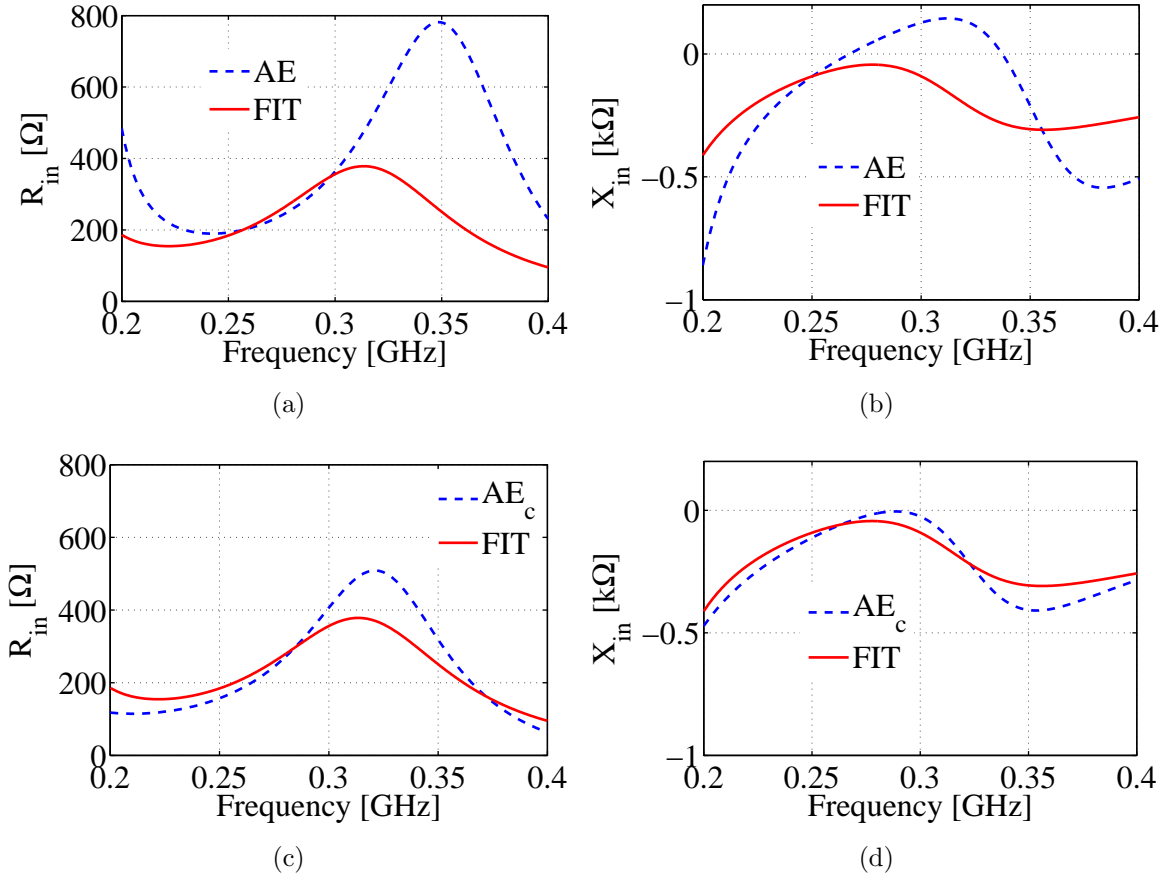


**Figure A.9.** Real and imaginary parts of the input impedance, using King-Middleton (KM), corrected King-Middleton ( $KM_c$ ) and the Finite Integration Technique (FIT). Cylindrical length = 5.5 cm, cylindrical radius = 2.5 mm.

### A.3 Strip Folded-Dipole Antenna

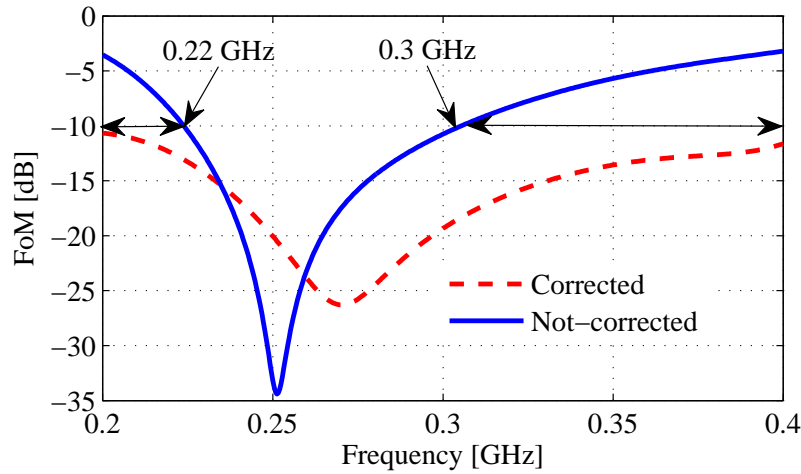
In this section, the accuracy of the analytical expressions for the strip folded dipole antenna is discussed. Two simulation examples implementing the analytical expressions introduced in Sec. 4.3 at 300 MHz and at 1.5 GHz are presented. Fig. A.10 shows the input impedance (real and imaginary parts) of a strip folded-dipole antenna possessing the following dimensions,  $W_1 = 0.04$  m,  $W_2 = 0.03$  m,  $d = 0.0125$  m,  $L = 0.25$  m, calculated with and without the correction factor (see Eq. (4.9)) for the inter-element spacing  $d$ .

In the same figure FIT-results are shown.



**Figure A.10.** Real (a) and imaginary (b) parts of the input impedance vs. frequency. And the corrected real (c) and imaginary (d) parts of the input impedance versus frequency.  $W_1 = 0.04$  m,  $W_2 = 0.03$  m,  $d = 0.0125$  m,  $L = 0.25$  m.

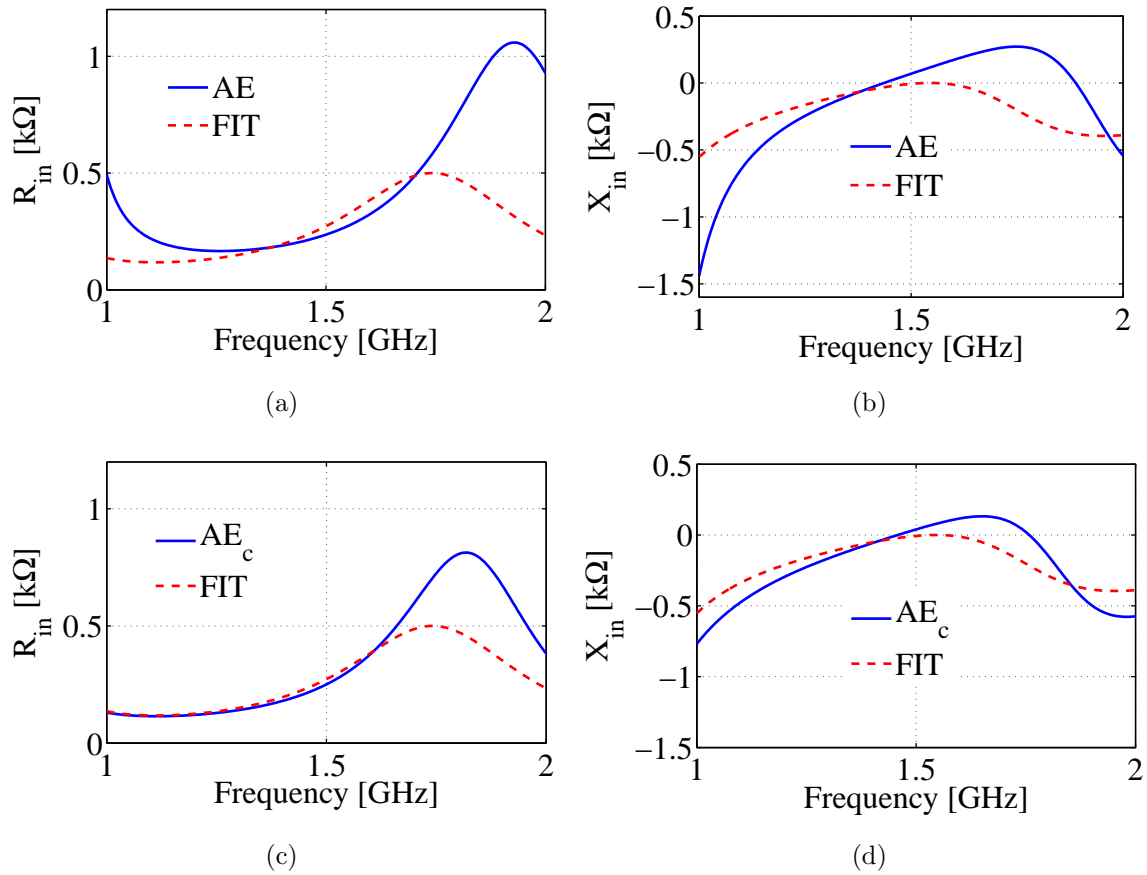
To quantify the improvement of the correction factor in terms of a single Figure of Merit, Eq.(1.2) is used to transform the deviations into power reflection coefficients. Fig. A.11 shows the resulting FoM as a function of frequency with (dashed curve) and without (solid curve) implementing the correction factor in the analytical expressions. Both results are compared to the results of the Finite Integration Technique (FIT). It is clear from the figure that when the correction factor is implemented, the validity range (0.2 GHz - 0.4 GHz) is extended 1.5 times compared to the validity range without implementing the correction factor (0.22 GHz - 0.3 GHz).



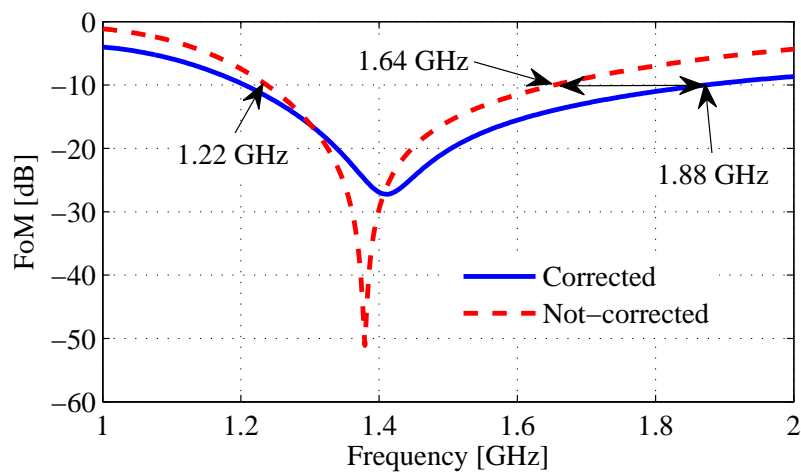
**Figure A.11.** FoM as a function of frequency due to the mismatch between AE and FIT.

Fig. A.12 shows the input impedance (real and imaginary parts) of a strip folded-dipole antenna possessing the following dimensions,  $W_1 = 0.004$  m,  $W_2 = 0.002$  m,  $d = 0.004$  m,  $L = 0.0475$  m, calculated with and without the correction factor (see Eq. (4.9)) for the inter-element spacing  $d$ . Figs. A.12(a) and A.12(b) show the real and imaginary parts, consecutively, of the input impedance calculated using the analytical expressions presented in Sec. 4.3 without implementing the correction factor for the inter-element distance  $d$ . In addition, the Figures show the real and imaginary parts of the input impedance calculated by the FIT using CST Microwave Studio.

The results after using the correction factor are plotted in Figs. A.12(c) and A.12(d). It is indicated in the figures that when the correction factor is implemented, the deviations between the results of the FIT and the results of the analytical expressions decreases. To quantify the improvement when the correction factor is implemented, the FoM is used to transform the deviations into reflection coefficients. Fig. A.13 shows the resulting FoM as a function of frequency with (solid curve) and without (dashed curve) implementing the correction factor in the analytical expressions. It is clear from the figure that when the correction factor is implemented, the validity range (1.22 GHz - 1.88 GHz) is extended more than 50 % compared to the validity range without implementing the correction factor (1.22 GHz - 1.64 GHz).



**Figure A.12.** Real (a) and imaginary (b) parts of the input impedance versus frequency. And the corrected real (c) and imaginary (d) parts of the input impedance versus frequency.  $W_1 = 0.004\text{m}$ ,  $W_2 = 0.002\text{m}$ ,  $d = 0.004\text{m}$ ,  $L = 0.0475\text{ m}$ .



**Figure A.13.** FoM as a function of frequency due to the mismatch between AE and FIT.



# Frequency Selective Surfaces Equivalent Circuit Model

---

## B.1 Correction Factor G

In [119] the first order correction term G, at oblique angle of incidence is obtained as:

$$G(p, d, \lambda, \theta, \varphi) = \frac{A}{B}, \quad (\text{B.1.1})$$

where:

$$A = \frac{1}{2}(1 - \beta^2)^2 \left[ \left(1 - \frac{\beta^2}{4}\right) (C_{+1} + C_{-1}) + 4\beta^2 C_{+1} C_{-1} \right], \quad (\text{B.1.2})$$

$$B = \left(1 - \frac{\beta^2}{4}\right) + \beta^2 \left(1 + \frac{\beta^2}{2} - \frac{\beta^2}{8}\right) (C_{+1} + C_{-1}) + 2\beta^6 C_{+1} C_{-1}. \quad (\text{B.1.3})$$

In the above:

$$\beta = \sin \left( \frac{\pi w}{2p} \right). \quad (\text{B.1.4})$$

The coefficients  $C_{\pm 1}$  are obtained from:

$$C_n = \frac{1}{tS_n} - \frac{1}{|n|}, \quad n = \pm 1, \pm 2, \dots \quad (\text{B.1.5})$$



For a  $TE$  polarized incident plane wave:

$$t = j \frac{p \cos(\theta)}{\lambda}, \quad (\text{B.1.6})$$

$$S_n = \frac{\gamma_n}{\gamma_0}. \quad (\text{B.1.7})$$

The propagation constant  $\gamma_n$  is given by:

$$\gamma_n = -j \sqrt{\left(\sin(\theta) + \frac{n\lambda}{p}\right)^2 - 1}, \quad (\text{B.1.8})$$

from which follows that  $\gamma_0 = \cos(\theta)$ . From B.1.12 and B.1.7:

$$S_n t = -j \sqrt{\left(\frac{p \sin(\theta)}{\lambda} \pm n\right)^2 - \frac{p^2}{\lambda^2}}, \quad (\text{B.1.9})$$

and from B.1.5:

$$C_n^{TE} = \frac{1}{\sqrt{\left(\frac{p \sin(\theta)}{\lambda} + n\right)^2 - \frac{p^2}{\lambda^2}}} - \frac{1}{|n|}. \quad (\text{B.1.10})$$

Therefore:

$$C_{\pm 1}^{TE} = \frac{1}{\sqrt{\left(\frac{p \sin(\theta)}{\lambda} \pm 1\right)^2 - \frac{p^2}{\lambda^2}}} - 1. \quad (\text{B.1.11})$$

For the dual case of a  $TM$  polarized incident plane wave:

$$t = j \frac{p \sec(\varphi)}{\lambda}, \quad (\text{B.1.12})$$

$$S_n t = \gamma_n \gamma_0, \quad (\text{B.1.13})$$

where:

$$\gamma_n = -j \sqrt{\left(\sin(\varphi) + \frac{n\lambda}{p}\right)^2 - 1}, \quad (\text{B.1.14})$$

from which  $\gamma_0 = \cos(\varphi)$  is obtained. Therefore:

$$S_n t = \sqrt{\left(\frac{p \sin(\varphi)}{\lambda}\right)^2 + n^2 - \frac{p^2}{\lambda^2}}, \quad (\text{B.1.15})$$

and from B.1.5:

$$C_n^{TM} = \frac{1}{\sqrt{\left(\frac{p \sin(\varphi)}{\lambda}\right)^2 + n^2 - \frac{p^2}{\lambda^2}}} - \frac{1}{|n|}, \quad (\text{B.1.16})$$

from which follows that

$$C_{\pm 1}^{TM} = \frac{1}{\sqrt{1 - \left(\frac{p \cos(\varphi)}{\lambda}\right)^2}} - 1. \quad (\text{B.1.17})$$



# Bibliography

---

- [1] Available at: <http://www.itu.int/ITU-D/ict/statistics/ict/graphs/mobile.jpg> (accessed 25 February 2014).
- [2] Dave Evans, *The Internet of Things, How the Next Evolution of the Internet is Changing Everything*, Cisco White Paper, April 2011.
- [3] *More than 50 Billion Connected Devices*, Ericsson White Paper, February 2011.
- [4] K. David, S. Dixit, and N. Jefferies, “2020 vision, the wireless world research forum looks to the future,” *IEEE Vehicular Technology Magazine*, pp. 22–29, September 2010.
- [5] BCC Research, *Global Markets and Technologies for Wireless Sensors*, Report Nr. IAS019A, February 2012.
- [6] R. Thusu, “Wireless sensor use is expanding in industrial applications,” *Sensors*, June 2010.
- [7] R. J. M. Vullers, R. V. Schaijk, H. J. Visser, J. Penders, and C. V. Hoof, “Energy harvesting for autonomous wireless sensor networks,” *IEEE Solid-State Circuits Magazine*, pp. 29–38, 2010.
- [8] D. Snoonian, “Smart buildings,” *IEEE Spectrum*, vol. 40, no. 8, pp. 18–23, August 2003.
- [9] Qi Wireless Power Consortium. Available at: <http://www.wirelesspowerconsortium.com/technology/> (accessed 16-01-2014).
- [10] A. Kurs, A. Karalis, R. Moffet, J. Joannopoulos, P. Fisher, and M. Soljacic, “Wireless power transfer via strongly coupled magnetic resonances,” *Science*, vol. 317, no. 5834, pp. 83–86, July 2007.
- [11] I. Mayordomo, T. Dräger, P. Spies, J. Bernhard, and A. Pflaum, “An overview of technical challenges and advances of inductive wireless power transmission,” *Proceedings of the IEEE*, vol. 101, no. 6, pp. 1302–1311, June 2013.
- [12] H. Visser and R. Vullers, “RF energy harvesting and transport for wireless sensor network applications: Principles and requirements,” *Proceedings of the IEEE*, vol. 101, no. 6, pp. 1410–1423, June 2013.
- [13] RFID Journal. [Online]. Available: [www.rfidjournal.com/faq/28/139](http://www.rfidjournal.com/faq/28/139).
- [14] J. Heikkinen, P. Salonen, and M. Kivikoski, “Planar antennas for 2.45 ghz wireless power transfer,” in *Proc. Radio Wireless Conf., Denver, CO, USA*, pp. 63–66, 2000.
- [15] J. Hagerty, F. Helmbrecht, W. McCalpin, R. Zane, and Z. Popovic, “Recycling ambient microwave energy with broad-band rectenna arrays,” *IEEE Transactions on Microwave Theory and Techniques*, vol. 53, no. 3, pp. 1014–1024, March 2004.
- [16] B. Strassner and K. Chang, “5.8-GHz circularly polarized rectifying antenna for wireless microwave power transmission,” *IEEE Transactions on Microwave Theory and Techniques*, vol. 50, no. 8, pp. 1870–1876, August 2000.

- [17] A. Safarian, A. Shameli, A. Rofougaran, M. Rofougaran, and F. Flaviis, "RF identification (RFID) reader front ends with active blocker rejection," *IEEE Transactions of Microwave Theory and Techniques*, vol. 57, no. 5, pp. 1320–1329, May 2009.
- [18] Y. Tikhov, I.-J. Soon, and Y.-H. Min, "Rectenna design for passive RFID transponders," in *European Microwave Conference*, 2007, pp. 995–998.
- [19] V. Marian, B. Allard, C. Vollaie, and J. Verdier, "Strategy for microwave energy harvesting from ambient field or a feeding source," *IEEE Transactions on Power Electronics*, vol. 27, no. 11, pp. 4481–4491, 2012.
- [20] E. Falkenstein, M. Roberg, and Z. Popovic, "Low-power wireless power delivery," *IEEE Transactions on Microwave Theory and Techniques*, vol. 60, no. 7, pp. 2277–2286, 2012.
- [21] S. Ladan, N. Ghassemi, A. Ghiotto, and K. Wu, "Highly efficient compact rectenna for wireless energy harvesting application," *IEEE Microwave Magazine*, vol. 14, no. 1, pp. 117–122, 2013.
- [22] M. Pinuela, P. D. Mitcheson, and S. Lucyszyn, "Ambient RF energy harvesting in urban and semi-urban environments," *IEEE Transactions on Microwave Theory and Techniques*, vol. 61, no. 7, pp. 2715–2726, 2013.
- [23] Electrical Review, Intelligent buildings A holistic perspective on energy management, Oct. 2009. [Online]. Available: <http://www.electricalreview.co.uk/features/6495-118645>.
- [24] Z. Zheng, S. Yu, W. Shin, and J. Hou, "PAS: A wireless-enabled cell-phone incorporated personal assistant system for independent and assisted living," in *Proc. Int. Conf. Distrib. Comput.*, pp. 233–242, 2008.
- [25] A. Aggarwal and R. Joshi, "A system for mobile assisted living," in *Proc. IEEE Int. Conf. Netw. Sens. Control*, pp. 233–237, 2012.
- [26] Sarah Romero, Creatively Address Rising Costs and Environmental Concerns, AutomatedBuildings.com, December 2008.
- [27] BusinessWire, European home automation market is set to double, Aug. 2007. [Online]. Available: <http://www.businesswire.com/news/home/20070814005177/en/European-Home-Automation-Market-Set-Double>.
- [28] Markets and Markets European smart homes and assisted living - Advanced technologies and global market (2010-2015) April 2011 Available at: <http://www.marketsandmarkets.com/Market-Reports/smart-homes-385.html>.
- [29] Smart Homes and Home Automation - 2nd Edition, November 2013. Research and Markets Available at: [http://www.researchandmarkets.com/reports/2699603/smart\\_homes\\_and\\_home\\_automation\\_2nd.edition](http://www.researchandmarkets.com/reports/2699603/smart_homes_and_home_automation_2nd.edition).
- [30] Macktez, XO name servers, 2004. [Online]. Available: <http://www.macktez.com/2004/wiring-a-building>.
- [31] M. Dugre, F. Freyer, and A. Anders, "BACNet and EnOcean enable energy efficient buildings," White paper.
- [32] Ivory Egg, Energy harvesting, wireless and next generation energy management explained, Mar. 2010. [Online]. Available: <http://ivoryegg.co.uk/2010/03/energyharvesting-wireless-and-next-generationenergy-management-explained/>.
- [33] H. J. Visser, *Approximate Antenna Analysis for CAD*. John Wiley & Sons, Chichester, UK, 2009.
- [34] J. Rahola, "Power waves and conjugate matching," *IEEE Transactions on Circuits and Systems II: Express Briefs*, vol. 55, no. 1, pp. 92–96, 2008.
- [35] W. C. Brown, "The history of power transmission by radio waves," *IEEE Transactions of Microwave Theory and Techniques*, vol. 32, no. 9, pp. 1230–1242, 1984.

- [36] G. Monti, L. Tarricone, and M. Spartano, "X-band planar rectenna," *IEEE Antennas and Wireless Propagation Letters*, vol. 10, pp. 1116–1119, 2011.
- [37] S. Keyrouz and H. J. Visser, "Efficient direct-matching rectenna design for rf power transfer applications," in *J. Phys.: Conf. Ser.* 476012093, 2013.
- [38] H. J. Visser and R. J. M. Vullers, "Time efficient method for automated antenna design for wireless energy harvesting," in *Proc. Loughborough Antennas and Propagation Conf. (LAPC)*, 2010, pp. 433–436.
- [39] M. Stoopman, S. Keyrouz, H. J. Visser, K. Philips, and W. A. Serdijn, "A self-calibrating RF energy harvester generating 1 V at  $-26.3$  dBm," in *Symposium on VLSI Circuits*, 2013.
- [40] D. A. Fleri and C. L. D., "Nonlinear analysis of the Schottky-barrier mixer diode," *IEEE Transactions on Microwave Theory and Techniques*, vol. 21, no. 1, pp. 39–43, 1973.
- [41] S. Keyrouz, H. J. Visser, and A. G. Tjihuis, "Rectifier analysis for radio frequency energy harvesting and power transport," in *42th European Microwave Conference*, 2012.
- [42] J. A. C. Theeuwes, H. J. Visser, M. C. van Beurden, and G. J. N. Doodeman, "Efficient, compact, wireless battery design," in *Proc. European Conf. Wireless Technologies*, 2007, pp. 233–236.
- [43] HSMS-285x, 282x surface mount zero bias Schottky diodes data sheet. [Online]. Available: <http://www.avagotech.com>.
- [44] Advanced Design System (ADS) 2009 — Agilent [Online]. Available: [www.home.agilent.com](http://www.home.agilent.com).
- [45] *Agilent PNA-X series , N5242A Microwave Network Analyzer manual*. Agilent technology, 2010.
- [46] R. G. Harrison and X. Le Polozec, "Nonsquarelaw behavior of diode detectors analyzed by the ritz-galerkin method," *IEEE Transactions on Microwave Theory and Techniques*, vol. 42, no. 5, pp. 840–846, 1994.
- [47] K. Fujimori, S. Tamaru, K. Tsuruta, and S. Nogi, "The influences of diode parameters on conversion efficiency of rf-dc conversion circuit for wireless power transmission system," in *41st European Microwave Conference (EuMC)*, 2011, pp. 57–60.
- [48] L. Turicchia, M. Mandal, S.; Tavakoli, V. Fay, L.; Misra, J. Bohorquez, W. Sanchez, and R. Sarpeshkar, "Ultra-low-power electronics for non-invasive medical monitoring," in *IEEE Custom Integrated Circuits Conference*, 2009, pp. 85–92.
- [49] J. Dickson, "On-chip high-voltage generation in mnos integrated circuits using an improved voltage multiplier technique," *IEEE Journal of Solid-State Circuits*, vol. 11, no. 3, pp. 374–378, 1976.
- [50] C. A. Balanis, *Antenna Theory - Analysis and Design*. 3rd ed., John Wiley & Sons, New York, 2005.
- [51] P. V. Nikitin, K. V. S. Rao, S. F. Lam, V. Pillai, R. Martinez, and H. Heinrich, "Power reflection coefficient analysis for complex impedances in RFID tag design," *IEEE Transactions of Microwave Theory and Techniques*, vol. 53, no. 9, pp. 2721–2725, 2005.
- [52] B. G. Duffley, G. A. Morin, M. Mikavica, and Y. M. M. Antar, "A wide-band printed double-sided dipole array," *IEEE Transactions on Antennas and Propagation*, vol. 52, no. 2, no. 2, pp. 628–631, 2004.
- [53] R. P. Ghosh, B. Gupta, and S. K. Chowdhury, "Broadband printed dipole antennas with shaped ground plane," in *Proc. TENCON 2010 - 2010 IEEE Region 10 Conf.*, 2010, pp. 416–421.
- [54] C. Su, H. Chen, and K. Wong, "Printed dual-band dipole antenna with U-slotted arms for 2.4/5.2 GHz WLAN operation," *IET Electronic Letters*, vol. 38, pp. 1308–1309, October 2002.

- [55] Y. Chi, K. Wong, and S. Su, "Broadband printed dipole antenna with a step-shaped feed gap for dtv signal reception," *IEEE Transactions on Antennas and Propagation*, vol. 55, no. 11, pp. 3353–3356, 2007.
- [56] Y. Chi and K. Wong, "Wideband printed dipole antenna for dtv signal reception," in *Proc. TENCON 2007 - 2007 IEEE Region 10 Conf*, 2007, pp. 1–4.
- [57] C. S. T. SUITE, *CST Microwave Studio user manual*, 2010.
- [58] H. Yagi, "Beam transmission of ultra short waves," *Proceedings of the Institute of Radio Engineers*, vol. 16, no. 6, pp. 715–740, 1928.
- [59] N. Kaneda, W. R. Deal, Y. Qian, R. Waterhouse, and T. Itoh, "A broad-band planar quasi yagi antenna," *IEEE Transactions on Antennas and Propagation*, vol. 50, no. 8, pp. 1158–1160, August 2002.
- [60] J. M. Floc'h and H. Rmili, "Desing of multiband printed dipole antennas using parasitic elements," *Microwave and Optical Technology Letters*, vol. 48, No 8, pp. 1639–1645, August 2006.
- [61] J. M. Floc'h, "Wide band printed dipole design," in *Mediterranean Microwave Symposium (MMS)*, *IEEE*, 2011.
- [62] R. Cai, S. Lin, G. Huang, X. Zhang, W. Zhang, and J. Wang, "Research on a novel yagi-uda antenna fed by balanced microstrip line," in *Proc. (CJMW) China-Japan Joint Microwave*, 2011, pp. 1–4.
- [63] U.S. Frequency Allocations, Office of Spectrum Mangement, National Telecommunications and Information Administraion [Online]. Available: <http://www.ntia.doc.gov/osmhome/allochrt.html>.
- [64] S. Keyrouz, H. J. Visser, and A. G. Tijhuis, "Multi-band simultaneous radio frequency energy harvesting," in *7th European Conference on Antennas and Propagation (EuCAP)*, 2013, pp. 3058–3061.
- [65] Ultra Low Power Harvester Power Management IC with Boost Charger, and Nano-Powered Buck Converter, Texas Instruments. Available: <http://www.ti.com/product/bq25570>.
- [66] D. De Donno, L. Catarinucci, and L. Tarricone, "An UHF RFID energy-harvesting system enhanced by a DC-DC charge pump in silicon-on-insulator technology," *IEEE Microwave and Wireless Components Letters*, vol. 23, no. 6, pp. 315–317, June 2013.
- [67] H. Kanaya, S. Tsukamoto, T. Hirabaru, and D. Kanemoto, "Energy harvesting circuit on a one-sided directional flexible antenna," *IEEE Microwave and Wireless Components Letters*, vol. 23, no. 3, no. 3, pp. 164–166, March 2013.
- [68] A. Georgiadis, A. Collado, S. Via, and C. Menses, "Flexible hybrid solar/em energy harvester for autonomous sensors," in *IEEE MTT-S International Microwave Symposium Digest*, 2011.
- [69] H. J. Visser, "Analytical equations for the analysis of folded dipole array antennas," in *Proc. 38th European Microwave Conference*, 2008, pp. 706–709.
- [70] R. S. Elliot, *Antenna theory and design*. Prentice Hall, 1981.
- [71] W. C. Gibson, *The method of moment in electromagnetics*. Chapman & Hall/CRC, 2008.
- [72] M. C. T. Weiland, "Discrete electromagnetism with the finite integration technique," *Progress In Electromagnetics Research*, vol. 32, pp. 65–87, 2001.
- [73] C. Butler, "The equivalent radius of a narrow conducting strip," *IEEE Transactions on Antennas and Propagation*, vol. 30, no. 4, pp. 755–758, 1982.
- [74] T. S. Rappaport, *Wireless Communications: Principles and Practices*. Prentice Hall PTR, 2nd edition, 2002.

- [75] G. Thiele, E. Ekelman, and L. Henderson, "On the accuracy of the transmission line model of the folded dipole," in *Proc. Antennas and Propagation Society Int. Symp.*, vol. 17, 1979, pp. 744–747.
- [76] H. J. Visser, "Improved design equations for asymmetric coplanar strip folded dipoles on a dielectric slab," in *Proc. Second European Conf. Antennas and Propagation*, 2007, pp. 1–6.
- [77] J. Yang, D. Nyberg, and J. Yin, "Impedance matrix of a folded dipole pair under eleven configuration," *IET Microwaves, Antennas and Propagation*, vol. 4, Iss. 6, no. 6, pp. 697–703, 2010.
- [78] R. Lampe, "Design formulas for an asymmetrical coplanar strip folded dipole," *IEEE Transactions on Antennas and Propagation*, vol. 33, pp. 1028–1031, 1985.
- [79] —, "Correction to "design formulas for an asymmetric coplanar strip folded dipole"," *IEEE Transactions on Antennas and Propagation*, vol. 34, no. 4, p. 611, 1986.
- [80] D. M. Pozar, *Microwave Engineering*. New York: Wiley, 2nd edition, 2002.
- [81] W. Hilberg, "From approximations to exact relations for characteristic impedances," *IEEE Transactions on Microwave Theory and Techniques*, vol. 17, no. 5, pp. 259–265, 1969.
- [82] S. Keyrouz, H. J. Visser, R. J. M. Vullers, and A. Tijhuis, "Novel analytical procedures for folded strip dipole antennas," in *6th European Conference on Antennas and Propagation*, 2012, pp. 2479–2482.
- [83] EMPIRE Xccel IMST GmbH, 2012 [Online]. Available: [www.empire.de](http://www.empire.de).
- [84] S. Kane, "Numerical solution of initial boundary value problems involving maxwell's equations in isotropic media," *IEEE Transactions on Antennas and Propagations*, vol. 14, no. 3, pp. 302–307, 1966.
- [85] H. Wheeler, "The radianshpere around a small antenna," *Proceedings of the IRE*, pp. 1325 – 1331, August 1959.
- [86] C. Mendes and C. Peixeiro, "Theoretical and experimental validation of a generalized Wheeler cap method," in *The Second European Conference on Antennas and Propagation*, 2007, pp. 1–6.
- [87] E. Newman, P. Bohley, and C. Walter, "Two methods for the measurement of antenna efficiency," *IEEE transactions on Antennas and Propagations*, vol. AP-23, pp. 457–461, July 1975.
- [88] H. Choo, R. Rogers, and H. Ling, "On the Wheeler cap measurement of the efficiency of microstrip antennas," *IEEE Transactions on Antennas and Propagation*, vol. 53, no. 7, pp. 2328–2332, 2005.
- [89] D. Agahi and W. Domino, "Efficiency measurements of portable-handset antennas using the Wheeler cap," *Applied Microwave and Wireless*, pp. 34–42.
- [90] I. Ida, K. Ito, and Y. Okano, "Accurate measurement of small input resistances using a conventional network analyzer," *IEEE Transactions on Antennas and Propagation*, vol. 47, no. 2, pp. 389–391, 1999.
- [91] R. Maaskant, D. Bekers, M. Arts, W. van Cappellen, and M. Ivashina, "Evaluation of the radiation efficiency and the noise temperature of low-loss antennas," *IEEE Antennas and Wireless Propagation Letters*, vol. 8, pp. 1166–1170, 2009.
- [92] H. J. Visser, A. C. F. Reniers, and J. A. C. Theeuwes, "Ambient RF energy scavenging: GSM and WLAN power density measurements," in *Proc. 38th European Microwave Conference*, 2008, pp. 721–724.
- [93] G. Monti, L. Corchia, and L. Tarricone, "UHF wearable rectenna on textile materials," *IEEE transactions on Antennas and Propagations*, vol. 61, no. 7, pp. 3869–3873, 2013.
- [94] S. Kawasaki, "Microwave wpt to a rover using active integrated phased array antennas," in *5th European Conference on Antennas and Propagation*, 2011, pp. 3909–3912.
- [95] H. J. Visser, "Design considerations for low-power, high-sensitivity rectennas," in *8th European Conference on Antennas and Propagation*, 2014.



- [96] C. Mikeke, H. Arai, A. Georgiadis, and A. Collado, "DTV band micropower RF energy-harvesting circuit architecture and performance analysis," in *IEEE International Conference on RFID-Technologies and Applications RFID-TA*, 2011, pp. 561–567.
- [97] M. Stoopman, S. Keyrouz, H. J. Visser, K. Philips, and W. A. Serdijn, "Co-design of a CMOS rectifier and small loop antenna for highly sensitive RF energy harvesters," *IEEE Journal of Solid-State Circuits*, vol. 49, No. 3, March 2014.
- [98] M. Stoopman, W. A. Serdijn, and K. Philips, "A robust and large range optimally mismatched RF energy harvester with resonance control loop," in *IEEE International Symposium on Circuits and Systems*, 2012, pp. 476–479.
- [99] S. Scorcioni, L. Larcher, and A. Bertacchini, "A reconfigurable differential CMOS RF energy scavenger with 60 % peak efficiency and -21 dBm sensitivity," *IEEE Microwave and Wireless Components Letters*, vol. 23, no. 3, pp. 155–157, 2013.
- [100] L. Vincetti, K. Maini, E. Pinotti, L. Larcher, S. Scorcioni, A. Bertacchini, D. Grossi, and A. Taccchini, "Broadband printed antenna for radiofrequency energy harvesting," in *International Conference on Electromagnetics in Advanced Applications*, 2012, pp. 814–816.
- [101] S. Mandal and R. Sarpeshkar, "Low-power cmos rectifier design for rfid applications," *IEEE Transactions on Circuits and Systems*, vol. 54, no. 6, pp. 1177–1188, June 2007.
- [102] T. Le, K. Mayaram, and T. Fiez, "Efficient far-field radio frequency energy harvesting for passively powered sensor networks," *IEEE Journal of Solid-State Circuits*, vol. 43, no. 5, pp. 1287–1302, May 2008.
- [103] A. Papatto, F. Carrara, and G. Palmisano, "A 90-nm CMOS threshold-compensated RF energy harvester," *IEEE Journal of Solid-State Circuits*, vol. 46, no. 9, pp. 1985–1997, 2011.
- [104] Texas Instruments, Ultra Low Power Harvester Power Management IC with Boost Charger, and Nano-Powered Buck Converter, bq25570. [Online]. Available: [www.ti.com/product/bq25570](http://www.ti.com/product/bq25570).
- [105] User's Guide for bq25570 Battery Charger Evaluation Module for Energy Harvesting. [Online] Available: <http://www.ti.com/general/docs/lit/getliterature.tsp?baseLiteratureNumber=sluuaa7&fileType=pdf>.
- [106] Arduino Mega 2560 board. [Online] Available: <http://arduino.cc/en/Main/arduinoBoardMega2560>.
- [107] Powercast P2110CSR. [Online]. Available: <http://www.powercastco.com/products/development-kits/>.
- [108] Cresta WX688 weather station. [Online]. Available: <http://handleidingkwijt.com/cresta-wx688-weerstation/>.
- [109] J. Hautcoeur, F. Colombel, X. Castel, M. Himdi, and E. Motta Cruz, "Optically transparent monopole antenna with high radiation efficiency manufactured with silver grid layer (AgG1)," *Electronics Letters*, vol. 45, no. 20, pp. 1014–1016, 2009.
- [110] N. Outaleb, J. Pinel, M. Drissi, and O. Bonnaud, "Microwave planar antenna with RF-sputtered indium tin oxide films," *Microwave and Optical Technology Letters*, vol. 24, no. 1, pp. 3–7, 2000.
- [111] U. Olgun, C. C.C., and J. L. Volakis, "Investigation of rectenna array configurations for enhanced RF power harvesting," *IEEE Antennas and Wireless Propagation Letters*, vol. 10, pp. 262–265, 2011.
- [112] H. Sun, M. He, and Z. Zhong, "A dual-band rectenna using broadband yagi antenna array for ambient RF power harvesting," *IEEE Antennas and Wireless Propagation Letters*, vol. 12, pp. 918–921, 2013.
- [113] A. Georgiadis, G. Andia, and A. Collado, "Rectenna design and optimization using reciprocity theory and harmonic balance analysis for electromagnetic (em) energy harvesting," *IEEE Antennas and Wireless Propagation Letters*, vol. 9, pp. 444–446, 2010.

- [114] J. Hagerty, F. Helmbrecht, W. McCalpin, R. Zane, and Z. Popovic, "Broadband rectenna arrays for randomly polarized incident waves," in *30th European Microwave Conference*, 2000, pp. 1–4.
- [115] R. J. Langley and E. A. Parker, "Equivalent circuit model for arrays of square loops," *Electronics Letters*, vol. 18, no. 7, pp. 294–296, 1982.
- [116] A. Yilmaz and M. Kuzuoglu, "Design of the square loop frequency selective surfaces with particle swarm optimization via the equivalent circuit model," *Radio Engineering*, vol. 18, no. 2, pp. 95–102, June 2009.
- [117] E. Fuad Kent, B. Dken, and M. Kartal, "A new equivalent circuit based fss design method by using genetic algorithm," in *2nd International Conference on Engineering Optimization*, September 6 - 9, 2010, Lisbon, Portugal.
- [118] N. Marcuvitz, *Waveguide Handbook*. New York : McGraw-Hill, 1951.
- [119] C. K. Lee and R. J. Langley, "Equivalent-circuit models for frequency-selective surfaces at oblique angles of incidence," *IEE Proceedings*, vol. 132, no. 6, pp. 395–399, 1985.
- [120] M. J. Archer, "Wave reactance of thin planar strip gratings," *Int. J. Electronics*, vol. 58, pp. 187–230, 1985.
- [121] F. Costa, A. Monorchio, and G. Manara, "An equivalent circuit model of frequency selective surfaces embedded within dielectric layers," in *IEEE Antennas and Propagation Society Int. Symp.*, 2009, pp. 1–4.
- [122] P. Callaghan, E. A. Parker, and R. J. Langley, "Influence of supporting dielectric layers on the transmission properties of frequency selective surfaces," *IEE Proceedings Microwaves, Antennas and Propagation*, vol. 138, no. 5, pp. 448–454, 1991.
- [123] R. Luebbers and B. Munk, "Some effects of dielectric loading on periodic slot arrays," *IEEE Transactions on Antenna*, vol. 26, no. 4, pp. 536–542, 1978.
- [124] T. S. Mok and E. A. Parker, "Gridded square frequency selective surface," *Int. J. Electronics*, vol. 61, pp. 219–224, 1986.
- [125] P. Hannan and M. Balfour, "Simulation of a phased-array antenna in waveguide," *IEEE transactions on Antennas and Propagations*, vol. 13, no. 3, pp. 342–353, 1965.
- [126] J. Stockmann and R. Hodges, "The use of waveguide simulators to measure the resonant frequency of ku-band microstrip arrays," in *IEEE Antennas and Propagation Society International Symposium*, vol. 1, 2005, pp. 417–420.
- [127] R. C. Hansen, *Phased Array Antennas*. John Wiley & Sons, 2nd edition, Nov 19, 2009.
- [128] Yageo Capacitors, Available: <http://uk.farnell.com/yageo-phycomp/cc0603crnp09bnr47/cap-mlcc-c0g-np0-0-47pf-50v-0603/dp/721803>.
- [129] W. Li, B. Zhang, J. Zhou, and B. You, "High isolation dual-port MIMO antenna," *Electronics Letters*, vol. 49, no. 15, pp. 919–921, 2013.
- [130] H. Visser and R. Vullers, "Design equations for small loop-based rectennas," in *Loughborough Antennas and Propagation Conference*, 2011, pp. 1–4.
- [131] H. Visser, "Printed folded dipole antenna design for rectenna and RFID applications," in *7th European Conference on Antennas and Propagation (EuCAP)*, 2013, pp. 2852–2855.
- [132] H. J. Visser, *Array and Phased Array Antenna Basics*. John Wiley & Sons, Chichester, UK, 2005.



# List of publications

---

## Journal publications

- [J1] S. Keyrouz, G. Perotto, and H. J. Visser, “Frequency Selective Surface for RF Energy Harvesting Applications,” *IET Microwaves, Antennas and Propagation*, Vol. 8, Issue 7, May 2014.
- [J2] M. Stoopman, S. Keyrouz, H. J. Visser, K. Philips and W. A. Serdijn, “A Co-design of a CMOS Rectifier and Small Loop Antenna for Highly Sensitive RF Energy Harvesters,” *IEEE Journal of Solid State Circuits*, vol. 49, no. 3, March 2014.
- [J3] S. Keyrouz, H. J. Visser and A. G. Tijhuis, “Novel Empirical Equations to Calculate the Impedance of a Strip Dipole Antenna,” *RadioEngineering*, vol. 22, no. 4, pp. 1258-1261 December 2013.
- [J4] S. Keyrouz, H. J. Visser, C. Vollaire and A. G. Tijhuis, “Highly Efficient 50 $\Omega$  Rectenna System for Smart Building Initiative,” In preparation.

## Conference publications

- [C1] H. J. Visser and S. Keyrouz, “Radiative RF Power Transfer Solutions for Wireless Sensors,” in *2011 IEEE International Symposium on Antennas and Propagation*, July 2014, Memphis, USA.
- [C2] S. Keyrouz, G. Perotto, and H. J. Visser, “Lumped-Element Tunable Frequency Selective Surfaces,” in *Proceedings of the 8th European Conference on Antennas and Propagation*, April 2014, The Hague, The Netherlands.
- [C3] S. Keyrouz and H. J. Visser, “RF Energy Harvesting and Transport for Wireless Autonomous Sensor Network Applications: Principles and Requirements,” in *Power Autonomous Communicating Objects*, October 2013, France.
- [C4] M. Stoopman, S. Keyrouz, H.J. Visser, K. Philips and W. A. Serdijn, “Co-Design of a 90 nm CMOS Rectifier and Small Loop Antenna for Large Range RF Energy

- Harvesters,” in *Progress In Electromagnetics Research Symposium*, August 2013, Stockholm, Sweden. (abstract)
- [C5] S. Keyrouz and H. J. Visser, “Efficient Direct-Matching Rectenna Design for RF Power Transfer Applications,” *Journal of Physics: Conference Series 476 012093*, December 2013, London, UK.
- [C6] M. Stoopman, S. Keyrouz, H.J. Visser, K. Philips and W. A. Serdijn, “A Self-Calibrating RF Energy Harvester Generating 1V at -26.3 dBm,” in *Symposia on VLSI Technology and Circuits*, 2013, pp. C226 - C227, June 2013, Kyoto, Japan.
- [C7] S. Keyrouz and H. J. Visser, “Multi-band Simultaneous Radio Frequency Energy Harvesting,” in *Proceedings of the 7th European Conference on Antennas and Propagation*, pp. 3058 3061, April 2013, Gothenburg, Sweden.
- [C8] S. Keyrouz, H. J. Visser and A. G. Tijhuis, “Ambient RF Energy Harvesting From DTV Stations,” in *Loughborough Antennas and Propagation Conference*, pp. 1-4, November 2012, Loughborough, UK.
- [C9] H. J. Visser and S. Keyrouz, “Optimizing RF Energy Transport: Channel Modeling and Transmit Antenna and Rectenna Design,” *Loughborough Antennas and Propagation Conference*, pp. 1-8, November 2012, Loughborough, UK.
- [C10] S. Keyrouz, G. Perotto, and H. J. Visser, “Novel Broadband Yagi-Uda Antenna for Ambient Energy Harvesting” in *Proceedings of the European Microwave Week*, pp. 518 521, October 2012, Amsterdam, the Netherlands.
- [C11] S. Keyrouz, H. J. Visser and A. G. Tijhuis, “Rectifier Analysis for Radio Frequency Energy Harvesting and Power Transport,” *Proceedings of the European Microwave Week*, pp. 428 431, October 2012, Amsterdam, the Netherlands.
- [C12] S. Keyrouz, H. J. Visser and A. G. Tijhuis, “Ambient RF Energy Harvesting and Power Transport”, in *Proceedings of the 2nd International Workshop on Wireless Energy Transport and Harvesting*, May 2012, Leuven, Belgium.
- [C13] S. Keyrouz, H. J. Visser R. J. M. Vullers and A. G. Tijhuis, “Novel Analytical Procedures for Folded Strip Dipole Antennas,” in *Proceedings of the 6th European Conference on Antennas and Propagation*, pp. 2479-2482, March 2012, Prague, Czech Republic.
- [C14] S. Keyrouz, H. J. Visser and A. G. Tijhuis, “Novel Design Equations for Cylindrical Dipole Antennas”, in *Proceedings of the 1st International Workshop on Wireless Energy Transport and Harvesting*, June 2011, Eindhoven, The Netherlands.

# Acknowledgements

---

It is my pleasure to thank many people who in different ways have contributed to the completion of this thesis.

First and foremost, I would like to thank my promoter Hubregt Visser. Without your constant motivation, support and guidance, I would have never been able to grow and become an independent researcher. Without your help, especially during the writing phase, this thesis would have never been completed on time. I greatly appreciate the high degree of freedom and the trust you gave me.

Additionally, I am thankful to my second promotor Anton Tjihuis. You were always there when I really needed your help. You have always encouraged and guided me. Thank you for your critical questions, remarks and comments concerning this thesis that improved greatly thanks to your feedback. You have always encouraged and taught me to think beyond the antenna-rectifier research more into the ‘Helicopter view’ system level.

I am grateful to Gianluca Perotto, together we shared the same office for almost one year. Thank you for the pleasant atmosphere. I was really lucky to co-supervise your internship and your Master’s thesis project. Your work contributed to Chapter 7 of this thesis.

Many thanks also to all the members of my Ph.D. committee for their comments that improved the consistency of the thesis. I would especially like to thank, Prof.dr. E.A. Lomonova, Prof.dr.ir. P.G.M. Baltus and Prof.dr.ir. G.A.E Vandenbosh. Thank you for your time and your comments. I wish to thank Prof.dr. Cristian Vollaire for all the discussions and comments and also for the warm welcome during my three months exchange period in Lyon. Thank you for taking care about my accommodation in Lyon and providing all the necessary components and equipment needed for the project.

I would like to thank all my colleagues and friends at the EM group, special thanks to Mojtaba Zamanifekri. We have started our Ph.D together and we have shared almost everything, I enjoyed the conferences that we have attended together and also the coffee

breaks during several years. Also I would like to thank Satoru Sakai for proof-reading different parts of this thesis. Furthermore, I would like to thank Ulf Johansen and Rob Mestrom for providing me with their LaTeX template. I am really grateful to Suzanne Kuijlaars. Thank you for taking care about all the administrative stuff especially by fixing my defence date. I especially would like to mention Ad Reniers for his time and assistance during most of the measurements presented in this thesis, especially for the radiation efficiency measurements. I would also like to thank Rainier van Dommele for taking care about all the software licenses. I express my gratitude to Martijn van Beurden, especially during the writing phase of my thesis. Your exceptional organization skills are inspiring all the EM group members. Thank you for helping me structuring my thesis, also thank you for answering different questions regarding the rectifier's impedance modeling and antenna feed modeling. I would also like to thank Bas de Hon for providing time and answering different questions during the last three years.

It has been a great pleasure to work with all the colleagues at the Holst Centre. I am thankful to Hans Pflug, who contributed directly to the completion of this thesis by building the measurement setup and providing all the measurement results of Chapter 6. Thank you Hans for answering all my questions. A special thanks goes to Ruud Vullers and Rob van Schaijk. Thank you both for your support and motivation especially during the initial phase of my Ph.D. I would like also to thank Nauman Kiyani for his advices, especially during the writing phase of the thesis. A special thank goes to Mark Stoopman for designing the CMOS rectifier and the control loop that allowed us to considerably decrease the size of the rectenna. It has been a pleasure working together on the same project.

I am indebted to my brother Fakher El-Dine Keyrouz. You have encouraged and helped me to come to Germany and continue my Master studies. Thank you for your support on all different levels. I am deeply thankful to my parents for their unconditional support and sacrifices.

Last but certainly not least, I want to thank my life-companion Rosy. Thank you for all your sacrifices, all the weekends you spent with me in the office while writing this thesis. Without your love, I probably would have lost a great deal of my discipline, endurance, and eagerness.

# Curriculum Vitae

---

Shady Keyrouz was born on January 21st, 1984, in Bsharri, Lebanon. He enrolled in electrical engineering at the Notre Dame University (NDU) in Beirut, Lebanon, in 2003 and obtained his BE degree in 2008. He received his M.Sc. degree in Communication Technology from Ulm University, Germany, in 2010. In the same year he started as a Ph.D.-student at the Electromagnetics group (EM) of the Faculty of Electrical Engineering of Eindhoven University of Technology (TU/e), Eindhoven, The Netherlands. In 2010 he joined Holst Centre/imec as a Ph.D. researcher. His research interests include antenna modeling, rectenna design, wireless power transmission and reflect-array antennas.



.